NANYANG TECHNOLOGICAL UNIVERSITY

SHEAR BEHAVIOUR OF STEEL MEMBERS AND BEAM-TO-COLUMN JOINTS UNDER ELEVATED TEMPERATURES

QIAN ZHENHAI

SCHOOL OF CIVIL AND ENVIRONMENTAL ENGINEERING

2007

SHEAR BEHAVIOUR OF STEEL MEMBERS AND BEAM-TO-COLUMN JOINTS UNDER ELEVATED TEMPERATURES

QIAN ZHENHAI

2007

Shear Behaviour of Steel Members and Beam-to-Column Joints under Elevated Temperatures

Qian Zhenhai

School of Civil and Environmental Engineering

A thesis submitted to the Nanyang Technological University
in fulfilment of the requirement for the degree of
Doctor of Philosophy

2007

DEDICATION

To My Wife, Hong Yan

and My Daughter, Xin Qi

ACKNOWLEDGEMENTS

First and foremost, I would like to express my special gratitude to Associate Professor K. H. Tan, for his endless support and wonderful supervision in my PhD study.

I would also like to gratefully acknowledge Dr. Vanissorn Vimonsatit, Dr. Toh Wee Siang, Dr. Huang Zhan Fei, Dr. Yuan Wei Feng, Mr. Phng Guan Hwee, Eugene and Mr. Ronny Budi Dharma, for their precious suggestions and comments throughout my research course.

Special thanks should also go to all technical staffs of Construction Technology Laboratory of School of Civil and Environmental Engineering in NTU, for their valuable advices and helps along my study.

Finally, I am indebted to my wife and parents for their unceasing love and moral encouragements.

ABSTRACT

The objective of current research is to investigate the possibility of using "Component-Based" method to predict steel joint behaviour at elevated temperatures. In this study, the beam web shear component of a joint has first been simplified into an equivalent girder web panel subjected to shear force. Five series of beams have been tested at both ambient and elevated temperatures, without thermal restraints. In addition, three more series of specimens have been tested subjected to thermal restraints at higher temperatures. All plate girders tested at elevated temperatures exhibit web buckling failure mode, similar to ambient temperature tests. A mechanical model for the shear component in present work has been improved from plate theory. In addition, simple analytical procedures have been developed to obtain a clear description for deflection behaviour of the shear component. Detailed finite element simulations have also been conducted, to investigate both single web and overall beam behaviour. Apart from structural component analyses, six steel beam-to-column joints have been tested as "Cruciform" assemblies, which consisted of three cruciform specimens tested at 700^{o}C with three restrained levels, and another three specimens tested at three isothermal temperatures, without thermal restraints. Detailed finite element simulations have also been conducted with good agreement with test results. With the utilization of "Component-Based" method, a simple analytical model has been established with incorporation of shear component in beam web. Moment-rotation results obtained from this analytical model show acceptable agreements compared with test results. Thus, proposed mechanical model is able to predict behaviour for extended end-plate joint at elevated temperatures.

CONTENT

Acknowledgements I

Abstract II

Contents III

List of Tables IX

List of Figures XI

List of Symbols XVIII

Chapter 1 Introduction

1.1 Introduction 1

1.2 Fire Characteristic and Fire Experiments 2

1.3 Analysis of Steel Structural Member Fire Resistance 4

1.4 Characteristics of Semi-rigid Joints 5

1.5 “Component-Based” Method for Steel Joint Analysis 7

1.6 Scope and Objective of Research 9

1.7 Thesis Layout 11

Chapter 2 Literature Review

2.1 Introduction 13

2.2 Mathematical (Curve-Fitting) Analytical Methods 14

2.3 Finite Element Analysis (FEA) Methods 21

2.4 Experimental Investigations 28

2.5 Simplified Analytical Models 37

2.6 Mechanical Models (Spring Models) 40

2.7 Conclusion 46

Chapter 3 Elevated Temperature Material Properties

3.1 Introduction 48

3.2 Steel Mechanical Properties Degradation in Fire 48

3.2.1 Steel Material Properties Tests 49

3.2.2 Steel Stress-Strain Models 50

3.3 Thermal Characteristics of Steel in Fire 59

3.3.1 Thermal Expansion of Steel 59

3.3.2 Thermal Conductivity of Steel 60

3.3.3 Specific Heat of Steel 61

3.4 Degradation of Bolts in Fire 62

3.5 Conclusion 64

Chapter 4 Behaviour of Shear Zone in Steel Beam-to-Column Joint

4.1 Introduction 66

4.2 Mechanical Modelling of Shear Zone with Plate Girder Theory 68

4.2.1 Mechanical Models of Plate Girder under Shear Load 68

4.2.2 Mechanical Models of Plate Girder under Shear at Elevated Temperatures 74

4.2.3 Effects of Thermal Axial Restraint on Mechanical Behaviour of Plate Girder at Elevated Temperatures 77

4.3 Pre-buckling and Post-buckling Deflection Investigation 80

4.3.1 Background of Elastic Plate Buckling Theory 81

4.3.2 Elastic Pre- and Post-buckling Behaviour Investigations 85

4.3.2.1 Boundary Condition Assumptions 85

4.3.2.2 Plate Out-of-Plane Deflection Functions 87

4.3.2.3 Governing Differential Equations and Airy-Type Stress Function 87

4.3.2.4 Analytical Method of Governing Differential Equations 89

4.3.3 Analytical Predictions and Comparisons 91
4.3.3.1 One-Directional Compression Analysis 92
4.3.3.2 Pure Shear Load Analysis 93
4.3.3.3 Analysis of Combination of Shear and Compression Loads 96
4.4 Pre- and Post-buckling In-Plane Deflection Investigation 98
4.5 Conclusion 101

Chapter 5 Experimental Investigation of Shear Zone in Steel

5.1 Introduction 102
5.2 Unrestrained Plate Girder Experimental Set-up and Programme 103
5.2.1 Development of Unrestrained Plate Girder Test Programme 103
5.2.2 Test Specimen Preparations 104
5.2.3 Heating Furnace Configuration and Loading Device 109
5.2.4 Deformation Acquisition System 109
5.2.5 Strain Measurement System 110
5.2.6 Temperature Measurement and Thermal Insulation 111
5.2.7 Unrestrained Plate Girder Test Procedure 112
5.3 Unrestrained Plate Girder Experiment Results 114
5.3.1 Plate Girder Shear Buckling and Ultimate Shear Capacity 114
5.3.2 Test Results of Ambient Tests (TG3-1, TG4-1 and TG5-1) 115
5.3.3 Elevated-Temperature Test Results (TG3, TG4 and TG5 series) 118
5.3.4 Ultimate Shear Capacity Results 125
5.3.5 Failure Mode of Web Panel 127
5.4 Restrained Plate Girder Experimental Set-up and Programme 130
5.4.1 Development of Restrained Plate Girder Test Programme 130
5.4.2 Design of Test Specimens 131
5.4.3 Loading Facility and Axial Restrained System 133

5.4.4 Hearing Facility 134
5.4.5 Deformation and Temperature Acquisition Instrumentations 135
5.4.6 Restrained Plate Girder Test Procedure 136
5.5 Restrained Plate Girder Experimental Results 136
5.5.1 Plate Girder Ultimate Shear Capacity 137
5.5.2 Temperature Distribution 138
5.5.3 Deflection Characteristics 139
5.5.4 Effect of Axial Restraints 142
5.6 Deflection Characteristics and Analytical Predictions 145
5.7 Conclusion 148

Chapter 6 Finite Element Analysis of Shear Zone within Steel Beam-to-Column Joint

6.1 Introduction 150
6.2 Finite Element Analysis Models 151
6.2.1 Unrestrained Plate Girder Single Web Panel Model 155
6.2.2 Unrestrained and Restrained Whole Beam FE Model 160
6.3 Finite Element Analysis Results 162
6.3.1 FE Predictions of Unrestrained Shear Component at Ambient Temperature 163
6.3.2 FE Predictions of Unrestrained Shear Component at Elevated Temperatures 164
6.3.3 FE Results of Whole Beam Simulation for Unrestrained and Restrained Tests 165
6.4 Comparisons of FE Predictions with Test and Analytical Results 167
6.4.1 FE Predictions of Ambient Temperature Tests 167
6.4.2 FE Predictions of Thermally Unrestrained Tests at Elevated Temperatures 170
6.4.3 FE Predictions of Whole Beam Unrestrained Simulations 175

6.4.4 FE Predictions of Thermally Restrained Tests 176
6.5 Conclusion 180

Chapter 7 Steel Beam-to-Column Joint Numerical and Mechanical Modelling

7.1 Introduction 181
7.2 Steel Beam-to-Column Joint Experimental Set-up 181
7.2.1 Development of Cruciform Test Programme 182
7.2.2 Cruciform Specimen Specifications 183
7.2.3 Heating Facility 185
7.2.4 Loading Facility and Restraint Systems 186
7.2.5 Deflection Acquisition System (LVDTs) 188
7.2.6 Temperature Distribution Acquisitions 189
7.3 Cruciform Test Procedure 190
7.4 Cruciform Experimental Results and Discussions 191
7.4.1 Restrained Cruciform Test Temperature Measurement 191
7.4.2 Restrained Cruciform Test Deflection Characteristics 194
7.4.3 Beam Web Measurements of Restrained Cruciform Tests 200
7.4.4 Initial Imperfection Measurement of Unrestrained Tests 202
7.4.5 Unrestrained Cruciform Test Temperature Measurements 204
7.4.6 Unrestrained Cruciform Test Deflection Characteristics 207
7.5 Conclusion 211

Chapter 8 Steel Beam-to-Column Joint Numerical and Mechanical Modelling

8.1 Introduction 213
8.2 Steel Beam-to-Column Numerical Joint Modelling 214

8.2.1 FE Model of Restrained Steel Beam-to-Column Joint 216
8.2.2 FE Model of Unrestrained Steel Beam-to-Column Joint 217
8.2.3 Verifications of FE Steel Beam-to-Column Joint Model 219
8.3 FE Predictions of Steel Beam-to-Column Joint 221
8.3.1 FE Predictions of Thermally Restrained Steel Joint 221
8.3.2 FE Predictions of Thermally Unrestrained Steel Joint 223
8.3.3 Failure Modes and Comparisons of Cruciform Tests 224
8.4 Steel Beam-to-Column Joint Spring Stiffness Model at Elevated Temperatures 233
8.4.1 "Component-Based" Mechanical Model for Extended End-plate Steel Joint 234
8.4.2 Simplified Mechanical Predictions for Tension Zone 237
8.4.3 Simplified Mechanical Predictions for Compression Zone 240
8.4.4 Simplified Mechanical Predictions for Shear Zone 241
8.4.5 Moment-Rotation Relationship of Steel Joints 243
8.5 Conclusion 246

Chapter 9 Conclusions and Further Recommendations

9.1 Introduction 248
9.2 Mechanical Investigations of Beam Web Shear Component 249
9.2.1 Experimental Investigation of Shear Component 249
9.2.2 Mechanical and FEM Investigations of Shear Component 250
9.3 Experimental Investigations of Steel Beam-to-Column Joint 251
9.4 Numerical and Mechanical Investigations of Steel Joint 253
9.5 Recommendations for Future Works 254

References 255

LIST OF TABLES

Table	Title	Page
1.1	Main Mechanical Zones and Components of Joint	8
2.1	Curve Fitting Constants and Standardization Constant (Frye *et al.*1975)	18
3.1	EC 3 Stress-strain Relationship for Steel at Elevated Temperatures (ENV 1993-1-2)	53
3.2	Reduction Factors of Steel at Elevated Temperatures according to Eurocode 3 (ENV 1993-1-2)	54
3.3	Strength Retention Factors for Steel in BS 5950: Part 8 (BS 5950-8)	56
3.4	Strength Retention Factors for Grade 8.8 Bolts in Fire (BS 5950-8)	62
3.5	Strength Reduction Factors for Bolt in EC 3: Part1.2 (EN 1993-1-2)	64
4.1	Coefficients of Airy Stress Function	91
5.1	Properties of Unrestrained Test Girders	105
5.2	Detailed Measurement Datum for TG3-1 Flange Curvatures	107
5.3	Top and Bottom Flange Thicknesses of TG3-1	107
5.4	Detailed Measurement for TG3-1 Web Panel Curvatures	107
5.5	Material Properties of TG1, TG2, TG3, TG4 and TG5 series	108
5.6	Shear Buckling Load and Ultimate Shear Strength of Test Girders	114
5.7	Comparison of Results obtained from Analytical Approach, and Experiments	126
5.8	Details of Restrained Test Specimen Series	133
5.9	Experimental Results of Restrained Plate Girder Tests	137
6.1	Geometric and Material Properties of Isolated Web Panel Models	154
6.2	Boundary Conditions for Unrestrained Plate Girder Model	158
6.3	Boundary Conditions for Whole Beam FE model	162

Table	Title	Page
6.4	Comparisons among FE, Analytical Predictions and Test Results of TG1 to TG5 series at Ambient Temperature	168
6.5	Comparisons among FE, Analytical Predictions and Test Results of G1 to G5 Series at Ambient Temperature	170
6.6	Comparisons among FE, Analytical Predictions and Test Results of Unrestrained TG2-TG5 series at Elevated Temperatures	171
6.7	Comparisons among FE and Analytical Predictions of Unrestrained G1 to G5 series at Elevated Temperatures	172
6.8	Comparisons of Experimental Results with FE Predictions for RTG3, RTG4 and RTG5 Series	177
7.1	Material and Geometrical Property of Cruciform Specimen	184
7.2	Relative Temperature Measurements for CR1, CR2 and CR3	194
7.3	Maximum Initial Out-of-Plane Measurements for Unrestrained Cruciform Beam Sections	204
7.4	Relative Temperature Measurements for CR4, CR5 and CR6	206
8.1	Boundary Conditions for Restrained Cruciform FE Model	217
8.2	Boundary Conditions for Unrestrained Cruciform FE Model	218
8.3	Comparisons of Experimental Results with FE and Analytical Predictions	233

LIST OF FIGURES

Figure	Title	Page
1.1	Development of Real Fire	2
1.2	ISO Standard Fire Curve (ISO 834, 1975)	3
1.3	Different Modelling for Beam-to-Column Joints	5
1.4	Effects of Different Types of Joint on Beam Bending Moment	6
1.5	Rotation versus Moment of Steel Beam-to-Column Joint	6
1.6	Component Identifications of Steel End-plate Joint	8
2.1	Geometry Parameters of Flexible Joint (Romstad *et al.* 1970)	15
2.2	Tri-linear Moment-Rotation Curve-Fitting Method (Moncarz *et al.* 1981)	16
2.3	Semi-Rigid Joint Type and Geometrical Parameters (Frye *et al.* 1975)	17
2.4	Steel Beam-to-Column Joint Types (Jones *et al.* 1980)	28
2.5	Typical Moment-Rotation Curves (Jones *et al.* 1980)	28
2.6	Critical Zones of Steel Bolted Beam-to-Column Joint (Witteveen *et al.* 1982)	41
2.7	Simplified Model for Double Angle Joint (Wales *et al.* 1982)	41
2.8	Spring Models for Welded Joints (Tschemernegg and Hummer, 1988[a], 1988[b])	42
2.9	Idealized Spring Stiffness Model for Bare-Steel Flush End-plate Joint (Leston-Jones *et al.* 1997[a], 1997[b])	45
2.10	General Spring Model for Flexible End-plate Joint (Al-Jabri, 1999)	45
3.1	Bi-Linear Model for Steel Stress-Strain Curve	50
3.2	Tri-Linear Model for Steel Stress-Strain Curve	51
3.3	Idealized Bilinear-Elliptical Stress-Strain Model	51

Figure	Title	Page
3.4	Basic Formulation of Stress-strain Relationship of Steel at Elevated Temperature	52
3.5	Reduction Factor for Steel at Elevated Temperature (ENV 1993-1-2)	54
3.6	Variation of Stress-strain Relationship for Grade S275 Steel (ENV 1993-1-2)	55
3.7	Strength Retention Factors according to BS 5950: Part 8 and EC 3: Part 1.2	56
3.8	Stress-Strain Curve of Steel at Elevated Temperatures (ECCS 1983)	57
3.9	Thermal Elongation of Steel (EN 1993-1-2)	60
3.10	Thermal Conductivity Coefficient of Steel (EN 1993-1-2)	61
3.11	Specific Heat of Steel (EN 1993-1-2)	62
3.12	Strength Reduction Factor for Grade 8.8 Bolts (Kirby 1995)	64
4.1	Local Buckling of Beam in the Cardington Test (Wald *et al.* 2004)	67
4.2	Equivalent Shear Zone Model for Steel Beam-to-Column Joint	67
4.3	Collapse Mechanism for Plate Girders under Shear	69
4.4	Membrane Tensile Stress Distribution and Collapse Behaviour	72
4.5	Stress and Moments Distribution at Compressive Hinge	73
4.6	Collapse Mechanism for Plate Girders under Shear with Restraints	77
4.7	Restrained Beam Model for Thermal Restrained Plate Girder	80
4.8	Load Distributions and Geometrical Property	86
4.9	Strain ε_x Derivation due to Plate Out-of-Plane Deflection	87
4.10	Load Distribution and Geometrical Property for One-Directional Compression	92
4.11	Comparisons between Different Analytical Approaches	93
4.12	Non-Dimensional Load-Deflection Behaviour of Different Imperfect Plates	94

Figure	Title	Page
4.13	Comparisons of Load-Deflection Behaviour between Numerical and Analytical Predictions (Square Plate)	95
4.14	Comparisons of Load-Deflection Behaviour between Numerical and Analytical Predictions (Rectangular Plates $\lambda = 1.5$)	96
4.15	Comparisons of Load-Deflection Behaviour between Numerical and Analytical Predictions for Square Plates under Combination of Shear and Compression	97
4.16	Comparisons of Load-Deflection Behaviour between Square and Rectangular Plates under Combination of Shear and Compression	98
4.17	In-Plane Deflection Development of Web Panel Shear Component	99
5.1	Unrestrained Shear Component Test Set-up	104
5.2	Unrestrained Test Girder Configurations	106
5.3	Location for Geometrical Imperfection Measurement	106
5.4	Typical LVDT Measurement Location	110
5.5	Locations of Strain Gauges for TG5-1	111
5.6	Location of Thermocouple Wires for TG5 series	111
5.7	Strain Measure points for TG5-1 Panel 2	115
5.8	Strain Measurements for TG5-1 Panel 2	115
5.9	Principal and Maximum Shear Strain for Web Panel 2 of TG5-1	116
5.10	Load versus Vertical Deflection of TG3-1 Web Panels	117
5.11	Load versus Mid Span Deflection of TG3-1	117
5.12	Load versus Vertical Deflection of TG3-2 Web Panels	118
5.13	Load versus Out-of-Plane Deflection of TG3-2 Web Panels	119
5.14	Load versus Mid-Span deflection and Web Panel Deformation of TG3-2 Web Panels	119
5.15	Southwell Plot for TG3-2 Web Panel	120
5.16	Shear Load versus Out-of-Plane Deflection for TG4 series	121
5.17	Interaction between Shear and Bending Moment for Plate Girder	122
5.18	Temperature versus Time for Web Panel 1 and 2 of TG3-2	123

Figure	Title	Page
5.19	Typical Temperature Distribution for TG4-4 tested at 700 ^{o}C	125
5.20	Typical Longitudinal Temperature Distribution at Web of TG4-4	125
5.21	Failure Modes of Unrestrained Plate Girder Tests	128
5.22	Shear Capacity Ratios of Unrestrained Plate Girder Tests	129
5.23	Shear Capacity Ratios of Unrestrained Plate Girder Tests	130
5.24	Restrained Plate Girder Test Set-up (Elevation View)	131
5.25	Details of Steel Plate Girder Specimen (all dimensions are in mm)	133
5.26	Restrained Plate Girder Test Set-up (Plan View)	134
5.27	Typical Temperature Distribution for RTG4-1	138
5.28	Typical Longitudinal Temperature Distribution at Top Flange of RTG5-1	139
5.29	Load versus Out-of-Plane Deflection Characteristics	139
5.30	Deformed Shape for RTG4 Series	141
5.31	Load versus Deflection (mid-span) Characteristics	142
5.32	Axial Restraint Force Development	143
5.33	Panel Shear Strength Ratios for RTG3, RTG4 and RTG5 Series	144
5.34	Panel Shear Strength Ratios for axial restraint 8.2 kN/mm and 9.6 kN/mm at 670 ^{o}C	145
5.35	Out-of-Plane Deflection Characteristics Comparisons between Experimental and Analytical Predictions	146
5.36	In-Plane Deflection Characteristics Comparisons among Analytical Prediction, Experimental Measurements and Numerical Predictions	147
6.1	Simplified FE model of Shear Components of Steel Joint	152
6.2	FE Model for Unrestrained Shear Component	156
6.3	TG4-1 Load versus Out-of-Plane Deflection with Different initial Out-of-Plane Deflection	159
6.4	Load vs. Central Out-of-Plane Deflection for Different Meshes	160
6.5	von Mises Stress Distribution of TG5-1 Prior to Collapse	163

Figure	Title	Page
6.6	Shear Stress versus Out-of-Plane Deflection (TG3-1 TG4-1 TG5-1)	164
6.7	von Mises Stress Distribution of TG5-2 Prior to Collapse	165
6.8	Test Beam FEA Model (TG5 series)	166
6.9	von Mises Stress Distribution of TG5-2 Prior to Buckling	167
6.10	Vertical Deflection versus Load for TG5-1 Specimen	167
6.11	Shear Stress versus Principal and Maximum Shear Strain	169
6.12	Ultimate Shear Stress versus Temperature for G1-G5 and TG1-TG3 Series	173
6.13	Shear Stress Capacity Ratio versus Temperature for TG3, TG4 and TG5	174
6.14	Whole Beam Vertical Deflection Comparison of TG5-1 at Ambient Temperature between FEA and Test Results	175
6.15	Whole Beam Vertical Deflection Comparisons of TG4-4 at Elevated Temperature between FEA and Test Results	176
6.16	Shear Strength Ratio Comparisons between FE Predictions and Experimental Results	178
6.17	Comparisons of Shear Load versus Out-of-Plane Deflection between Experimental Results and FE Predictions	179
6.18	FE and Experimental Deformed Shape for RTG4-1 tested at 400 ^{o}C	179
7.1	Elevation View of Cruciform Test Set-Up	182
7.2	Bare Steel Extended End-plate Joint Detail (CR1, CR2, CR3)	183
7.3	Bare Steel Extended End-plate Joint Detail (CR4, CR5, CR6)	184
7.4	Elevation View of Electrical Heating Furnace	185
7.5	Unrestrained Cruciform Test Set-up	187
7.6	Plan View of Lateral Restraint System for CR4, CR5 and CR6	187
7.7	Plan View of Deflection Locations (CR1, CR2 and CR3)	188
7.8	Thermocouple Wire Locations	189
7.9	Typical Temperature Distribution of CR1	192

Figure	Title	Page
7.10	Deflection and Rotation Measurements of CR1	196
7.11	Deflection and Rotation Measurements of CR2	197
7.12	Deflection and Rotation Measurements of CR3	199
7.13	Measurement Scanning System Details	201
7.14	Measurement Reference Line for Left Beam Section of Cruciform	201
7.15	Test Web Panel Out-of-Plane Deflection Measurement for CR2	202
7.16	Measurement Reference Lines for Unrestrained Cruciforms	202
7.17	Initial Out-of-Plane Deflection Measurement for CR4 Left Beam Web	203
7.18	Typical Temperature Distribution of CR4	205
7.19	Deflection and Rotation Measurements of CR4	208
7.20	Deflection and Rotation Measurements of CR5	209
7.21	Deflection and Rotation Measurements of CR6	210
8.1	Steel Beam-to-Column Joint Finite Element Model	214
8.2	Web Buckling Test Cruciform Specifications (Bailey, 1999)	219
8.3	Failure Mode for Ambient Temperature Cruciform Test	220
8.4	FE and Test Results for Ambient Temperature Cruciform Test	220
8.5	Comparison between FE Predictions and Experimental Results for CR2	222
8.6	Comparison between FE Predictions and Experimental Results for CR5	224
8.7	Comparisons of Failure Modes for Restrained Cruciform Test	225
8.8	Comparisons of Failure Modes for Unrestrained Cruciform Test	227
8.9	Typical Failure Mode Comparison between FE Perdition and CR4 Test	229
8.10	Moment versus Maximum Out-of-Plane Deflection for CR4	229
8.11	Equivalent von Mises Stress and Principal Stress Distribution for Beam Web of CR4 at Separate Stages	231
8.12	Beam Out-of-Plane Deflection Distribution at Failure Stage of CR4	232

Figure	Title	Page
8.13	Steel Beam-to-Column End-plate Joint Spring Model	235
8.14	Simplified T-stub Model and Dimensions (EN 1993-1-8)	237
8.15	Failure Modes for T-stub Assembly	237
8.16	Trilinear Approximation of Steel Joint Moment-Rotation Relationship (EN 1993-1-8)	243
8.17	Comparison between Analytical Prediction and Test Results without Shear Component in Beam Web	245
8.18	Comparison between Analytical Prediction and Test Results with Shear Component in Beam Web	246

LIST OF SYMBOLS

a_p	Throat thickness of weld between beam flange and end-plate
c	Plastic hinge position
d , d_w	Depth of web panel between flanges
d_{cw}	Column depth between root fillet
$f_{p,T}$	Proportional limit strength at elevated temperatures (MPa)
$f_{y,20}$, f_y^{20}	Nominal yield stress at room temperature (MPa)
$f_{y,T}$, f_y^T	Effective yield strength at elevated temperatures (MPa)
h_t	Lever arm length of steel joint
$k_{y(T)}$	Retention ratios of yield strength at elevated temperatures
$k_{E(T)}$	Retention ratios of elastic modulus at elevated temperatures
r_c	Fillet root radius
t	Testing time; Thickness of web panel
t_{bf}	Beam flange thickness
t_{bw}	Beam web thickness
t_{cw}	Column web thickness
t_{cf}	Column flange thickness
t_{ep}	End-plate thickness
t_w	Thickness of web panel
m_{cf}	Distance between bolt shank center and column flange root fillet

m_{ep}	Distance between bolt shank center and beam welds
w	Plate out-of-plane deflection
w'	Initial imperfection of plate
A_s	Shaft area of bolt
A_{vb}	Shear area of beam web panel
A_{vc}	Shear area of column web panel
C_a	Specific heat of steel
D	Plate flexural rigidity
E , $E_0^{20}, E_{(20)}$	Elastic Stiffness at ambient temperature (MPa)
$E_{a,T}, E_0^T, E_{(T)}$	Elastic Stiffness at elevated temperatures (MPa)
$E_{b,T}$	Young's modulus of bolt at elevated temperature
K	Shear buckling coefficient of web panel
K_{bws}	Equivalent rotational shear stiffness of beam web panel
K_c	Compressive buckling coefficient of web panel
K_{cwc}	Compressive stiffness of column web
K_{cws}	Equivalent shear stiffness of column web
K_{sf}	Shear buckling coefficient for plates with two opposite edges simply supported and fixed
K_{ss}	Shear buckling coefficient for plates simply supported around four edges
K_t	Equivalent overall tensile stiffness
K_{ti}	Equivalent tensile stiffness of the $i-th$ bolt row
$K_{B(20)}$	Axial Stiffness of tested beam

K_{RS}	Stiffness of restrained system
K_{φ}	Initial rotational stiffness of steel joint
$k_{\Phi,cr}$	Pre-buckling rotational stiffness of beam web shear component
$k_{\Phi,u}^{'}$	Post-buckling rotational stiffness of beam web shear component
L_B, L_b	Effective length of the bolt
M	Bending moment applied on steel joint
M_{cfp}	Column flange plastic moment capacity
$M_{j,Rd}$	Moment capacity of steel joint
M_P	Plastic moment resistance of T-stub flange
M_{pfr}	Plastic moment capacity of flange
$M_{pfr}^{'}$	Reduced plastic moment capacity of flange
M_u	Ultimate moment capacity of steel joint
T_0	The ambient temperature (20^oC)
T	The furnace temperature; Steel temperature; Thickness of flange
V_{cr}	Critical shear force at ambient temperature
V_{test}	Experimental shear capacity
$V_{yw(T)}$	Maximum shear force in web panel at elevated temperature
V_{ult}	Ultimate shear force at ambient temperature
$V_{ult,(T)}$	Ultimate shear force at elevated temperatures
α	The thermal expansion coefficient of steel
β	Axial Restraint Ratio
$\varepsilon_{l,T}$	Limiting strain for yield strength at elevated temperatures

$\varepsilon_{p,T}$	Proportional limit strain at elevated temperatures
$\varepsilon_{u,T}$	Ultimate strain at elevated temperatures
$\varepsilon_{y,T}$	Yield strain at elevated temperatures
θ_d	Diagonal degree of web panel
λ_a	Thermal Conductivity Coefficient of Steel
$\sigma_{by,T}$	Yield strength of bolt at elevated temperature
$(\sigma_c)_{cr}$	Critical compressive stress for simply supported plate
$\sigma_{cwf,T}$	Yield strength of column flange at elevated temperature
$\sigma_{cwy,T}$	Yield strength of column web at elevated temperature
σ_c^T	Thermally restrained compressive force
σ_t^y	Tensile yield stress of web panel at ambient temperature
$\sigma_{ty(T)}$	Tensile yield stress of web panel at elevated temperatures
$\sigma_{ty}^{'}$	Modified tensile yield stress of restraint web panel
σ_{yw}	Yield strength of web panel at ambient temperature
τ_c	Modified critical shear stress for simply supported plate
τ_{cr}	Critical shear stress of web panel at ambient temperature
τ'_{cr}	Reduced buckling shear stress of web panel
$\tau_{cr(T)}$	Critical shear stress of web panel at elevated temperatures
τ_{yw}	Yield shear strength of web panel
ϕ	Joint rotation in radians
Φ	Airy stress function

CHAPTER 1
INTRODUCTION

1.1 Introduction

Steel has been widely used in the construction industry as an important type of construction material. During 1991-1992, in the United Kingdom and Sweden, steel construction enjoyed a high market share in both single and multi-storey buildings, totally consumed 850,000 tones of steel (Latter, 1994). Steel is often the preferred construction form due to speed of construction, reduction of site work, ease of application and competitive cost over similar concrete structures. However, compared to other construction materials, steel performs rather poorly under fire conditions. Steel has high value of thermal conductivity, therefore steel temperature increases rapidly in fire conditions, resulting in rapid loss of strength and stiffness. Recognizing these disadvantages when choosing steel as structural material, the establishment of the British Fire Protection Committee in 1899 commenced research on structural fire resistance. The first international fire prevention congress was convened in 1903. In 1932, the first structural fire resistance standard BS 476:1932 was issued (Shields *et al.* 1987). To date, a great amount of effort has been placed into the application of new protective materials and design methods for fire protection of steel structures.

For steel structures, the most popular method to provide fire protection is by applying insulating material on structure to delay the temperature rise. The objective of such a design method is to ensure that sufficient strength and stiffness

of steel can be retained within the specified duration. However, this kind of method is costly due to additional expenditure and construction time. Over recent years, it has been a trend to design steel beams and single storey portal frames to withstand fire without any fire protection (Bailey *et al.* 1998). There have been a great interest to understand the structural behaviour of different steel elements under fire conditions (Cooke *et al.* 1987, Faris *et al.* 1998, Liu *et al.* 2002, Huang *et al.* 2004, Tan *et al.* 2006, etc.). As steel framed structures normally consist of steel joints to assemble steel structural elements together, it is necessary to study the steel joint behaviour and their effects on the behaviour of steel framed structures. This leads to the purpose of current study to investigate the behaviour of steel beam-to-column joints in steel framed structures under fire conditions.

1.2 Fire Characteristic and Fire Experiments

To study fire resistance of structural elements, it is essential to understand the growth and development of fires. Generally, fire starts as the material ignites. The growth and decay of fire is complicated as it depends on the heat source and surrounding environment. It can be simplified into several phases as shown in Figure 1.1.

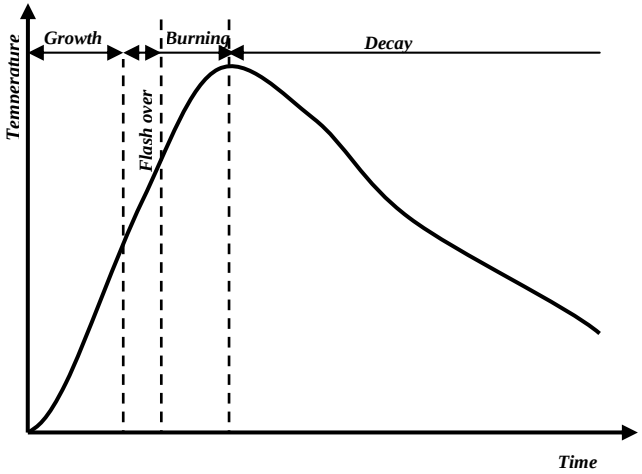

Figure 1.1Development of Real Fire

In the growth period, after ignition, fire spreads from the source towards other combustibles. In the early stage, the fire behaves similarly to that in the open situation. When the fire becomes fully developed and temperature increases rapidly, the compartment fire starts to experience growth. When the fire spreads to all available ignition sources within the compartment, there is a sudden transition from a growing fire to a fully developed fire, which is known as the "flashover" stage. After the flashover phase, the fire temperature rises quickly as the heat release rate within compartment reaches a peak. The rate of fire temperature rise continues until the fire sources deplete and decrease. Beyond the peak of fire temperature, the gas temperature begins to decrease as the fuel supply decreases. The fire reduces gradually and eventually dies out. As the fire growth is affected by the fire source, thermal characteristics of walls and ventilation area, etc., there is a need to define the standard fire temperature-time (T-t) relationship. Figure 1.2 shows the commonly used standard fire T-t relationship as defined in the ISO 834 (ISO, 1975), that is:

$$T = T_0 + 345\log_{10}(8t + 1) \tag{1.1}$$

in which: T = furnace temperature (^{o}C); T_0 =ambient temperature (20 ^{o}C); t =testing time (minute).

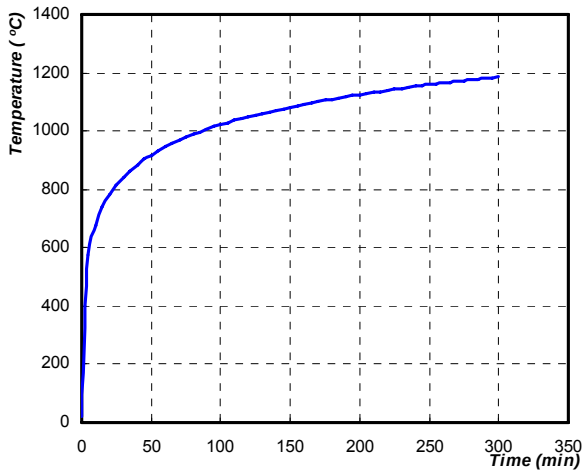

Figure 1.2 ISO Standard Fire Curve (ISO 834, 1975)

Obviously, ISO 834 standard fire curve does not represent the pattern of a natural fire as neither growth phase nor decay phase is defined in this curve. However, it establishes a common basis for comparing fire resistance tests conducted in different laboratories.

1.3 Analysis of Steel Structural Member Fire Resistance

In conventional practice, there are two most commonly used steel framed systems to resist lateral forces, viz. moment-resisting frames and braced frames (Chen *et al.* 1985). For moment-resisting frames, the flexural rigidities of steel beams and columns provide lateral stiffness, and the beams and columns are connected by moment-resisting joints. For both types of steel frames, the most conventional method of providing adequate fire protection is using some kind of insulation material to limit the growth of temperature of steel so as to maintain sufficient strength and stiffness in the event of a fire.

The British Steel Design Standard (BS 5950-8) specifies two design approaches for member fire resistance design in steel framed structures. The first method is the limiting temperature approach in which thermal insulation is provided to limit the rise in temperature in steel member to a value dependent on the type of member and stress level. The second approach is to calculate the strength capacity of a member using temperature-dependent material properties and temperature profile.

The method of fire resistance design of steel members used in Eurocode 3 (EN 1993-1-2) was first formulated in the European Convention for Constructional Steelwork Recommendations (ECCS, 1983). The original approach was to calculate the ratio of required strength at elevated temperatures to that at ambient temperature, for ensuring that the element would not collapse. Eurocode 3 gives two approaches for the fire resistance design of steelworks (EN 1993-1-2). The first approach is to

satisfy the load carrying criterion and the second is a limiting, or critical temperature approach. The second approach is only applicable to structural members which do not have stability problem. However, as discussed in Section 1.1, provision of fire protection is costly and time delay in construction due to the complexity of fire protection of steelworks. In recent years there have been more experimental investigations on structural response under fire conditions. This has resulted in the development of new engineering methods of analysis and design of steel members utilizing the inherent fire resistance of steel, and fire protection material, where necessary. As such, both insulation costs and construction time have been reduced significantly. It should be noted that in the UK practice, all columns are to be protected against fire. It is the secondary beams that can be designed to resist fire without insulation.

1.4 Characteristics of Semi-rigid Joints

In conventional steel frame analysis at ambient temperature, beam-to-column joint is assumed as "pinned" (no moment resistance) or "rigid" (full moment resistance). However, actual behaviour of joint is often intermediate between these two extreme situations (Jaspart, 2000). The moment-rotation characteristic of these beam-to-column joints are illustrated in Figure 1.3.

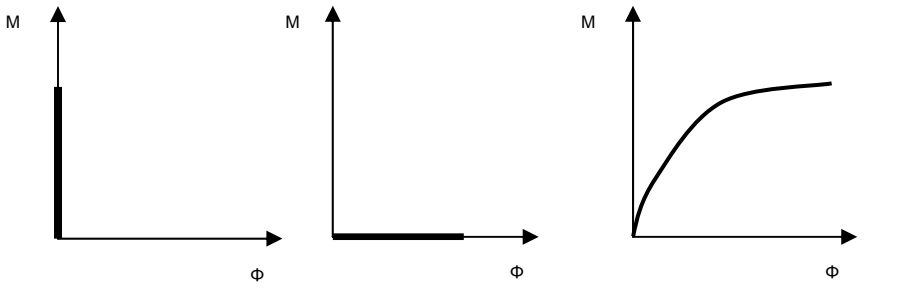

Figure 1.3 Different Modelling for Beam-to-Column Joints

Semi-rigid joint reduces the mid-span sagging moment of a beam by transferring the sagging moment to adjacent columns. This leads to a reduction of beam section

for design purpose. Moreover, Nethercot observed that semi-rigid joints can provide certain restraints against column buckling (Nethercot, 1985[a]). The relationship between different joint types and bending moment diagram is shown in Figure 1.4.

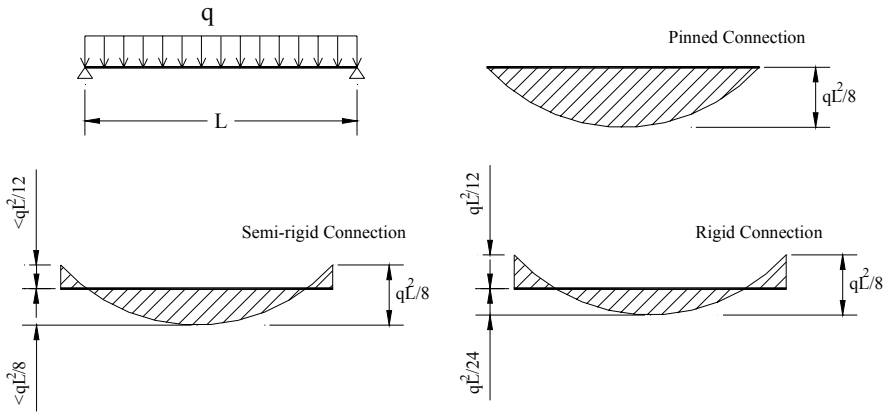

Figure 1.4 Effects of Different Types of Joint on Beam Bending Moment

The flexural behaviour of a semi-rigid joint is commonly defined by the relationship between moment transmitted by the joint and relative rotation of joint, as shown in Figure 1.5. The gradients of the moment-rotation curves from different experimental results represent the rigidity of joints. The moment-rotation characteristics of joints are nonlinear over the complete range of loading. Aggarwal *et al.* (1986) tested eight beam-column joints under increasing static load. The fixity provided by the test joints in the elastic region was close to ideal, but beyond 60% of moment capacity, the joint behaviour deviated from linearity.

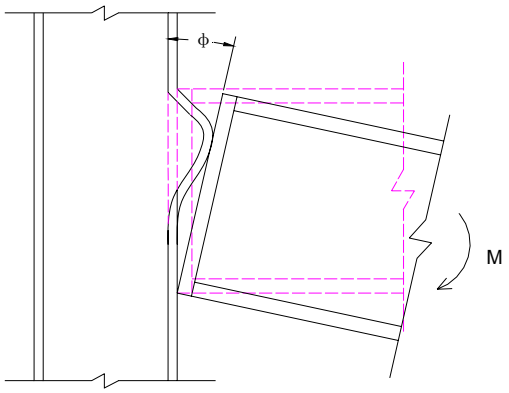

Figure 1.5 Rotation versus Moment of Steel Beam-to-Column Joint

In order to obtain the moment-rotation characteristics at the beam-to-column joints at elevated temperatures, Leston-Jones carried out several tests on small scale flush end-plate joints subjected to fire conditions (Leston-Jones, 1997[a]). However, until today, characteristics of steel joint moment-rotation responses at elevated temperatures are still not fully understood. The joint behaviour is affected by thermal restraint effects and material degradation at high temperatures. Three different approaches have been used to study the behaviour of joints, viz. mathematical model, finite element analysis and "Component-Based" method. The mathematical model is to fit expressions to experimental data for different joint types. This method can accurately describe the response of steel joints at elevated temperatures, but it is completely empirical in nature and requires a wide range of experiments. Finite element analysis is used to simulate the behaviour of joints at different temperatures. But as the complexity of steel joint increases, this method cannot accurately fit the experimental results. The "Component-Based" model identifies the behaviour of individual components and assembling them together to describe the whole joint behaviour. A detailed description of "Component-Based" method is included in the Section 1.5 and Section 2.6. It is also used to describe the test results of cruciform specimens in Section 8.4.

1.5 "Component-Based" Method for Steel Joint Analysis

The "Component-Based" analytical method at elevated temperatures stems from the ambient temperature model from the Eurocode 3: Annex J (ENV 1993-1-1), considering the steel degradation of mechanical properties at elevated temperature according to Eurocode 3 Part1.2 (EN 1993-1-2). With the "Component-Based" method, it is necessary to identify different components within a steel joint. For typical beam-to-column end-plate joint subjected to bending moment (as shown in Figure 1.6), these components can be divided into three main zones, viz. shear zone,

compression zone and tension zone. Each zone has different components as listed in Table 1.1.

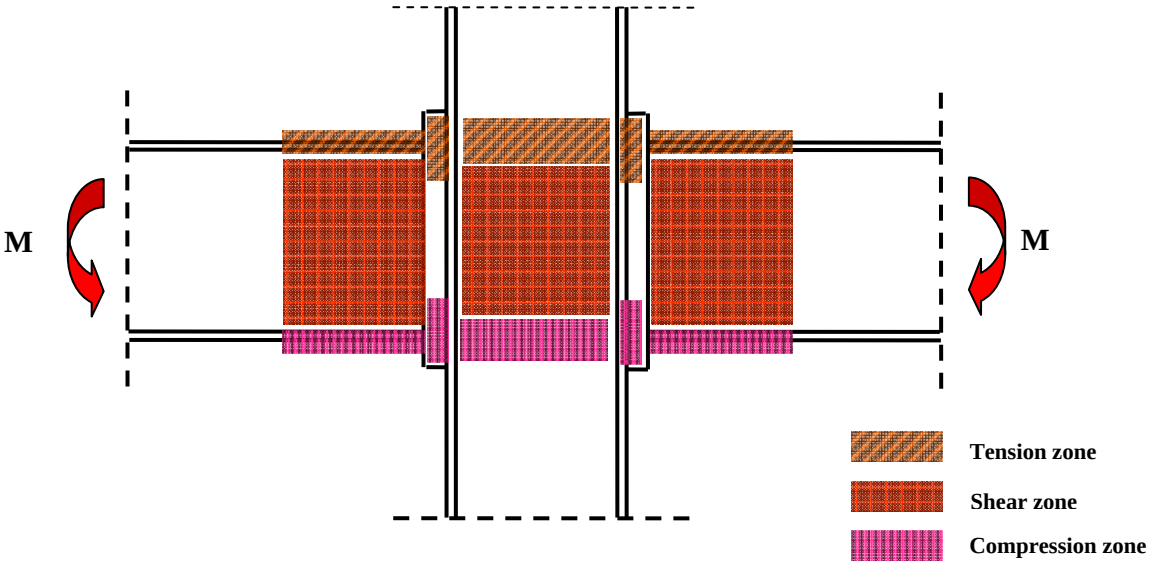

Figure 1.6 Component Identifications of Steel End-plate Joint

Table 1.1 Main Mechanical Zones and Components of Joint

Compression Zone	Shear Zone	Tension Zone
Column Web	Column Web Panel*	End-plate
Column Flange	Beam Web Panel	Column Flange
Beam Bottom Flange		Column Web
Beam Web		Beam Top Flange

* Not incorporated for steel joint subjected to symmetrical end moments.

The application of "Component-Based" method requires the following three steps:

- Identification of active components in steel joint;
- Evaluation of the stiffness or resistance capacity for each individual component;
- Assembly of all components and evaluation of entire joint stiffness or resistance characteristics.

In order to establish the "Component-Based" model at elevated temperatures, separate tests must be conducted to investigate behaviour of each component or a

group of components. Moreover, adequate analytical descriptions will need to be developed for each component to form the basis for overall mechanical modelling for steel beam-to-column joint, with the "Component-Based" method at different temperatures.

1.6 Scope and Objective of Research

Current steel design standards (BS 5950-8 and EN 1993-1-8) provide insufficient information about the behaviour of steel joints at elevated temperatures. Therefore, there is a growing need to study moment-rotation characteristics of steel joints in fire conditions. Some experimental studies based on steel joints show that it is possible to describe the moment-rotation characteristics at elevated temperature. But due to the diversity of steel joints, it is difficult to describe the different moment-rotation relationships for a wide range of joints types, dimensions and material properties. Furthermore, the finite element method is limited as it requires sophisticated modelling skill. Spyrou (2002) adopted the "Component-Based" method to investigate the behaviour of different components at elevated temperatures. Analytical models have been established for tension and compression components, with verifications from analytical predictions, finite element analyses and experimental results. However, in Spyrou's investigations (Spyrou, 2002), there is still a lack of information about the shear component behaviour in beam web at elevated temperatures. The Cardington tests on frames and beams revealed that some beams actually failed in shear modes near the support region. Therefore, the mechanical behaviour of ***structural beam web shear component*** requires further in-depth investigations, in order to obtain a simplified model that can predict realistic moment-rotation-temperature characteristics arising from the geometrical and material properties of steel joints.

This study also focuses on establishing full moment-rotation-temperature relationships for an ***extended end-plate beam-to-column steel joint***, which is commonly used as a rigid joint in construction industry. In this study, the component within the shear zone at elevated temperatures has been investigated experimentally and analytically under both axially restrained and unrestrained boundary conditions. The first stage of tests will be conducted to study the behaviour of beam web panels under shear force at three isothermal conditions, without any axial restraint effect. In the second stage, web panels will be subjected to axial restraint force. Furthermore, finite element and analytical models will be presented to predict the behaviour of beam web panel under shear force. Finally, the finite element and analytical predictions will be compared with test results.

Observations from such component tests will be beneficial for developing a mechanical model incorporating different components. Thus, the overall joint behaviour can be obtained by assembling components together. In addition to experimental and analytical studies of joint component, full-scale steel joints tests will be conducted under different temperatures to verify the moment-rotation-temperature relationships derived from the "Component-Based" approach. The ***ultimate goal*** of this study is to explore the possibility of using the "Component-Based" method to incorporate non-linear load-deformation characteristics of each component and to obtain the overall joint behaviour at elevated temperatures. Thus, this proposed method will provide sufficient information on the joint properties under elevated temperatures without recourse to testing or finite element analysis (FEA). Moreover, this analytical approach will provide great help to other researchers, especially those developing numerical studies of steel and composite structures in fire.

1.7 Thesis Layout

The thesis consists of nine chapters. The contents of the following chapters are briefly described as follows:

In Chapter 2, a brief literature review about investigations of steel beam-to-column joint moment-rotation behaviour will be presented. Both simplified curve-fitting method and analytical models will be discussed in detail. In addition, finite element method was also used to simulate the behaviour of joints at different temperatures, which will also be presented in this chapter. Then various experimental investigations, the "Component-Based" method and spring stiffness models will be discussed and presented.

In Chapter 3 the influence of elevated temperatures on the mechanical properties of steel and bolt will be presented. Different mathematical models for stress-strain relationship at elevated temperatures will be discussed. Other temperature dependent properties, such as thermal expansion, specific heat and thermal conductivity will also be presented.

In Chapter 4, simple mechanical models capable of defining the behaviour of shear component of steel joint will be presented. Analytical predictions of ultimate shear stress and deflection characteristics will be compared with experimental and finite element analyses in the following chapters.

In Chapter 5, a series of tests has been conducted to investigate the behaviour of beam web panel under shear at ambient and elevated temperatures. Details of test procedure, apparatus and results will be presented. Besides the unrestrained tests, the procedure and observations for restrained tests at elevated temperatures will also be discussed.

Chapter 6 describes finite element models used to study the behaviour of beam web panel under shear action at ambient and elevated temperatures. Both unrestrained and restrained boundary conditions will be considered. Comparisons among test results, finite element analyses and analytical predictions will be discussed.

In Chapter 7, a series of overall steel beam-to-column testes is introduced to investigate the overall behaviour of steel joint at elevated temperatures. Details of specimens, procedure and test results will be presented in this chapter. Both restrained and unrestrained steel joint behaviour at elevated temperatures are also addressed in details.

Chapter 8 describes the finite element simulations to investigate the behaviour of steel beam-to-column joints for restrained and unrestrained boundary conditions. A simple mechanical spring-stiffness model will be presented to incorporate the influences of shear components within steel joints. Comparisons among experimental results, finite element analyses and "Component-Based" analytical predictions will be discussed.

Finally in Chapter 9, this research work will be summarized and general conclusion will be drawn. Future study for other components of steel joints will be presented.

CHAPTER 2

LITERATURE REVIEW

2.1 Introduction

For steel framed structures, the most adequate fire protection method is by applying insulating material on members to delay the temperature rise. The objective of such approach is to ensure that sufficient strength of steel can be retained within the specified fire time. However, this kind of protection method is costly due to additional expenditure and construction time. Over recent years in the UK, there is a trend to design secondary steel beams to withstand fire without any insulation due to inherent fire resistance and thermal insulation provided by concrete slabs placed on top of supporting beams (Bailey *et al.* 1998). For single-storey industrial or commercial structures, Building Regulations (1991) do not stipulate any fire resistance, so long as the fires will be contained and will not spread to adjacent structures. However, for high-rise buildings or basement structures, Building Regulations (1991) stipulates minimum fire resistance, which can be met through the provision of fire protections to steel members based on member type of, shape and the required fire resistance. Therefore, it has generated a great deal of interest to understand the structural behaviour of different elements under fire conditions for a greater cost-effective design.

Steel beam-to-column joints are crucial components linking up structural members together to form an integrated steel-frame structure. They affect the integrity of whole system. Thus, there are some investigations to study the behaviour of typical steel beam-to-column joints and their effects on integrity of steel framed structures

under fire conditions. There are different forms of steel beam-to-column joint modelling ranging from simple curve-fitting, to empirical expressions, mechanical modelling and finite element analysis (FEA). These are commonly classified into five main categories as follows:

- ✧ *Mathematical (Curve-Fitting) Method;*
- ✧ *Finite Element Analysis;*
- ✧ *Experimental Investigations;*
- ✧ *Simplified Analytical Models;*
- ✧ *Mechanical Models (Spring Models).*

The various forms of investigation methods are discussed in following sections, with their respective advantages and limitations for both ambient and elevated-temperature analysis.

2.2 Mathematical (Curve-Fitting) Analytical Methods

It is well known that mathematical analytical method, especially curve-fitting method, is one of the powerful methods to directly represent both experimental observations and numerical simulations. It can also be in a suitable form to be incorporated into structural analysis. The derived equation should represent steel joint curves in terms of key parameters, such as rotational stiffness, moment capacity and rotational capacity, etc.

The earliest mathematical model to describe joint moment-rotation behaviour was proposed by Baker (1934) and Rathburn (1936) (as cited by Sherbourne *et al.*, 1997). This mathematical model only represented the initial joint stiffness with a linear form and was simple enough to be adopted. However, it was not suitable for full-range analysis of joint behaviour. It also over-estimated the joint stiffness and was obviously inaccurate and unconservative at high rotation values.

In 1970, Romstad and Subramanian (1970) adopted a bi-linear curve fitting technique to represent the load-deformation characteristics of flexible riveted and bolted angle joints. From experimental observations, it was noticed that the mechanical behaviour of joint angle segments (as shown in Figure 2.1) was influenced by behaviour of three stages of loading, i.e. *(a)* elastic; *(b)* partially elastic and partially plastic; *(c)* plastic hinges formed at critical locations within steel joints. Based on a detailed analysis of the joint through these three stages, an empirical expression was developed which gave excellent agreement with test results as follows:

$$M = \frac{0.345l^2(0.72\phi l)^n}{(1-0.3\phi l)^{1+n}} \qquad \text{for} \quad \phi l_1 \geq 0.1inch$$

$$M = \frac{0.345Kl^2(0.72\phi l)^{0.4}}{(1-0.3\phi l)^{1.4}} \qquad \text{for} \quad \phi l_1 < 0.1inch \tag{2.1}$$

in which: l_1 is the distance from the tension end to the centre of rotation; l is the joint height; ϕ is joint rotation in radians; $\phi l_1 = \Delta$ is the displacement at the tension end of joints; n is determined according to the range of joints considered; K is determined by solving the second stage equation with values of M and ϕ associated with $\phi l_1 = 0.1inch$ derived from the first stage equation.

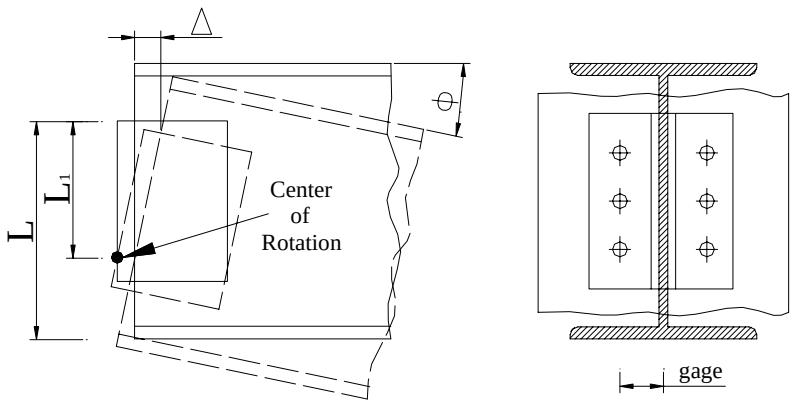

Figure 2.1 Geometry Parameters of Flexible Joint (Romstad *et al.* 1970)

Due to limitations of bi-linear curve fitting method to represent the transition procedure between the steel joint elastic and plastic behaviour, Moncartz *et al.* (1981) obtained the following information from joint tests under monotonically increasing moment as: *(1)* initial stiffness k_{e1}; *(2)* proportional limit M_{PL}; *(3)* shape of nonlinear portion of curve; and (4) linear strain-hardening envelope. This tri-linear curve fitting method incorporated an additional linear slope between the elastic proportional limit M_{PL} and the yield moment M_Y as shown in Figure 2.2 with k_1, k_2 and k_3 as the respective stiffness in each stage.

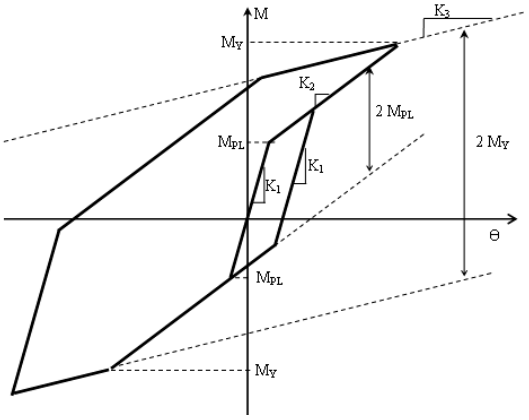

Figure 2.2 Tri-linear Moment-Rotation Curve-Fittings (Moncarz *et al.* 1981)

In addition to multi-linear forms of curve fitting technique, Frye and Morris (1975) idealized the non-linear behaviour of joint moment-rotation curves into polynomial forms. Moment-rotation curves of different types of joints (Figure 2.3) were expressed by an odd power polynomial as follows:

$$\theta = C_1(kM)^1 + C_2(kM)^3 + C_3(kM)^5 \qquad (2.2)$$

in which: k is the standardization constant depending on joint types and geometrical properties; C_1, C_2, C_2 are curve-fitting constants, which are shown in Table 2.1 in accord with different types of joints (Figure 2.3). Although the polynomial curve-fitting method (Equation 2.2) can accurately represent steel joint

moment-rotation characteristics, it showed a curve with a peak and a trough within the range of rotation, as it seeks to produce a curve as close as possible to the experimental data. Therefore, the curve sometimes has a negative joint tangent stiffness value, contrary to actual behaviour.

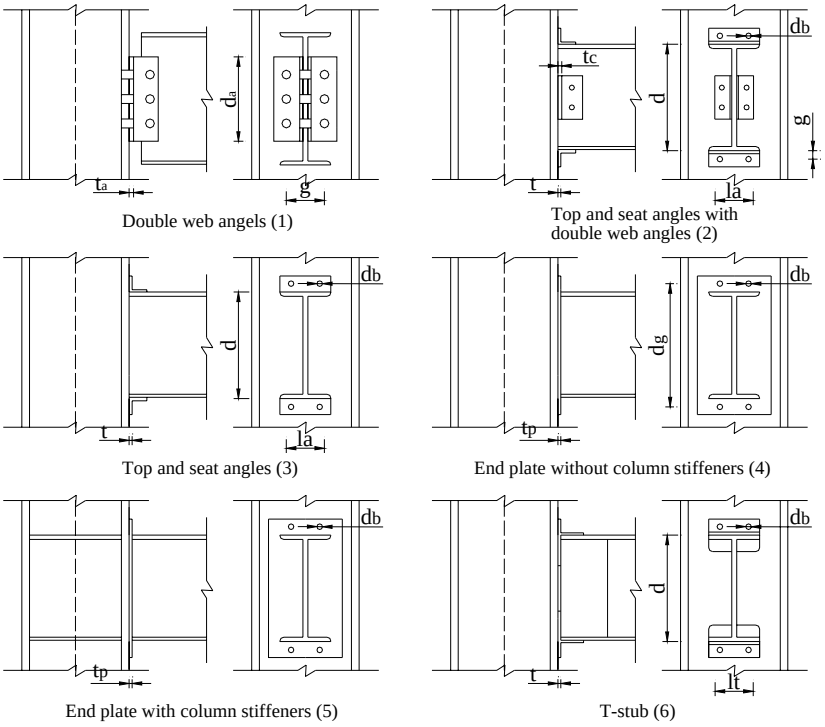

Figure 2.3 Semi-Rigid Joint Type and Geometrical Parameters (Frye *et al.* 1975)

To avoid descriptive inaccuracies of polynomial curve-fitting method, Jones *et al.* (1980) used cubic B-spline curve fitting technique to achieve a more accurate representation of the joint behaviour. This curve-fitting method required the division of joint rotation range into a finite number of smaller segments. Within each range, a cubic function was fitted with the first and second derivative continuity being maintained between adjacent segments. This method produced smooth curve representations of experimental moment-rotation data. However, its nonlinear characteristics require iterative and special numerical procedure for implementation.

Table 2.1 Curve Fitting and Standardization Constants (Frye *et al.* 1975)

Joint Type	Curve Fitting Constants	Standardization Constant
Double Web Angles	$C_1 = 3.66\times10^{-4}$ $C_2 = 1.15\times10^{-6}$ $C_3 = 4.57\times10^{-8}$	$k = d_a^{-2.4} t_a^{-1.81} g^{0.15}$
Top and Seat Angles with Double Web Angles	$C_1 = 2.23\times10^{-5}$ $C_2 = 1.85\times10^{-8}$ $C_3 = 3.19\times10^{-12}$	$k = d^{-1.287} t^{-1.128} t_c^{-0.415} l_a^{-0.694} g^{1.35}$
Top and Seat Angles	$C_1 = 8.46\times10^{-4}$ $C_2 = 1.01\times10^{-4}$ $C_3 = 1.24\times10^{-8}$	$k = d^{-1.5} t^{-0.5} l_a^{-0.7} d_b^{-1.5}$
End-plate without Column Stiffeners	$C_1 = 2.10\times10^{-4}$ $C_2 = 1.04\times10^{-4}$ $C_3 = 6.38\times10^{-6}$	$k = d_g^{-2.4} t_p^{-0.4} d_b^{-1.5}$
End-plate with Column Stiffeners	$C_1 = 1.79\times10^{-3}$ $C_2 = 1.76\times10^{-4}$ $C_3 = 2.04\times10^{-4}$	$k = d_g^{-2.4} t_p^{-0.6}$
T-Stub	$C_1 = 2.10\times10^{-4}$ $C_2 = 6.20\times10^{-6}$ $C_3 = -7.60\times10^{-9}$	$k = d^{-1.5} t^{-0.5} l_t^{-0.7} d_b^{-1.1}$

In 1983, Colson and Louveau proposed a simplified power model to represent joint moment-rotation characteristics. This model adopted a power function as follows:

$$\theta_r = \frac{|M| \times |M_{cu}|^n}{R_{ki}(|M_{cu}|^n - |M|^n)} \tag{2.3}$$

in which: R_{ki} is initial joint stiffness; M_{cu} is joint ultimate moment capacity; n is a parameter to account for curvature of joint moment-rotation relationship. As this model has only three parameters, it was not as accurate as the B-Spline model (Jones *et al.* 1980). However, the required data for this model is considerably reduced compared with other curve-fitting models.

Later Kishi and Chen (1987) proposed another power model to predict moment rotation characteristics of beam-to-column joints. In this procedure, the initial tangent stiffness and ultimate moment capacity of joint were determined analytically. With these values, the moment-rotation relationship of joint can be expressed in a general form as follows:

$$M = \frac{R_{ki}\theta_r}{\left\{1+\left(\theta_r / \theta_0\right)^n\right\}^{1/n}} \tag{2.4}$$

where: R_{ki} is initial joint stiffness; θ_o is a reference plastic rotation, which is equal to M_u / R_{ki} ; M_u is ultimate moment capacity; and n is a shape parameter determined by a least-squares curve fitting with experimental results. This suggested model could be implemented easily and it gave good correlation with experimental curves. However, this model may be difficult to be implemented for moment-rotation curves without any plateau.

In Lui and Chen's study about flexible joint frames in 1986, a multi-parameter and exponential model of joint was proposed as below:

$$M = M_0 + \sum_{i-1}^{n} C_i \left[1 - \exp\left(\frac{-\left|\theta_r\right|}{2i\alpha}\right)\right] + R_{kf}\left|\theta_r\right| \tag{2.5}$$

in which: M_0 is initial moment; C_j joint model parameters derived by curve fitting to a set of moment-rotation data; $\left|\theta_r\right|$ is absolute value of rotational deformation of joint; R_{kf} is strain hardening rotational stiffness of joint; α is scaling factor. This model could provide efficient descriptions of flexible joint characteristics in the plane frame analysis (Lui and Chen, 1986).

To predict moment-rotation behaviour of bolted end-plate joints, Yee and Melchers (1986) proposed a four-parameter exponential model as:

$$M = M_p\left\{1-\exp\left[\frac{-\left(K_i - K_p + C\theta\right)\theta}{M_p}\right]\right\} + K_p\theta \tag{2.6}$$

in which: M_p is plastic moment capacity of joint; K_i is initial elastic stiffness; K_p is strain hardening stiffness and C is a constant controlling the slope of curve, which was empirically determined from test data. However, values of M_p, K_i and K_p were analytically predicted. The ultimate moment capacity of joint was governed by the weakest joint component, which was accounted by Yee and Melchers (1986) as bolt tension failure, plastic mechanism in end-plate, shear yielding of column web and column web buckling. Similarly, the overall deformation of joint included flexural deformation of end-plate, bolt extension, shear deformation of column web and flexural deformation of column flange, etc. Yee and Melchers (1986) also proposed methods to evaluate the elastic displacements corresponding to the deformation of each element and the plastic resistances of the joint elements. This approach was probably within the earliest examples of "Component-Based" method which was later specified in Eurocode 3 (EN 1993-1-8).

In 1984, Ang and Morris first suggested to use standardized Ramberg-Osgood function (Ramberg, Osgood 1943, as cited by Ang and Morris, 1984) to predict the moment-rotation relationship for five different types of joints as follows:

$$\frac{\theta}{\theta_{ro}} = \frac{M}{(M)_0} + \left[\frac{M}{(M)_0}\right]^n \tag{2.7}$$

in which: θ_{ro} is permanent rotation after unloading; $(M)_0$ is reference moment equal to $K\theta_{ro}$; K is initial stiffness of joint and n is a shape factor characterizing the knee of moment-rotation curves. Equation 2.9 represents the nonlinear moment-rotation behaviour of a variety of joints reasonably well.

From bare steel and composite two-dimensional cruciform joint tests conducted at elevated temperatures by Lawson (1990), El-Rimawi *et al.* (1997) developed a series of moment-rotation curves based on the Ramberg-Osgood relationship (Ramberg, Osgood 1943) as below:

$$\theta = \frac{M}{a} + 0.01\left(\frac{M}{b}\right)^n \tag{2.8}$$

where: a, b and n are temperature-dependent constants; θ and M are joint rotation and moment, respectively. Different values of these temperature-dependent constants for flush end-plate and extended end-plate joints were postulated (El-Rimawi *et al.* 1997).

2.3 Finite Element Analysis (FEA) Methods

The behaviour of steel beam-to-column joint is complex under fire conditions due to non-linear material characteristics and sophisticated interactions among the components of the joint. Hence, finite element analysis (FEA) can be used to simulate the complex behaviour of the full joint at elevated temperatures.

- Finite Element Investigations at Ambient Temperature

Finite element modelling for investigations of steel beam-to-column joint behaviour at normal temperature began in the early 1970s. In 1972, Bose *et al.* first applied FEA method to study the steel beam-to-column joint at ambient temperature. Fully welded joints were studied, with a greater emphasis on column web panels as they involved plate stability and strength problem. From the comparisons with analytical predictions and experimental results, the numerical simulations provided sufficient accuracy to predict the actual behaviour of steel beam-to-column joints.

Later Krishnamurthy and Graddy (1976) conducted two and three-dimensional finite element analyses of steel bolted joints. Thirteen commonly used eight-bolted extended end-plate joints were modelled using two-dimensional constant strain triangle element, and eight-node subparametric brick element. The joints were

analyzed elastically, under bolt pretension alone and pretension with additional half or full service loads. The objective of this investigation was to obtain correlation factors between two FE methods which could be used to extrapolate results for other joint configurations without the need of three-dimensional FE models. From numerical simulations, the corresponding correlation factors were determined to be 1.4 for displacement and rotation, 1.2 for average stress and 1.8 for maximum stress. Since the contact problem was not modelled, this correlation factor could not accurately represent the rotational characteristics of the steel joint.

In 1984, Patel and Chen performed a two-dimensional nonlinear analysis of different types of beam-to-column joints. The general-purpose NONlinear Structural Analysis Programme (NONSAP) has been used for this analysis. Due to symmetry about the centre of column web, only half of the beam-to-column joint structure was modelled. The first part of these analyses on beam-to-column flange moment joint was calibrated with full scale test results. The second part of this study was nonlinear FEA of the joint plate of beam-to-column web joint assemblage. From comparisons with test observations, despite the simplifications of two-dimensional finite element models, the numerical predictions gave acceptable correlation.

In 1988, Sibai and Frey discretized one-sided welded flange joints of hot-rolled sections into a 3D FE model consisting of shell elements for webs and flanges and beam elements for end-plates and stiffeners. In their FE simulations, the influence of steel material strain-hardening was considered. However, welding imperfections were not incorporated in their FEA model. Although this would limit the accuracy of welded joints analysis, close agreement was achieved between numerical and test results.

Connecting bolts of steel joints are influenced by the prying forces between contact areas. Thus, it is necessary to use a more complex numerical method to represent the bolt behaviour. In 1980, Krishnamurthy conducted a series of finite element simulations of three different types of bolted joints, such as top and seat angle joint, T-stub joint and end-plate joint. Based on their previous two-dimensional finite element work (Krishnamurthy *et al.* 1976), bolt shanks and plate with bolt holes were simulated as two separate but overlapping regions. Using different sets of nodes and elements assigned to each, the two regions were joined together by common nodes at the front face of the plate on which the bolt head was idealized as rectangular elements. Based on these idealizations, a close correlation was observed between numerical and experimental results. This demonstrated there were significant effects of bolts and welds to accurately represent the joint rotational behaviour.

In 1994, Gebbeken *et al.* used different finite element modelling techniques to predict the loading-carrying behaviour of joints and to calculate their limit loads. A series of beam-to-column end-plate joints, which consisted of weak column flange and stiff end-plate, or stiff column flange and weak end-plate, was considered. First, a two-dimensional finite element model was used with bilinear stress-strain form for steel material property. Friction between column flange and end-plate was neglected. However, this analysis presented a larger limit load compared with experimental results. The two-dimensional finite element models were too stiff although material strain-hardening was neglected and a fine grid was used. Three-dimensional finite element models provided limited success in predicting the moment-rotation behaviour of the joints. Numerical results compared well with experimental observations if material strain-hardening was considered. However, simplifying a joint into a T-stub may not be suitable for other types of joints, or end-plate joints that failed in ways other than tension.

In 1997, Bursi and Jaspart presented a series of finite element simulations of bolted steel joints. First, they proposed numerical simulations of T-stub joints, based on LAGAMINE software package. Nonlinear finite element analysis that incorporated large displacements, large rotations and large deformations was employed in this study. Due to symmetry of T-stub joint, only a quarter of the joint was modelled. Preloading forces inside the bolts were considered by using applied initial stresses. A series of T-stub joints was tested and they yielded close comparison with finite element predictions. Slight differences in deflections might be due to residual stresses in T-stub joint, which was omitted in the FE models.

Later, Bursi and Jaspart (1997[b]) conducted the second part of finite element investigations of bolted steel joints. Finite element code ABAQUS was utilized to analyze the four-bolt unstiffened extended end-plate joint tests as well as previous numerical simulations of T-stub joints by LAGAMINE software package. The end-plate and beam flange were simulated with eight-node brick element. Special contact elements in ABAQUS were used to describe the interactions between the end-plate and the column flange. This reduced computational work when compared with conventional surface contact elements. Compared with corresponding experimental results, numerical results showed that the FE models could predict moment-rotation characteristics of bolted joints quite accurately. However, due to a lack of experimental results of strain measurements in bolts during tests, there was no comparison between experimental and numerical results of bolt force. Numerical work was presented in the following paper by Bursi and Jaspart (1998).

At about the same time, Baharri and Sherbourne (1997) conducted a series of finite element investigations of end-plate bolted joints. In the first part of study, a three-dimensional finite element model of four-bolted unstiffened extended end-plate joint was developed using ANSYS. The finite element model was the

same with those numerical models used for hand-tightened bolt joints (Sherbourne and Baharri, 1994), except bolt preload was defined with truss elements representing the bolt shank. The bolt head and nut were simulated using eight-node isoparametric solid elements, which were compatible with end-plate and column flange, respectively. Special 3D interface elements were used to define the contact between the back of end-plate and the outer surface of column flange. Material nonlinearity was included. Experimental moment-rotation results agreed well with finite element predictions. In particular, the column flange was stiffened to provide additional rotation. In the second part of Sherbourne and Baharri's investigation (Baharri and Sherbourne, 1997), from their parametric study, Richard-Abbot (1975) power functions was used to represent the moment-rotation relationship of extended end-plate joints. Based on a series of test results, an empirical equation was developed to describe the moment-rotation characteristics incorporating end-plate thickness, bolt size, beam and column dimensions. Similarly, Bose *et al.* (1997) developed FEA of unstiffened flush end-plate bolted joints. A sophisticated three-dimensional model of the joint was developed using LUSAS finite element package and was validated by a number of full scale tests of flush end-plate joints. Special bar element was used to model the bolts in tension and compression. In addition, 3D solid element was used to model column web, flange, end-plate and beam web, and flange. In particular, a three-dimensional joint element was chosen to simulate the contact between the column flange and the end-plate. The study showed the finite element models could present good predictions of moment-rotation behaviour of joints. However, effects of welds, bolt heads and column fillet were not addressed in this finite element analysis, which might have some effects on the joint rotational behaviour.

- Finite Element Investigations at Elevated Temperature

Based on previously developed end-plate joint model at ambient temperature, Liu (1996) first developed a 3D model to simulate the response of steel joints in fire at

the Manchester University. This finite element model incorporated material plasticity, deterioration with temperature, and non-uniform thermal expansion across the section. In addition to the eight-node shell element used to discretize the webs and flanges of beams, columns, stiffeners and end-plate, a thick beam element with special characteristics was used to simulate the bolts and the contact between the end-plate and the column flange. Two sets of extended end-plate joint tests conducted by Lawson (1990) were used as verifications of this model. Reasonable simulations of responses of joints were achieved, and the discrepancy between experimental and modelling results was partly due to limited information about the temperature distributions in the specimens, especially in some crucial areas like the end-plate, column flange and beam web near to the joint. More importantly, the material stress-strain relationships were only based on a generalized recommendation in Eurocode 3 (ENV 1993-1-2) which might be different from actual material behaviour.

Then in 1999, Liu improved his three-dimensional model to simulate the response of bare steel and steel-concrete composite joints to predict the moment-rotation-temperature relationships. A special type of element was developed to simulate the bolt behaviour, which consisted of one conventional beam element joining two connecting nodes of column flange and end-plate and a fictitious node that represented the free end of bolt. A number of fire tests on steel beam-to-column joints have been simulated to calibrate the finite element predictions. The tests consisted of composite and bare steel joint tests by Lawson (1990), Lennon and Jones (1995), Leston-Jones (1997[a]) and Al-Jabri (1998). Both rotational behaviour and limiting failure temperatures of the joint were predicted with a small difference compared with experimental results. However, discrepancies between numerical predictions and measured experimental results

might be caused by temperature-dependent material properties in numerical simulations, a lack of information on temperature distributions in critical elements.

With the development of "Component-Based" method for the analysis of steel joints, it is necessary to validate the modelling of different components using FEA method. In 2002, Spyrou used ANSYS to simulate the compression component in column web, and other tension components in the form of T-stub. In the first part of this finite element analysis, plane stress quadrilateral eight-node element was used to represent the column flange, web and end-plate of T-stub component. The contact forces between surfaces i.e. bolt head and flange plate, bolt shank and bolt hole, were simulated by special point-to-surface contact elements. Typical stress-strain relationship at elevated temperatures according to Eurocode 3, Part 1.2 (ENV 1993-1-2) was applied. Comparison between numerical and experimental results showed acceptable accuracy. In the second part of FEA, half of column specimen was simulated in accord with compression component test of column flange and web. The 2D finite element model consisted of 8-noded quadrilateral element and 6-noded triangular element for column flange, web and hot-roll section root radius. Numerical results, particularly stress distribution, showed almost the same behaviour with analytical assumptions. Due to 2D simulation, the out-of-plane buckling of column web could not be modelled.

Recently, Al-Jabri *et al.* (2006) presented one finite element study on the behaviour of flush end-plate bare steel joints at elevated temperatures using ABAQUS. The joint components were simulated with three-dimensional, eight-node reduced-integration brick elements. In addition, contacts between end-plate and column flanges were modelled using the surface interaction command in ABAQUS, which allowed limited relative sliding at the interface. Numerical predictions were compared with experimental results by Al-Jabri, Burgess *et al.* (2005), and showed

good agreement between the two results.

2.4 Experimental Investigations

The best description for rotational behaviour of steel beam-to-column joint behaviour is moment-rotational curve, which is the relationship between the bending moment transmitted by joint, and the rotation of beam relative to column axis. During the past few decades, quite a number of experimental investigations on different joint types with various parameters were conducted (Figure 2.4). The joint behaviour is in between two extremes, viz., perfectly rigid as vertical axis and perfectly pinned as horizontal axis as shown in Figure 2. 5.

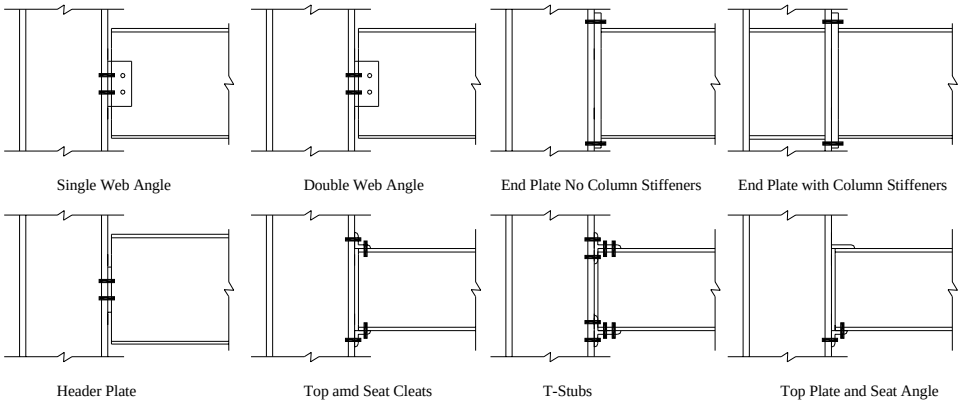

Figure 2.4 Steel Beam-to-Column Joint Types (Jones *et al.* 1980)

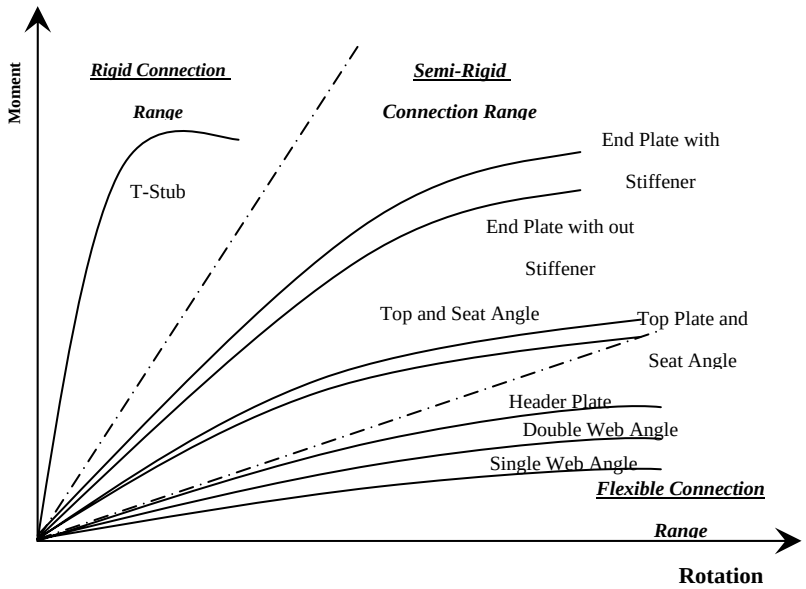

Figure 2. 5 Typical Moment-Rotation Curves (Jones *et al.* 1980)

- Experimental Investigations at Ambient Temperature

The first experimental work of steel joint was conducted by Wilson and Moore (1917) to determine the joint rigidity in steel structures. However, research work on behaviour of semi-rigid joints continued to grow at a slow rate as the moment-rotation curves are highly non-linear throughout the entire range of rotations. Due to a lack of experimental data for a wide range of joint types with different beam and column arrangements, it was difficult to incorporate the semi-rigid joint characteristics into modelling and design. Since then, many experiments have been carried out to study the behaviour of different types of steel joints, such as Batho and Rowan (1934), Johnston and Deits (1942), Sherbourne (1961), Lipson (1968), Lewitt (1969), Bailey (1970) and Surtees and Mann (1970), etc. (as cited by Nethercot, 1985[b]).

Johnson *et al.* (1960) conducted six tests with different end-plate joint details and with high-strength preloaded bolts. Test specimens consisted of four joints with bolts in equivalent shear, and two joints with bolts in combined tension and shear. Experimental results showed that the end-plate joint with high-strength bolts can develop full plastic capacity of connected members. This allowed the formation of plastic hinges in the beams which resulted in inelastic rotation capacity.

In 1984, Hendrick *et al.* conducted a series of tests on two four-bolted flush end-plate moment joint configurations. The measured yield patterns were in general agreement with finite element modelling. In 1987, Davison *et al.* conducted a series of steel joint tests which consisted of web cleat, flange cleat, seat and web joint, flush end-plate joint and extended end-plate joint. The test cruciform specimens were assembled by two beams (UB 254x102x22kg/m) and one column (UC 152x152x23kg/m). From this wider range of joint types, it can be concluded that web cleat joints showed more flexible behaviour than other types of joints. The

flange cleat joints exhibited bi-linear moment-rotation characteristics. However, the flush and extended end-plate joints showed large difference compared to other joints, which was due to distortions in the relatively thin column flange.

In order to verify proposed analytical procedure and prediction modelling equations, Kukreti *et al.* (1987) tested eight flush end-plate joints subjected to increasing loads until failure. Each specimen was subjected to bending moment without shear by a symmetric two-point loading. The main failure phenomenon was separation of end-plate against column flanges, monitored by means of caliper gauges during tests. The experimental moment-rotation curves were compared with finite element analysis and prediction equations with acceptable agreement.

Aggarwal and Coates (1986) conducted fifteen tests on extended end-plate joints. The joints consisted of three types of bolts and three end-plate thicknesses which were tested under static and pulsating loads. It was concluded that the design criteria (Australia Design Standard) gave conservative assessment of plate strength and bolt strength. In addition, the margin of safety of weld failures was rather low when joints were subjected to dynamic loads.

In 1989, Janss *et al.* performed twenty-two beam-to-column joint tests at the University of Liège. Three types of beam-to-column joints were tested as: *I.* End-plate joint; *II.* Double web cleat joint; *III.* Flange cleat joint. For two end-plate joint tests, axial forces were applied to column heads with a combination of transverse load at the beam end. In addition to static loading, eight joints were tested under cyclic loading. From experimental results, it was found that the axial force of column had little effect on the initial stiffness of the end-plate joint. For joint with double web cleats, the initial stiffness was not altered by bolt-tightening forces; only bending moment capacity increased proportionally to preload in the

bolts. For joints with flange cleats, the initial stiffness and ultimate strength were not affected by the level of bolt tightening.

Zandonini and Zanon (1989) tested two types of end-plate beam-to-column joints as end-plates with extension on one side and on two sides of beams. The beams were connected to a counterbeam with negligible deformations. Measured moment-rotation relationships showed that the extension of end-plate on the compression zone had little effect on the joint behaviour and strength. The responses of end-plate and bolts on joint behaviour were investigated separately. It was found that the bolts contribution on joint behaviour depended on the end-plate thickness; with greater thickness, the bolt contribution was great. Furthermore, the end-plate deformations contributed more to the joint flexibility than the bolt contributions.

To determine the nonlinear moment-rotation relationship for joints in structural steel frame, Tschemernegg (1988) conducted four series of tests. The target of this study was to analyze the characteristic values of the moment-rotation curves as elastic, plastic limits of bending moment and elastic, plastic limits of rotation. From the experimental results, these critical characteristics values were determined easily which could be used for a wide range of steel joints.

In 1990, Ghobarah *et al.* conducted five tests on bolted end-plate beam-to-column joints under cyclic loadings. The objectives of this investigation were to determine the behaviour of this type of joint under cyclic loading, and to evaluate the effect of joint parameters, such as end-plate thickness, column flange stiffener and bolt pre-tension force on the overall joint behaviour. The specimens consisted of one beam connected to a stub column on each side, by both extended end-plates, with and without column flange stiffeners. From testing results, it can be concluded that

the joints with unstiffened columns showed weak moment-rotation behaviour compared with those that were stiffened. The experimental results also showed that the end-plate thickness could be reduced significantly if it was properly stiffened.

In 1991, Altmann *et al.* conducted an experimental research to study the behaviour of beam-to-column composite joints at the University of Liège. Totally, there were twenty-four tests conducted with two-cleat and three-cleat beam-to-column composite joints in a cruciform arrangement. Three different failure modes were observed as: buckling of column web, failure of reinforcement in reinforced concrete slab and shear failure of bolts. In addition, a parametric study was conducted based on experimental results; this included thickness and quantity of cleats, and the percentage of reinforcement in slab. However, there were few explanations on the non-significant effects of cleat thickness and quantity on the ultimate moment capacity of joints.

Later, Xiao *et al.* (1994) and Li *et al.* (1996[a]) conducted a series of composite joint tests at the University of Nottingham. The main objectives were to assess the moment capacity, rotational stiffness and rotational capacity of composite joints. In the first part of study, the test specimens consisted of two types: cruciform and cantilever configurations. The joints had seating cleat with double cleats, flush end-plate, partial depth end-plate and finplate. Different failure modes were observed according to each type of joints. As an extension of study, Li *et al.* (1996[a]) reported a series of seven end-plate beam-to-column joint tests which consisted of six composite joints and one bare steel joint. The objective of this part of experimental work was to clarify the influences of unbalanced moment and the shear/moment ratio. It was concluded that variation of shear force had little effect on the moment capacities of flush end-plate composite joint and reinforcement of concrete slab mainly contributed to the moment capacity of composite joints.

In 2000, Liew *et al.* conducted an experimental investigation of composite steel beam-to-column joints. There were a total of six full scale flush end-plate beam-to-column joint tests, in which, three column types were used as bare steel, partially encased and fully encased. Although the objective was to study the effects of reinforcement area in concrete slab and the stiffeners in column web, on the moment-rotation relationships of this type of beam-to-column joint under monotonic loads. In addition to experimental works, a simple theoretical model was presented based on Eurocode 3 Annex J (ENV 1993-1-1) with an extension to include composite end-plate joint. The predicted tri-linear moment-rotation curves showed a close agreement with experimental results.

Later, Sumner and Murray (2002) tested six bare steel beam-to-column joint specimens and one composite slab beam-to-column joint specimen under cyclic loads. Two types of extended end-plate were adopted: viz. four-bolted unstiffened and eight-bolted stiffened between end-plate and beam flanges. From test programme, they concluded that the extended end-plate joints were suitable for use under seismic circumstances. In addition, from the composite end-plate joint test, reinforcement in composite slab should be considered since it significantly increased the moment capacity of end-plate joints.

As an extension of earlier experimental works by Liew *et al.* (2000), Liew *et al.* (2004[a]) conducted tests on composite end-plate joints under reversal loads. In this study, eight cruciform composite joint specimens were tested with one side of the joint under negative moment and another side positive moment. There were different types of joints tested in this study, viz. flush, extended end-plate and with haunched plates. All the cyclic loading tests showed that initial stiffness and moment capacity of flush end-plate composite joint were higher for negative bending than positive bending. Besides, shear deformation of column web panel

zone due to unbalanced moments required a special strengthening method to avoid shear buckling and failure in this area.

- Experimental Investigations at Elevated Temperature

In 1990, Lawson presented an experimental investigation of eight beam-to-column joint tests under fire conditions. The objective of this study was to establish the moment capacity of beam-to-column joints at elevated temperatures. This programme consisted of five tests of non-composite steel joints, two composite steel joint tests and one shelf-angle flush end-plate joint. Three different joint types have been chosen as extended end-plate, flush end-plate and web cleat joints representing rigid, semi-rigid and flexible joints. From experimental investigations, it was seen that the temperature of bolts (especially the upper bolts) determined the moment capacity of joints in fire. Besides, temperatures in the bolts were significantly lower than those in the bottom flange of the beam; the latter was defined as the limiting temperature of the beam section.

In 1997, with the aim of developing of full moment-rotation-temperature characteristics for typical bare-steel and composite joints and assessing the effects of semi-rigid joint on frame responses, Leston-Jones *et al.* (1997[a], 1997[b]) tested two series of bare steel and composite flush end-plate joints at ambient and elevated temperatures at the UK's Building Research Establishment. A cruciform arrangement was chosen consisting of two 254x102x22UB Grade 43 beams of 1.7 m length, symmetrically framing into both flanges of 152x152x23UC Grade 43 column of 2.7 m length. A 12 mm thick end-plate was selected with six M16 Grade 8.8 bolts (18 mm diameter). To maintain continuity, all bolts were tightened to a torque of approximately 160 Nm. The moment capacities of test joint at ambient temperature were calculated as 18.14 kNm and 14.07 kNm according to Eurocode 3 (ENV 1993-1-1) and Horne and Morris (1981) respectively. Joint stiffness was

predicted to be $8.7x10^9$ Nmm/rad according to the recommendations presented in Eurocode 3 (ENV 1993-1-1). The bare steel flush end-plate joint test programme consisted of one test under ambient temperature to determine moment capacity, one test under elevated temperature without any loads to investigate the influence of heating rate, and another five tests under elevated temperatures with different loading levels. From experimental observations, it can be seen there was significant deformation of column web in compression zone and column flange in tension zone for all bare steel joint tests. The composite steel joint specimens have an identical joint arrangement as bare steel joint tests, with additional 130 mm thick lightweight concrete slab. From ambient temperature test, it was observed that the failure of this type of joint was similar to that for the bare-steel joint tests. However, there was greater compression deformation in the column web. In addition to the ambient temperature test, another three composite joints were tested with different loading levels to obtain temperature-rotation characteristics. Based on experimental observations, a simple elevated-temperature spring stiffness model was constructed, which gave reasonable agreement with test results.

In order to obtain a clear understanding of joint behaviour at elevated temperature conditions, a series of transient tests was conducted on beam-to-column flush and flexible end-plate joints at the UK's Building Research Establishment (Al-Jabri, 1999, 2005). The objective of this study was to obtain moment-rotation curves of joints at increasing temperatures for different load levels. In all cases the test specimens consisted of a symmetric cruciform arrangement of a single column 2.7 m high with two cantilever beams 1.9 m long connected to the column. As a whole, twenty tests were conducted in five groups, namely, FB1, FB2, FLB3, FLC4 and FLC 5. FB1 and FB2 tests were conducted with bare steel flush end-plate joints with various section sizes and end-plate properties. In addition to flush end-plate joint tests, another flexible end-plate bare steel joint assembly group (FLB3) was

tested at elevated temperatures. To obtain rotational characteristics of composite joint at elevated temperatures, two more groups of composite flexible end-plate joints were also tested at both ambient and elevated temperatures. All elevated-temperature tests were conducted in a gas-fired portable furnace at a linear rate of 10 ^{o}C per minute. For FB1 and FB2 groups, the cruciform specimens were tested at load levels as joint movements of 0.2, 0.4, 0.6 and 0.8 of the calculated moment capacity of the joints. The flexible end-plate joint type tested in FLB3 was chosen as typical of the joints used in Cardington full-scale test frame and were tested at joint moments of 0.1, 0.2 and 0.5 of the joint moment capacity. For two groups of composite joint tests (FLC4 and FLC5), joint tests have been conducted at ambient temperature to determine the joint moment capacities. Therefore, load levels of elevated-temperature testes could be selected based on ambient temperature joint tests. From the measured temperature-rotation curves, it was observed that the rotational characteristics have three distinct stages as: *I.* Linear stage; *II.* Onset of yielding stage in one or more of the joint components; *III.* Joint failure stage with a plateau. From experimental findings, Al-Jabri *et al.* developed simplified mathematical expressions to represent the elevated temperature test data for incorporation in numerical modelling of steel-framed structures. Ramberg-Osgood equations were adopted to describe the moment-rotation versus temperature relationships in this study. However, these derivations were limited to certain types of joints.

Since the introduction of "Component-Based" method, there has been some research works conducted on the investigations of separated component behaviour of steel joints at elevated temperatures. Recently, some experimental works on the compression and tension zones of steel joint have been conducted at elevated temperatures (Spyrou, S. 2001, 2002, 2004[a]. 2004[b] and 2004[c]). The experimental programme consisted of two parts: I. T-Stub tests; II. Compression tests of column

flange and web. A specially designed image processing system has been calibrated and used as a deflection measurement aid. From experimental observations, the bolt flexibility was crucial in the behaviour of the T-Stub specimen. Furthermore, three different failure modes of T-Stub were investigated analytically and numerically with good agreement in load-deflection relationships. From tests of column compression zone, it was noticed that current design standards gave very conservative values for the ultimate capacity of column sections. Furthermore, a simplified semi-empirical model has been derived based on the theory of partial edge loading on thick plate girder. Both analytical and numerical predictions were in good agreement with experimental measurements. However, there was no consideration of axial restraint effect in this study. This effect will be induced in fire situations by surrounding cooler structures.

As an extension of Spyrou's study, Block *et al.* (2004[a], 2004[b]) conducted another experimental investigation on the compression zone in the column web with axial compression in column due to superstructure loading. A universal column section (UC 152x152x37kg/m) was chosen and tested under 20, 450, 550 and 600 ^{o}C, respectively, with axial load ratios of 0.0, 0.2 and 0.3. Numerical simulations showed close agreement with experimental force-deflection measurements. Furthermore, a semi-empirical model has been developed based on the parametric study with combination of initial elastic stiffness and final deflection at ultimate load. This derived analytical model compared well with the compression tests performed at high temperatures.

2.5 Simplified Analytical Models

From experimental investigations of different steel beam-to-column joints, various failure modes were identified. Based on these failure modes, major deformation sources and the collapse mechanism of joints can be identified. Initial rotational

stiffness can be predicted in addition to ultimate moment capacity. A number of researchers have considered the behaviour of crucial components for a wide range of joint configurations.

In 1981, Johnson and Law provided an investigation of bending moment-rotation relationship for a beam-column joint in a composite frame. A typical flush end-plate beam-to-column joint was studied in this case. The general form of joint stiffness was assumed:

$$K = \frac{1}{0.5\left[\left(1/K_b\right)+\left(1/K_c\right)\right]\lambda + 1/K_e} \tag{2.9}$$

in which: K_b, K_c and K_e were stiffnesses of the bolts, column flange and end-plate, respectively.

The respective contribution from each component inside the joint was identified. Different components of joint were then superimposed without considering the interactions among the various components. From this analytical procedure, the elastic stiffnesses of bare steel and composite flush end-plate joint were provided by Johnson and Law. Therefore, the overall joint behaviour was expressed with a three-stage form using simplified elastic-plastic curve fitting. From comparison with experimental data, the approach gave a close agreement with test results. However, there was still a lack of clear description of other failure modes which might occur within the joint.

In 1986, Yee and Melchers developed a mathematical model to predict the moment-rotation relationships of bolted extended end-plate joints. Both stiffened and unstiffened extended end-plate joints were considered in this study. They adopted a nonlinear mathematical expression to simulate the moment-rotation relationship of joints, as follows.

$$M = M_p\left\{1-\exp\left[\frac{\left(K_p - K_i - C\theta\right)\theta}{M_p}\right]\right\} + K_p\theta \tag{2.10}$$

in which: M_p is moment capacity of joint, K_i and K_p are initial and strain-hardening stiffnesses of joints, C is shape parameter. In their study, Yee and Melchers derived and presented the corresponding key parameters of two types of joints based on respective failure modes from different components within the joint. The shape parameter C was dependent on the type of bolted joint and assembly, which must be obtained from test measurements. Although discrepancies existed between experimental and predicted results, their method appeared to be the first example of "Component-Based" method.

For joints consisting of top and seat angles with web cleats, Kishi *et al.* (1987, 1988[a], 1988[b]) derived the initial stiffness (Equation 2.13) based on certain assumptions

$$R_{ki} = \frac{3EI_t d_1^{\,2}}{g_1(g_1^{\,2} + 0.78t_t^{\,2})} + \frac{6EI_a d_3^{\,2}}{g_3(g_3^{\,2} + 0.78t_a^{\,2})} \tag{2.11}$$

in which: EI_t and EI_a are bending stiffnesses of legs of top angle and web angle.

The ultimate moment capacity was given by:

$$M_u = \frac{\sigma_y l_s t_s^{\,2}}{4} + \frac{V_{pt}\left(g_1 - k_t\right)}{2} + V_{pt}d_2 + 2V_{pa}d_4 \tag{2.12}$$

For the top and seat angle joints, the bending stiffness and ultimate moment capacity were given as:

$$R_{ki} = \frac{3EI_t d_1^{\,2}}{g_1(g_1^{\,2} + 0.78t_t^{\,2})} \qquad M_u = \frac{\sigma_y l_s t_s^{\,2}}{4} + \frac{V_{pt}\left(g_1 - k_t\right)}{2} + V_{pt}d_2 \tag{2.13}$$

In case of single web angle joints, the corresponding characteristics were given as:

$$R_{ki} = G\frac{t^3}{3}\frac{\alpha\cosh(\alpha\beta)}{(\alpha\beta)\cosh(\alpha\beta) - \sinh(\alpha\beta)} \qquad M_u = \frac{2V_{pu} + V_0}{6} l_p^{\,2} \tag{2.14}$$

After obtaining R_{ki} and M_u, Kishi *et al.* adopted a power model to describe the moment-rotation curves for joints, given as:

$$M = \frac{R_{ki}\theta_r}{\left[1+(\theta_r/\theta_o)^n\right]^{1/n}} \tag{2.15}$$

in which: $\theta_o = M_u / R_{ki}$; n is shape parameter. Detailed shape parameters were obtained and presented by Liew *et al.* (1993[a]) with good agreement with test data. With these detailed moment-rotation descriptions of beam-to-column angle joints, the inelastic response of semi-rigid steel frame could be determined based on a second-order plastic hinge analytical method by Liew *et al.* (1993[b]).

$$\begin{aligned}
n &= 0.520\log_{10}\theta_o + 2.291 \geq 0.70 && \text{for single web angle joints}\\
n &= 1.322\log_{10}\theta_o + 3.952 \geq 0.60 && \text{for double web angle joints}\\
n &= 2.003\log_{10}\theta_o + 6.070 \geq 0.30 && \text{for top and seat angle joints}\\
n &= 5.483\log_{10}\theta_o + 14.745 \geq 0.80 && \text{for top and seat angle joints with double web angles}
\end{aligned} \tag{2.16}$$

2.6 Mechanical Models (Spring Models)

Steel beam-to-column joints consist of several deformable and rigid elements within the mechanical zones of joint. Simplified analytical models cannot define clearly the separated and overall behaviour of components within the joints. Therefore, mechanical models (spring models) have been developed to better describe the moment-rotational characteristics of steel beam-to-column joints. This procedure consists of a set of analytical model derivations for various elements within the joint. Overall joint characteristics then can be obtained by assembling all the separate mechanical models together. Therefore, this analytical method for the determination of joint mechanical property is defined as “Component-Based” method.

The concept of “Component-Based” method was first proposed by Witteveen *et al.* at 1982. They found that the beam-to-column joint could not reach its maximum

capacity when one or more of the different mechanical zones became critical, i.e. compression zone, tension zone and shear zone as shown in Figure 2.6.

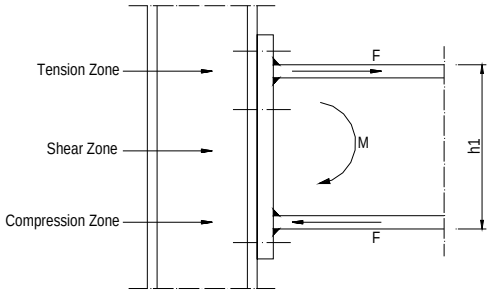

Figure 2.6 Critical Zones of Steel Beam-to-Column Joint (Witteveen *et al.* 1982)

The corresponding failure forces for three modes of failure have been derived, from which the lowest value gave the beam-to-column joint moment capacity. In addition, the interactions of forces acting on the column web panel have been investigated experimentally. It was noticed that for tension and shear zones, effects of interacting forces on separately calculated failure loads were negligible. For the compression zone, the redistribution of stresses was influenced by buckling of column web panel. This was governed by normal force and bending moment in the column.

In 1982, Wales and Rossow proposed a general model for double angle bolted joint. This model simplified the web angle bolted joint into two rigid bars connected by nonlinear distributed springs as shown in Figure 2.7

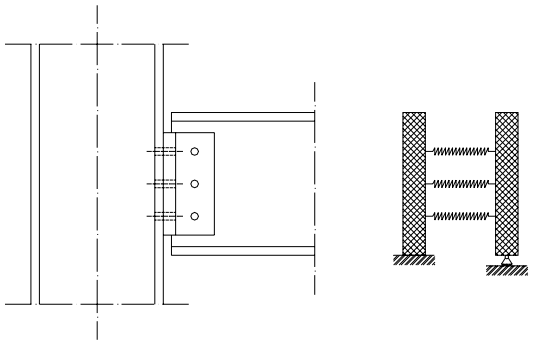

Figure 2.7 Simplified Model for Double Angle Joint (Wales *et al.* 1982)

The stiffness within the tensile area was obtained from simple analysis with consideration of deformations from angles and bolts. However, the stiffness of springs within the compression area was obtained from assuming that the column web mainly resisted compressive forces in the joint. The derived moment-rotation relationships were in good agreement with experimental results.

Later in 1988, Tschemernegg and Huber conducted a series of welded and bolted joint tests. Based on experimental observations, a general spring model was developed incorporating the springs as shown in Figure 2.8. For welded beam-to-column joint, in which, the connection spring was assumed to be infinitely rigid. The load introduction spring was defined to describe the load-deformation relationship, due to the load transmitted by the beam flanges. The shear spring represented the shear deformation of the panel zone of column. Therefore, the nonlinear behaviour of joints can be obtained by superposition of the moment-deflection relationships of these three springs. This modelling technique was verified by several tests conducted by Tschemernegg and Humer. However, the mechanical characteristics of individual springs must be obtained from experiments or simplified analytical methods, which might cause discrepancies compared with actual behaviour of steel joints.

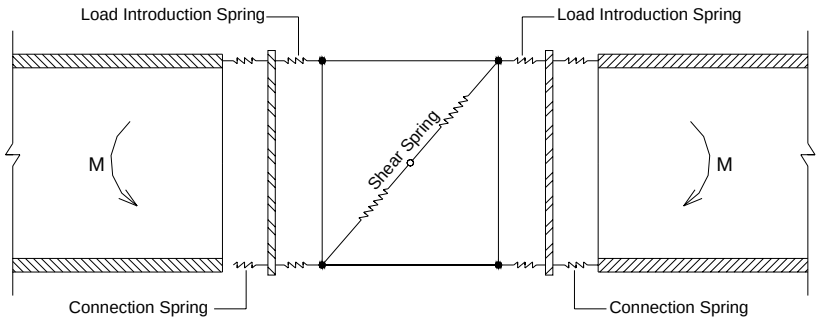

Figure 2.8 Spring Models for Welded Joints (Tschemernegg *et al.* 1988[a], 1988[b])

From then on, it is realized that the active joint components and their mechanical descriptions can be collected and assembled together for overall analysis of the beam-to-column joints. This method for the determination of the mechanical properties of the joint becomes known as the "Component-Based" method. The principles of this method were also proposed by Zoetemeijer at 1983. Later, the "Component-Based" method was standardized in Eurocode 3 (ENV 1993-1-1). This analytical method has the following advantages compared with the simple analytical expressions and finite element models:

- "Component-Based" method focuses on the mechanical, geometrical and material properties of different components within the joint;
- "Component-Based" model is appropriate for failure load calculations under different failure modes, due to the changes in geometrical and material properties of the investigated joint;
- "Component-Based" method can easily be implemented into frame analysis.

With the "Component-Based" method, it is necessary to identify the different components within a steel joint. For instance, as shown in Figure 1.6, the components in a typical end-plate joint subjected to bending moment can be divided into three main zones, as shear zone, compression zone and tension zone. Each zone has different components as listed in Table 1.1.

Based on a series of experimental investigation, Li *et al.* (1996[b]) presented a comprehensive method for predicting the moment capacities of flush end-plate composite joints. This approach was similar to Eurocode 3 (ENV 1993-1-1). In this method, both unbalanced moment effects and varying shear/moment ratios were taken into account. Li *et al.* (1996[b]) have identified twelve failure modes for the flush end-plate composite joint, with the exclusion of weld and shear stud failures. A series of simplified equations was given to calculate the resistance of each bolt row, buckling resistance of column web and resistance of reinforcement for both

symmetrical and unsymmetrical loadings. With this procedure, predictions of joint moment capacity were conducted with reasonable agreement with test results from Xiao *et al.* (1994), Anderson and Najafi (1994) and Li *et al.* (1996[a]).

Based on a detailed experimental investigation, Leston-Jones *et al.* (1997[a], 1997[b]) proposed spring stiffness models for bare steel and composite flush end-plate joints for a clearer representation of moment-rotation characteristics at elevated temperatures. This spring stiffness model was developed based on existing ambient-temperature studies, with modified material properties to account for temperature effects. However, time-dependent factors such as thermal creep and expansion were neglected in this modelling technique. To simplify the modelling procedure, the stiffness of various components within the tension zone was considered as a single spring with an equivalent stiffness (Figure 2.10). The detailed mechanical descriptions for different components within the tension and the compression zone were explained by Leston-Jones *et al.* However, due to typical balanced two-sided joint, there was no consideration of the shear deformation of column web panel. Initially, the proposed spring stiffness model for flush end-plate joint was compared with ambient-temperature tests. It can be seen that the proposed mechanical model provided a reasonable prediction of the initial stiffness of joint. Although, the predicted ultimate capacity of joint seemed to overestimate experimental results, it could provide a close prediction of ultimate capacity. Experimental results were compared with predicted values for two key parameters: stiffness and strength. From comparison, it was found that the predicted stiffness seemed higher than experimental measurement below 600 ^{o}C. However, the predicted moment capacity compared closely with experimental ones.

Following the similar approach suggested by Leston-Jones *et al.* (1997[a]), Al-Jabri (1999) developed a component spring model for bare steel and composite flexible

end-plate joint. The joint components in this model were chosen as bolts, column flange end-plate in tension zone and column web panel in compression zone as shown in Figure 2..

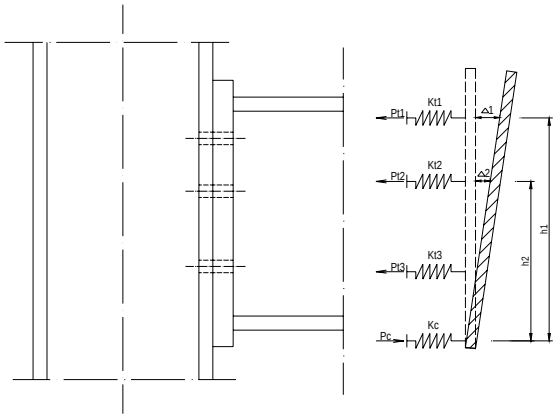

Figure 2.9 Idealized Spring Stiffness Model for Bare-Steel Flush End-plate Joint (Leston-Jones *et al.* 1997[a], 1997[b])

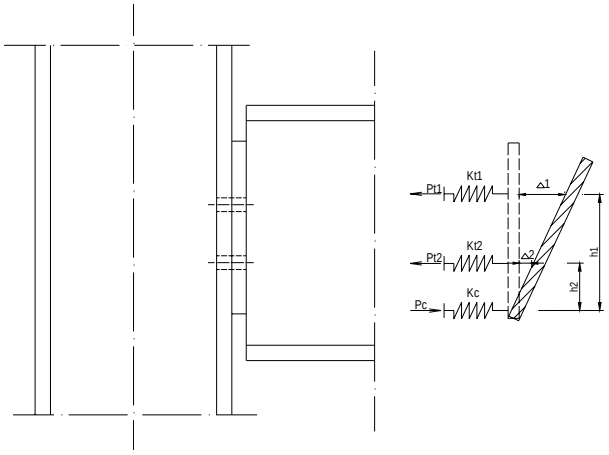

Figure 2.10 General Spring Model for Flexible End-plate Joint (Al-Jabri, 1999)

Due to a lack of experimental data, only rotational behaviour before contact between the beam bottom flange and the column flange was considered. From comparison with experimental result at ambient temperature, the proposed model could predict closely the initial stiffness of joint but underestimate the influence of material strain-hardening stage. Furthermore, from comparison with test results at elevated temperatures, the proposed model predicted joint stiffness well for temperature up to 400 ^{o}C. It then overestimated the joint stiffness beyond this limit.

In addition, the proposed model gave slightly conservative values between 500 ^{o}C and 600 ^{o}C.

Recently, Liew *et al.* (2004[b]) presented an additional analytical assessment of moment capacity and initial rotational stiffness of the beam-to-column joints based on the previous experimental investigations conducted by Liew *et al.* (2000, 2004[a]). The "Component-Based" method from Eurocode 3 (ENV 1993-1-1) was used to determine the hogging moment capacity and initial rotational stiffness. With the same methodology, the method was extended to include joints subjected to sagging moment. In this model, the respective stiffness and capacity of each component within the steel joint was described, with expressions for column web in shear, slab reinforcement and shear stud slip. Comparison between predictions and experimental results showed reasonable agreement. However, it was found that Eurocode 3 (ENV 1993-1-1) overestimated the rotational stiffness of joints subjected to hogging moment.

2.7 Conclusion

As described in this chapter, there were quite a number of investigations on steel beam-to-column joint moment-rotation behaviour. Many researchers tried to obtain a clear understanding of different rotational characteristics of joints and then incorporated these derivations into analyses of practical steel framed structures. However, due to a wide range of joint types and assemblies, simplified curve-fitting method and analytical models can not provide satisfactory solutions. Finite element method was also used to simulate behaviour of joints at different temperatures, but as the complexity of steel joint increases, this method becomes very costly and ineffective for practical designs. On the other hand, "Component-Based" model involves identifying the behaviour of individual components and assembling them together to describe the whole joint behaviour. Through experimental and analytical

investigations, it is possible to obtain an in-depth understanding of the relative importance of individual components of joints. The overall joint rotational behaviour can be achieved and better utilized for different joints. Although some components have yet to be investigated, the method seems the most promising. There is still a complete lack of information on the shear component behaviour at elevated temperatures. Therefore, investigation of the behaviour of this component forms the central theme of this thesis.

CHAPTER 3
ELEVATED-TEMPERATURE MATERIAL PROPERTIES

3.1 Introduction

To obtain a clear understanding of the behaviour of steel beam-to-column joint exposed to fire, it is necessary to investigate effects of temperature on the mechanical properties of structural steel and connecting bolts. The important mechanical parameters defining the performances of steel and connecting elements at elevated temperatures are yield strength, elastic modulus, thermal expansion coefficient, specific heat and thermal conductivity. Extensive investigations have been conducted to study the influence of elevated temperature on the mechanical behaviour of steel, most of which have been adopted in Eurocode 3 (EN 1993-1-2) and BS 5950: Part 8 (BS 5950-8). But there are insufficient studies on the effects of elevated temperature on additional connecting bolts.

3.2 Steel Mechanical Properties Degradation in Fire

Steel strength reduces sharply at temperature exceeding 400 ^{o}C, approximately in a linear rate up to 800 ^{o}C, where it only has 11% of original strength at ambient temperature. There have been different recommendations for the strength decaying rates as a function of increasing temperature, but there are still variations within these recommendations. Different testing procedures and different steel constitutive properties account for the variations among these recommendations.

3.2.1 Steel Material Properties Tests

There are two test methods for determining the steel stress-strain characteristics:

- *Isothermal (or Steady-State) test*

This method has been traditionally used for mechanical engineering applications. In this test, the tensile specimen is subjected to a constant temperature, and strain is mechanically induced at a steady rate. Therefore, the strain-stress response is appropriate for a given constant temperature.

- *Anisothermal (or Transient) test*

In this test, the specimen is subjected to a constant load with temperature increasing at a pre-determined rate, to certain temperature level. The total strains measured consist of mechanical, thermal and creep strain. The thermal strain can be deducted using "dummy" specimens heated at the same rate in an unloaded condition. The stress-strain curves may be interpolated from a series of curves at different stress levels.

Kirby and Preston (1988) reviewed both testing methods and compared the test results from the two methods. In their investigation, two series of steel qualities (Grade 43A and 50B) were tested according to BS 4360 (BS 4360, 1979). Test results demonstrated that when only low strains were involved, predictions using stress-strain curves from steady-state tests on behaviour of steel would be optimistic, compared with material characteristics derived from transient tests. However, when considering strains approaching very high values, such as the limits of deflection or instability in standard fire resistance test, there should be some justifications in using data from either source of test procedures to predict the behaviour of steel elements in fire.

3.2.2 Steel Stress-Strain Models

Traditionally, investigations on mechanical characteristics of steel under elevated temperatures were restricted to the maximum temperature of 550 ^{o}C. This was because, normally, the critical temperature of steel would be lower than 550 ^{o}C. Therefore, detailed knowledge of steel properties above 550 ^{o}C was deemed not necessary. As research progressed and resulted in a better understanding of structural response at elevated-temperature, there has been a gradual realization that steel structures have some reserve strength beyond this limit. Consequently, different stress-strain models for steel at elevated temperature are established. Experimental strain-stress curves should be nonlinear, but in actual analysis, simplified bi-linear or tri-linear curves are often used for simplicity. The stress-strain relationships are idealized as a bi-linear model, as shown in Figure 3.1. However, the bi-linear model does not have smooth transition from the elastic to plastic range, and therefore unable to represent the highly nonlinear steel property at elevated temperature. To overcome this problem, a tri-linear model (Figure 3.2) is introduced in which there is a smoother transition from the elastic to plastic range to account for material nonlinearity.

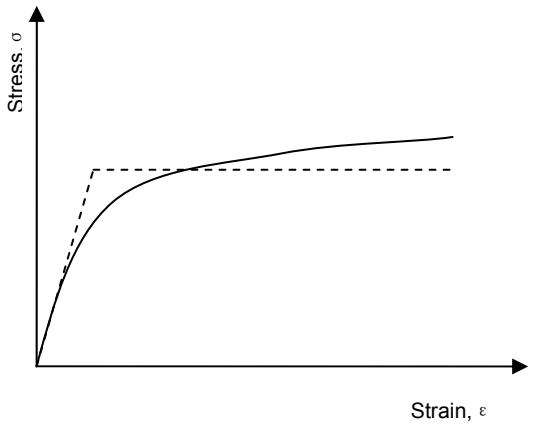

Figure 3.1 Bi-Linear Model for Steel Stress-Strain Curve

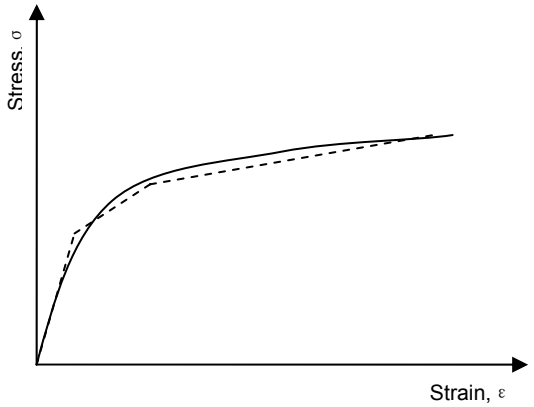

Figure 3.2 Tri-Linear Model for Steel Stress-Strain Curve

➢ *Eurocode 3 Stress-Stain model (Adopted Model)*

Eurocode 3 Part 1.2 (ENV 1993-1-2) suggests a mathematical model based on the data from Kirby and Preston (1988). This stress-strain model consists of two straight lines connected by an elliptic curve, which is named as bilinear-elliptic model (Figure 3.3). It is smoother than bi-linear and tri-linear stress-strain models, and it has continuously differentiable characteristic which is beneficial for computational analysis. .

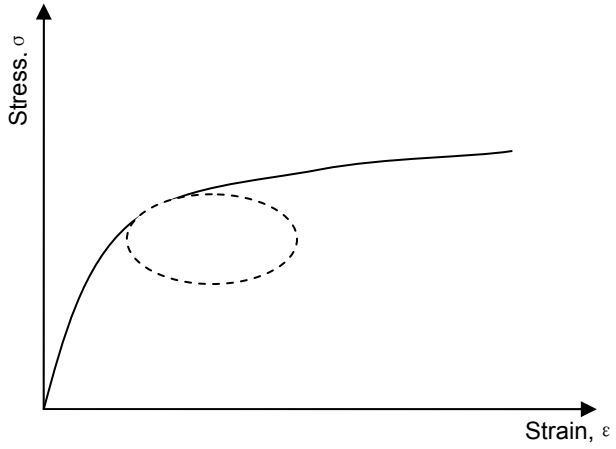

Figure 3.3 Idealized Bilinear-Elliptical Stress-Strain Model

This idealized bilinear-elliptical stress-strain relationship is depicted in Figure 3.4. The first straight line represents the elastic stage up to the proportional limit $f_{p,T}$ with the corresponding strain $\varepsilon_{p,T}$. The second elliptic curve models the

transition from the elastic to the yield strength $f_{y,T}$ with the corresponding yield strain $\varepsilon_{y,T}$. The third horizontal line represents the non-hardening plastic stage until the strain reaches the limit strain $\varepsilon_{l,T}$ at the yield strength $f_{y,T}$. The last declining line represents the steel strength reduction after the plastic stage until the strain reaches the ultimate strain $\varepsilon_{u,T}$. In this bilinear-elliptical stress-strain model, the yield strain $\varepsilon_{y,T}$, the limit strain $\varepsilon_{l,T}$ for the yield strength and the ultimate strain $\varepsilon_{u,T}$ are all specified to be temperature-independent. The stress-strain model relationship at various elevated temperature is defined in Table 3. 1. Table 3.2 shows the different values of reduction factors with respect to temperature: the effective yield strength $f_{y,T}$, the proportionality limit $f_{p,T}$, and the elastic modulus $E_{a,T}$ relative to the appropriate value at 20 °C. The variation of these three reduction factors with temperature is illustrated in Figure 3.5. As listed in Table 3.2, there is also a modified reduction factor $k_{x,T}$ for use in place of $k_{y,T}$ where it is necessary to satisfy deformation criterion. Figure 3.6 shows the stress-strain relationship of steel grade S275 at different temperatures.

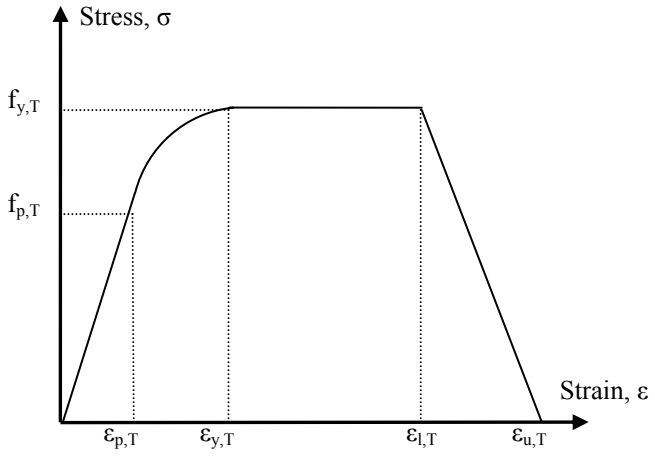

Figure 3.4 Basic Formulation of Stress-strain Relationship of Steel at Elevated Temperature

Table 3. 1 EC 3 Stress-strain Relationship for Steel at Elevated Temperatures (ENV 1993-1-2)

Strain range	Stress σ	Tangent modulus
$\varepsilon \le \varepsilon_{p,T}$	$\varepsilon E_{a,T}$	$E_{a,T}$
$\varepsilon_{p,T} < \varepsilon \le \varepsilon_{y,T}$	$f_{p,T} - c + (b/a)\left[a^2 - (\varepsilon_{y,T} - \varepsilon)\right]^{0.5}$	$\dfrac{b(\varepsilon_{y,T} - \varepsilon)}{a\left[a^2 - (\varepsilon_{y,T} - \varepsilon)^2\right]^{0.5}}$
$\varepsilon_{y,T} < \varepsilon \le \varepsilon_{t,T}$	$f_{y,T}$	0
$\varepsilon_{t,T} < \varepsilon \le \varepsilon_{u,T}$	$f_{y,T}\left[1 - (\varepsilon - \varepsilon_{t,T})/(\varepsilon_{u,T} - \varepsilon_{t,T})\right]$	---
$\varepsilon = \varepsilon_{u,T}$	0.000	---

in which: $a^2 = (\varepsilon_{y,T} - \varepsilon_{p,T})(\varepsilon_{y,T} - \varepsilon_{p,T} + c/E_{a,T})$ $b^2 = c(\varepsilon_{y,T} - \varepsilon_{p,T})E_{a,T} + c^2$

$$c = \frac{(f_{y,T} - f_{p,T})^2}{(\varepsilon_{y,T} - \varepsilon_{p,T})E_{a,T} - 2(f_{y,T} - f_{p,T})}$$

where: $f_{y,T}$ =effective yield strength at elevated temperatures (MPa);

$f_{p,T}$ =proportional limit strength at elevated temperatures (MPa);

$E_{a,T}$ =slope of the linear elastic range at elevated temperatures (MPa);

E =slope of the linear elastic range at ambient temperatures (MPa);

$\varepsilon_{p,T}$ =the strain at proportional limit at elevated temperatures is equal to $\varepsilon_{p,T} = f_{p,T} / E_{a,T}$;

$\varepsilon_{y,T}$ =the yield strain at elevated temperatures, equals to 2%;

$\varepsilon_{l,T}$ =the limiting strain for yield strength at elevated temperatures (15%);

$\varepsilon_{u,T}$ =the ultimate strain at elevated temperatures is equal to 20%;

T =steel temperature.

Table 3.2 Reduction Factors for Stress-Strain Relationship of Steel at Elevated Temperature (ENV 1993-1-2:1995)

Temperature (°C)	Effective Yield Stress $K_{yT} = f_{yT} / f_y$	Modified Factor for Yield Strength $K_{xT} = f_{yT} / f_y$	Proportionality Limit Stress $K_{pT} = f_{pT} / f_y$	Elastic Modulus $K_{ET} = E_T / E$
20	1.000	1.000	1.000	1.000
100	1.000	1.000	1.000	1.000
200	1.000	0.922	0.807	0.900
300	1.000	0.845	0.613	0.800
400	1.000	0.770	0.420	0.700
500	0.780	0.615	0.360	0.600
600	0.470	0.354	0.180	0.310
700	0.230	0.167	0.075	0.130
800	0.110	0.087	0.050	0.090
900	0.060	0.051	0.0375	0.0675
1000	0.040	0.034	0.0250	0.0450
1100	0.020	0.017	0.0125	0.0225
1200	0.000	0.000	0.000	0.0000

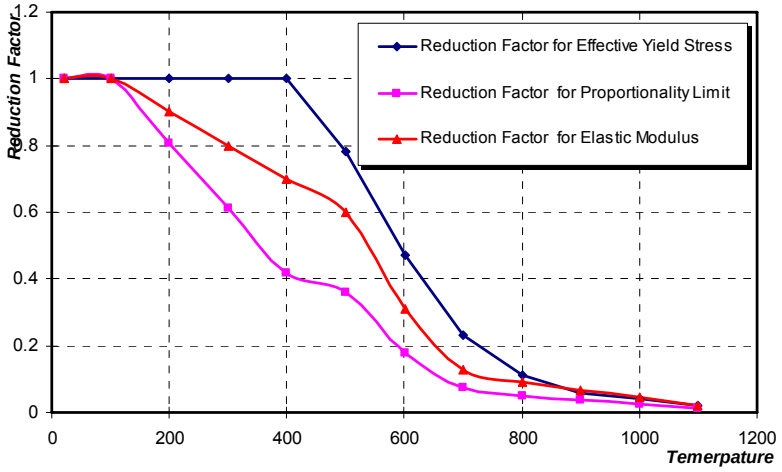

Figure 3.5 Reduction Factors for Steel at Elevated Temperature (ENV 1993-1-2)

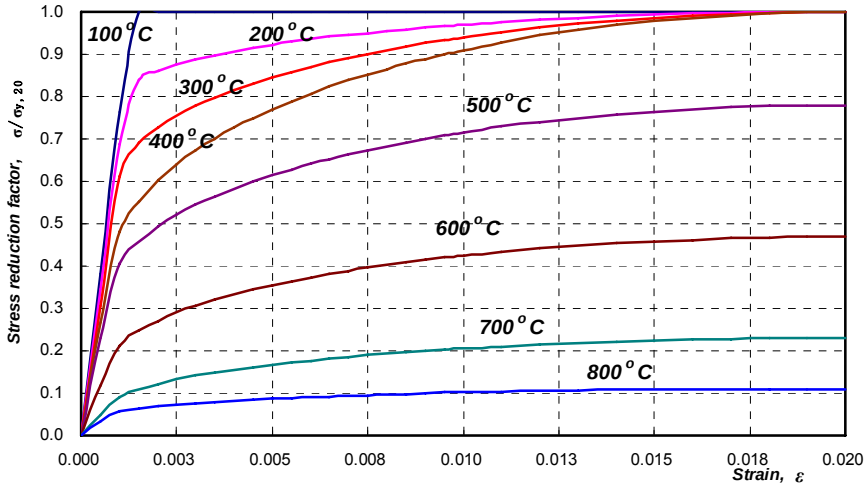

Figure 3.6 Variation of Stress-strain Relationship for Grade S275 Steel (ENV 1993-1-2)

➢ *British Standard 5950 Stress-Strain Model*

BS 5950: Part 8 (BS 5950-8) adopts the concept of "strength reduction factor" to represent the steel strength deterioration at elevated temperatures. The strength reduction factors are specified as ratios of strengths at elevated temperatures to design strength at room temperature. At room temperature, the stress-strain characteristics of steel are approximately bi-linear. With temperature increasing, the stress-strain curves become increasingly nonlinear resulting in difficulty to define the exact yield point and elastic modulus. However, when assessing the structural performance in fire, consideration should be given to both the limiting strain in the steel and the corresponding strain in fire protection materials. As specified in BS 5950: Part 8 (BS 5950-8), for composite members with or without fire protection materials, the limit level of strain demonstrated ability to remain intact is 2.0%. For non-composite members with or without protection materials, the limit level of strain is 1.5%. For steel members not coved in previous two categories, the strain level is suggested as 0.5%. The strength retention factors for Grade S275 to S355 steels are given in Table 3.3. The degradation of steel strength according to strain limit of 0.5% and 2.0% as specified in both BS 5950: Part 8 (BS 5950-8) and EC3:

Part 1.2 (ENV 1993-1-2) (viz. K_{xT} and K_{yT} in Table 3.2) is shown in Figure 3.7. Since the same test data was used for both design codes (Al-Jabri, 1999), it is explicit that there are quite similar degradation trends between these two design standards.

Table 3.3 Strength Retention Factors for Steel in BS 5950: Part 8 (BS 5950-8)

Temperature (°C)	Strength reduction factors at a strain (%) of:			Temperature (°C)	Strength reduction factors at a strain (%) of:		
	0.5	1.5	2.0		0.5	1.5	2.0
100	0.97	1	1	550	0.492	0.612	0.627
150	0.959	1	1	600	0.378	0.46	0.474
200	0.946	1	1	650	0.269	0.326	0.337
250	0.884	1	1	700	0.186	0.223	0.232
300	0.854	1	1	750	0.127	0.152	0.158
350	0.826	0.968	1	800	0.071	0.108	0.115
400	0.798	0.956	0.971	850	0.045	0.073	0.079
450	0.721	0.898	0.934	900	0.03	0.059	0.062
500	0.622	0.756	0.776	950	0.024	0.046	0.052

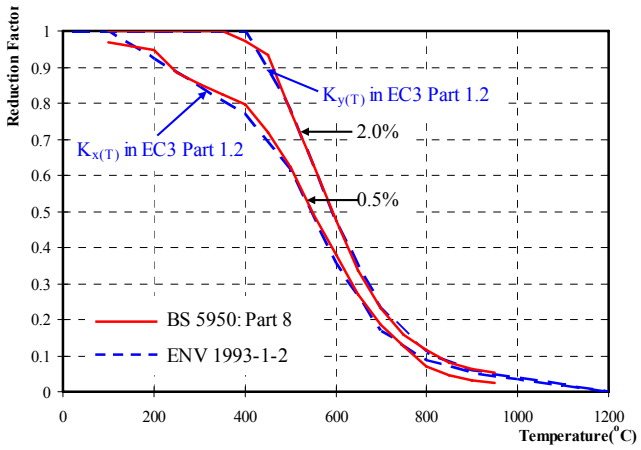

Figure 3.7 Strength Retention Factors according to BS 5950: Part 8 and EC 3: Part 1.2

➢ *ECCS model (ECCS 1983)*

The European Convention for Constructional Steelworks (1983) provides recommendations for fire resistance calculations of load bearing steel elements and structural assemblies exposed to standard fire. In ECCS model (1983), the

stress-strain curve is cut off at a certain stress level, defined as effective yield stress, as shown by the dashed line in Figure 3.8.

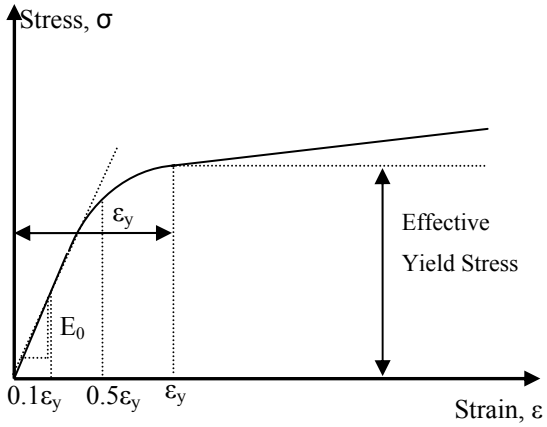

Figure 3.8 Stress-Strain Curve of Steel at Elevated Temperatures (ECCS 1983)

The effective yield stress decreases with increasing temperature, and can be calculated using the following equations for different range of temperatures:

$$f_{y,T} = f_{y,20}\left[1+\frac{T}{767\ln(T/1750)}\right] \quad \text{for} \quad 0 \le T \le 600℃$$
$$f_{y,T} = f_{y,20}\left[\frac{108(1-(T/1000))}{T-440}\right] \quad \text{for} \quad 600 \le T \le 1000℃ \tag{3.1}$$

where: $f_{y,T}$ =effective yield stress at elevated temperature (MPa);

$f_{y,20}$ =nominal yield stress at room temperature (MPa);

T =steel temperature (^{o}C).

The elastic modulus E_0^T at elevated temperature can be obtained from the following equations:

$$E_0^T = E_0^{20}\left(1-17.2\times10^{-12}T^4+11.8\times10^{-9}T^3-34.5\times10^{-7}T^2+15.9\times10^{-5}\right) \quad \text{for} \quad 0 \le T \le 600℃ \tag{3.2}$$

For $T \ge 600℃$, E_0^T is undefined as there is a lack of test data about steel properties beyond this temperature.

- *Improved ECCS Stress-Strain Model (Franssen 1987)*

To overcome the limitations of the ECCS model beyond 600 °C, Franssen (1987) suggested the following relationships to describe the stress-strain characteristics of steel for temperature greater than 600 °C.

$$f_y^T = f_y^{20} \qquad E_o^T = E_0^{20} \qquad \text{for } T \le 100℃ \tag{3.3}$$

For temperature between 100 °C and 500 °C,

$$\begin{aligned} f_y^T &= f_y^{20}\left[0.00295\left(\frac{T}{100}\right)^3 - 0.0488\left(\frac{T}{100}\right)^2 + 0.0877\left(\frac{T}{100}\right) + 0.957\right] \\ E_o^T &= E_0^{20}\left[-0.018\left(\frac{T}{100}\right)^2 + 0.036\left(\frac{T}{100}\right) + 0.982\right] \end{aligned} \tag{3.4}$$

For temperature between 500 °C and 600 °C,

$$\begin{aligned} f_y^T &= f_y^{20}\left[-0.000421\left(\frac{T}{100}\right)^3 + 0.02344\left(\frac{T}{100}\right)^2 - 0.3806\left(\frac{T}{100}\right) + 1.919\right] \\ E_o^T &= E_0^{20}\left[-0.018\left(\frac{T}{100}\right)^2 + 0.036\left(\frac{T}{100}\right) + 0.982\right] \end{aligned} \tag{3.5}$$

For temperature beyond 600 °C,

$$\begin{aligned} f_y^T &= f_y^{20}\left[-0.000421\left(\frac{T}{100}\right)^3 + 0.02344\left(\frac{T}{100}\right)^2 - 0.3806\left(\frac{T}{100}\right) + 1.919\right] \\ E_o^T &= E_0^{20}\left[0.0000925926\left(\frac{T}{100}\right)^3 + 0.0125\left(\frac{T}{100}\right)^2 - 0.34\left(\frac{T}{100}\right) + 2.12\right] \end{aligned} \tag{3.6}$$

- *Ramberg-Osgood Stress-Strain Model (El-Rimawi, 1989)*

Based on Ramberg-Osgood equations (Ramberg-Osgood, 1942), which are characterized by three parameters, viz., A^T, B^T and n^T, El-Rimawi (1989) suggested a mathematical model to fit the test data. The relationship between the stress and strain at certain temperature is expressed as follows:

$$\varepsilon^T = \frac{\sigma^T}{a^T A^T} + 0.01\left(\frac{\sigma^T}{b^T B^T}\right)^{n^T} \tag{3.7}$$

in which: $a^T = \dfrac{E^{20^oC}}{180000}$; $b^T = \dfrac{f_y^{20^oC}}{250}$.

For temperature between 20 °C and 100 °C,

$$A^T = 180000 \qquad B^T = 0.00134T^2 - 0.26T + 254.67 \qquad n^T = 237 - 1.58T \tag{3.8}$$

For temperature between 100 °C and 400 °C,

$$A^T = 194000 - 140T^3 \qquad B^T = 242 \qquad n^T = 15.3(400 - T)^{3.1} \times 10^{-7} + 6 \tag{3.9}$$

For temperature between 400 °C and 700 °C,

$$A^T = 295333 - 393.33T^3 \qquad B^T = 492.667 - 0.6266T \qquad n^T = 6 \tag{3.10}$$

For temperature between 700 °C and 800 °C,

$$A^T = 30500 - 15T \qquad B^T = 306 - 0.36T \qquad n^T = 0.04T - 22 \tag{3.11}$$

3.3 Thermal Characteristics of Steel in Fire

Under elevated temperatures, there are three crucial thermal properties for steel, viz. thermal expansion, thermal conductivity and specific heat of steel.

3.3.1 Thermal Expansion of Steel

It is well known that expansion of steel is significant at elevated temperatures. At a temperature between 200 °C and 600 °C, thermal expansion coefficient is generally assumed to be 14×10^{-6} / °C. Cooke (1988) suggested that when a solid material is heated up, it increases in length according to the following equation:

$$L_T = L_0\left(1 + \alpha T + \alpha_1 T^2 + \alpha_2 T^3\right) \tag{3.12}$$

where: L_0 =length at the initial temperature; L_T = length after a temperature rise.

For pure constitutive metal, the constants α, α_1, α_2 have values of the order of 10^{-5}, 10^{-11} and 10^{-14} respectively. Since α_1 and α_2 are smaller than α, the following equation is adequate for engineering calculations:

$$L_T = L_0(1+\alpha T) \tag{3.13}$$

From elevated temperature tests conducted on 22 different steels but with similar carbon contents, Cooke (1988) obtained a mean value of 12.18×10^{-6} per ^{o}C for thermal expansion coefficient in the range of 0-100 ^{o}C to 14.81×10^{-6} per ^{o}C in the range of 0-1200 ^{o}C. Over the range of 0-550 ^{o}C, the mean value is 14.17×10^{-6} per ^{o}C. Therefore, a nominal value of 14×10^{-6} per ^{o}C was recommended for structural steel in fire.

In BS 5950: Part 8 (BS 5950-8), the total elongation $\Delta L / L$ of steel is defined by a single coefficient 14×10^{-6} per ^{o}C above 100 ^{o}C. This has been further defined by a tri-linear relationship in EC 3: Part1.2 (EN 1993-1-2) to describe the different phases of heating in steel in the following equations and Figure 3.9.

$$\begin{aligned}
&\Delta l / l = 1.2\times10^{-5}T + 0.4\times10^{-8}T^2 - 2.416\times10^{-4} && 20\,^{o}\text{C} < T < 750\,^{o}\text{C} \\
&\Delta l / l = 1.1\times10^{-2} && 750\,^{o}\text{C} < T < 860\,^{o}\text{C} \\
&\Delta l / l = 2\times10^{-5}T - 6.2\times10^{-3} && 860\,^{o}\text{C} < T < 1200\,^{o}\text{C}
\end{aligned} \tag{3.14}$$

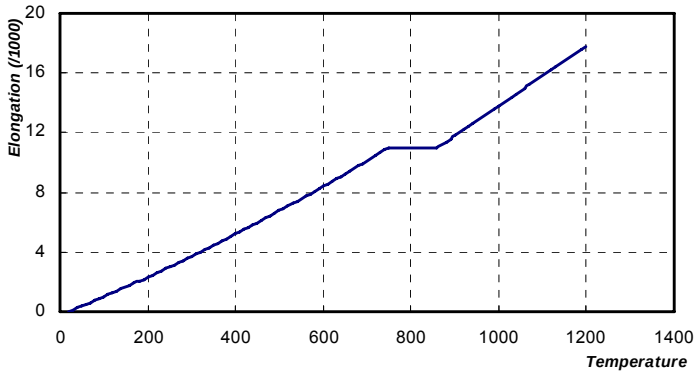

Figure 3.9 Thermal Elongation of Steel (EN 1993-1-2)

3.3.2 Thermal Conductivity of Steel

Thermal conductivity is defined as the heat flow rate arising from temperature gradient. Thermal conductivity in steel is high, approximately 50 times greater than that of concrete. For most calculations a constant value of 37.5W/m^{o}C is

recommended in BS 5950: Part 8 (BS 5950-8), but it is defined more accurately in EC 3: Part1.2 (EN 1993-1-2) for different temperature ranges.

$$\lambda_a = 54 - 3.33 \times 10^{-2} T \quad 20\,^{o}\text{C} < T < 800\,^{o}\text{C} \quad \text{and} \quad \lambda_a = 27.3 \quad 800\,^{o}\text{C} < T < 1200\,^{o}\text{C} \tag{3.15}$$

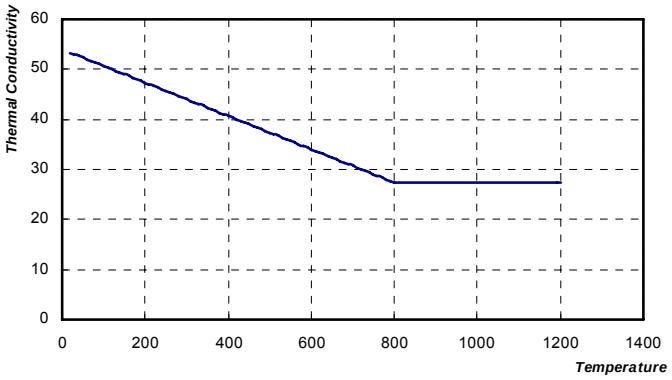

Figure 3.10 Thermal Conductivity Coefficient of Steel (EN 1993-1-2)

3.3.3 Specific Heat of Steel

The specific heat of steel is the amount of heat stored in a unit mass of steel for 1 ^{o}C rise in temperature. The greater the specific heat capacity, the smaller is the rise in temperature for a given amount of heat energy absorbed. For steel material, the widely used value of specific heat of steel is 520J/Kg ^{o}C in BS 5950: Part 8 (BS 5950-8), but it rises rapidly at temperature above 600 ^{o}C. It is described in detail by EC 3: Part1.2 (EN 1993-1-2) for different temperature ranges.

$$\begin{aligned}
C_a &= 425 + 7.73 \times 10^{-1} T - 1.69 \times 10^{-3} T^2 + 2.22 \times 10^{-6} T^3 && 20\,^{o}\text{C} < T < 600\,^{o}\text{C} \\
C_a &= 666 + 13002/(738 - T) && 600\,^{o}\text{C} < T < 735\,^{o}\text{C} \\
C_a &= 545 + 17820/(T - 731) && 735\,^{o}\text{C} < T < 900\,^{o}\text{C} \\
C_a &= 650 && 900\,^{o}\text{C} < T < 1200\,^{o}\text{C}
\end{aligned} \tag{3.16}$$

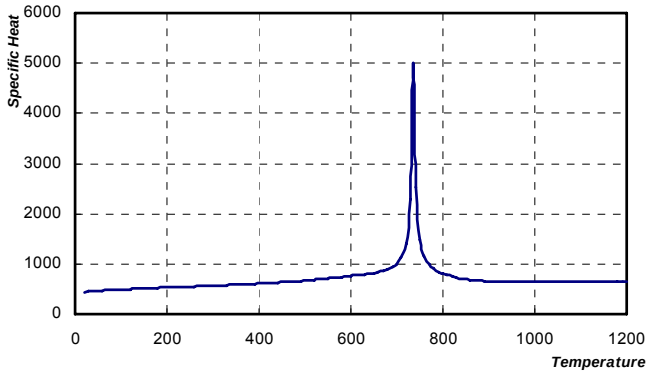

Figure 3.11 Specific Heat of Steel (EN 1993-1-2)

3.4 Degradation of Bolts in Fire

There have been extensive information on the influence of elevated temperature on the mechanical properties of steel, but unfortunately insufficient consideration has been given to the behaviour of bolts in fire. There have been limited recommendations for the degradation of bolts at elevated temperature in previous vision of Eurocode 3 (ENV 1993-1-2) due to insufficient experimental data. At the time of first drafting of BS 5950: Part 8 (BS 5950-8), there was no suitable experimental data, consequently the capacity of bots at elevated temperatures was defined to be 80% of the strength reduction factor used structural steel corresponding to 0.5% strain (as shown in Table 3.4).

Table 3.4 Strength Retention Factors for Grade 8.8 Bolts in Fire (BS 5950-8)

Temperature (^oC)	Strength Reduction Factors	Temperature (^oC)	Strength Reduction Factors
20	0.8	550	0.394
100	0.776	600	0.302
150	0.767	650	0.215
200	0.757	700	0.149
250	0.707	750	0.102
300	0.683	800	0.057
350	0.661	850	0.036
400	0.638	900	0.024
450	0.577	950	0.019
500	0.498		

However, in Japan, fire-resistant steels (FR steels) have been developed and put into practice (Sakumoto, 1992). The corresponding fire resistant bolts (FR bolts) were tested to verify the high-temperature mechanical property of bolts developed for FR steel joints (Sakumoto, 1993). The specimens were chosen as F10T torque-control bolts in accord with JSS II-09-1981 (1981). The experimental investigation consisted of elevated-temperature tensile and relaxation tests of bolts. In addition, high-temperature shear tests of joints were also conducted with temperature ranging between 20 ^{o}C and 800 ^{o}C. Experimental results showed that the strength and stiffness of bolts reduced with increasing temperature. In particular, it was noticed that a marked loss of strength occurred between 300 ^{o}C and 700 ^{o}C.

A similar series of tests has been conducted by Kirby (1995) to quantify the degradation of high strength Grade 8.8 bolts at elevated temperatures. M20 nuts and bolts have been investigated through tests which have mechanical properties meeting the requirement of BS 3692 (BS 3692, 1967). Both tension and double shear tests were conducted over the temperature range between 20 ^{o}C and 800 ^{o}C. In all tests, the bolts showed a marked strength reduction between 300 ^{o}C and 700 ^{o}C. Tension tests also highlighted the problems of premature failure by thread failure, between the bolt and the nut. Based on experimental observations, a proposal was made to amend the design recommendations in BS 5950: Part 8 (BS 5950-8) to reflect more closely the influence of temperature on the bolt capacity, taking into account of possible occurrence of thread failure in tension. For bolts acting in tension and shear, Kirby (1995) recommended a strength reduction factor for the ultimate capacity of bolts by a tri-linear relationship as follows.

$$\begin{aligned} SRF &= 1.0 && T \le 300^{o}C \\ SRF &= 1.0 - (T - 300) \times 0.2128 \times 10^{-2} && 300^{o}C < T \le 680^{o}C \\ SRF &= 0.17 - (T - 680) \times 0.5312 \times 10^{-3} && 680^{o}C < T \le 1000^{o}C \end{aligned} \tag{3.17}$$

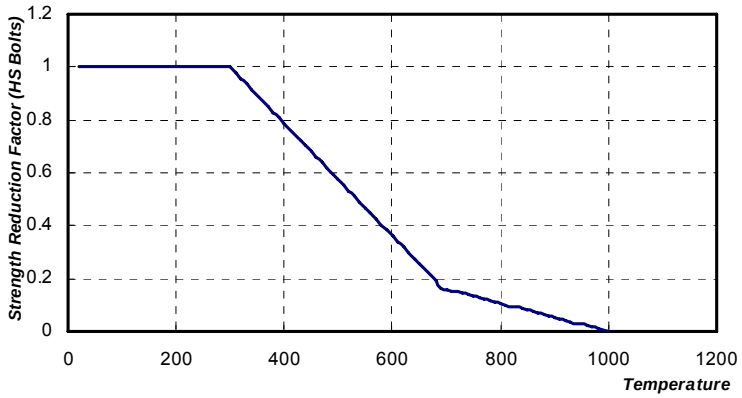

Figure 3.12 Strength Reduction Factor for Grade 8.8 Bolts (Kirby, 1995)

These experimental findings have been incorporated into current Eurocode 3: Part1.2 (EN 1993-1-2), where $K_{b,\theta}$ is used to describe the strength reduction factor with elevated temperature of bolts (as shown in Table 3.5).

Table 3.5 Strength Reduction Factors for Bolts in EC 3: Part1.2 (EN 1993-1-2)

θ_a (°C)	$K_{b,\theta}{}^*$	θ_a (°C)	$K_{b,\theta}{}^*$	θ_a (°C)	$K_{b,\theta}{}^*$	θ_a (°C)	$K_{b,\theta}{}^*$
20	1.000	200	0.935	500	0.550	800	0.067
100	0.968	300	0.903	600	0.220	900	0.033
150	0.952	400	0.775	700	0.100	1000	0.000

$K_{b,\theta}{}^*$:Strength reduction factor for bolts in tension and shear.

Based on nominal bolt properties at ambient temperature specified in BS 3692 (BSI 1967), it is possible to ascertain the tensile strength of bolts at any given temperatures. However, since no recommendations or experimental results are presented for the degradation of elastic modulus for bolts at elevated temperatures, it is suggested to use recommendations in Eurocode 3: Part1.2 (ENV 1993-1-2) for Grade 50 steel (Leston-Jones, 1997).

3.5 Conclusion

When steel framed structures are subjected to fire, steel mechanical properties will deteriorate with increasing temperature. Since the stress-strain relationship at

elevated temperatures in Eurocode 3: Part1.2 (EN 1993-1-2) has been widely accepted in European countries, these same properties are adopted in the experimental and finite element analyses of currently study. With regard to thermal expansion characteristic of steel at elevated temperatures, the simplified thermal expansion coefficient of 14×10^{-6} per ^{o}C above 100 ^{o}C described in Eurocode 3: Part1.2 (EN 1993-1-2) is used. In addition, strength reduction factor for bolts specified in Eurocode 3: Part1.2 (EN 1993-1-2) is used for tensile and shear strengths in current research. Since there is no recommendation on the degradation of elastic modulus for bolts at elevated temperatures, the recommendations in Eurocode 3: Part1.2 (ENV 1993-1-2) for Grade 50 steel is used instead.

CHAPTER 4
BEHAVIOUR OF SHEAR ZONE IN STEEL BEAM-TO-COLUMN JOINT

4.1 Introduction

As described in Chapter 1, it is crucial to predict overall behaviour of steel beam-to-column joint at ambient and elevated temperatures in steel framed structural analysis. Therefore, in current study, a "Component-Based" method has been adopted to evaluate mechanical characteristics of individual components and eventually assemble all components together to evaluate the whole joint stiffness at different temperatures.

In a typical steel beam-to-column joint under fire conditions, mechanical components associated with shear zone consist of the column web and the beam web panels. They are possibly subjected to restrained compressive force induced by adjacent unheated structures. Mechanical investigations for column web panel shear behaviour have been conducted by several researchers (Krawinker *et al.* 1975, Liew *et al.* 1995 and Kato *et al.* 1998, etc.). Structural descriptions for column web panel have also been specified in Eurocode 3 (EN 1993-1-8) as "Component-Based" steel beam-to-column joint modelling at ambient temperature. However, the column web panels are normally not critical under shear force for interior joints with connecting beams subjected to equal but opposite direction bending moments. Besides, there is a lack of information about beam web panel shear component. Therefore, the first part of current study focuses on the shear strength and deflection characteristics of

beam web panel at elevated temperatures. This work will then be implemented into the "Component-Based" method for steel beam-to-column joint modelling in Section 8.4. Moreover, a number of beams in the Cardington fire tests (Wald *et al.* 2004) exhibited tensile field action (TFA) failure mode in the beam web near the supports (Figure 4.1). This mode is similar to the shear failure of plate girders at ambient temperatures. Thus, the behaviour of beam web component under shear can be investigated using a girder web panel subjected to approximately pure shear force as shown in Figure 4.2. This also represents the upper limit of slenderness limit. In addition, UC sections were also used to investigate the lower slenderness limit of web component. These specimens are typical of column web shear component. Due to constraint in time and resources, the test programme did not include any UB sections. It felt that the behaviour of UB sections can be inferred from the upper limit (plate girder) and lower limit (UC section) of web slenderness ratios (as described in Section 5.2).

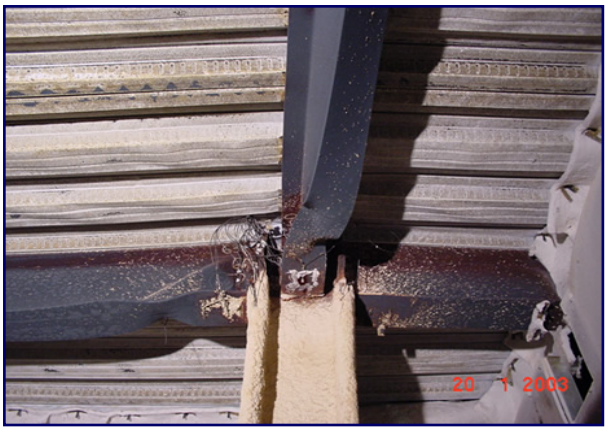

Figure 4.1 Local Buckling of Beam in the Cardington Test (Wald *et al.* 2004)

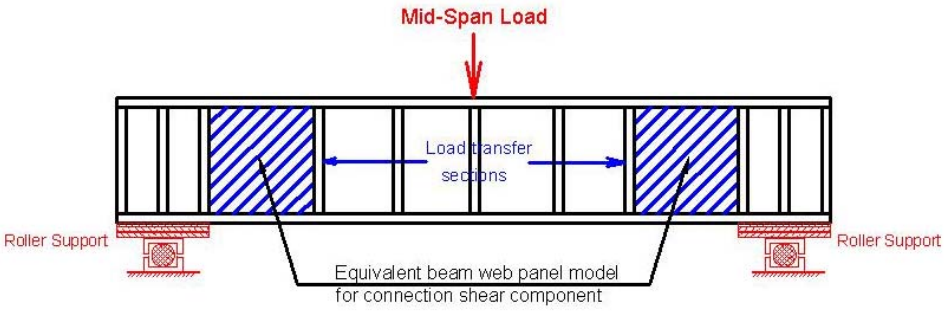

Figure 4.2 Equivalent Shear Zone Model for Steel Beam-to-Column Joint

4.2 Mechanical Modelling of Shear Zone with Plate Girder Theory

In recent years, significant developments have been made on investigations of structural members at elevated temperature, either as an individual member, or as part of a frame, or as a whole structure. Due to a wide range of configurations of steel beam-to-column joint, a "Component-Based" method has been recommended in the Eurocode 3 (EN 1993-1-8) for modelling a joint as a set of different components. From research works at the University of Sheffield, the "Component-Based" method has been applied to compression and tension zones at elevated temperatures. Both experimental and analytical works have been conducted (Leston-Jones *et al.* 1997[a]; Al-Jabri *et al.* 1998; Spyrou, 2002). Nevertheless, there still remain some other components that need to be investigated in order to form an accurate integrated joint modelling at higher temperatures. One example is beam web panel in shear mode. To investigate beam web panel behaviour, one way is to load a plate girder web panel in shear as shown in Figure 4.2.

4.2.1 Mechanical Models of Plate Girder under Shear Load

During the 1930s, the first investigation on buckling and post-buckling behavior of web plates subjected to shear was undertaken by Wagner for aircraft structures. However, findings from this investigation were not directly adopted into the design of plate girders until 1960s. In 1959, Basler and Thurlimann conducted an extensive study on the post-buckling behavior of plate girder web panels under shear. Based on these and the following investigations (Basler, 1961[a] and 1961[b]), the American Institute of Steel Construction (AISC, 1963) first adopted post-buckling shear strength into its specifications. Subsequently, in the 1970s, Rockey and his collaborators in the United Kingdom proposed a unified method to predict the ultimate strength of webs loaded in shear (Rockey and Skaloud 1972; Porter *et al.* 1975; Rockey *et al.* 1978). The failure theory (Rockey *et al.* 1978) assumes that the flanges can develop plastic hinges after the formation of diagonal tensile field

action, and finally the web plate fails in a sway mechanism accompanied by excessive out-of-plane web deformation. Rockey's method was eventually adopted by the British standard (BS 5950-1). Other notable contributions to this area are listed in a monograph by Narayanan (1983). To name a few are the work done by Calladine (1973), Harding and Dowling (1978), and Murray (1983, 1986), among others. At 2006, the classical mechanical models for plate girder under shear at ambient temperature have been extended to elevated temperatures by Vimonsatit et al. (2005) with incorporation of axial restraint compressive forces. Mechanical theories of plate girders at normal ambient condition have been well defined (Murray 1986; Narayanan 1992). For a plate girder under small loads, bending theory may be used to determine internal force distributions, i.e. transverse shear force and bending moment, are carried by the web and the flanges. When the applied load is increased, the failure mode of a plate girder will depend largely on the panel aspect ratio (b/d) and the web slenderness ratio (d/t), where b is the clear distance between vertical stiffeners, d and t are the clear depth and thickness of web panel, respectively. When the panel is stocky enough the web will fail by yielding in shear, which is governed by theoretical shear yield strength $\tau_{yw} = \sigma_{yw}/\sqrt{3}$, where σ_{yw} is the uniaxial tensile yield strength of the web. For most practical plate girders, however, web panels are generally slender, and therefore buckle first before yielding. The overall behaviour of a web panel can be divided into three stages, (1) *Unbuckled*, (2) *Post-buckled*, and (3) *Collapsed*, as shown in Figure 4.3 (a), (b) and (c), respectively.

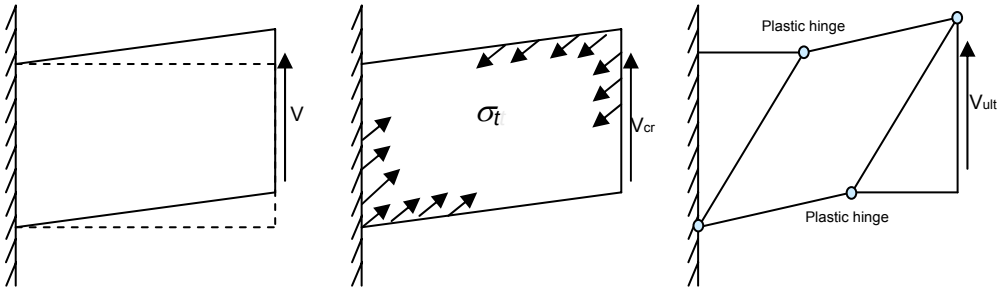

Figure 4.3 Collapse Mechanism for Plate Girders under Shear

➢ *Unbuckled Stage*

If a uniform shear force is applied to the web, principal tensile stress acting at 45° to the flange will be developed and is equal in magnitude with the web shear stress. At the same time, principal compressive stress of an equal magnitude is developed at 135°. This stress state will continue until the applied shear stress reaches the critical shear stress τ_{cr}. The value of τ_{cr} of an isolated panel can be determined from classical stability theory (Timoshenko and Gere 1985). Consequently, if the boundaries of the web are assumed as simply supported, the critical shear stress is given by

$$\tau_{cr} = K\left[\frac{\pi^2 E}{12(1-\nu^2)}\right]\left(\frac{t}{d}\right)^2 \tag{4.1}$$

The buckling coefficient K is obtained from

$$K = 5.35 + 4\left(\frac{d}{b}\right)^2 \text{ if } \frac{d}{b} < 1.0; \quad K = 5.35\left(\frac{d}{b}\right)^2 + 4 \text{ if } \frac{d}{b} > 1.0 \tag{4.2}$$

where: d is the clear depth of web plate between flanges; t is thickness of web plate; b is the clear width of web plate between vertical stiffeners; E is the modulus of elasticity; and ν is the Poisson's ratio. Therefore, the critical shear load that causes web plate buckling is as following equation.

$$V_{cr} = \tau_{cr} dt \tag{4.3}$$

Recent studies show that the restraints provided by flanges can enhance the buckling coefficient K, which will lead to greater calculated shear strength. The increased values of K can be obtained from charts (Bradford 1996), in which a semi-analytical finite strip method of analysis was used to incorporate the interaction between flanges and web of I-beams. Alternatively, simple design equations based on results of numerical analyses using 3-dimensional finite element modelling can be used to determine the shear buckling coefficients (Lee *et al.* 1996). The effects of large initial deformations on web panel shear strength have also been

studied (Lee *et al.* 1998). From numerical investigations by Lee *et al.* it was found that the shear buckling coefficient K of a plate girder web can be determined as follows:

$$K = K_{ss} + \frac{4}{5}\left(K_{sf} - K_{ss}\right)\left[1 - \frac{2}{3}\left(2 - \frac{t_f}{t_w}\right)\right] \quad \text{for} \quad \frac{1}{2} \le \frac{t_f}{t_w} < 2$$
$$K = K_{ss} + \frac{4}{5}\left(K_{sf} - K_{ss}\right) \quad \text{for} \quad \frac{t_f}{t_w} \ge 2 \tag{4.4}$$

in which: K_{ss} is shear buckling coefficient for plates simply supported around four edges as shown in Equation 4.2, and K_{sf} is shear buckling coefficient for plates with two opposite edges simply supported and fixed as shown in Equation 4.5.

$$K_{sf} = \frac{8.98}{(a/d)^2} + 5.61 - 1.99(a/d) \quad \text{for} \quad a/d < 1$$
$$K_{sf} = 8.98 + \frac{5.61}{(a/d)^2} - \frac{1.99}{(a/d)^3} \quad \text{for} \quad a/d \ge 1 \tag{4.5}$$

➢ *Post-buckled Stage*

Once the critical shear stress is reached, web cannot carry any increase in shear stress. Additional shear ΔV has to be supported by another load-carrying system. When web slenderness ratio (d/t) is low, as for standard I-sections, failure of the web panel is governed by yielding. The mechanical system that takes up additional shear load after the web yielding will be provided by the top and bottom flanges. For a plate girder with a high d/t ratio, the web buckles before it yields. After the web has buckled, additional shear force will be supported by the mobilization of tensile membrane stress σ_t in the diagonal band of web, as shown in Figure 4.4. For a web panel subjected to pure shear, the value of σ_t that causes the web to yield can be written, based on the von Mises equation, as:

$$\sigma_t^{\ y} = -\frac{3}{2}\tau_{cr}\sin 2\theta + \sqrt{\sigma_{yw}^2 + \tau_{cr}^2\left[\left(\frac{3}{2}\sin 2\theta\right)^2 - 3\right]} \tag{4.6}$$

where: unknown angle θ is the inclination of tensile stress at membrane yielding strength σ_t^y.

➢ *Collapse Stage*

The failure of plate girder occurs when plastic hinges have formed in flanges, which together with the diagonal yield zone, form a plastic mechanism. In Figure 4.4, the distance between plastic hinges in the compression flange c_c, and in the tension flange c_t, can be determined from the equilibrium of forces acting on the flanges. For a panel with symmetrical top and bottom flanges subjected to pure shear, it can be assumed that $c_c = c_t = c$, which will occur at the location of maximum bending moment on the flanges where shear force is zero.

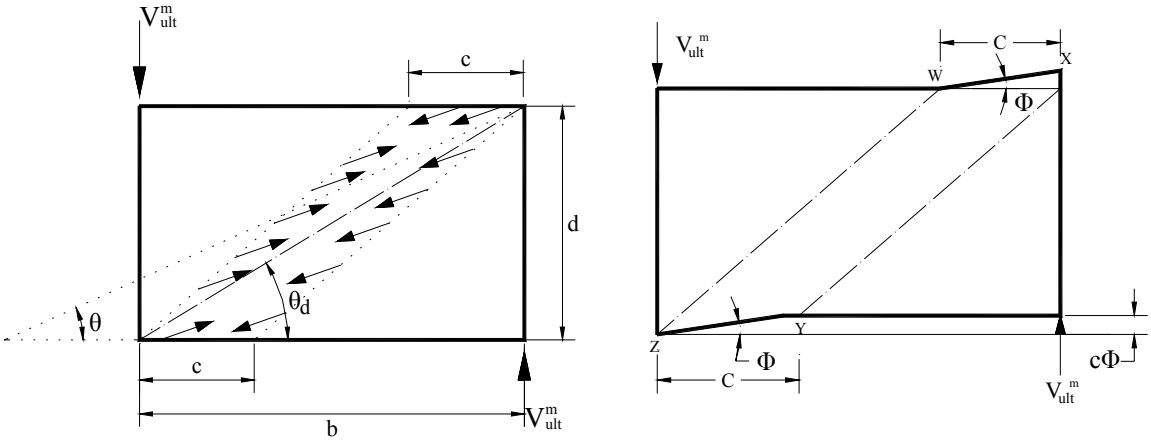

Figure 4.4 Membrane Tensile Stress Distribution and Collapse Behaviour

The membrane tensile stress has a resultant force F calculated from:

$$F = \sigma_t^y \left(d \times ctg\theta - b + c\right)\sin\theta \times t \tag{4.7}$$

From the virtual work principle, external work done by the vertical component of F and work done by shear force V_{ult}^m should be equal to the internal work done at the four plastic hinge locations as follows:

$$V_{ult}^m \left(c\phi\right) - \sigma_t^y t\left(d \times ctg\theta - b + c\right)\sin^2\theta\left(c\phi\right) = 4M_{pfr}\phi \tag{4.8}$$

$$V_{ult}^{m} = \frac{4M_{pfr}}{c} + \sigma_t^y ct\sin^2\theta + \sigma_t^y dt(ctg\theta - ctg\theta_d)\sin^2\theta$$

where: c = plastic hinge position;

M_{pfr} =plastic moment capacity of flange;

θ_d =diagonal degree of web panel, $ctg\theta_d = b/d$.

At collapse stage, the internal plastic hinges at the top and bottom flanges will form at the point of maximum moment where shear acting across a section is zero. Considering the equilibrium of the panel between the two plastic hinges in the flange, the position of plastic hinge can be derived as follows:

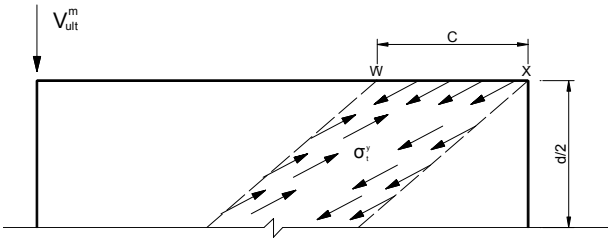

Figure 4.5 Stress and Moments Distribution at Compressive Hinge

$$2M_{pfr} - \frac{1}{2}\sigma_t^y c^2 t\sin^2\theta = 0 \qquad c = \frac{2}{\sin\theta}\sqrt{\frac{M_{pfr}}{\sigma_t^y t}} \tag{4.9}$$

The total shear load is then equal to the sum of shear load which causes buckling and subsequent increase in load carried by the diagonal tensile field and the formation of plastic hinges in flanges, thus,

$$V_{ult} = V_{cr} + V_{ult}^{m}$$
$$V_{ult} = 4\sqrt{M_{pfr}\sigma_t^y t}\sin^2\theta + \sigma_t^y dt(\cot\theta - \cot\theta_d)\sin^2\theta + \tau_{cr} dt \tag{4.10}$$

Since the inclination of web tensile field θ in Equation 4.8 is unknown, an iterative method is required to determine the value of θ that provides the ultimate shear force V_{ult}. The shear strength Equations 4.1 to 4.10 form the basis of many standard classical solutions as discussed in Porter *et al.* (1975). These include the case *I.* with flexible flange (M_{pfr} = 0), *II.* with a sufficiently thick web

(low d/t ratio), and (iii) with an infinitely thin web ($\tau_{cr} = 0$). In the present work, the Equations 4.1 to 4.10 will be extended to consider the panel shear strength under the effects of elevated temperature.

4.2.2 Mechanical Models of Plate Girder under Shear at Elevated Temperatures

As described in Section 3.2, material properties of steel would deteriorate at elevated temperature. For steel material, the temperature-dependent yield strength $\sigma_{y(T)}$ and the elastic modulus $E_{(T)}$ at temperature T can be expressed as a fraction of their ambient values, which are denoted by subscript $_{(20)}$, in the following forms:

$$\sigma_{y(T)} = k_{y(T)}\sigma_{y(20)} \qquad E_{(T)} = k_{E(T)}E_{(20)} \tag{4.11}$$

where: subscript $_{(T)}$ denotes the value corresponding to elevated temperature T; $k_{y(T)}$ and $k_{E(T)}$ are the retention ratios of the material yield strength and elastic modulus, respectively.

The behaviour of web panel under steady-state temperature is assumed to follow the three stages as under normal ambient condition. The critical shear at buckling stage, the tensile yield stress at the post-buckling stage and the ultimate shear strength at the collapse stage can be derived to take into account the degraded material properties. In all three stages, it is assumed that there is uniform temperature distribution across and along the web panel. In what follows, subscripts $_{(20)}$ and $_{(T)}$ will be associated with terms at the ambient and elevated temperature, respectively, to avoid confusion. Thus, for the case when elastic buckling occurs in the web panel, the critical shear strength becomes as:

$$\tau_{cr(T)} = k_{E(T)}\tau_{cr(20)} \tag{4.12}$$

In the post-buckled stage, the tensile yield stress can be written as:

$$\sigma_{ty(T)} = -\frac{3}{2}k_{E(T)}\tau_{cr(20)}\sin 2\theta + \sqrt{k_{y(T)}^2\sigma_{yw(20)}^2 + k_{E(T)}^2\tau_{cr(20)}^2[(\frac{3}{2}\sin 2\theta)^2 - 3]} \tag{4.13}$$

Substituting Equation 4.12 and 4.13 into Equation 4.1 to 4.10, ultimate shear force $V_{ult(T)}$ is given by:

$$V_{ult(T)} = k_{Ew(T)}\tau_{cr(20)}dt + \sigma_{ty(T)}dt\sin^2\theta(\cot\theta - \cot\theta_d) + 4t\sigma_{ty(T)}\sin\theta\sqrt{\frac{M_{Pf(T)}}{\sigma_{ty(T)}t}} \tag{4.14}$$

Equation 4.12 to 4.14 are suitable for both ambient and elevated temperature cases. The ambient case can be considered by simply taking all the retention ratios equal to 1. Furthermore, similar to ambient equations, the ultimate shear load $V_{ult(T)}$ and the inclination of principal tensile stress θ in Equation 4.13 and 4.14 are unknown. A parametric study for the ambient case (Rockey *et al.* 1978) shows that the variation of $V_{ult(T)}$ with θ is not abrupt. It was suggested that the assumption of $\theta = 2\theta_d/3$, where $\cot\theta_d = d/b$, would lead to either the correct value of $V_{ult(T)}$ or to a slight underestimation. BS 5950: Part 1 (BS 5950-1:1990), on the other hand, provided a simplified version of the shear strength based on the assumption that $\theta = \theta_d/2$. Therefore, the equations given in the BS 5950 (BS 5950-1:1990) can not be extended directly to elevated temperature case. The shear load ratio $V_{ult(T)}/V_{yw(T)}$ is given by Equation 4.15, in which the term $V_{yw(T)}$ represents the maximum shear force in the web panel at elevated temperature ($V_{yw(T)} = \sigma_{yw(T)}dt/\sqrt{3}$).

$$\frac{V_{ult(T)}}{V_{yw(T)}} = k_{1(T)}\frac{\tau_{cr(20)}}{\tau_{yw(20)}} + 4\sqrt{3}\sin\theta\left[\frac{Y_{b(T)}}{\sigma_{yw(20)}}\right]^{1/2}[k_{2(T)}K_{f(20)}]^{1/2} + D_\theta\frac{Y_{b(T)}}{\tau_{yw(20)}} \tag{4.15}$$

in which:

$$k_{1(T)} = k_{Ew(T)} / k_{yw(T)} \tag{4.16}$$

$$k_{2(T)} = k_{yf(T)} / k_{yw(T)} \tag{4.17}$$

$$Y_{b(T)} = (\sigma_{yw(20)}^2 - k_{1(T)}^2 3\tau_{cr(20)}^2 + k_{1(T)}^2 \phi_{t(20)}^2)^{1/2} - k_{1(T)}\phi_{t(20)} \tag{4.18}$$

$$\phi_{t(20)} = 1.5\tau_{cr(20)} \sin 2\theta \tag{4.19}$$

$$D_\theta = \sin^2 \theta(\cot\theta - \cot\theta_d) \tag{4.20}$$

$$K_{f(20)} = \frac{M_{Pf(20)}}{4M_{Pw(20)}} \tag{4.21}$$

$$M_{Pw(20)} = \sigma_{yw(20)} d^2 t / 4 \tag{4.22}$$

The subscripts $_f$ and $_w$ denote the values corresponding to flange and web properties, respectively. Equations 4.15 to 4.22 are written to resemble the equations recommended in the British standard, BS 5950: Part 1 (BS 5950-1:1990) for the shear strength calculations at ambient temperature. The first two terms on the right hand side of Equation 4.15 are referred to in BS 5950: Part 1 (BS 5950-1:1990) as the basic shear strength of the web, which combines the critical buckling strength and the post-buckling strength from web tension field action. The last term of Equation 4.15 represents the contribution from flanges. Thus, it can be seen that the effect of temperature rise on the web strength depends on the retention ratio between the web elastic modulus and yield strength, viz. $k_{1(T)}$ in Equation 4.16. The flange contribution to shear strength depends on the retention ratio between the flange and the web yield strengths, viz. $k_{2(T)}$ in Equation 4.17. Since then, there have been some changes on the shear strength calculations of plate girders in BS 5950: Part 1 (BS 5950-1:2000), that bring the new version closer to Eurocode 3 Part 1.1 (ENV 1993-1-1), but quite different from original Rockey's work (Rockey *et al.* 1978).

4.2.3 Effects of Thermal Axial Restraint on Mechanical Behaviour of Plate Girder at Elevated Temperatures

When the panel is subjected to the combined action of shear and compression at elevated temperatures, for example, due to a thermal axial restraint provided by adjoining cooler structures, their interaction phenomenon has to be considered. Under ambient condition, it was suggested in the Eurocode 3 Part 1.1 (EN 1993-1-1) that if the acting shear is less than 50% of the shear buckling resistance, no interaction exists, otherwise the interaction has to be taken into account.

In extending the pure shear case for a panel to include axial stress, earlier work by Porter *et al.* (1975) and Murray (1986) assumed that the flanges are subjected to additional axial forces, while the stress system in the web remains the same as for pure shear. In current work, both flanges and webs are subjected to additional axial stress, which may be due to thermal axial restraint. The extensions of Equation 4.1 to 4.10 include the panel axial compressive stress will be presented next.

At the buckling stage, the elastic buckling of simply supported thin flat plate can be predicted by an approximate interaction between the two stresses. Thus, for panels subjected to shear and compression at ambient condition as shown in Figure 4.6, the following formula suggested by Horne (Harding and Dowling 1978) is used.

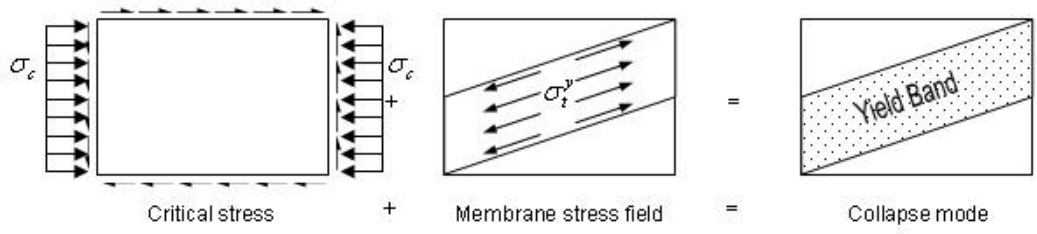

Figure 4.6 Collapse Mechanism for Plate Girders under Shear with Restraints

$$\frac{\sigma_c^T}{(\sigma_c)_{cr}} + \left(\frac{\tau_c}{\tau_{cr}}\right)^2 = 1 \qquad (4.23)$$

where: σ_c^T = thermal restraint compressive force;

$(\sigma_c)_{cr}$ = critical compressive stress for simply supported plate under a longitudinal compressive force;

τ_{cr} = critical shear stress for simply supported plate under pure shear force;

τ_c = modified critical shear stress for simply supported plate under a combination of shear force and restraint compressive force.

The critical-buckling compressive stress for a plate when it is subjected to a pure compression is given by:

$$\sigma_{xcr} = K_c \left[\frac{\pi^2 E}{12(1-\mu^2)} \right] (\frac{t}{d})^2 \tag{4.24}$$

in which: K_c is the buckling coefficient, obtained as:

$$K_c = \frac{m^2}{(b/d)^2} + \frac{(b/d)^2}{m^2} + 2 \tag{4.25}$$

where: m is a number of sinusoidal half-waves in z direction of compression. It is well known that for a simply supported flat plate with an aspect ratio $b/d \geq 1$, K_c approaches the value 4 (Murray 1983). Thus for a panel under a compressive stress σ_c, the reduced buckling shear stress, denoted by τ'_{cr}, can be calculated from Equation 4.23 as:

$$\tau'_{cr} = \tau_{cr} (1 - \frac{\sigma_c}{\sigma_{xcr}})^{1/2} \tag{4.26}$$

After elastic buckling, the panel behaviour is expected to undergo the post-buckling and collapsed stages, as in the pure shear case. The stress components developed in the post-buckling stage include the compressive stress σ_c, the shear stress τ, and the tensile stress developed in the diagonal band of the panel σ_t, as shown in

Figure 4.6. The elemental stresses on the inclined plane at θ and $90^0+\theta$ are given by Equation 4.27. Substituting these equations into the von Mises yield equation for the web (Equation 4.28), the value of σ'_{ty} which results in the web yielding is given in Equation 4.29.

$$\sigma_1 = -\frac{\sigma_c}{2} - \frac{\sigma_c}{2}\cos 2\theta + \tau'_{cr}\sin 2\theta + \sigma_t$$

$$\sigma_2 = -\frac{\sigma_c}{2} + \frac{\sigma_c}{2}\cos 2\theta - \tau'_{cr}\sin 2\theta \qquad (4.27)$$

$$\tau_\theta = \frac{\sigma_c}{2}\sin\theta + \tau'_{cr}\cos 2\theta$$

$$\sigma_1{}^2 + \sigma_2{}^2 - \sigma_1\sigma_2 + 3\tau_\theta = \sigma_{yw}{}^2 \qquad (4.28)$$

$$\sigma'_{ty} = -\frac{3}{2}\tau'_{cr}\sin 2\theta + \sqrt{\sigma_{yw}^2 + \tau'^2_{cr}[(\frac{3}{2}\sin 2\theta)^2 - 3] + \tau'_{cr}\sigma_c D_c} + \frac{\sigma_c}{4}(3\cos 2\theta + 1)$$

$$D_c = \frac{1}{4}(3\cos 2\theta + 1)(3\sin 2\theta) + \frac{1}{16}(3\cos 2\theta + 5)(3\cos 2\theta - 3)\frac{\sigma_c}{\tau'_{cr}} \qquad (4.29)$$

In the presence of axial stress σ_c in the flanges, the reduced plastic moment of resistance of the compression and tension flanges that attain the yield strength σ_{fw}, is given by Equation 4.30. Thus, the location of the plastic hinges in this case is given by Equation 4.30.

$$M'_{Pf} = M_{Pf}[1 - (\frac{\sigma_c}{\sigma_{yf}})^2] \qquad (4.30)$$

$$c = \frac{2}{\sin\theta}\sqrt{\frac{M'_{Pf}}{\sigma_{ty}t}} \qquad (4.31)$$

Based on virtual work principle described in Section 4.2.1, from the equilibrium of internal and external forces acting in the post-buckled range, the ultimate shear capacity can be obtained as:

$$(V_{ult})_T = 4\sqrt{M'_{pf}\,\sigma_{ty}{}^{t}t}\sin^2\theta + \sigma_{ty}{}^{t}dt(\cot\theta - \cot\theta_d)\sin^2\theta + \tau_{cr}{}^{t}dt \qquad (4.32)$$

The proposed equations were derived to consider the panel axial stresses due to the thermal axial restraint (Vimonsatit *et al.* 2005). The magnitude of σ_c in Equation 4.23 depends on the temperature increment and the level of restraint factor. For instance, for a simply supported plate girder with an axial restraint at the end as shown in Figure 4.7, the axial stress in the panel when the panel temperature is uniformly increased to T is given by

$$\sigma_c = (\frac{\beta}{1+\beta})E_{(T)}\alpha\Delta T \qquad (4.33)$$

in which: β is ratio of axial stiffness of the restrained member k_s to axial stiffness of girder panel k_b; α is thermal expansion coefficient of steel; and $E_{(T)}$ is elastic modulus of plate girder member at T.

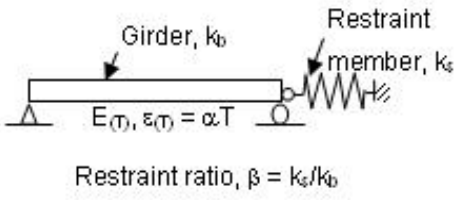

Figure 4.7 Restrained Beam Model for Thermal Restrained Plate Girder

4.3 Pre- and Post-buckling Out-of-Plane Deflection Investigation

As described in Section 4.2, shear strength predictions of beam web panel at elevated temperatures have been developed based on classical plate girder theory at ambient temperature (Vimonsatit *et al.* 2005). With this analytical approach, the pre- and post-buckling stages of plated structures under shear loads can be described with derivations of corresponding buckling and ultimate shear strengths. Nevertheless, in addition to strength predictions for beam shear web component, the corresponding deflection characteristics for shear component need to be addressed

as well. This will be incorporated into the overall steel beam-to-column joint modelling using the "Component-Based" method, as presented in Section 8.4. Thus, to obtain a clear understanding of deformation mode for the shear component with different geometries, particularly for different initial imperfections, mathematical models have been used to study the in-plane and out-of-plane deflections under pure shear and combination of shear and induced compression under fire conditions.

4.3.1 Background of Elastic Plate Buckling Theory

Theoretical investigations of mechanical behaviour of plate structures have been carried out by some researchers over the past few centuries. The first membrane theory of plate was formulated by Euler (1766). Later, Bernoulli (1789) and Navier (1823) derived the differential equation of square plate. It was Kirchhoff (1877) who first combined bending and stretching in the plate theory. Saint Venant (1883) transferred Kirchhoff's work into mathematical expressions, which have since then been referred to the basis of modern plate theory. This governing equation for the thin-plate loaded transversely with Y per unit area and in-plane loads, viz., N_x, N_y and N_{xy} per unit length, as follows.

$$D\left[\frac{\partial^4 w}{\partial x^4}+2\frac{\partial^4 w}{\partial x^2\partial y^2}+\frac{\partial^4 w}{\partial y^4}\right]=Y+N_y\frac{\partial^2 w}{\partial x^2}++2N_{xy}\frac{\partial^2 w}{\partial x\partial y}+N_x\frac{\partial^2 w}{\partial y^2} \tag{4.34}$$

in which: $D=\dfrac{Et^3}{12\left(1-\nu^2\right)}$

Equation 4.34 demonstrates relationship between loads and deflection for isotropic plates in which the out-of-plane deflection is very small and its effects on membrane stresses can be neglected.

Later, with introduction of stress function Φ, von Karman (1910) first proposed the governing equation which satisfied force equilibrium and deflection compatibility of a perfectly flat thin plate, as:

$$D\nabla^4 w = \frac{\partial^2 \Phi}{\partial y^2}\frac{\partial^2 w}{\partial x^2} - \frac{\partial^2 \Phi}{\partial x^2}\frac{\partial^2 w}{\partial y^2} + 2\frac{\partial^2 \Phi}{\partial x \partial y}\frac{\partial^2 w}{\partial x \partial y} + Y$$
$$\nabla^4 \Phi + Et\left[\frac{\partial^2 w}{\partial x^2}\frac{\partial^2 w}{\partial y^2} - \left(\frac{\partial^2 w}{\partial x \partial y}\right)^2\right] = 0 \tag{4.35}$$

To consider effects of initial imperfections of plate, Marguerre (1938) modified von Karman's governing Equation 4.34 as follows.

$$D\nabla^4 w = \frac{\partial^2 \Phi}{\partial y^2}\frac{\partial^2 (w+w_0)}{\partial x^2} - \frac{\partial^2 \Phi}{\partial x^2}\frac{\partial^2 (w+w_0)}{\partial y^2} + 2\frac{\partial^2 \Phi}{\partial x \partial y}\frac{\partial^2 (w+w_0)}{\partial x \partial y} + Y$$
$$\nabla^4 \Phi + Et\left[\frac{\partial^2 w_0}{\partial x^2}\frac{\partial^2 w}{\partial y^2} + \frac{\partial^2 w_0}{\partial y^2}\frac{\partial^2 w}{\partial x^2} - 2\frac{\partial^2 w_0}{\partial x \partial y}\frac{\partial^2 w}{\partial x \partial y} + \frac{\partial^2 w}{\partial x^2}\frac{\partial^2 w}{\partial y^2} - \left(\frac{\partial^2 w}{\partial x \partial y}\right)^2\right] = 0 \tag{4.36}$$

Marguerre's equation allows for plate post-buckling behaviour analysis, which is known as large-deflection plate analysis. This forms the theoretical basis for plate mechanical model in current study, which will be presented in Section 4.3.2. Besides, Marguerre derived analytical solutions for a simply supported plate subjected to a uniform transverse load with freely extending edges. His solutions were obtained through Rayleigh-Ritz energy method.

In 1942, Levy and Greeman used six terms of truncated double Fourier series to find solutions for Marguerre's equations. However, the assumed boundary conditions suggested the edge either has zero translation displacement or remains straight during translation. Although their solutions have these disadvantages, they obtained explicit solutions for both simply supported and clamped square plate under a combination of transverse and in-plane compression loads.

Later, in 1946, Green and Southwell solved the plate problems with finite difference method. Instead of solving von Karman's differential equation, they first modified the equation to be expressed in three unknown displacements, u, v and w. The derived equations were transformed into three sets of simultaneous equations by

finite difference method and solved by the relaxation method. However, in their analysis, the initial imperfections of plate were not incorporated and the boundaries of plate were constrained with zero transverse displacement. With this method, they obtained solutions for a built-in plate under uniform transverse load and a clamped plate subjected to a uniform in-plane shear stress along the edges.

Wang (1948) first transformed von Karman's equations into simultaneous equations by finite difference method. He used relaxation method and successive approximation technique in his analyses. He presented solutions for some rectangular plates with different aspect ratios. Later, Coan (1951) improved Levy's method with allowance of non-uniform edge in-plane displacements. With consideration of initial out-of-plane imperfections, the deflected shape of a simply supported rectangular plate was approximated by a double Fourier series, in which the initial deflection has the same shape with the final deflection. The detailed stress function Φ included, has incorporated complementary functions of the edge in-plane loads. With the compatibility conditions specified at the plate edges, the different coefficients of the double Fourier series can be obtained by successive approximation method. His analysis method has been applied to a square plate with central initial deflection as $w' = 0.1t$. This gives good comparison with experimental results. Later, Yamaki (1959) used Levy's method in his analysis of plate behaviour under in-plane compressive forces, which consisted of four different boundary conditions as: *I.* All edges simply supported; *II.* Loaded edges simply supported, the other edges clamped; *III.* Loaded edges clamped, the other edges simply supported; *IV.* All edges clamped. Analytical solutions for flat plate and plate with initial deflection as $w' = 0.1t$ gave good agreement with Levy and Coan's results.

In 1961, Timoshenko and Gere developed a linear solution for plate buckling problem. They assumed the membrane stresses of plate remain uniform during

bending. A double Fourier series was used in this analysis with energy method. However, in their solutions, the in-plane loading can not be greater than the critical buckling load (which can be considered as small deflection problem solution) and the membrane force effects were neglected.

In 1969, Walker investigated the behaviour of rectangular plate subjected to edge compressive loadings. In this analysis, he used similar double Fourier series and Galerkin's method to analyze simply supported plates. Later Williams and Walker (1975) incorporated perturbation technique into the plate behaviour investigations. In this method, the plate central deflection, stress and bending moments, etc. were derived as truncation series. Therefore, the non-linear problem could be transformed to a set of linear problems. Various explicit expressions for different edge conditions have been presented. Although divergence occurred in large initial imperfection case, their results were quite reasonable for practical design.

Rhodes and Harvey (1971) also examined the buckling and post-buckling behaviour of plate. They assumed the stress function Φ as a combination of trigonometric and hyperbolic functions. Their method was based on energy method which gave good agreement with experimental observations by Walker (1967). With aid of computer, Cheung (1976) and Murray (1980) applied finite strip method to the solutions of plate buckling problems. Based on a similar theory with finite element method, the plate was divided into long strips which reduced the total number of degrees of freedom of the plate system.

In 1980, Fok conducted a series of finite difference analyses and experimental tests to investigate elastic post buckling behaviour of thin compressed plates. The initial imperfections have been detected and input into the finite difference analyses. Fok's predictions gave better comparison with test results. In his investigations, the form

of initial imperfection has a marked effect on the behaviour of plate. Also the maximum load capacity of a plate is dependent on the smoothness and uniformity of the elastic buckling shape.

In 1992, Zaras *et al.* investigated buckling and post-buckling behaviour of thin rectangular plates subjected to compression and shear simultaneously. In this analysis, double Fourier series was used to represent the deflected shape of simply supported plate. Energy method was used to minimize the total potential energy to obtain the coefficients of assumed deflection shape functions. The analytical results showed that post-buckling behaviour of plate was greatly influenced by the magnitude of shear loads. In 2003, Rhodes presented a brief examination of the research on the post-buckling analysis of plates and plated structures. Only the behaviour of plates under compression load was considered with a lower bound analysis method. The influences of eccentric compression loads were also studied.

4.3.2 Elastic Pre- and Post-buckling Behaviour Investigations

As described in Section 4.3.1, analytical and experimental investigations of pre- and post-buckling behaviour of plate have been conducted extensively. Load-deflection behaviour of plate with elastic-plastic material characteristic in the pre- and post-buckling stages may be found experimentally, numerically and analytically. However, there is still a lack of studies of mechanical behaviour of imperfect plates under a combination of compression and shear loads, and under elevated temperatures.

4.3.2.1 Boundary Condition Assumptions

In current study, the shear component in beam web of a steel joint is simplified into one simply supported flat plate subjected to shear load τ and compression load σ as shown in Figure 4.8. The longitudinal compression load represents thermal

restraint force induced by surrounding structures. The uniformly distributed shear stress τ acts along both longitudinal and vertical edges of the plate.

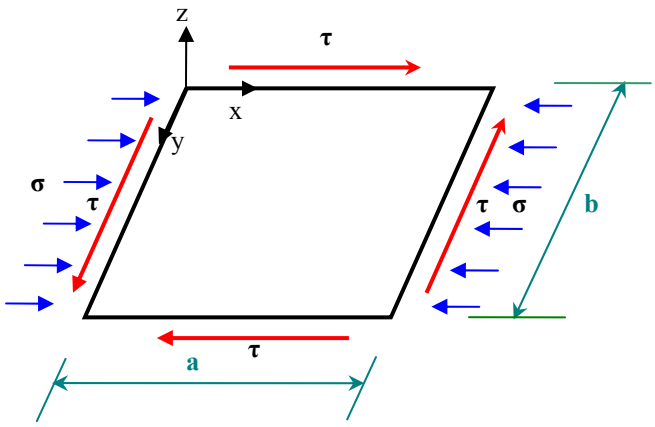

Figure 4.8 Load Distributions and Geometrical Property

The simple-supported boundary conditions at $x = 0$ and $x = a$ simulate nodal lines which form at the edges of compression loading. Although the simply supported boundary conditions at $y = 0$ and $y = b$ are less accurate for junction lines between the web panel and the flanges, these assumptions become more reliable since these junction lines are normally kept straight lines in practical estimations. Detailed boundary conditions are presented as follows.

$$w = 0 \qquad \text{at} \quad x = 0, x = a \quad \text{and} \quad y = 0, y = b$$

$$M_x = \frac{\partial^2 w}{\partial x^2} + \nu \frac{\partial^2 w}{\partial y^2} = 0 \qquad \text{at} \quad x = 0, x = a \tag{4.37}$$

$$M_y = \frac{\partial^2 w}{\partial y^2} + \nu \frac{\partial^2 w}{\partial x^2} = 0 \qquad \text{at} \quad y = 0, y = b$$

in which: w is out-of-plane deflection; M_x and M_y are bending moments about the $x-$ and the $y-$ axis, respectively, along four edges of plate.

4.3.2.2 Plate Out-of-Plane Deflection Functions

For simply supported plate, the out-of-plane deflection w of buckled plate can be represented by the double sine series as follows.

$$w = \sum_{m=1}^{\infty}\sum_{n=1}^{\infty} w_{mn} \sin\frac{m\pi x}{a}\sin\frac{m\pi y}{b} \tag{4.38}$$

The infinite sine series solution for the out-of-plane deflection generally converges quickly. However, it has been noticed that acceptable accuracy can be achieved by considering only the first few items in this series. Timoshenko *et al.* (1961) used five terms of double sine series to calculate the shear buckling strength of simply supported plate, in which the error between obtained shear strength and exact value was less than one per cent. Therefore, to save computational time, a double sine series consist of first five items is also adopted in current study.

$$\begin{aligned} w = {} & w_{11}\sin\frac{\pi x}{a}\sin\frac{\pi y}{b} + w_{21}\sin\frac{2\pi x}{a}\sin\frac{\pi y}{b} + w_{22}\sin\frac{2\pi x}{a}\sin\frac{2\pi y}{b} \\ & + w_{23}\sin\frac{2\pi x}{a}\sin\frac{3\pi y}{b} + w_{33}\sin\frac{3\pi x}{a}\sin\frac{3\pi y}{b} \end{aligned} \tag{4.39}$$

4.3.2.3 Governing Differential Equations and Airy-Type Stress Function

Considering geometrical changes of an infinitesimal plate element, a series of compatibility equations can be established with consideration of the effects of large-deflection of plate (Figure 4.9 represents derivation of ε_x, Murray, 1983).

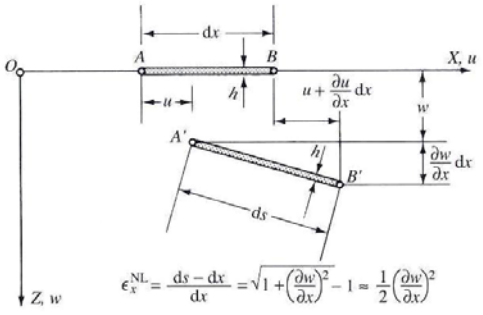

Figure 4.9 Strain ε_x Derivation due to Plate Out-of-Plane Deflection

$$\varepsilon_x = \frac{\partial u}{\partial x} + \frac{1}{2}\left(\frac{\partial w}{\partial x}\right)^2 = \frac{1}{E}\left(\sigma_x - \nu\sigma_y\right)$$

$$\varepsilon_y = \frac{\partial v}{\partial y} + \frac{1}{2}\left(\frac{\partial w}{\partial y}\right)^2 = \frac{1}{E}\left(\sigma_y - \nu\sigma_x\right) \tag{4.40}$$

$$\gamma_{xy} = \frac{\partial u}{\partial y} + \frac{\partial v}{\partial x} + \frac{\partial w}{\partial x}\frac{\partial w}{\partial y} = -\frac{2(1+\nu)}{E}\tau_{xy}$$

For plate with initial out-of-plane imperfection, the detailed strains can be expressed as following equations.

$$\varepsilon_x = \frac{\partial u}{\partial x} + \frac{\partial w_0}{\partial x}\frac{\partial w}{\partial x} + \frac{1}{2}\left(\frac{\partial w}{\partial x}\right)^2 = \frac{1}{E}\left(\sigma_x - \nu\sigma_y\right)$$

$$\varepsilon_y = \frac{\partial v}{\partial y} + \frac{\partial w_0}{\partial y}\frac{\partial w}{\partial y} + \frac{1}{2}\left(\frac{\partial w}{\partial y}\right)^2 = \frac{1}{E}\left(\sigma_y - \nu\sigma_x\right) \tag{4.41}$$

$$\gamma_{xy} = \frac{\partial u}{\partial y} + \frac{\partial v}{\partial x} + \frac{\partial w_0}{\partial y}\frac{\partial w}{\partial x} + \frac{\partial w_0}{\partial x}\frac{\partial w}{\partial y} + \frac{\partial w}{\partial x}\frac{\partial w}{\partial y} = -\frac{2(1+\nu)}{E}\tau_{xy}$$

in which: w_0 represents the initial imperfection of plate, which is assumed to relate with w as follows.

$$w_0 = w' \sin\frac{\pi x}{a}\sin\frac{\pi y}{b} + w' \sin\frac{2\pi x}{a}\sin\frac{\pi y}{b} + w' \sin\frac{2\pi x}{a}\sin\frac{2\pi y}{b} + w' \sin\frac{2\pi x}{a}\sin\frac{3\pi y}{b} + w' \sin\frac{3\pi x}{a}\sin\frac{3\pi y}{b} \tag{4.42}$$

where: w' represents the half magnitude of initial imperfection of plate central point.

Similarly, considering the equilibrium of external and internal forces acting on the infinitesimal plate element, the membrane stress can be expressed as follows.

$$\sigma_x = \frac{\partial^2 \Phi}{t\partial y^2}, \quad \sigma_y = \frac{\partial^2 \Phi}{t\partial x^2}, \quad \tau_{xy} = \frac{\partial^2 \Phi}{t\partial x \partial y} \tag{4.43}$$

in which: $\Phi(x, y)$ represents Airy stress function (Szilard, 2004).

Therefore, by eliminating u and v from Equation 4.41, the compatibility equation can be obtained as.

$$\nabla^4\Phi + Et\left[\frac{\partial^2 w_0}{\partial x^2}\frac{\partial^2 w}{\partial y^2} + \frac{\partial^2 w_0}{\partial y^2}\frac{\partial^2 w}{\partial x^2} - 2\frac{\partial^2 w_0}{\partial x\partial y}\frac{\partial^2 w}{\partial x\partial y} + \frac{\partial^2 w}{\partial x^2}\frac{\partial^2 w}{\partial y^2} - \left(\frac{\partial^2 w}{\partial x\partial y}\right)^2\right] = 0 \quad (4.44)$$

By similar derivations, the relationship between membrane forces and large out-of-plane deflection can be represented as below.

$$D\nabla^4 w - \frac{\partial^2\Phi}{\partial y^2}\frac{\partial^2(w+w_0)}{\partial x^2} - \frac{\partial^2\Phi}{\partial x^2}\frac{\partial^2(w+w_0)}{\partial y^2} + 2\frac{\partial^2\Phi}{\partial x\partial y}\frac{\partial^2(w+w_0)}{\partial x\partial y} = 0 \quad (4.45)$$

in which, $D = \dfrac{Et^3}{12(1-\nu^2)}$

These two differential equations represent compatibility and equilibrium conditions of plate under in-plane loading, which were first derived by von Karman in 1910 and improved by Marguerre in 1938 with considerations of initial imperfections.

Appling the compatibility Equation 4.45, Airy stress function can be obtained:

$$\Phi = Et\sum_{i=1}^{30} a_i \cos\frac{m_i\pi x}{a}\cos\frac{n_i\pi y}{b} + \left(-\frac{\sigma_x}{2}ty^2 - \tau txy\right) \quad (4.46)$$

in which: the first term is an integral solution of Equation 4.44. The second term is a particular solution which satisfies Equation 4.43. The corresponding coefficients of a_i, m_i and n_i are derived by Zaras (1992) for perfect flat plates. Considering the effects of initial imperfection, the detailed coefficients can be obtained (Table 4.1).

4.3.2.4 Analytical Method of Governing Differential Equations

The exact solution of governing differential Equation 4.36 and Equation 4.37 is very rare. However, some indirect analytical methods have been developed which gave satisfactory results, such as Galerkin's method, energy method, iteration method, etc. In current investigation, Galerkin's method is applied in the mathematical procedure to solve the governing differential equations.

In Galerkin's method, a complete set of functions is assumed to represent the out-of-plane deflections as shown in Equation 4.47, which is a general form of assumed deflection shape defined in Equation 4.38.

$$w(x,y)=\sum_{i=1}^{n} w_i f_i(x,y) \tag{4.47}$$

Since the assumed deflection shape for w is only an approximation to the real deflection shape, the values of w and the stress function Φ may not satisfy equilibrium (Equation 4.45). Thus the error can be treated as a force acting normal to the plate surface. The total work performed by this force during a small defection dw increment should be equal to zero as following form.

$$\iint_A \left[D\nabla^4 w - \frac{\partial^2\Phi}{\partial y^2}\frac{\partial^2(w+w_0)}{\partial x^2} - \frac{\partial^2\Phi}{\partial x^2}\frac{\partial^2(w+w_0)}{\partial y^2} + 2\frac{\partial^2\Phi}{\partial x\partial y}\frac{\partial^2(w+w_0)}{\partial x\partial y} \right] dwdxdy = 0 \tag{4.48}$$

The small deflection increment can be expressed as:

$$dw(x,y)=\sum_{i=1}^{n} dw_i f_i(x,y) \tag{4.49}$$

Thus, Equation 4.48 can be obtained:

$$\sum_{i=1}^{n} dw_i \iint_A \left[D\nabla^4 w - \frac{\partial^2\Phi}{\partial y^2}\frac{\partial^2(w+w_0)}{\partial x^2} - \frac{\partial^2\Phi}{\partial x^2}\frac{\partial^2(w+w_0)}{\partial y^2} + 2\frac{\partial^2\Phi}{\partial x\partial y}\frac{\partial^2(w+w_0)}{\partial x\partial y} \right] f_i(x,y)dxdy = 0 \tag{4.50}$$

Since this Equation must satisfy any dw_i, therefore:

$$\begin{aligned}
&\iint_A \left[D\nabla^4 w - \frac{\partial^2\Phi}{\partial y^2}\frac{\partial^2(w+w_0)}{\partial x^2} - \frac{\partial^2\Phi}{\partial x^2}\frac{\partial^2(w+w_0)}{\partial y^2} + 2\frac{\partial^2\Phi}{\partial x\partial y}\frac{\partial^2(w+w_0)}{\partial x\partial y} \right] f_1(x,y)dxdy = 0 \\
&\iint_A \left[D\nabla^4 w - \frac{\partial^2\Phi}{\partial y^2}\frac{\partial^2(w+w_0)}{\partial x^2} - \frac{\partial^2\Phi}{\partial x^2}\frac{\partial^2(w+w_0)}{\partial y^2} + 2\frac{\partial^2\Phi}{\partial x\partial y}\frac{\partial^2(w+w_0)}{\partial x\partial y} \right] f_2(x,y)dxdy = 0 \\
&\cdots\cdots\cdots\cdots \\
&\iint_A \left[D\nabla^4 w - \frac{\partial^2\Phi}{\partial y^2}\frac{\partial^2(w+w_0)}{\partial x^2} - \frac{\partial^2\Phi}{\partial x^2}\frac{\partial^2(w+w_0)}{\partial y^2} + 2\frac{\partial^2\Phi}{\partial x\partial y}\frac{\partial^2(w+w_0)}{\partial x\partial y} \right] f_n(x,y)dxdy = 0
\end{aligned} \tag{4.51}$$

From Equation 4.51, the undetermined coefficients w_i can be calculated by mathematical programming.

Table 4.1 Coefficients of Airy Stress Function

i	m_i	n_i	a_i	i	m_i	n_i	a_i
1	1	0	$\lambda^2\left(-w_{21}w_{12}+9w_{23}w_{33}+8w'^2\right)/4$	16	1	5	$36\lambda^2\left(w_{22}w_{33}+w'^2\right)/\left(1+25\lambda^2\right)^2$
2	2	0	$\lambda^2\left(w_{11}{}^2+w'^2\right)/32$	17	1	6	$225\lambda^2\left(w_{23}w_{33}+w'^2\right)/4\left(1+36\lambda^2\right)^2$
3	3	0	$\lambda^2\left(w_{11}w_{21}+w'^2\right)/36$	18	2	4	$9\lambda^2\left(w_{11}w_{33}+w'^2\right)/16\left(1+4\lambda^2\right)^2$
4	4	0	$\lambda^2\left(w_{21}{}^2+4w_{22}{}^2+9w_{23}{}^2+14w'^2\right)/128$	19	3	1	$4\lambda^2\left(w_{11}w_{22}+w'^2\right)/\left(9+\lambda^2\right)^2$
5	5	0	$9\lambda^2\left(w_{23}w_{33}+w'^2\right)/100$	20	3	2	$\lambda^2\left(-w_{11}w_{21}+25w_{11}w_{23}+24w'^2\right)/4\left(9+4\lambda^2\right)^2$
6	6	0	$\lambda^2\left(w_{33}{}^2+w'^2\right)/32$	21	3	4	$\lambda^2\left(-w_{11}w_{23}-w'^2\right)/4\left(9+16\lambda^2\right)^2$
7	0	1	$\left(-w_{21}w_{22}+w_{22}w_{23}\right)/\lambda^2$	22	4	1	$\lambda^2\left(9w_{21}w_{22}+25w_{22}w_{23}+34w'^2\right)/\left(16+\lambda^2\right)^2$
8	0	2	$\left(w_{11}{}^2+4w_{21}{}^2-8w_{21}w_{23}-3w'^2\right)/32\lambda^2$	23	4	2	$\lambda^2\left(9w_{11}w_{33}+16w_{21}w_{23}+25w'^2\right)/16\left(4+4\lambda^2\right)^2$
9	0	3	$\left(w_{21}w_{22}+w'^2\right)/9\lambda^2$	24	4	3	$\lambda^2\left(-w_{21}w_{22}-w'^2\right)/\left(16+9\lambda^2\right)^2$
10	0	4	$\left(w_{22}{}^2+2w_{21}w_{23}+3w'^2\right)/32\lambda^2$	25	4	4	$\lambda^2\left(-w_{21}w_{23}-w'^2\right)/\left(64+64\lambda^2\right)^2$
11	0	5	$\left(w_{22}w_{23}+w'^2\right)/25\lambda^2$	26	4	6	$\lambda^2\left(-w_{22}w_{23}-w'^2\right)/\left(16+25\lambda^2\right)^2$
12	0	6	$\left(4w_{23}{}^2+9w_{33}{}^2+13w'^2\right)/288\lambda^2$	27	5	1	$36\lambda^2\left(w_{22}w_{33}+w'^2\right)/\left(25+\lambda^2\right)^2$
13	1	2	$\dfrac{\lambda^2\left(9w_{11}w_{33}-w_{11}w_{23}-9w_{21}w_{33}-w'^2\right)}{\left(1+4\lambda^2\right)^2}$	28	5	2	$81\lambda^2\left(w_{21}w_{33}+w'^2\right)/4\left(25+\lambda^2\right)^2$
14	1	3	$\dfrac{\lambda^2\left(4w_{11}w_{22}+4w'^2\right)}{\left(1+9\lambda^2\right)^2}$	29	5	4	$-9\lambda^2\left(w_{21}w_{33}+w'^2\right)/4\left(25+16\lambda^2\right)^2$
15	1	4	$\dfrac{\lambda^2\left(25w_{11}w_{23}+81w_{21}w_{33}+106w'^2\right)}{4\left(1+16\lambda^2\right)^2}$	30	5	6	$-9\lambda^2\left(w_{23}w_{33}+w'^2\right)/4\left(25+36\lambda^2\right)^2$

In which: $\lambda = a/b$.

4.3.3 Analytical Predictions and Comparisons

As mentioned in Section 4.3.2.4, the formulation of mathematical models in dimensionless system and the discretization of governing equations (Equation 4.51)

by successive approximation and optimization methods, has made it possible to create a numerical code in Matlab environment. Analytical predictions are calculated and compared with numerical results as follows.

4.3.3.1 One-Directional Compression Analysis

In order to verify correctness of the analytical perditions, the load-deflection characteristics of a one-directional compression plate (as shown in Figure 4.10) have been studied with different initial imperfection ratios, which were then compared with numerical results from Coan (1951) and perturbation analysis results by Dawson (1971, cited by Murray, 1986).

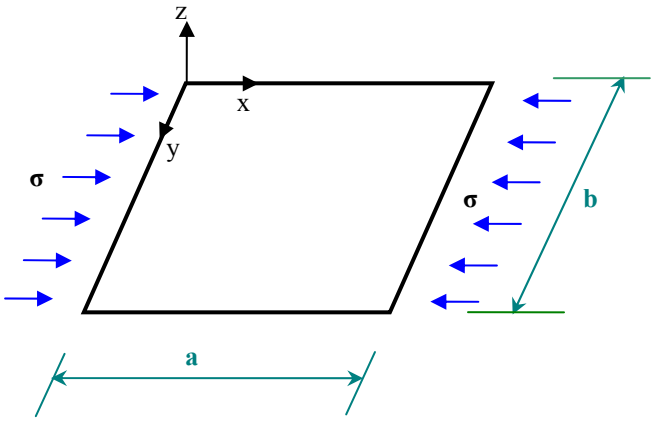

Figure 4.10 Load Distribution and Geometrical Property for One-Directional Compression

As described in Section 4.3.1, Coan (1951) utilized three terms of double Fourier series to represent out-of-plane deflection of simply supported square plate loaded in edge compression. After iterative procedure, the central out-of-plane deflection was derived with different initial imperfection magnitudes. In 1975, Williams and Walker first adopted perturbation method to study the pre- and post-buckling behaviour of isolated plate. With this method, an explicit load-deflection expression was obtained for one square plate loaded in one-directional compression as follows.

$$\frac{w_{\max}}{t} = 1.721188\varepsilon - 0.022411\varepsilon^3 \quad \text{in which,} \quad \varepsilon = \left(\frac{\sigma}{\sigma_{cr}} - 1\right)^{1/2}, \quad \nu = 0.316 \qquad (4.52)$$

To incorporate the effect of initial imperfection, this perturbation method can be easily extended by using the findings by Dawson (1971, cited by Murray, 1986), which resulted in the following expression.

$$\frac{w_{\max}}{t} = 1.721188\varepsilon - 0.022411\varepsilon^3 \tag{4.53}$$

Where: $\varepsilon = \left[\sigma/\sigma_{cr} - 1 + w'/\left(w_{\max} + w'\right)\right]^{1/2}$; $\nu = 0.316$; $w_{\max}$ is plate central out-of-plane deflection; w' is plate central initial out-of-plane imperfection.

The detailed comparisons among analytical predictions are given in Figure 4.11. Two cases have been studied with both perfectly flat plate and plate with initial imperfection as $t/10$. In both cases the Poisson's ratio was set as 0.316 which was the same as Coan's predictions. It can be seen that the analytical predictions in current study are in good agreement with Dawson's equation. However, Coan's predictions show a less stiff behaviour compared with both analytical predictions.

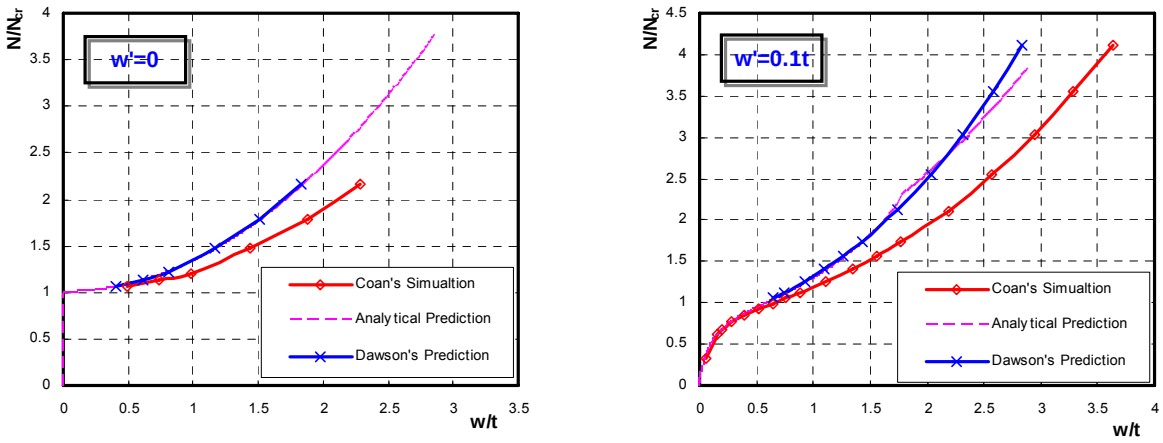

Figure 4.11 Comparisons between Different Analytical Approaches

4.3.3.2 Pure Shear Load Analysis

Similarly, the behaviour of plate under pure shear load along four edges was also investigated with different initial imperfection magnitudes. Firstly, the effect of plate thickness at certain initial imperfections was considered. Square plates (305

mmx305 mm) with thickness as 1.5, 2 and 2.7 mm (which were selected as the same geometrical properties with unrestrained and restrained plate girder beam web panels in Section 5.3 and 5.4) have been examined with three initial imperfection magnitudes ($w'=t/10$, $w'=t/100$ and $w'=t/1000$). The derived shear strength ratios (V/V_{cr}, V_{cr} is shear buckling load) are plotted with central plate defection ratios (w/t) as shown in Figure 4.12 (a), (b) and (c). It can be noticed that, for certain initial imperfection level, the curves for different plate thicknesses illustrate the same dimensionless load-deflection behaviour, which can be derived from Equation 4.51. Secondly, with higher initial imperfection ($w'=t/10$), the plates buckle at much lower shear loads compared with perfect flat plates or plates with small initial imperfections ($w'=t/100$, $w'=t/1000$). The transition between pre- and post-buckling stage for plates with larger initial imperfections, is not distinguishable.

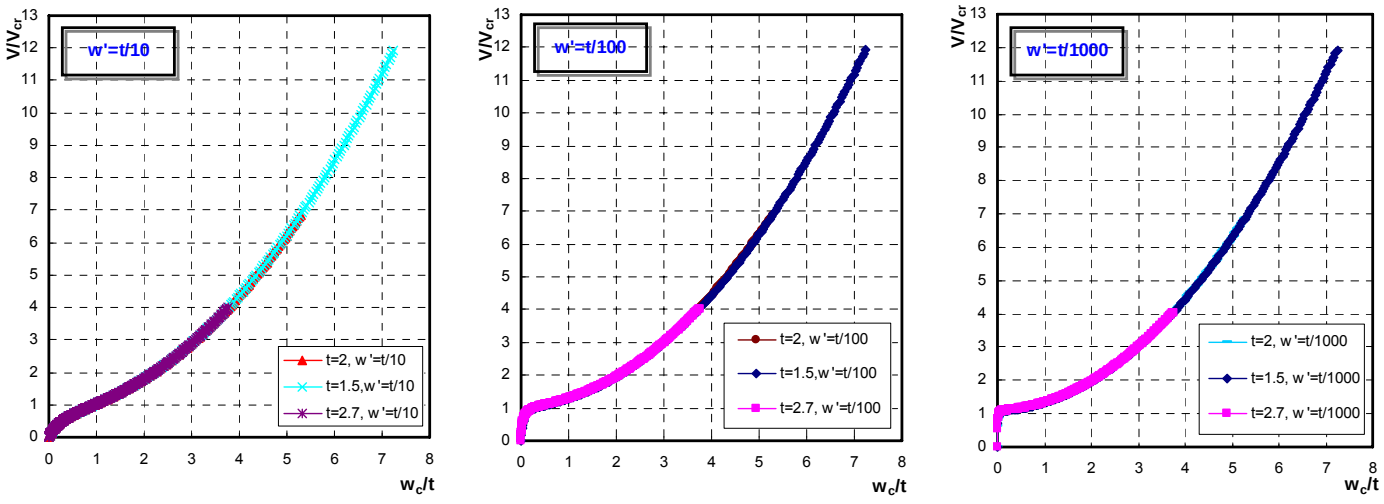

(a) (b) (c)

Figure 4. 12 Non-Dimensional Load-Deflection Behaviour of Imperfect Plates

Numerical investigations have been conducted to verify the derived load versus out-of-plane equations. Simply-supported square plates with different thicknesses and initial imperfections are simulated using a commercial finite element (FE)

software MSC.Marc (2001). An eight-noded shell element is used to simulate the web and flange plates, with initial imperfections applied directly onto the mesh nodes. Numerical predictions have been compared with analytical predictions as shown in Figure 4.13 (a) and (b). Clearly, the analytical approach can predict the load-deflection behaviour of square plates with reasonable accuracy, especially at pre-buckling stage due to second-order linear elastic analysis. Thus, superimposing the ultimate shear strength predictions (Vimonsatit *et al.*, 2005), and truncating the elastic behaviour beyond this strength, one can obtain the limit of elastic behaviour as shown in Figure 4.13 (a) and (b). Although the post-buckled behaviour cannot be modelled, current analytical approach gives reasonable behaviour up to the ultimate shear strength, which is sufficient for practical design purpose.

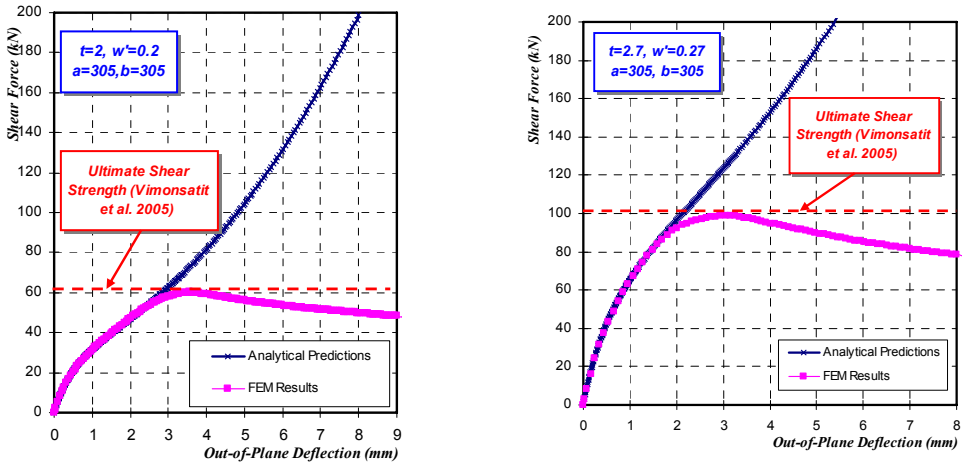

(a) (b)

Figure 4.13 Comparisons of Load-Deflection Behaviour between Numerical and Analytical Predictions (Square Plate)

In addition to square plate analyses, another series of studies have also been conducted for rectangular plates (457.5 mm x 305 mm plate, with aspect ratio $\lambda = 1.5$), based on the same thicknesses with square plates. As shown in Figure 4.14 (a) and (b), similarly, it can be noticed that even for rectangular plates, the proposed approach gives acceptable accuracy compared with numerical simulations.

Analytical predictions for plates with the same initial imperfection ratio ($w' = t/10$) are summarized in Figure 4.14, with two aspect ratios ($\lambda = 1.0$ and 1.5). Clearly, for square and rectangular plates, load-deflection characteristics are in a similar form. However, for plates with a larger initial imperfection ($w' = t/10$), the transition from pre- to post-buckling stages is much less obvious, causing difficulty to obtain elastic shear buckling strength. Also rectangular plates ($\lambda = 1.5$) present relatively lower shear buckling strengths compared with square plates, due to higher plate aspect ratios.

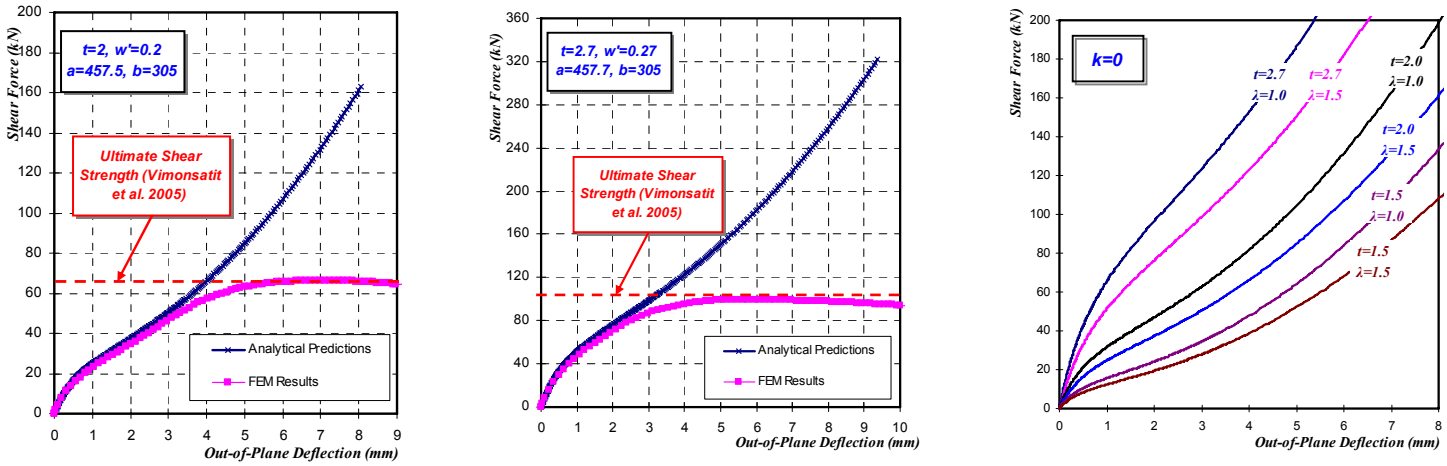

(a) (b) (c)

Figure 4.14 Comparisons of Load-Deflection Behaviour between Numerical and Analytical Predictions (Rectangular Plates $\lambda = 1.5$)

4.3.3.3 Analysis of Combination of Shear and Compression Loads

Since there is thermal restraint effect when beam or plate girders are subjected to heating, the load-deflection relationships of plates under a combination of shear and compression loads is also necessary to be derived and compared with corresponding numerical simulations. Only square (305 mm x 305 mm, $\lambda = 1$) and rectangular plates (457.5 mm x 305 mm, $\lambda = 1.5$) have been studied with plate thicknesses as 2 mm and 2.7 mm, both of which have initial imperfection magnitude, typically assumed as $w' = t/100$. For each plate model, two compression stress ratios were considered as $k = \sigma/\sigma_{cr} = 0.1$ and $k = \sigma/\sigma_{cr} = 0.3$ (σ_{cr} is the compressive

buckling stress for simply supported plates under one-direction compression load presented by Timoshenko *et al.*, 1961), which were selected to ensure the plate fails predominantly due to shear. Typical comparisons between analytical and numerical predicted load-deflection curves are presented in Figure 4.15 (a). Predicted load-deflection behaviour is in close agreement with numerical curves. In order to obtain a clear understanding of the effect from compressive stress, analytical predictions are summarized in Figure 4.15 (b) for plates subjected to three compressive stress ratios ($k = 0, 0.1$ and 0.3). A typical feature that characterizes the analytical results is a visible increase of web plate out-of-plane deflections at the same shear load level, due to compressive stress. Also, for lower compressive stress ratios, the plates still show similar shear-deflection relationships compared to the pure-shear case ($k = 0$). In addition, there exists much more obvious transition from pre- to post-buckling stages, if compared with Figure 4.14 (c). This shows the effect of initial imperfections on the buckling behaviour of web plate.

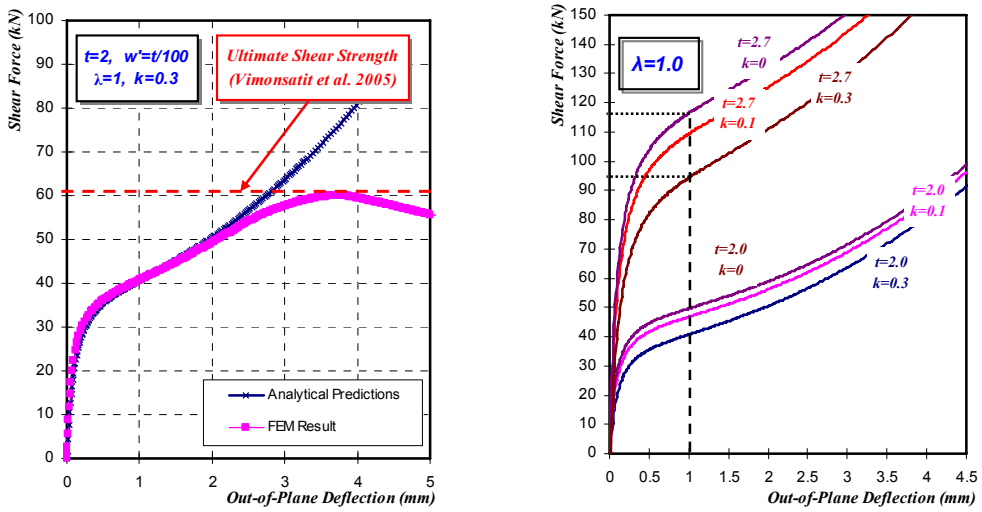

(a) (b)

Figure 4.15 Comparisons of Load-Deflection Behaviour between Numerical and Analytical Predictions for Square Plates under Shear and Compression

Similar to square plate analyses, rectangular plates (457.5 mm x 305 mm, $\lambda = 1.5$) have also been examined with various compressive stress ratios. Figure 4.16 (a)

presents load-deflection relationships for investigated plates. In combination with Figure 4.16 (b), it can be noticed that influences from compressive stress at certain out-of-plane deflection level (1 mm) are relatively less significant for rectangular plates. Instead of load-deflection characteristics, relationships between shear stress and out-of-plane deflection for both square and rectangular plates are compared in Figure 4.16 (b), with the same compressive stress ratio ($k = 0.3$). It is explicit that shear buckling stresses decrease proportionally with a larger plate aspect ratio (λ), which is in accord with analytical predictions (Vimonsatit *et al.*, 2005). However, all stress-deflection curves exhibit similar feature, that is, the shear stress dominates deflection developments for low compressive stress ratios.

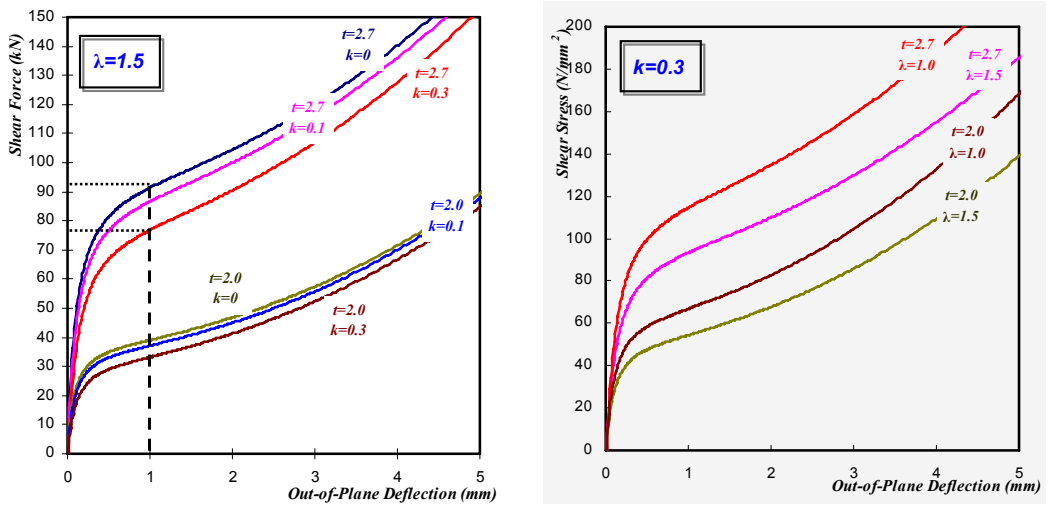

(a) (b)

Figure 4.16 Comparisons of Load-Deflection Behaviour between Square and Rectangular Plates under Combination of Shear and Compression

4.4 Pre- and Post-buckling In-Plane Deflection Investigation

In addition to analytical out-of-plane deflection predictions (Section 4.3), in-plane deflection of beam web shear component plays an important role in the joint rotation. Thus, the analytical predictions are crucial for obtaining an accurate representation of steel beam-to-column joint modelling using the "Component-Based" technique.

As described in Section 4.2, the overall behaviour of a web panel under shear can be divided into three stages, viz. *(1) Unbuckled*, *(2) Post-buckled*, and *(3) Collapsed stage*. Similar to pre- and post-buckling out-of-plane deflection, the development of in-plane deflection of shear component (Figure 4.17(a)) can be divided into two stages, that is, pre- and post-buckling behaviour as shown in Figure 4.17(b). This analytical model has been improved by the author, based on the research works conducted by Kharrazi *et al.* (2004) about bending and shear analysis of ductile steel plate walls.

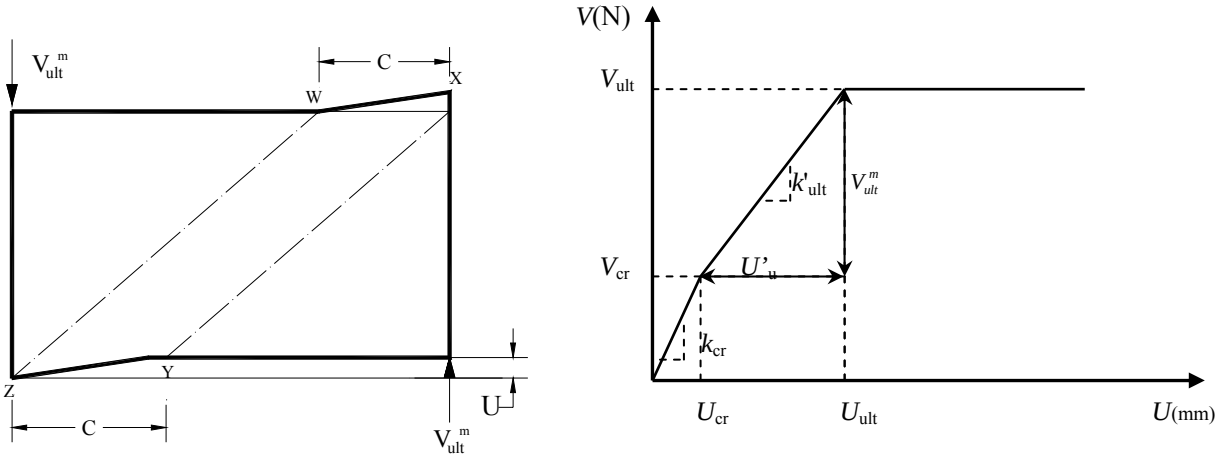

(a) (b)

Figure 4.17 In-Plane Deflection Development of Web Panel Shear Component

➢ *Pre-buckling Stage:*

Critical shear stress of a web panel can be obtained from Equation 4.1 and 4.12 for pure shear at both ambient and elevated temperatures. Furthermore, critical shear stress for a web panel subjected to a combination of shear and compression can be obtained from Equation 4.26:

$$V_{cr} = \tau_{cr} dt \tag{4.54}$$

in which: τ_{cr} is shear buckling stress of web panel; d and t are the height and thickness of web panel.

Critical shear displacement U_{cr} is obtained as:

$$U_{cr} = \tau_{cr} b / G = 2\tau_{cr} b(1+\nu)/E \tag{4.55}$$

where: b is width of web plate; E is elastic modulus of web plate.

➢ *Post-buckling Stage:*

After the web panel has buckled, shear displacement $U_u^{'}$ from post-buckling component of shear force can be derived by equating work done through post-buckling component of shear force, with work done by normal stresses acting on flanges (internal work done at four plastic hinge locations, viz. Point W, X, Y and Z, as shown in Figure 4.4) and strain energy of tension field (Figure 4.17 (a)). This leads to:

$$\frac{V_{ult}^m U_u^{'}}{2} = \frac{\left(\sigma_t^y\right)^2}{2E} cdt + 4\frac{M_{pfr}}{2}\frac{U_u^{'}}{c} \qquad \Rightarrow U_u^{'} = \frac{\left(\sigma_t^y\right)^2 c^2 dt}{E\left(V_{ult}^m c - 4M_{pfr}\right)} \tag{4.56}$$

where: σ_t^y is tensile yield stress of plate under shear as described in Equation 4.13 and 4.29; V_{ult}^m is post-buckling shear force component; c is plastic hinge position as in Equation 4.9 and 4.31; M_{pfr} is plastic moment capacity of flanges.

Thus, ultimate shear displacement can be expressed as:

$$U_{ult} = \frac{\left(\sigma_t^y\right)^2 c^2 dt}{E\left(V_{ult}^m c - 4M_{pfr}\right)} + U_{cr} = \frac{\left(\sigma_t^y\right)^2 c^2 dt}{E\left(V_{ult}^m c - 4M_{pfr}\right)} + \frac{\tau_{cr} b}{G} \tag{4.57}$$

Therefore, with shear strength and deflection derivations, shear force versus plate in-plane deflection relationship can be expressed as a tri-linear curve as shown in Figure 4.17. Corresponding stiffness for pre- and post-buckling stages (k_{cr} and $k_u^{'}$) can be expressed as:

$$k_{cr} = \frac{Gdt}{b} = \frac{Edt}{2b(1+\nu)} \qquad k_u^{'} = \frac{EV_{ult}^m\left(V_{ult}^m c - 4M_{pfr}\right)}{\left(\sigma_t^y\right)^2 c^2 dt} \tag{4.58}$$

However, in order to incorporate the shear component into overall steel joint modelling in Section 8.4, in-plane deflection of web plate needs to be transformed

into shear rotation with relationship as $U = b\Phi$ and $U = c\Phi$ for pre- and post-buckling stages. Thus, rotational stiffnesses of plate for two stages can be expressed through the following relationships:

$$k_{\Phi,cr} = Gdt = \frac{Edt}{2(1+\nu)} \qquad k_{\Phi,u}' = \frac{EV_{ult}^{m}\left(V_{ult}^{m}c - 4M_{pfr}\right)}{\left(\sigma_t^{y}\right)^2 cdt} \tag{4.59}$$

4.5 Conclusion

Mechanical models presented in this chapter aims to predict both shear capacity and deformation behaviour of the shear component of joints at ambient and elevated temperatures. A series of girders have been analyzed and results presented here will be used to compare with both experimental and finite element analyses in Chapter 5. The experimental results and finite element predictions will be described in Chapter 5 and Chapter 6, respectively. Then, these mechanical models will be incorporated into the "Component-Based" mechanical modelling, which will be described in Section 8.4.

CHAPTER 5
EXPERIMENTAL INVESTIGATION OF SHEAR ZONE IN STEEL BEAM-TO-COLUMN JOINT

5.1 Introduction

In the steel end-plate joint, the major components within shear zone are column web and beam web subjected to shear force, and restrained compressive force, in fire conditions. As presented in Section 4.1, beam web shear component has been modelled by using an equivalent girder web panel subjected to shear force, as shown in Figure 4.2.

In this part of experimental investigations, five series of beams (TG1, TG2, TG3, TG4 and TG5 series) have been tested without thermal restraint effects. In addition, three more series of beams (RTG3, RTG4 and RTG5 series) were tested under thermal restraints to simulate more realistic situations of structural component. These test girders have different web slenderness ratios and material properties. TG1 and TG2 represented stocky sections, which are typical of column web shear component. The other specimens, TG3, TG4, TG5 and RTG3, RTG4, RTG5 have higher slenderness which represented slender beam web shear component as described in Section 4.1. Moreover, test results from unrestrained slender sections (TG3, TG4 and TG5 series) were used as benchmark cases to compare with three other series under thermal restraint conditions (RTG3, RTG4 and RTG5 series).

Under ambient condition, experimental results of unrestrained shear component test consisted of readings from strain gauges, affixed onto web panels and flanges, and from linear variable differential transducers (LVDTs). For specimens tested at elevated temperatures, there were no readings from strain gauges as it was not possible to obtain high temperature strain gauges at reasonable cost. Therefore, the deformation readings consisted only of the information from deflection transducers (LVDTs). In addition, thermocouples were fixed onto web panels and flanges for temperature measurements.

5.2 Unrestrained Plate Girder Experimental Set-up and Programme

In the first part of experimental work, five series of plate girder beams (TG1, TG2, TG3, TG4 and TG5 series) have been tested. These five series were tested under thermally unrestrained condition. The girders have different web slenderness ratios and material properties. The web slenderness ratio is defined as the ratio between the web depth and thickness (d/t). Each series consist of one specimen tested at ambient temperature, and three specimens tested at three respective furnace temperatures, viz. 400, 550 and 700 ^{o}C, using a specially designed and fabricated electrical heating furnace. These three temperatures were chosen since they represent significant degradations of steel material properties as shown in Figure 3.5 and Figure 3.6. These test results were considered as a benchmark to compare with three other series of tests performed under thermal restraint condition.

5.2.1 Development of Unrestrained Plate Girder Test Programme

The unrestrained shear component testing system (Figure 5.1) consist of one boxed-up electrical heating furnace, one hydraulic jack, and two steel supports ensuring roller end conditions for the specimens. The hydraulic jack is used as the loading device attached to an external portal frame system. The furnace is assembled from two electrical heating panels to affect elevated temperature conditions, and it is boxed up with two non-heating side panels and a top cover.

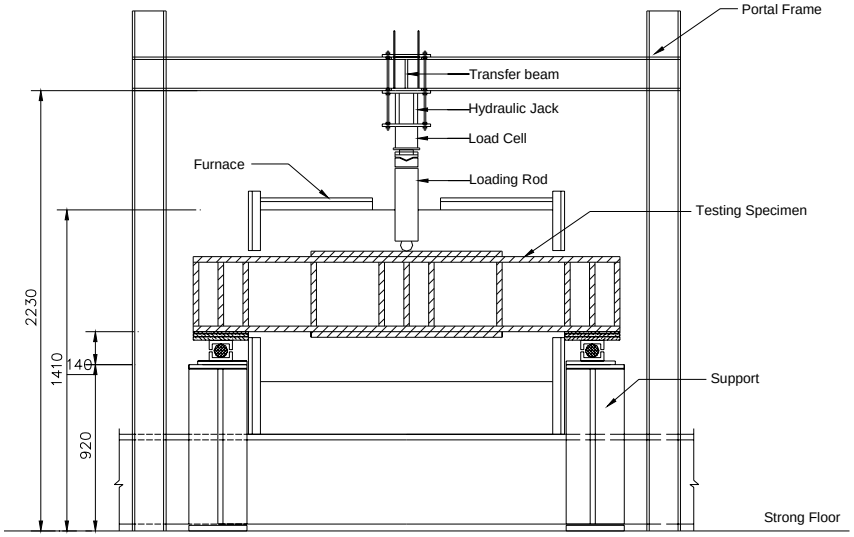

Figure 5.1Unrestrained Shear Component Test Set-up

5.2.2 Test Specimen Preparations

In total, five series of I-shaped test girders were designed and tested, namely, TG1, TG2, TG3, TG4, and TG5. The girders configurations are shown in Figure 5.2. TG1 and TG2 were selected from universal column sections, i.e. UC 152x152x23kg/m and UC 203x203x52kg/m, respectively. On the other hand, TG3, TG4, and TG5 were all fabricated from steel plates. The web and the flange plates were welded together using longitudinal fillet to ensure adequate shear force transfer between the two component plates. Clearly, from Table 5. 1, TG1 and TG2 series represented stocky plate panels with web slenderness ratio (d/t) as 22.8, and 22.6. On the other

hand, TG3, TG4, and TG5 were slender plate panels with d/t as 152.5, 112.9, and 203.3. All test girders had a total length of 1.90 m. The span measured from centre-to-centre of the support bearing blocks was 1.70 m for TG1 and TG2, and 1.66 m for TG3, TG4, and TG5 girders, respectively. Transverse web panel stiffeners were provided such that the ratio of the distance between vertical stiffeners to web depth, denoted by b/d, was 1, since it represents an intermediate value among those used in practice (BS 5950-1:2000) ranging from 0.4 to 3.0. It is also purposely chosen to have a relatively insignificant effect from bending moments for the end panels. The girders were symmetrical in cross section, with the load applied at centre. The purpose of the investigation was to study the web panel behaviour due to shear. Therefore, to prevent flexural failure caused by the plastic hinge formation at mid span, additional cover plates were welded onto the top and bottom flange plates of the test girders, as shown in Figure 5.2. The girders were designed such that the end panels would fail primarily due to shear force. These panels were marked as 1, 2, 3, and 4 in TG1, TG2, and TG5 girders, as seen in Figure 5.2. In TG3 and TG4, only panels 1 and 4 were investigated, as the other inner panels were stiffened by additional flange cover plates. In what follows, these panels would be referred to as the test panels. The detailed geometrical properties for these web panels are given in Table 5. 1.

Table 5. 1 Properties of Unrestrained Test Girders

Specimen	Web Details					Flange Details	
	b_w (mm)	d_w (mm)	t_w (mm)	b_w/d_w	d_w/t_w	b_f (mm)	t_f (mm)
TG1	139	139	6.1	1	22.8	152.4	6.8
TG2	181	181	8	1	22.6	203.9	12.5
TG3	305	305	2	1	152.5	80	6
TG4	305	305	2.7	1	112.9	80	6
TG5	305	305	1.5	1	203.3	80	6

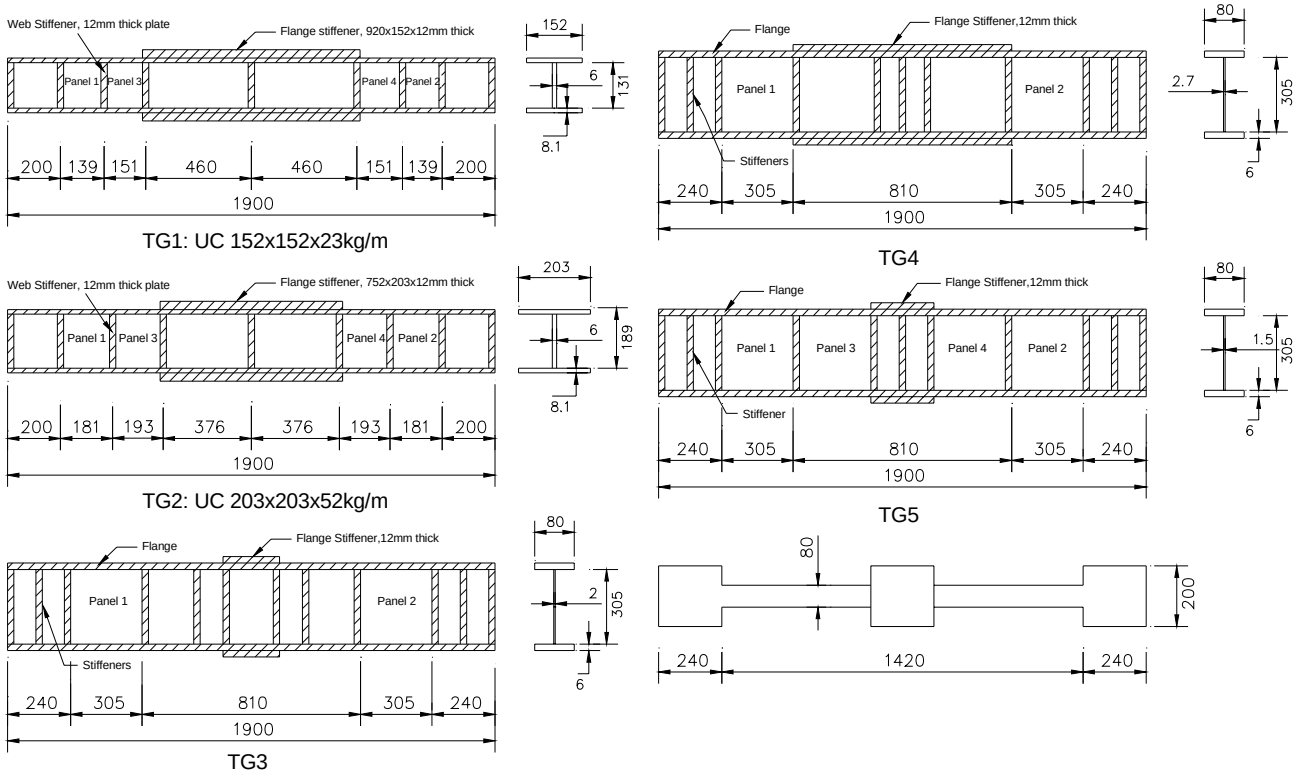

Figure 5.2 Unrestrained Test Girder Configurations

Before testing, geometrical imperfections along the longitudinal profile of flanges and web plates were measured at fourteen locations as shown in Figure 5.3. The measurement was conducted with the aid of Mitutoyo digimatic caliper and wood base ruler. The datum of the top and bottom flanges longitudinal profiles for TG3 series are listed in Table 5.2.

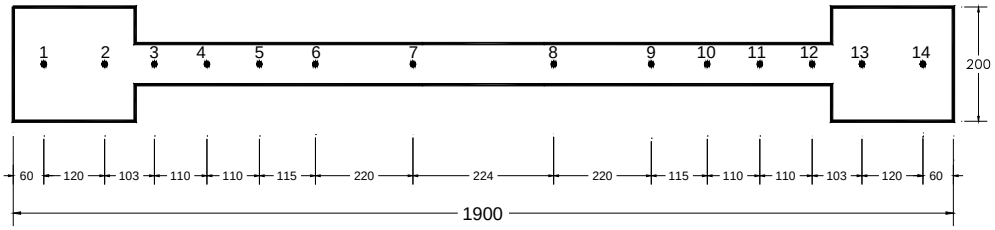

Figure 5.3 Location for Geometrical Imperfection Measurement

The numbers in Table 5.2 represent the distances between the measured face of the specimen and the base ruler. For a perfectly straight plate these numbers should be equal except for the middle section with additional flange stiffener plates. The

thickness measurements of the top and bottom flange were also conducted along the fourteen locations, and listed in Table 5.3. From Table 5.3, it can be observed that the measurement datum at No.6 to No.9 points were larger than the other measurements, as the top and bottom flange stiffeners attached shown in Figure 5.2. The longitudinal imperfection of the web was also measured at fourteen locations as shown in Figure 5.3. The measurement datum of the front and back faces of the web panel are listed in Table 5.4.

Table 5.2 Detailed Measurement Datum for TG3-1 Flange Curvatures

	Measure point	1 (mm)	2 (mm)	3 (mm)	4 (mm)	5 (mm)	6 (mm)	7 (mm)	8 (mm)	9 (mm)	10 (mm)	11 (mm)	12 (mm)	13 (mm)	14 (mm)
TG3-1	Top flange	229.41	230.62	229.88	229.73	229.85	224.70	224.29	224.23	224.15	230.19	230.07	230.03	229.98	229.38
	Bottom flange	229.28	229.34	229.69	229.76	229.84	223.95	223.85	223.69	223.42	229.42	229.63	229.86	229.30	229.40

Table 5.3 Top and Bottom Flange Thicknesses of TG3-1

	Measure point	1 (mm)	2 (mm)	3 (mm)	4 (mm)	5 (mm)	6 (mm)	7 (mm)	8 (mm)	9 (mm)	10 (mm)	11 (mm)	12 (mm)	13 (mm)	14 (mm)
TG3-1	Top flange	5.91	5.94	5.97	6.17	6.15	12.15	12.07	12.01	12.06	5.93	5.96	6.10	5.98	6.01
	Bottom flange	6.06	5.98	5.95	5.94	6.02	12.08	11.97	11.86	11.93	6.01	6.08	6.00	5.95	5.91

Table 5.4 Detailed Measurement for TG3-1 Web Panel Curvatures

	Measure point	1 (mm)	2 (mm)	3 (mm)	4 (mm)	5 (mm)	6 (mm)	7 (mm)	8 (mm)	9 (mm)	10 (mm)	11 (mm)	12 (mm)	13 (mm)	14 (mm)
TG3-1	Front beam	229.66	229.40	229.69	230.22	230.56	230.81	231.08	231.40	232.03	231.91	231.73	230.84	230.02	230.13
	Back beam	229.11	229.45	229.28	228.94	228.29	228.25	228.14	228.47	228.00	228.30	228.44	228.84	228.76	228.72

The objectives of initial imperfection measurement are to measure the crookedness of the top and bottom flanges, and the web panel imperfection. From initial out-of-straightness measurement of web panel for TG3-1, it can be found that the standard derivation of relative initial imperfection for web panel is approximate 0.8 mm and 0.4 mm at the respective front surface and back surfaces of the beam. These are much smaller than the permitted initial out-of-plane deflection

($d/120 \approx 2.5mm$) specified in the ANSI/AASHTO/AWS D1.5-96 Bridge Welding Code (AASHTO, 1996). Typically, for end panels 1 and 2 as shown in Figure 5.2, from measurements at points 3 to 5 and points 10 to 12 as listed in Table 5.4, the maximum relative out-of-plane imperfection is approximately 0.4 mm, which is within the acceptable fabrication tolerance by the above reference. For TG3 series, TG3-1 and TG3-2 had higher out-of-plane imperfections, approximately 0.8mm. However, corresponding measurements for TG3-3 and TG3-4 were around 0.7 mm and 0.5 mm respectively. A higher out-of-straightness imperfection caused TG3-1 beam web panels to buckle at a much lower shear force compared with analytical predictions as shown in Table 5.7, since analytical predictions are derived based on perfectly flat plates. However, this effect becomes less significant for TG3-3 and TG3-4 due to smaller initial imperfections. Discrepancy between experimental and analytical shear buckling load is also due to slightly non-uniform temperature distribution across the web panels as shown in Figure 5.18. Material coupon tests were conducted to determine the mechanical properties for each series of specimens. The detailed material properties for TG1, TG2, TG3, TG4 and TG5 series are listed in Table 5.5.

Table 5.5 Material Properties of TG1, TG2, TG3, TG4 and TG5 series

Specimen	Location	Thickness (mm)	Yield Stress (MPa)	Young's Modulus (MPa)
TG1	Flange	6.8	359	207000
	Web	6.1	342	197000
TG2	Flange	12.5	325	213000
	Web	8	332	205000
TG3	Flange	6	274.5	204000
	Web	2	287.8	200000
TG4	Flange	6	277	204000
	Web	2.7	232.8	200000
TG5	Flange	6	277	204000
	Web	1.5	332	200000

5.2.3 Heating Furnace Configuration and Loading Device

An enclosed furnace was assembled from two-sided, L-shaped, electric heating modules, two rectangular end panels with openings for the protruded specimen, and one top-piece cover. The assembled furnace was 1.5 m long, 1.2 m wide and 0.9 m high. The heating rate was monitored by a separate control panel. From a few trial heating tests, a rate of 7 ^{o}C per minute was chosen for the furnace temperature. This temperature increment is within the range described as a practical heating rate for steel sections by BS 5950 Part 8 (BS 5950-8), which stipulates a value from 5 to 20 ^{o}C/minute. An ENERPAC hydraulic jack was used to apply the load at midspan. The jack was supported by a two-portal-frame system which had a combined capacity of 1000 kN. The loading level was measured by an annular compression load cell, which was placed in between the hydraulic jack and the loading rod, as shown in Figure 5.1. A rocker bearing was also inserted between the load cell and the loading rod to ensure verticality of applied force. To minimize reading errors, load cells with different ranges were used for different test girders depending on the expected failure loads. For example, since TG1 was expected to fail at 400 kN loading, a 500 kN capacity load cell was used; for TG3 the expected failure load was 175 kN, thus, the 500 kN capacity load cell was replaced by a 300 kN load cell instead. The jack was manually driven and the load cell was connected to a data logger control system.

5.2.4 Deformation Acquisition System

Linear variable differential transducers (LVDTs) were used to measure vertical deformations of test panels, mid-span deformations, and support settlements. Typical LVDT locations for a test girder are shown in Figure 5.4. Support rotations on the right-hand end were obtained by taking the relative displacement between LVDT7 and LVDT8. Line LVDTs were used to measure the out-of-vertical-plane deformations at the centre of the web panels to determine if shear buckling has

occurred. Basically, line LVDTs were used only at the two end panels for all the test series, except for the TG5 series where two additional line LVDTs were also introduced at the two inner panels 2 and 3 (Figure 5.2). In the TG5 series, the inner panels were expected to fail before the end panels as the former were subjected to greater bending moment. For the elevated temperature tests, it should be noted that since the LVDTs were not heat-resistant, alsint ceramic rods were used to connect the external LVDTs (LVDT 1 to LVDT4) with the measured positions on the specimen inside the furnace.

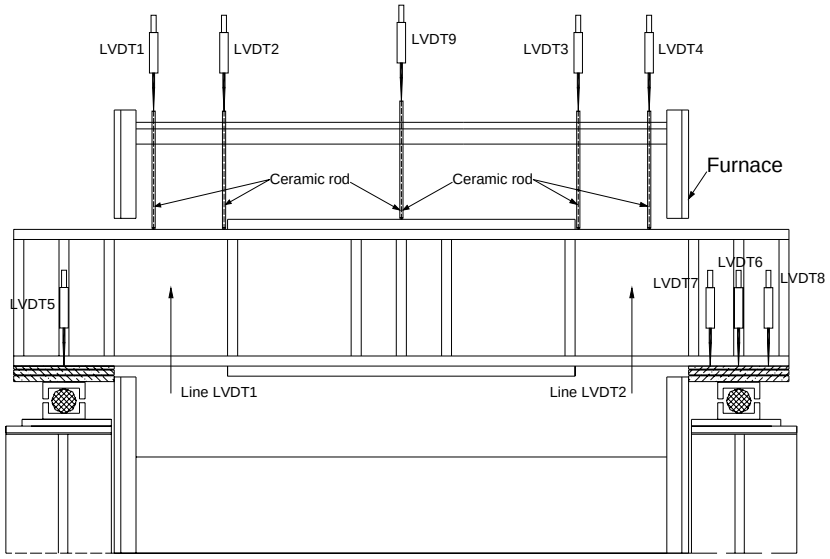

Figure 5.4 Typical LVDT Measurement Location

5.2.5 Strain Measurement System

To monitor median strain in each flange and centre of web panel, normal strain gauges were used for ambient-temperature tests. For the ambient-temperature test, the instrumentation procedure consisted of fixing the strain gauges onto the web panel and the flanges in addition of installing LVDTs. There were two types of strain gauges used in this experiment, single-element and three-element rectangular rosette strain gauges. The single-element strain gauges were used to measure strain in the top and bottom flanges, while the three-element rosette strain gauges were used to measure the horizontal, vertical, and diagonal strain in the web panel. One rosette strain gauge consists of three single-element strain gauges measuring the

respective strain at two perpendicular directions, and also an additional gauge at 45^{o} angle between the two directions. The locations of strain gauges for TG5 series are shown in Figure 5.5.

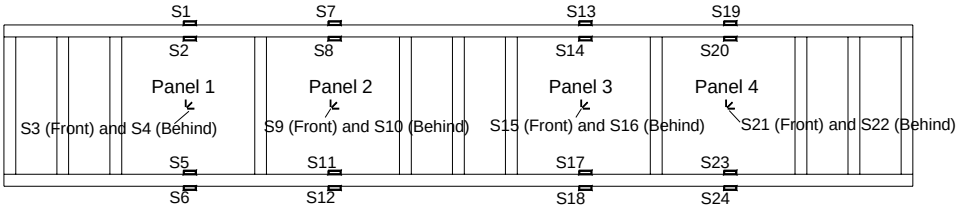

Figure 5.5 Locations of Strain Gauges for TG5-1

5.2.6 Temperature Measurement and Thermal Insulation

For elevated temperature tests, thermocouple wires were used to measure the temperatures of the specimen as well as the furnace temperature. The locations of thermocouple wires for TG5 series are shown in Figure 5.6.

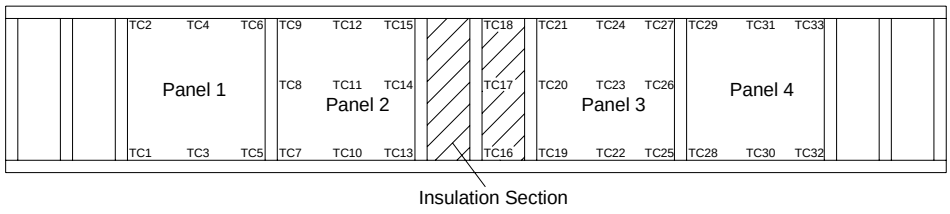

Figure 5.6 Location of Thermocouple Wires for TG5 series

To minimize effects of bending moments and to study behaviour of beam section under shear force conditions, only the end panels were tested at elevated temperatures. The middle panels were insulated with rock wool so that the temperature in this section would be below the end panel temperature to prevent flexure failure at mid-span. To prevent heat loss, two sides of the heating furnace and the ends of the specimens outside furnace were heavily insulated using rock wool and wrapped up with insulation cloth. The loading rod was also carefully wrapped up by rock wool to keep the temperature as low as possible.

5.2.7 Unrestrained Plate Girder Test Procedure

- *Ambient Temperature Test*

A total of 5 test girders, one from each series, were tested at ambient temperature. They served as control specimens within a series. Loading was applied incrementally at the centre of the girders. In addition to the use of LVDTs for displacement measurements, strain gages were used to measure strains at the centre of the web panel, and at the top and bottom flanges of the girders. Typical locations of the strain gages on the test panels are shown in Figure 5.5. It should be noted that S3, S4, S9 and S10 are rosettes, while the others are uni-axial strain gages.

- *Elevated Temperature Test*

There are two standard methods of elevated temperature tests, namely, transient-state and steady-state tests. In the transient-state test, external load is applied to the member first and held at a constant level, while the temperature is increased gradually at a specified rate, conforming to ISO834 fire curve. The test is continued until the member cannot sustain the constant applied load. On the other hand, the steady state test is similar to the ambient temperature test except that it is conducted at a constant elevated temperature isothermal condition. Load is then applied to the member while the temperature is held constant. In the present work, the steady state test method was selected as it is not possible for the electric furnace to achieve the ISO834 heating rate. During heating stage, specimens were allowed to move freely in the longitudinal direction, so that there was no thermal strain due to support restraint. The atmosphere and steel temperatures were monitored by K-type thermocouple wires, and recorded automatically every fifteen seconds. Factors that may have an effect on the failure loads at isothermal conditions include initial imperfections, ceramic rod expansion, and support movements were anticipated and measured. Before discussing the test results, the following points should be made on these factors.

I. Initial imperfections

As described in Section 5.2.2, the initial imperfections of the test girders were measured using a digital vernier caliper to determine the thickness of the top and bottom flanges. The measurements were made at fourteen locations along the specimen length on the top and bottom flanges. The maximum thickness variation of the flange plates were 0.44 mm within the specified tolerance of 0.5 mm (Hayward and Weare 1999).

II. Ceramic rod expansion

The ceramic rods used for deformation acquisition were calibrated under the present heating condition to check for thermal expansion. The average thermal expansion was found to be 7.744×10^{-6} /^{o}C, close to supplier's specification of 7.8×10^{-6} /^{o}C. In the actual test set-up, the heated length of ceramic rod for TG1 was 200 mm, for TG2 was 150 mm and for TG3, TG4 and TG5 girders was 70 mm. The maximum thermal expansions were found to be 1.04, 0.78 and 0.38 mm for TG1, TG2 and plate girder tests (TG3, TG4 and TG5 series) at 700 ^{o}C. Therefore, the effect of rod expansion was very minimal and, thus, was not considered in deflection result analyses.

III. Support movements

Support settlements were monitored and incorporated with the measurements to obtain actual vertical deflections of the girder panel at respective locations. Furthermore, to check if the roller support condition provided a free thermal expansion condition, horizontal support movements of TG5 were monitored. It was found that at 700 ^{o}C before loading, horizontal expansion obtained from an LVDT reading was 15.3 mm, while thermal expansion from the FE simulation of the whole beam was 14.5 mm, as described in Section 6.2.2. In this FE simulation, a quadratic thick shell element (MSC, 2001) was used for both the web and the flanges of tested specimens. Actual temperature measurements and material properties have also

been incorporated into these simulations respectively. Therefore, there was reasonable agreement between the two.

5.3 Unrestrained Plate Girder Experiment Results

In this section, the experimental results of three series of specimens (TG3, TG4 and TG5 series) are plotted and studied. Each series consisted of four specimens, tested at ambient temperature, 400, 550 and 700 ^{o}C, respectively.

5.3.1 Plate Girder Shear Buckling and Ultimate Shear Capacity

From the experiments of the 18 test girders at different isothermal temperatures, the ultimate shear capacity of each girder is listed in Table 5.6. The ultimate shear strengths from the analytical method and FEM analyses will be shown and discussed in Section 6.3.

Table 5.6 Shear Buckling Load and Ultimate Shear Strength of Test Girders

Test Series	Test Girder	Temp (^{o}C)	*Shear Buckling Load* V_{cr} *(kN)*	*Shear Ultimate Load* V_{test} *(kN)*
TG1	TG1-1	20	172.2	193.5
	TG1-2	550	79.85	97.3
TG2	TG2-1	20	270.3	343.8
	TG2-2	400	260	324.3
	TG2-3	550	183.6	234.6
	TG2-4	700	62.4	74.2
TG3	TG3-1	20	53.35	79.85
	TG3-2	400	30.08	67.63
	TG3-3	565	19.87	34.34
	TG3-4	690	7.05	17.15
TG4	TG4-1	20	101.4	111.8
	TG4-2	400	58.9	77.1
	TG4-3	550	24.54	37.75
	TG4-4	700	10.59	15.94
TG5	TG5-1	20	21.05	59.6
	TG5-2	400	17.63	46.4
	TG5-3	550	13	28.6
	TG5-4	700	4.5	10.16

5.3.2 Test Results of Ambient Tests (TG3-1, TG4-1 and TG5-1)

In this research, three specimens (TG3-1, TG4-1 and TG5-1) with different geometrical and material properties were tested at ambient temperature. The experimental datum consisted of readings from the strain gauges affixed onto the web panels and the flanges, and vertical deflections from the LVDTs.

- *Strain Results*

Strain measurements were recorded by strain gauges affixed onto the flanges and web panels shown in Figure 5.5. The strains of web panel 2 of TG5-1 specimen at locations shown in Figure 5.7 are plotted in Figure 5.8.

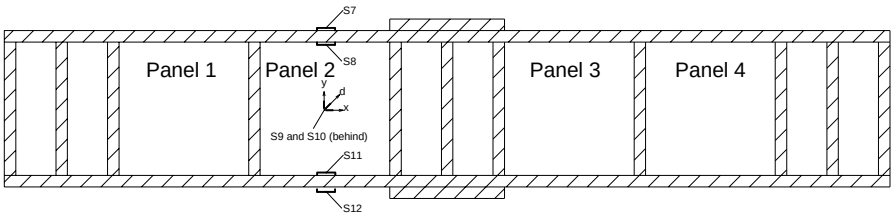

Figure 5.7 Strain Measure points for TG5-1 Panel 2

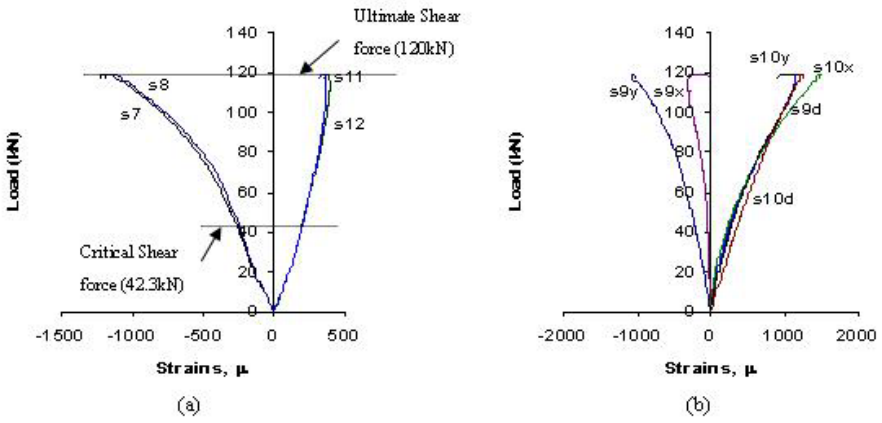

Figure 5.8 Strain Measurements for TG5-1 Panel 2

The top flange strains S7 and S8 are almost the same showing that the strain across the thickness of the flange plate is nearly uniform. The same can be said for the bottom flange strains S10 and S11. The negative sign of S7 and S8 indicated that the top flange is in compression and the positive sign of S10 and S11 confirmed tension in the bottom flange. The strain measurements for the top and bottom flanges (S7, S8 and S11, S12) were almost symmetrical before web panel started to

buckle. After web buckling occurred, the median strain in compression flange (S7 and S8) became greater than that in tension flange (S11 and S12) due to local buckling of flange and plastic hinge formation in the compression flange.

The rosette strain gauges (S9 and S10) measured the vertical (ε_V), horizontal (ε_H) and diagonal (ε_D) at 45^0 angle strains at the centre point of the web panel. From the rosette strain gauges readings, the principal strain and maximum shear strain of the web panel can be calculated as follows:

$$\varepsilon_H = \varepsilon_x \quad \varepsilon_V = \varepsilon_y \quad \varepsilon_D = \frac{1}{2}\left(\varepsilon_x + \varepsilon_y + \gamma_{xy}\right) \tag{5.1}$$

The shear strain (γ_{xy}) can be calculated as:

$$\gamma_{xy} = 2\varepsilon_D - \varepsilon_x - \varepsilon_y \tag{5.2}$$

The principal strains can be calculated from:

$$\varepsilon_{1,2} = \frac{\varepsilon_x + \varepsilon_y}{2} \pm \sqrt{\left(\frac{\varepsilon_x - \varepsilon_y}{2}\right)^2 + \left(\frac{\gamma_{xy}}{2}\right)^2} \tag{5.3}$$

The maximum shear strain is associated with axes at 45° to the directions of the principal strains. It can be calculated from the following equation:

$$\frac{\gamma_{\max}}{2} = \sqrt{\left(\frac{\varepsilon_x - \varepsilon_y}{2}\right)^2 + \left(\frac{\gamma_{xy}}{2}\right)^2} \tag{5.4}$$

The principal strains and maximum shear strain at the centre of the web panel 2 of TG5-1 are shown in Figure 5.9.

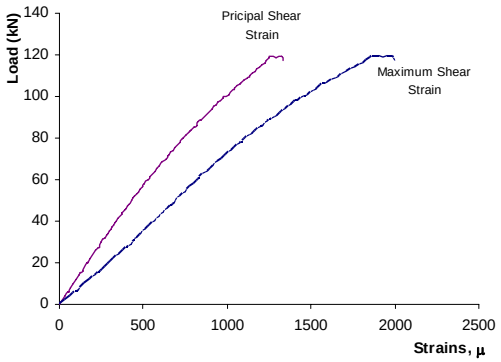

Figure 5.9 Principal and Maximum Shear Strain for Web Panel 2 of TG5-1

The strain-versus-load curves show that maximum and principal strains increase as increasing load. When the specimen approaches the ultimate load the strains increase more rapidly until failure occurs. The test results will be compared with numerical finite element simulations in Section 6.3.

- *Web panel vertical deflection measurement*

Vertical displacements of beam specimens were measured by LVDT. The positions of LVDTs for TG3-1, TG4-1 and TG5-1 are shown in Figure 5.4. There are no load-versus-out-of-plane-deflection curves as horizontal LVDTs were not used for the ambient test. For TG3-1, the vertical deflections of panel 1 and 2 are shown in Figure 5.10. The load-versus-mid-span-deflection of beam specimen is shown in Figure 5.11. The L1 to L4 indicate the measurements from LVDT1 to LVDT4 as shown in Figure 5.5.

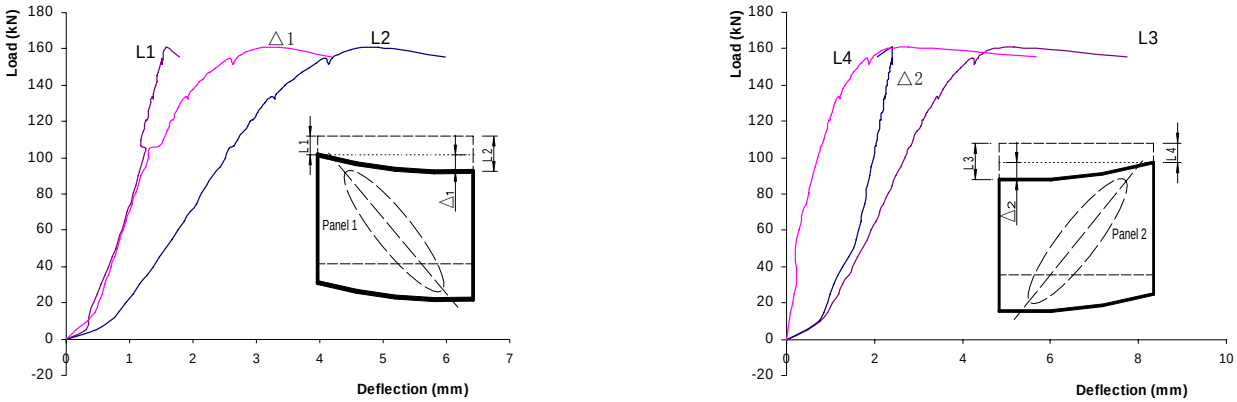

Figure 5.10 Load versus Vertical Deflection of TG3-1 Web Panels

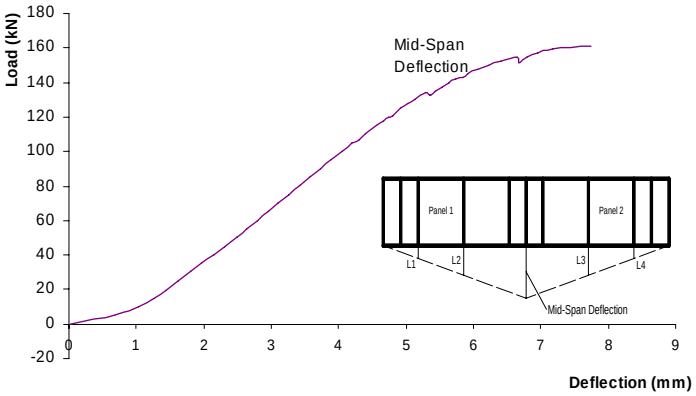

Figure 5.11 Load versus Mid Span Deflection of TG3-1

In Figure 5.10, the load-versus-vertical-deflection curves of the web panel indicate that the vertical deflections reach plateau at approximately 160 kN. Therefore the ultimate shear capacity of TG3-1 is approximately 80 kN. The buckling of the web panel can be identified from the load-versus-vertical-deflection curves. Before buckling, vertical deformation behaves linearly. After buckling, nonlinear behaviour is expected in the web panel deformation. The load versus mid-span deflection curve is plotted in Figure 5.11 and will be compared with the finite element analysis results in Section 6.4.

5.3.3 Elevated-Temperature Test Results (TG3, TG4 and TG5)

Each TG3, TG4 and TG5 series consisted of three specimens tested at 400, 550 and 700 ^{o}C, respectively. Steady-state test method was chosen, whereby the specimen was heated to the specified temperature and the temperature was held constant while load was applied at the beam centre until failure occurred.

- *Web panel vertical and out-of-plane deflection measurement*

For TG3-2 (tested at 400 ^{o}C), the vertical deflections of panel 1 and 2 are shown in Figure 5.12. The load-versus-out-of-plane-deflection curves of panel 1 and 2 are shown in Figure 5.13. The load-versus-mid-span-deflection and web panel out-of-plane deformation curves of beam are shown in Figure 5.14.

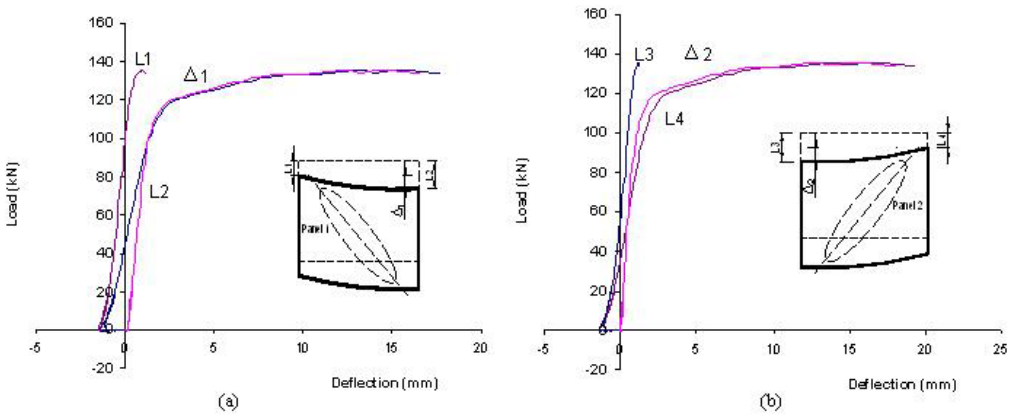

Figure 5.12 Load versus Vertical Deflection of TG3-2 Web Panels

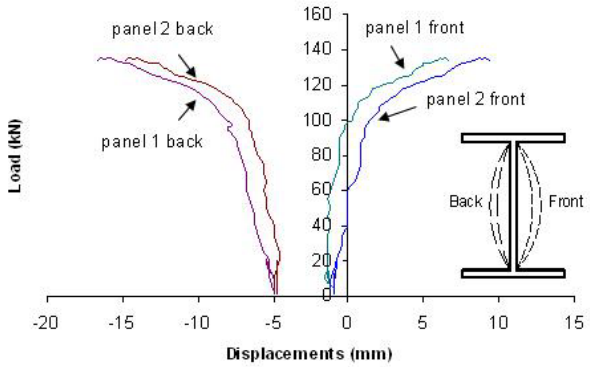

Figure 5.13 Load versus Out-of-Plane Deflection of TG3-2 Web Panels

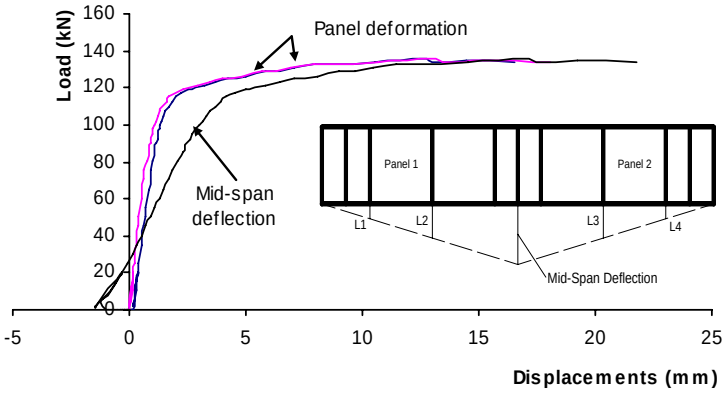

Figure 5.14 Load versus Mid-Span deflection and Web Panel Deformation of TG3-2 Web Panels

From Figure 5.12, it can be observed that the vertical displacements of both end panels show similar behaviour. The deformations at unloaded level were induced by thermal expansion during the heating stage. The panel deformation and mid-span curves in Figure 5.14 indicate that the panel failed at 136 kN since the panel deformation kept increasing without additional loads. From the load-versus-out-of-plane-deflection curves in Figure 5.13, it can be observed that the out-of-plane deflections of two web panels at the beginning of loading were very small and they increased slowly with applied load. However, after the load reached a certain value (at 136 kN), the out-of-plane displacements increased tremendously. This indicates the ultimate shear capacity of TG3-2 web panel (400

^{o}C) is 68 kN. In Section 6.4, the test results of web panel vertical deflections, out-of-plane deflections and mid-span deflection versus load will be compared with finite element analyses (FEA) predictions. Based on the out-of-plane measurements, Southwell plot method (Mandal, 2003) can be used to determine critical loads and effects of initial imperfections. Typical Southwell plot of w/P against w (w is out-of-plane deflection, P is vertical load) for TG3-2 is show in Figure 5.16. Critical load can be obtained from the best-fit straight line. Besides, principal mode of imperfection of web panel can be obtained, which is approximately 0.7 mm for TG3-2, in reasonable agreement with initial imperfection measurements as described in Section 5.2.2.

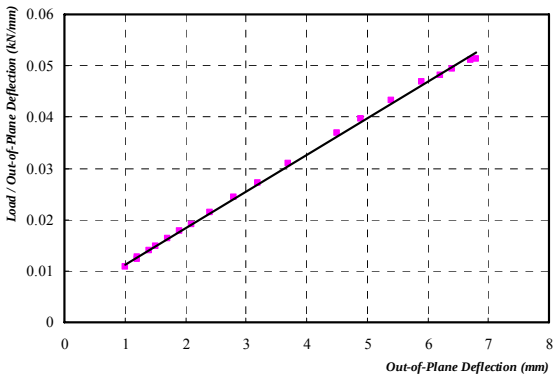

Figure 5. 15 Southwell Plot for TG3-2 Web Panel

The test results of all test panels showed similar behaviour, that is, the web panel behaved elastically before web buckling occurred. After web buckling, the line LVDTs used to measure the out-of-plane deformation indicated an increase in deformation, and the web panel load-deformation curves became non-linear. The deformation rate increased and failure occurred when the web panel could not take up any further load increments. As a typical example, shear failure can be observed from a sudden increase in out-of-plane deflection as shown in Figure 5.16 for web panel 1 of TG4-2 tested at 400 ^{o}C. The out-of-plane deflection increased lineally up to approximately 80% of the ultimate load and then web panel 1 showed a large increase in out-of-plane deflection with a small increase in load. A similar trend can

be observed for web panel 1 of TG4-3 tested at 550 ^{o}C with significant ultimate shear strength reduction. Nevertheless, the out-of-plane deflection of web panel 1 of TG4-4 (700 ^{o}C) developed rather smoothly. This is because at higher temperature, the steel material stress-strain relationship becomes highly nonlinear and the distinction between the elastic and the plastic stage is blurred.

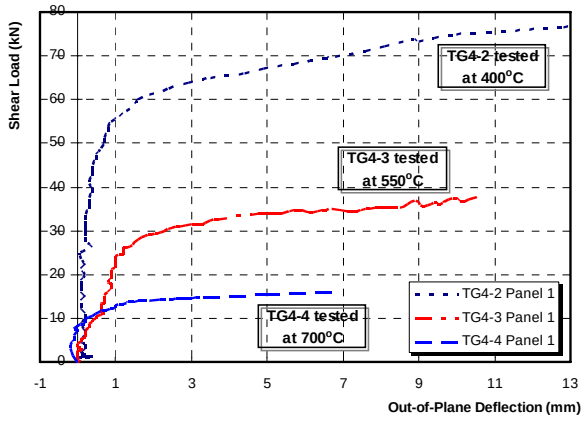

Figure 5.16 Shear Load versus Out-of-Plane Deflection for TG4 series

For TG3 and TG4, end panels 1 and 2 buckled and failed primarily due to shear force. For TG5, the inner panels 3 and 4 buckled and failed earlier than the two end panels 1 and 2 (Figure 5.2) due to a combined bending moment and shear force effect. The interaction between the effects of the shear force and bending moment can be represented by Figure 5.17, where M_D and V_D are the respective theoretical maximum pure bending and pure shear capacity of the panel section, and M_o and V_o are the respective bending moment and shear force acting simultaneously on the section. Although panel 3 and 4 of TG5 series were subjected to the same shear force as end panels 1 and 2, the inner web panels 3 and 4 were subjected to greater bending moment. Thus, inner panels 3 and 4 failed earlier (as expected) than the two end panels.

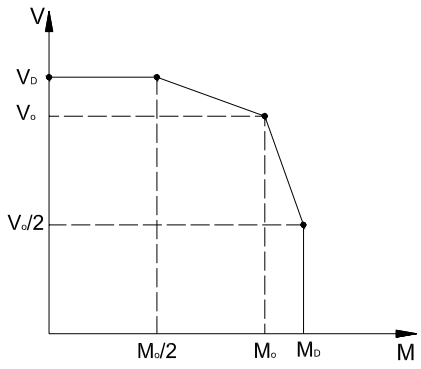

Figure 5.17 Interaction between Shear and Bending Moment for Plate Girder

➢ *Temperature measurement*

The temperatures of different points of specimens were measured by thermocouples attached onto the top and bottom flanges, and web panels. The locations of thermocouples for TG3, TG4 and TG5 series are shown in Figure 5.6. The temperature of the heating furnace was also monitored. The detailed temperature-versus-time curves for TG3-2 are shown in Figure 5.18.

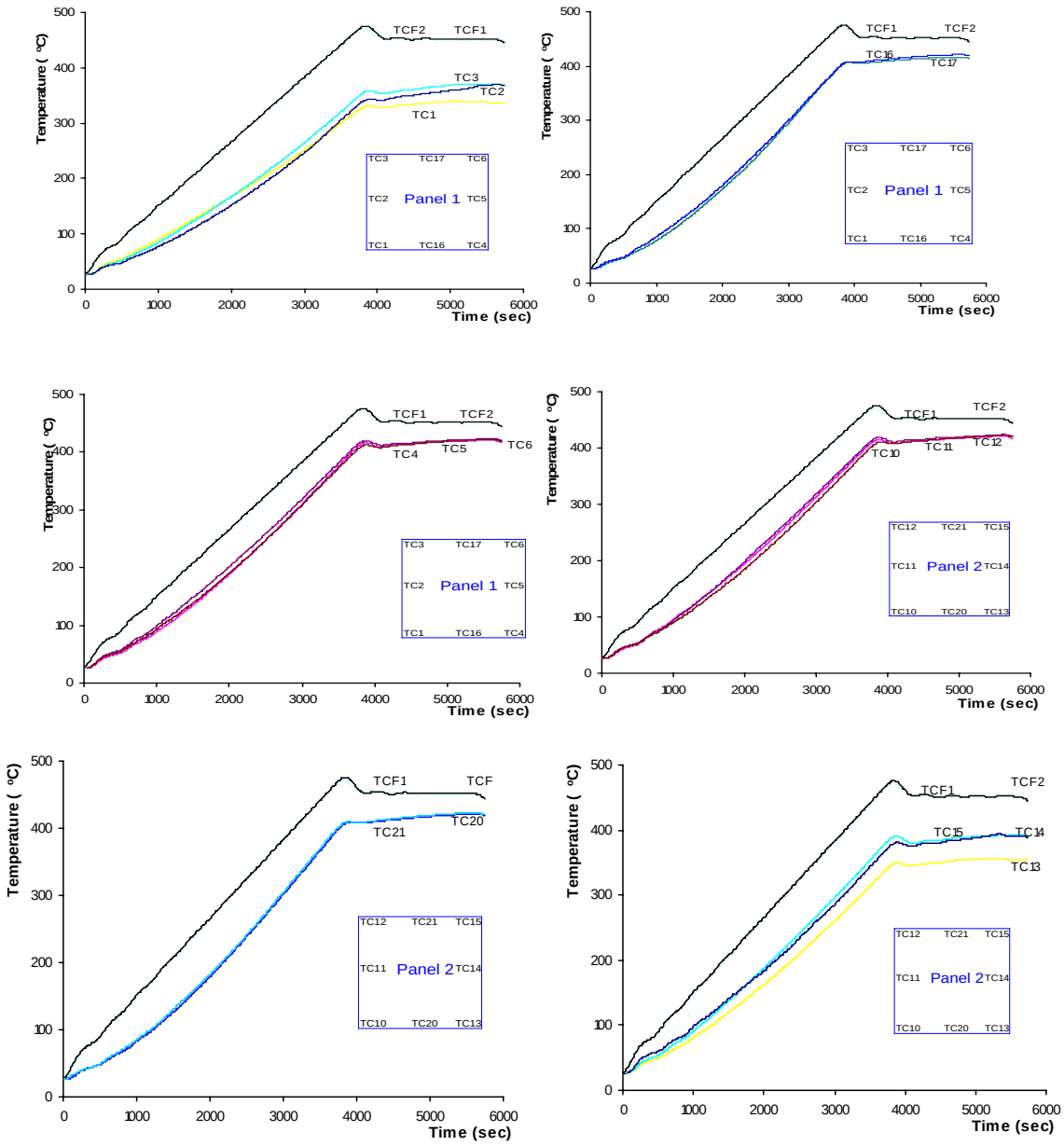

Figure 5.18 Temperature versus Time for Web Panel 1 and 2 of TG3-2

The furnace was programmed to provide a heating rate of 7 ^{o}C/min. The rate of heating was set to be higher than the required steel specimen rate. This was because from a few trial heating tests, it was found that the temperature of specimen would be lower than the furnace by 50-100 ^{o}C at the end of testing. After the furnace temperature has reached the predefined value, the furnace temperature was held constant while loading was applied to the specimen. For TG3-2 which was to be tested at 400 ^{o}C, the furnace temperature was programmed to reach 470 ^{o}C. From

the temperature results at various locations inside panel 1 and panel 2 as shown in Figure 5.18, respectively, it can be observed that the final heating temperatures at different locations varied form 370 ^{o}C to 420 ^{o}C longitudinally. The maximum temperature variation across the web panel was around 50 ^{o}C. Figure 5.19 shows typical temperature variations for specimen TG4-4 versus time. The temperatures of electrical furnace, top and bottom flanges, and web at mid-depth were plotted up to 700 ^{o}C. The top, bottom flanges and web showed little discrepancy in temperature distribution. Due to imperfect thermal insulation of furnace top cover panels, the top and bottom flange temperatures rose slowly compared to the centre of web. The temperature difference between the web and the top flange increased to approximately 50 ^{o}C after 3000 seconds. This was because the web was subjected to direct radiation from the heating elements placed on the side of furnace, while the top and bottom flanges were shielded from such radiation. However, due to somewhat uniform heating distribution within the electrical heating furnace, the temperature difference between the top flange and the rest of the section was reduced to 20 ^{o}C when the web and bottom flange temperatures reached the final desired temperature. In addition, the specimens were allowed to expand freely in the longitudinal direction, so that there were negligible induced stresses and strains across the section due to heating and support restraint. However, as the test panels were located near the beam ends which were not directly exposed to the heating coil in the furnace, there was a small temperature gradient in the longitudinal direction. Figure 5.20 presents typical longitudinal temperature distribution of TG4-4 tested at 700 ^{o}C. It shows that the temperatures of inner panels were about 15% lower than the corresponding temperatures of end panels due to thermal insulations at the inner panels to prevent flexural failure at mid-span. Nevertheless, a separate numerical simulation on the effect of longitudinal temperature variation showed that the panel shear capacity was not so sensitive to the recorded longitudinal temperature gradients within the end panels, as they were generally small.

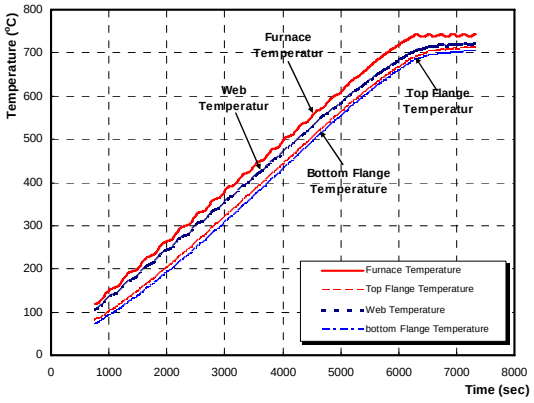

Figure 5.19 Typical Temperature Distribution for TG4-4 tested at 700 °C

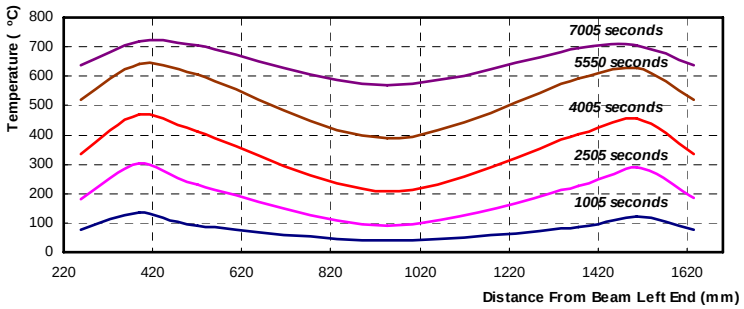

Figure 5.20 Typical Longitudinal Temperature Distribution at Web of TG4-4

5.3.4 Ultimate Shear Capacity Results

From the experiments of 18 girders at different isothermal temperatures, the ultimate shear capacity of each girder is listed in Table 5.7. The ultimate shear strengths from the analytical method are listed together for comparison purpose. These analytical predictions were derived based on an improved analytical approach as described in Section 4.2.2, with consideration of degradation of steel material properties at elevated temperatures. It can be seen that the mean deviations among the overall test results and the analytical predictions are very small. In general, the analytical V_{ult} and V_{test} agree well, as shown in Column (7) of Table 5.7, with the mean and standard deviation as 0.93, and 0.09, respectively. It can be said that all the results agree well, except for TG4-3, which was not symmetrically supported due to undetected set-up problem. It should be noted that in the analytical predictions, the strength of steel at elevated temperature was taken by considering

the strength retention ratio at 2% strain level for TG1 and TG2, and at 0.5% strain level for TG3, TG4, and TG5 series (BS 5950-8 and ENV 1993-1-2). For TG3, TG4 and TG5 series, plate buckling load and ultimate capacity mainly influenced by elastic modulus of steel at higher temperatures. In addition, degradation trend of steel strength at 0.5% strain level is close to that of steel elastic modulus at elevated temperatures. Also, from strain measurements at ambient temperature tests, it can be noticed that web panel reached ultimate shear strength at a much lower principal strain level, as shown in Figure 5.7. Therefore, reduction factor for steel strength at 0.5% strain level is chosen for current analytical investigations.

Table 5.7 Comparison of Results obtained from Analytical Approach, and Experiments

Test Girder	Temp (°C)	Analytical predictions		Test results		$\frac{V_{test}}{V_{ult}}$
		V_{cr} (kN)	V_{ult} (kN)	V_{cr} (kN)	V_{test} (kN)	
(1)	(2)	(3)	(4)	(5)	(6)	(7)
TG1-1	20	174	192.19	172.2	193.5	1.01
TG1-2	550	100.6	111.09	79.85	97.3	0.88
TG2-1	20	288.4	345.65	270.3	343.8	0.99
TG2-2	400	288.4	345.65	260	324.3	0.94
TG2-3	550	178.8	214.3	183.6	234.6	1.09
TG2-4	700	66.34	79.5	62.4	74.2	0.93
TG3-1	20	44.36	85.7	53.35	79.85	0.93
TG3-2	400	31.05	65.2	30.08	67.63	1.04
TG3-3	565	18.23	37.13	19.87	34.34	0.92
TG3-4	690	5.77	15.7	7.05	17.15	1.09
TG4-1	20	113.6	113.64	101.4	111.8	0.98
TG4-2	400	76.34	85.89	58.9	77.1	0.90
TG4-3	550	50.43	51.86	24.54	37.75	0.73
TG4-4	700	14.53	18.19	10.59	15.94	0.88
TG5-1	20	19.18	69.28	21.05	59.6	0.86
TG5-2	400	13.43	53.17	17.63	46.4	0.87
TG5-3	550	11.51	32.39	13	28.6	0.88
TG5-4	700	2.49	11.48	4.5	10.16	0.89
--	--	--	--	--	--	0.93 [a]
--	--	--	--	--	--	0.09 [b]

[a] Mean Value [b] Standard Deviation

5.3.5 Failure Mode of Web Panel

Two stocky panels, TG1 and TG2 with web slenderness ratio of 22.7 and 22.5 were tested at ambient, 400, 550, and 700 ^{o}C. From Figure 5.21 (a) and (b), it was evident that the panels failed due to yielding without buckling. The other three slender panels, TG3, TG4, and TG5, which were tested at ambient, 400, 550, and 700 ^{o}C, are also shown in Figure 5.21 (c), (d), and (e), respectively. The residual post-buckled, out-of-plane deformations are clearly evident. After the buckled phase, additional shear stresses were taken up by a diagonal band in the test panel. As the load increased, the width of diagonal band also increased, and tensile field action was mobilized until the membrane stress in the diagonal band reached the yield strength. At the ultimate state, plastic hinges were formed at both the top and bottom flanges, displaying a sway mechanism of the test panel. Clearly, towards the collapsed phase, the top and bottom flanges also participated in resisting the applied force, but with the web panel resisting majority of shear force.

It is also noticed from Figure 5.21 11(c) to 11(e) that the buckled shapes are more visible at ambient temperature and 400 ^{o}C. This is because at higher temperature, the material non-linearity is more pronounced (as shown in Figure 3.6). At 700 ^{o}C, the Eurocode material stress-strain curve does not have a distinct demarcation point between the elastic and the plastic curve. The material behaves more like rubber with continuous non-linearity. From Figure 3.5, around 400 ^{o}C, there is a steep decline in reduction factor $k_{E(T)}$ for elastic modulus, and beyond 600 ^{o}C, the curve $k_{E(T)}$ is almost flat.

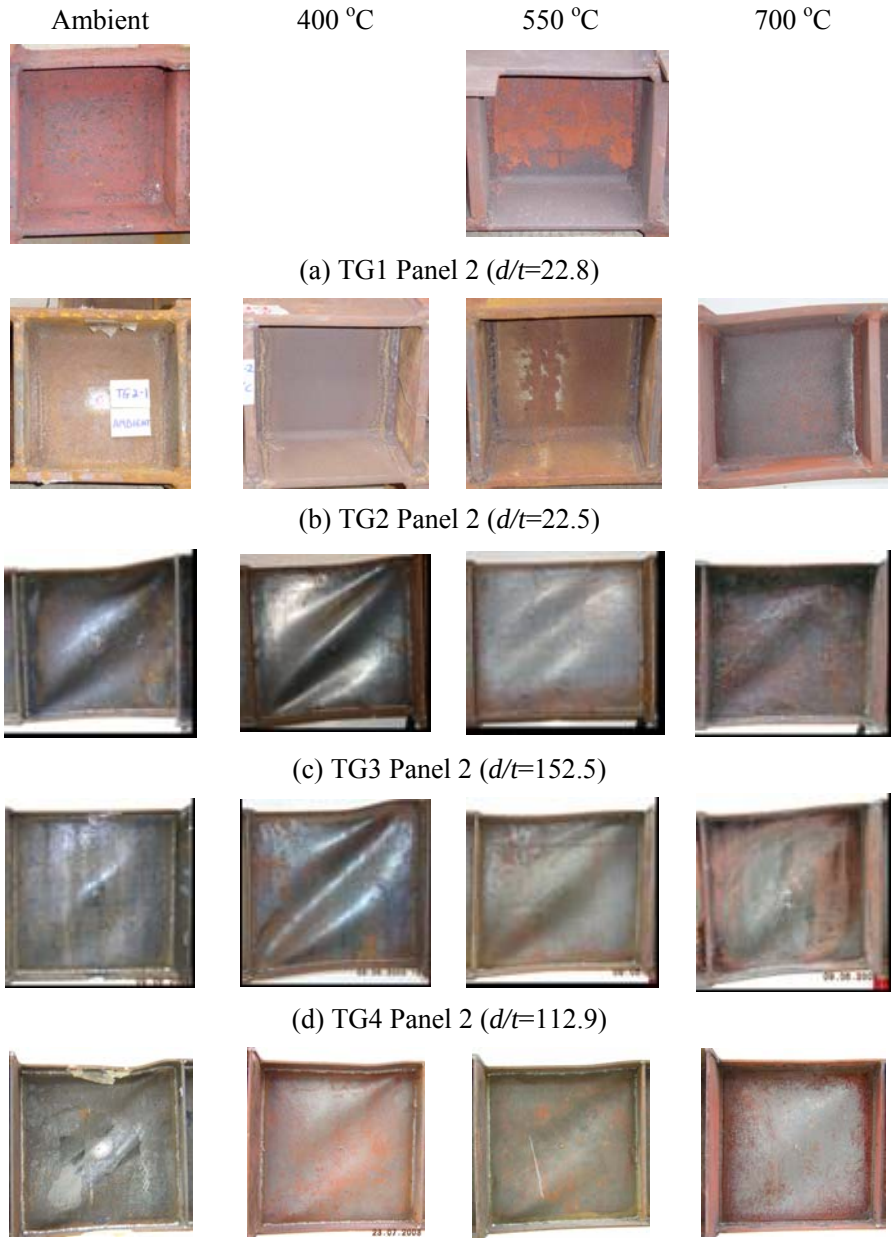

(a) TG1 Panel 2 (d/t=22.8)

(b) TG2 Panel 2 (d/t=22.5)

(c) TG3 Panel 2 (d/t=152.5)

(d) TG4 Panel 2 (d/t=112.9)

(e) TG5 Panel 3 (d/t=203.3)

Figure 5.21 Failure Modes of Unrestrained Plate Girder Tests

Another factor governing the panel buckling is the slenderness ratio (d/t). A plot of ultimate shear strength V_{test} (as shown in Table 5.7) to maximum shear strength V_{yw} $(= \tau_{yw(20)} A_V)$ versus increasing temperature is shown in Figure 5.22 and Figure 5.23, respectively, where A_V is shear area, and τ_{yw} is the shear yield strength of

web panel. The respective reduction factor of steel yield strength ($k_{y(T)}$ or $k_{x(T)}$) and elastic modulus $\left(k_{E(T)}\right)$ at elevated temperatures according to Eurocode 3 (ENV 1993-1-2) are also plotted as dashed lines in Figure 5.22 and Figure 5.23 for ease of comparison. From Figure 5.22 for stocky panels such as TG2, clearly, the ratio $V_{test}/V_{yw(20)}$ reduces with increasing temperature, following closely the trend of reduction ratio for steel yield strength, as TG2 failed due to yielding of web panels. It should be noted that for TG1 series, since there are only 2 points, they are not joined by a straight line. From Figure 5.23, it can be seen that the greater the d/t ratio, the lower is the starting point for the entire curve $V_{test}/V_{yw(20)}$ consisting of 4 temperature points for each series. Since TG5 has the greatest d/t ratio compared to TG3 and TG4, the post-buckling resistance is the least among the three series (cf. V_{cr} and V_{test} in Table 5.7). There is a significant difference between the reduction factors for yield strength of steel at 0.5% strain (dashed line in Figure 5.23) and at 2% strain (dashed line in Figure 5.22). For the former, the trend is closer to the reduction factor for elastic modulus (Figure 5.23). Thus, for TG3, TG4 and TG5, the ratio $V_{test}/V_{yw(20)}$ reduces with increasing temperature, following closely the trend of reduction ratio for steel elastic modulus and yield strength for 0.5% strain (ENV 1993-1-2) at elevated temperature.

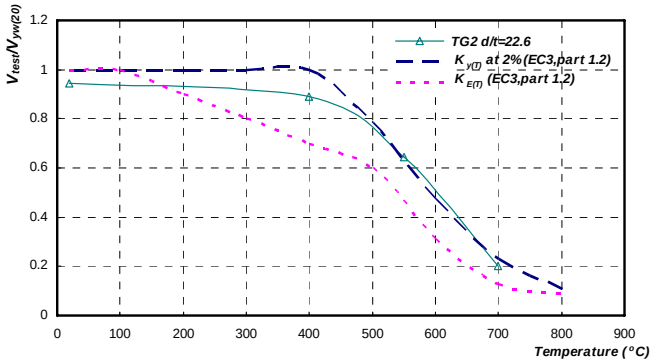

Figure 5.22 Shear Capacity Ratios of Unrestrained Plate Girder Tests

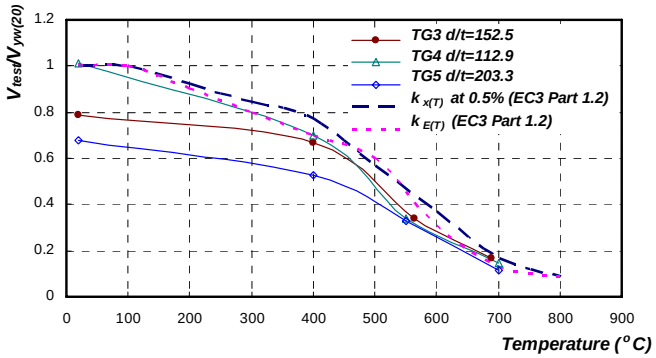

Figure 5.23 Shear Capacity Ratios of Unrestrained Plate Girder Tests

5.4 Restrained Plate Girder Experimental Set-up and Programme

For steel beam-to-column joint subjected to uniform heating conditions, shear component of beam web panel does not only resist the shear force but also the restraint axial force induced by boundary conditions. In this research, in addition to unrestrained shear component tests, a total of twelve plate girders have been tested predominately in shear at elevated temperature with thermal restrained effects. The test girders consisted of three series, namely, RTG3, RTG4, and RTG5, respectively. Each series consisted of three specimens (i.e. RTG3-1, RTG3-2, RTG3-3 etc.) tested at three respective furnace temperatures, viz. 400, 550 and 670 ^{o}C, with axial restraint stiffness as 9.6 kN/mm. In addition, each series consisted of one additional specimen tested at 670 ^{o}C but with axial restraint stiffness as 8.2 kN/mm.

5.4.1 Development of Restrained Plate Girder Test Programme

The configuration of the restrained plate girder test set-up is shown in Figure 5.24. The test specimen was enclosed in one electrical heating furnace and simply supported onto a steel rocker bearing at each end. The rocker bearing supports were placed external to the furnace to avoid damage due to heating. A horizontal beam supported onto a reaction frame was placed at each end of the test girder to provide axial restraint.

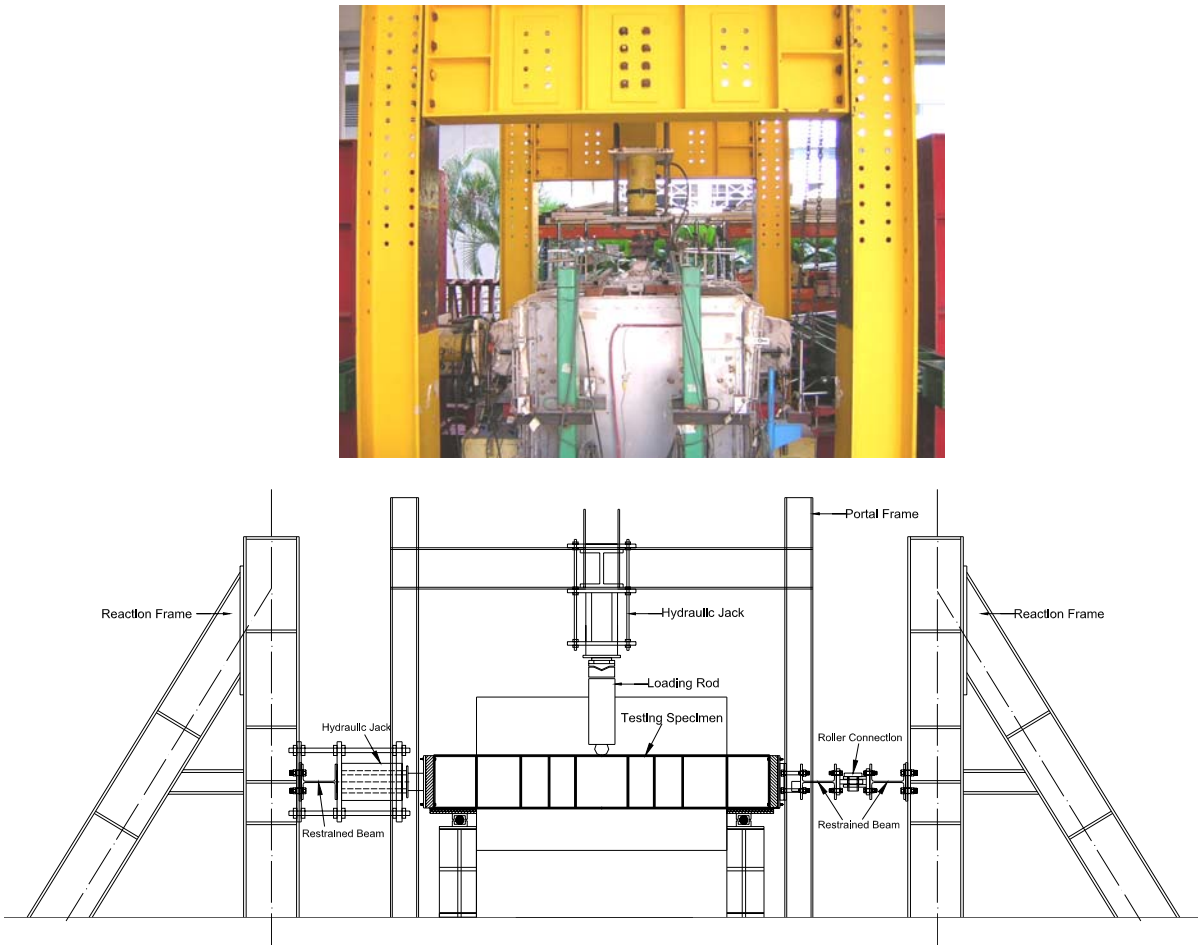

Figure 5.24 Restrained Plate Girder Test Set-up (Elevation View)

5.4.2 Design of Test Specimens

Three series of bare steel plate girders were tested to failure in this part of experimental works, namely, RTG3, RTG4, and RTG5. The web and the flange details of the specimens are included in Table 5.8 and shown in Figure 5.25. Each series consisted of three specimens (i.e. RTG3-1, RTG3-2, RTG3-3 etc.) tested at three respective furnace temperatures, viz. 400, 550 and 670 ^{o}C, with axial restraint stiffness as 9.6 kN/mm. It should be noted that in the specimen nomenclature, the number after the hyphen indicates constant temperature, viz. "1" is for 400 ^{o}C, "2" for 550 ^{o}C and "3" for 670 ^{o}C, respectively. In addition, each series consisted of one additional specimen marked as "4" tested at 670 ^{o}C but with axial restraint stiffness as 8.2 kN/mm. The plate girders configurations are shown in Figure 5.25. The

overall dimensions of all plate girders were identical so that they had a constant panel aspect ratio (b/d). Transverse web panel stiffeners were provided so that the ratio of the spacing between vertical stiffeners to web depth was unity. This value was chosen as it represented a practical design. The same configurations of plate girders have already been tested at elevated temperatures but without thermal restraint effect in the first part of experimental works as described in Section 5.2, that is, TG3, TG4 and TG5 series. The web and the flange plates were welded together through 6 mm longitudinal fillet to ensure adequate shear force transfer between the two component plates. The web slenderness (d/t) ratio was taken as the primary parameter in the investigation, with d/t less than 250 as prescribed in BS5950: Part 1. The three series of plate girders, RTG3, RTG4, and RTG5, represented slender web panels, with web slenderness ratio of 152.5, 112.9, and 203.3, respectively. All test girders had a total length of 1.90m. The span measured from centre-to-centre of the support bearing blocks was 1.66 m.

The purpose of this part of experimental investigation was to study the web panel behaviour due to shear under thermal restraint condition. Therefore, to prevent plastic hinge formation at mid span and flange local buckling, additional cover plates were welded onto the top and bottom flange plates of the test girders at mid-span, as shown in Figure 5.25. The girders were designed such that the end panels would primarily fail in shear. The four panels of a typical specimen were marked as 1, 2, 3, and 4 as shown in Figure 5.25. In RTG3 and RTG4, only panels 1 and 4 were investigated, as the other inner panels were stiffened with additional flange cover plates. In RTG5, the behaviour of inner panels 2 and 3 without cover plates was investigated as well.

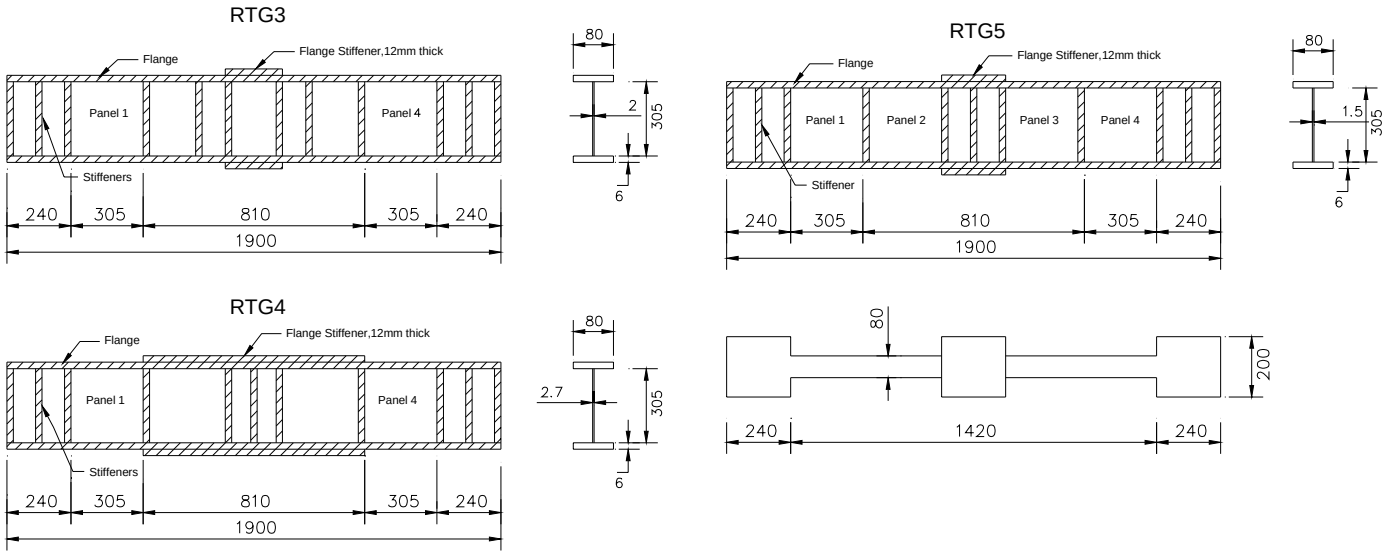

Figure 5.25 Details of Steel Plate Girder Specimen (all dimensions are in mm)

Table 5.8 Details of Restrained Test Specimen Series

Test Series	Web Details							Flange Details			
	b_w (mm)	d_w (mm)	t_w *(mm)*	b_w/d_w	d_w/t_w	Young's Modulus E (MPa)	Yield Stress, f_y (MPa)	b_f *(mm)*	t_f *(mm)*	Young's Modulus E (MPa)	Yield Stress, f_y (MPa)
RTG3	305	305	2	1	152.5	202000	264	80	6	200000	305
RTG4	305	305	2.7	1	112.9	218000	255	80	6	201000	368
RTG5	305	305	1.5	1	203.3	200000	332	80	6	204000	277

5.4.3 Loading Facility and Axial Restrained System

The main loading system used in unrestrained plate girder tests (Figure 5.1) was improved for restrained plate girder tests with additional axial restrained system as shown in Figure 5.24. The restraint system (Figure 5.26) consists of one beam (UC203x203x46kg/m) supported onto two reaction A-frames at each end of the testing specimen. One hydraulic jack was installed onto the mid-span of the right restraint beam to ensure adequate contact between the restraint beam and the specimen. On the left, a restraint beam (UC152x152x37kg/m) was connected with two flexible roller joints. The restraint force induced was monitored by one 300 kN

annular compression load cell at each end of the specimen. The stiffness of the whole restraint system was adjusted by altering the position of roller connections (Figure 5.26). The adjustable restraint stiffness varied between 8 and 10 kN/mm. Therefore, an axial restraint equal to 9.6 kN/mm was first selected at three temperature levels with corresponding restraint ratio $\beta = K_{RS} / K_{B(20^0 C)}$ as 3.8%, 3.5% and 5%. Moreover, in order to investigate influences of various restraint ratios at elevated temperatures, another axial restraint equal to 8.2 kN/mm (restraint ratio as 3.3%, 3.0% and 4.3%) was chosen to vary the different restraint effects at 670 ^{o}C. This was to simulate possible axial restraint provided by adjacent cooler structures.

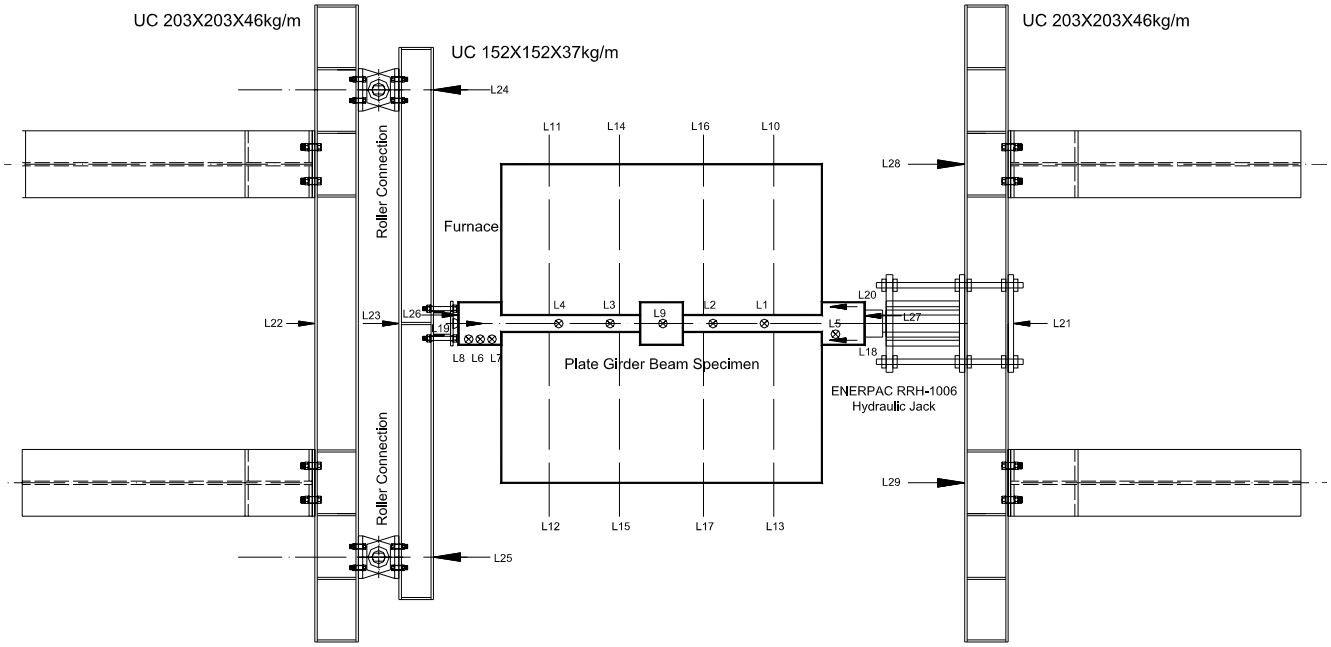

Figure 5.26 Restrained Plate Girder Test Set-up (Plan View)

5.4.4 Heating Facility

Same electrical-heating furnace as unrestrained plate girder tests was used in this part of experimental works. The heating rate was monitored by a separate electrical control panel. The heating rate for the furnace temperature was set to a rate of 7 ^{o}C per minute. The heating procedure consisted of four incremental steps. Between

each step, temperatures of electrical heating modules were kept identical for fifteen minutes to ensure uniform heating within the furnace (say, 100, 200, 300 and 400 ^{o}C for specimen RTG4-1).

5.4.5 Deformation and Temperature Acquisition Instrumentations

The deflection acquisition system (as shown in Figure 5.26) consisted of nine linear variable differential transducers (LVDT1 to LVDT9) to measure the vertical deformations of test panels, mid-span deformations, and support settlements. Ceramic rods were used to transfer vertical deflections from test specimen to LVDTs outside the furnace. In addition, eight line LVDTs (LVDT10 to LVDT17) were used to measure the out-of-vertical-plane deformations at the centre of the web panel to determine if shear buckling has occurred. Line LVDTs were used at the two end panels 1 and 4 for all the test series, except for the RTG5 series where two additional line LVDTs were also introduced at the two inner panels 2 and 3 (Figure 5.25). This was because in the RTG5 series, the inner panels were expected to fail before the end panels as the former were subjected to greater bending moment. Three additional LVDTs (LVDT18 to LVDT20) were placed to measure the horizontal movements of roller supports. To monitor flexural deformation and connection settlements of restraint system, three LVDTs (LVDT 21, 28 and 29) were used to measure the mid-span deformation and two roller connection settlements of the right restraint beam. Similarly, four LVDTs (LVDT22 to LVDT25) were used to monitor the mid-span deformations and the flexible roller joint settlements of the left restraint beams. During testing, temperatures of the plate girder were measured at several locations. Same with unrestrained plate girder tests, thermocouple wires were utilized to monitor temperatures inside test specimens as shown in Figure 5.6. Besides, furnace temperatures were also monitored by four K-type thermocouple wires. All thermocouple wires were connected to Fluke

HYDRA temperature acquisition system and temperatures were recorded at fifteen-second interval.

5.4.6 Restrained Plate Girder Test Procedure

The experimental procedure consisted of three main stages: *1*. Preload the test beam axially; *2*. Heat the plate girder specimen to the desired temperature and maintain a uniform temperature distribution throughout the cross section; *3*. Load the test beam at mid span until failure occurs in the web panel. Initially, a pre-load procedure was repeated to ensure proper contact of the specimen over the roller supports and proper functioning of the deformation acquisition system. Following the initialization of acquisition system, the electrical furnace was heated up to the desired temperature. This caused an increase in the axial force of the specimen due to restraint system. Subsequently, transverse load was applied onto the mid-span of specimen and deformation acquisition system readings were recorded for each load level. Transverse load was applied until the web panel buckled and the test continued with increasing deflection. The girders showed extensive out-of-plane deflection when the load approached failure. Ultimately, the vertical and out-of-plane deflections of beam started to increase rapidly with small load increments indicating impending failure of specimen.

5.5 Restrained Plate Girder Experimental Results

The objective of this part of experimental work is to investigate the effect of axial restraint due to adjacent cooler structures on the shear behaviour of steel plate girder. Material coupon tests were carried out at ambient temperature on the web, flange and stiffener plates. The results of the material yield strength and elastic modulus at ambient temperature are given in Table 5.8. The corresponding material properties at elevated temperatures were based on the Eurocode material reduction

factors for yield strength and elastic modulus (ENV 1993-1-2) as the material testing facility at elevated temperatures was not available at the time of writing.

5.5.1 Plate Girder Ultimate Shear Capacity

From the experiments of twelve plate girders at different temperatures and various restraint axial stiffnesses, the ultimate shear capacity of each girder is listed in Table 5.9. The ultimate shear strengths (V_{analy}) from the analytical predictions are also provided for comparison purpose. These analytical predictions were derived based on improved analytical approach as presented in Section 4.2.3 of Chapter 4. Clearly, analytical V_{ult} and experimental V_{test} agree well, as shown in Column (8) of Table 5.9, with the mean and standard deviation as 1.003, and 0.069, respectively. Finite element predictions of the ultimate shear capacities based on full beam models will be shown and discussed in Section 6.4.

Table 5.9 Experimental Results of Restrained Plate Girder Tests

Test Series	Test Girder	Temperature (°C)	Restraint Ratios β	Axial Force (kN)	V_{test} (kN)	V_{analy} (kN)	V_{test}/V_{analy}
(1)	(2)	(3)	(4)	(5)	(6)	(7)	(8)
RTG3	RTG3-1	400	3.8%	43.41	51.7	53.37	0.969
	RTG3-2	550	3.8%	48.27	26.6	29.64	0.897
	RTG3-3	670	3.8%	61.02	14	14.37	1.072
	RTG3-4	670	3.3%	53.92	15.4	13.29	1.053
RTG4	RTG4-1	400	3.5%	43.81	69.55	70.81	0.982
	RTG4-2	550	3.5%	51.32	28.95	27.24	1.063
	RTG4-3	670	3.5%	62.02	17.55	17.41	1.063
	RTG4-4	670	3.0%	57.78	18.5	16.3	1.077
RTG5	RTG5-1	400	5.0%	39.31	42.55	43.47	0.979
	RTG5-2	550	5.0%	45.59	17.8	20.38	0.873
	RTG5-3	670	5.0%	51.12	10.6	12.48	1.030
	RTG5-4	670	4.3%	49.69	12.85	10.82	0.980
—	—	—	—	—	—	—	1.003[a]
—	—	—	—	—	—	—	0.069[b]

[a] Mean Value [b] Standard Deviation

5.5.2 Temperature Distribution

Figure 5.27 shows typical temperature variations for specimen RTG4-1 versus heating time of electrical furnace, top and bottom flange temperatures and mid-depth web temperatures during the ramping up of temperature to 400 ^{o}C. The bottom flange and web showed little discrepancy in the temperature distribution. Due to imperfect thermal insulation effect of top cover panels, the top flange temperature rose much more slowly compared to the rest of the cross section. The temperature difference between the web and the top flange increased to approximately 50 ^{o}C after 4000 seconds. However, due to uniform heating within the electrical heating furnace, the temperature difference between the top flange and the rest of the section was reduced to as little as 20 ^{o}C when the web and bottom flange temperatures reached the desired temperature of 400 ^{o}C after 6000 seconds. As the test panels were located near the beam ends which were not directly exposed to the heating coil in the furnace, there was a temperature gradient in the longitudinal direction. Figure 5.28 shows the temperatures of the test panels near the beam ends were about 15% lower than the corresponding temperatures of inner panels. However, a separate numerical simulation on the effect of longitudinal temperature variation showed that the panel shear capacity was not so sensitive to the recorded longitudinal and cross-sectional temperature gradient.

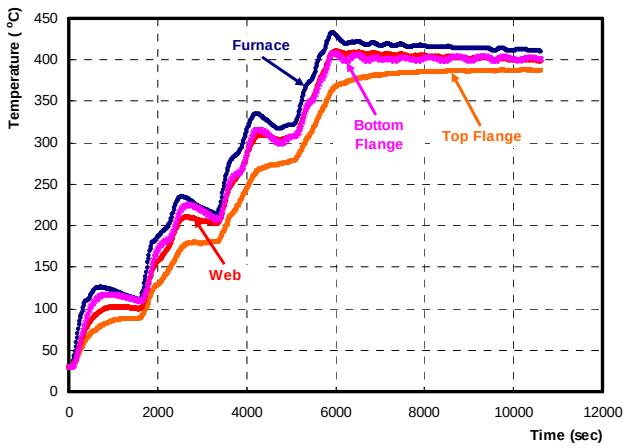

Figure 5.27 Typical Temperature Distribution for RTG4-1

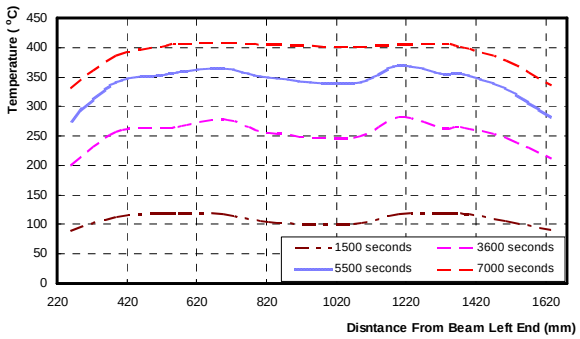

Figure 5.28 Typical Longitudinal Temperature Distribution at Top Flange of RTG5-1

5.5.3 Deflection Characteristics

The plate girder web slenderness ratios (as shown in Table 5.8) were greater than the 63ε limit for slender sections as defined in BS5950 Part 1, in which $\varepsilon = (275/\sigma_y)^{1/2}$, and σ_y is the material yield strength. These sections are defined by the BS5950 Part 1 as slender sections where local buckling governs instead of material yielding. Therefore, in the current tests, line LVDTs 10 to 17 (Figure 5.26) were installed to monitor the web buckling in the test panels. As a typical example, shear failure can be observed from a sudden increase in out-of-plane deflection as shown in Figure 5.29 (a) for web panel 4 of RTG4-4 tested at 670 ^{o}C. The out-of-plane deflection increased up to approximately 85% of the ultimate failure load and then web panel 4 showed a large out-of-plane deflection increase with a minor increase in load above this value.

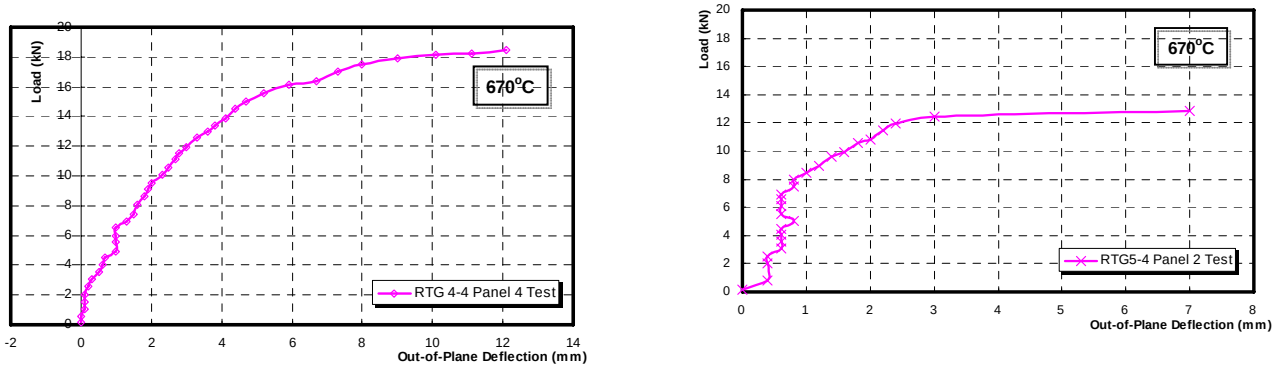

Figure 5.29 Load versus Out-of-Plane Deflection Characteristics

For RTG3 and RTG4, end web panels 1 and 4 buckled and failed primarily due to a combination of compression and shear forces. However, for RTG5, since there were no flange cover plates for inner web panels 2 and 3, the inner panels buckled earlier than end web panels 1 and 4. Out-of-plane web deformation results for RTG5-4 panel 2 are plotted in Figure 5.29(b). Clearly, it can be noticed that at the initial loading stage the panel remained relatively straight in the elastic range. After the transverse load reached approximately 12 kN, the out-of-plane web deformation started to increase rapidly with load. This can be taken as the web panel buckling load. Figure 5.30 (a), (b), and (c) shows the tensile membrane failure mode of web panels for RTG4 series. It can be seen that plastic hinges formed in the corners of web panels and in the flanges due to mobilization of tensile field action. However, at high temperature level, the web panel tensile membrane failure mode seemed indistinctive. This is because at higher temperature, the Eurocode material stress-strain curve (Eurocode 3 Part 1.2) does not have a clear demarcation point between the elastic and the inelastic curves. Thus, the experimental buckled pattern is not very distinctive at high temperature.

(a) Deformed shape for RTG4-1 tested at 400 °C

(b) Deformed shape for RTG4-2 tested at 550 °C

(c) Deformed shape for RTG4-3 tested at 670 ^{o}C

Figure 5.30 Deformed Shape for RTG4 Series

Figure 5.31 (a), (b), (c) and (d) show the mid-span vertical deflection measured by LVDT9 for different test series and restraint levels. As shown in Figure 5.31 (a), the load-deflection curve of RTG4-1 clearly consisted of three stages. For stage 1, plate girders bent upwards at the beginning of loading due to preheating to the specified isothermal temperature. When transverse load was applied in stage 2, the beam deflected downwards under increasing transverse load. However, due to the presence of induced compression force from stage 1, the mid-span vertical deflection response was not linear. This nonlinear effect was most pronounced in the most slender web panels, i.e. RTG5 series. At stage 3, the mid-span deflection increased markedly when web panels 1 and 4 buckled under tensile membrane actions, causing a reduction in beam stiffness. Moreover, the gradient of the load-deflection curve in Figure 5.31 , that is, the beam stiffness, is clearly dependent on web slenderness. With greater slenderness, the beam stiffness becomes smaller. It can also be seen that at high temperature, both the beam stiffness and the ultimate shear strength reduced. The three curves in Figure 5.31 (b) are similar in the elastic stage as well as in the post-elastic stage. The mid-span deflection of RTG3-2 was linear up to the web shear buckling load (approximately 20 kN) and then it became nonlinear subsequently. The ultimate load was 26.6 kN with corresponding deflection of approximately 15 mm. A similar behaviour was observed in Figure 5.31 (a), (c) and (d). The mid-span deflection of RTG4-4 was not available due to malfunctioning of LVDT9 during the loading stage.

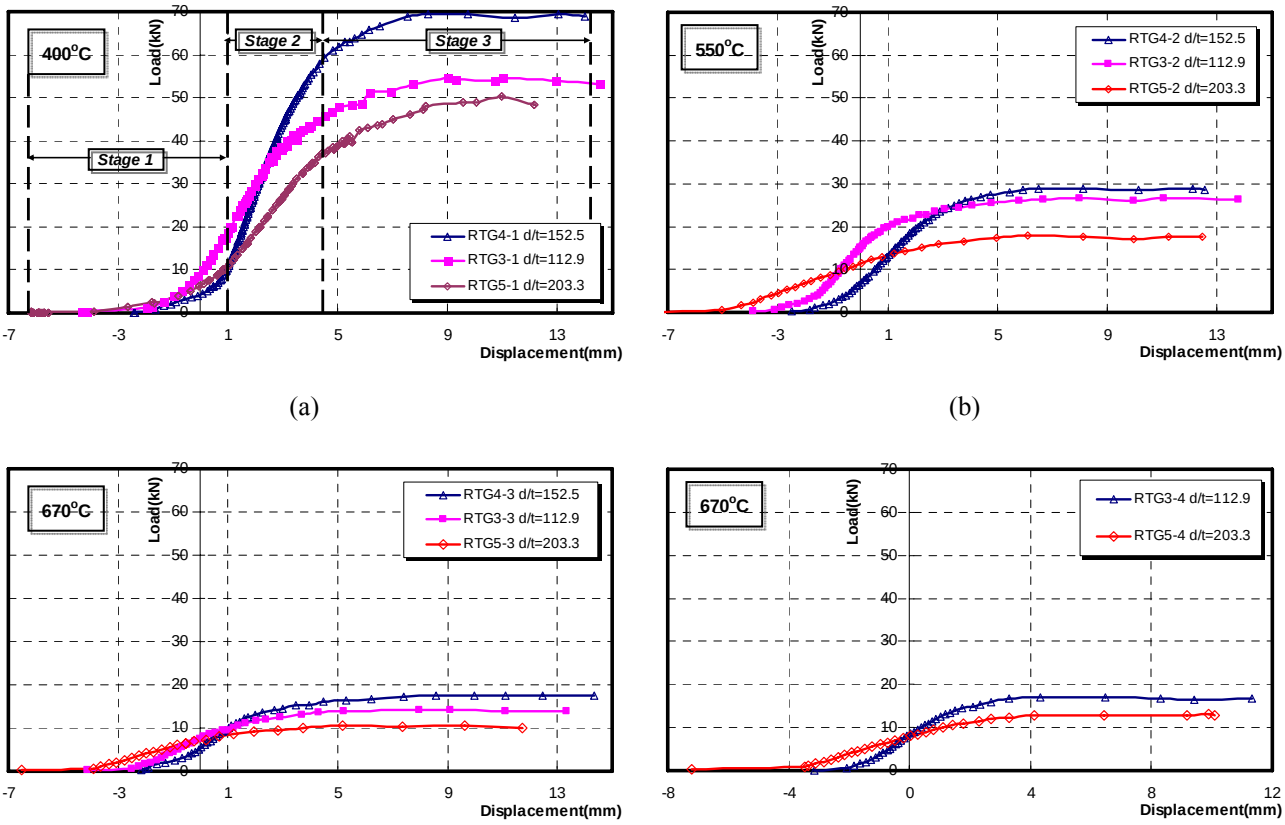

Figure 5.31 Load versus Deflection (mid-span) Characteristics

5.5.4 Effect of Axial Restraints

During heating-up stage, axial compressive force developed when thermal expansions of heated specimens were resisted by adjacent restraint beam systems. Figure 5.32 show the increase of axial compressive force versus web panel central temperatures. As shown in Figure 5.32, it is observed that three specimens (RTG3-1, RTG4-1 and RTG5-1) developed similar axial compressive force with increasing gradients, indicating the three specimens had similar rates of thermal expansion. In addition, due to four incremental temperature steps discussed in Section 5.5.2, the increase of axial compressive force was not completely linear (compare Figure 5.27 heating scheme with development of compressive force in Figure 5.32). The variations of maximum compressive force were mainly due to the variations of

section geometry. For thermal restraint stiffness of 9.6 kN/mm, the induced compressive force in RTG4 plate girder increased approximately to 21% when heated from 550 ^{o}C to 670 ^{o}C. This observation is in line with increasing temperature and consequent deterioration of axial stiffness of test specimens.

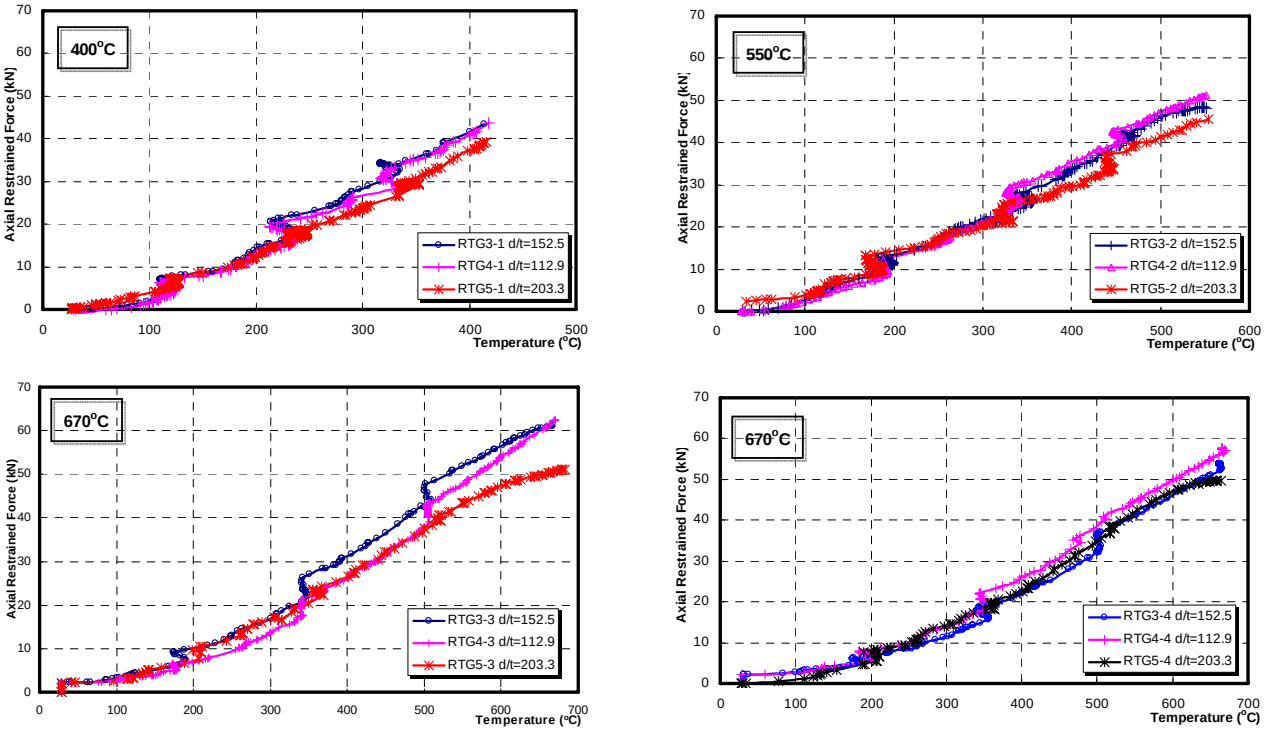

Figure 5.32 Axial Restraint Force Development

A comparison of shear strength V_{test} to maximum shear strength V_{yw} ($=\tau_{yw}d_w t_w = \sigma_{yw}d_w t_w/\sqrt{3}$) is plotted in Figure 5.33 (a), (b) and (c). Since RTG3, RTG4 and RTG5 series have the same configurations with TG3, TG4 and TG5 series tested in the first part of experimental works, the corresponding test shear strength ratios (V_{test}/V_{yw}) are also plotted. In addition, the respective reduction factor of yield strength $\left(k_{x(T)}\right)$ and elastic modulus $\left(k_{E(T)}\right)$ at elevated temperatures according to Eurocode 3 part 1.2 are also shown in Figure 5.32. Clearly, with increasing temperature the test shear strength ratio V_{test}/V_{yw} reduces, following the general trend of degradation of steel material properties. Since RTG5

has the greatest web slenderness ratio (d_w / t_w) compared to RTG3 and RTG4, the ultimate shear resistance ratio is the least at elevated temperatures. Besides, it was also noticed that the shear capacity ratio of restrained plate girders (V_{test}/V_{yw}) reduces compared to unrestrained plate girders. For RTG3, RTG4 and RTG5 series tested at 400 ^{o}C, the shear capacity ratio V_{test}/V_{yw} reduces to 83%, 82% and 90% in comparison with TG3, TG4 and TG5 series test observations. It was also noticed that the greater the d_w / t_w ratio, the greater is the reduction of V_{test}/V_{yw} of restrained girders compared to unrestrained test results.

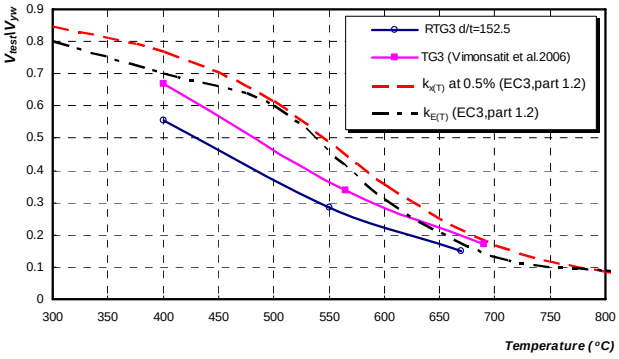

(a)

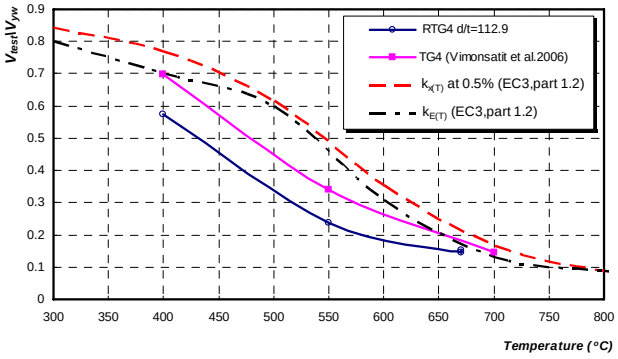

(b)

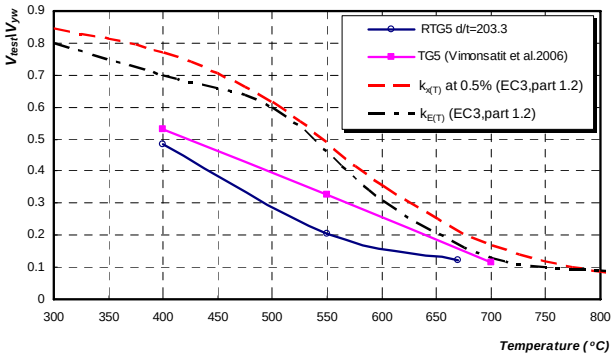

(c)

Figure 5.33 Panel Shear Strength Ratios for RTG3, RTG4 and RTG5 Series

As listed in Table 5.9, each test series consisted of two specimens tested at 670 ^{o}C with two different restraint stiffnesses (9.6 kN/mm and 8.2 kN/mm), through which, the effects of various thermal restraints were investigated at isothermal condition. A

comparison of shear strength ratios (V_{test}/V_{yw}) between two restraint stiffnesses at 670 ^{o}C is plotted in Figure 5.34. For RTG4, RTG3 and RTG5 series, the shear capacity ratio (V_{test}/V_{yw}) with restraint stiffness of 9.6 kN/mm reduces to 95%, 91% and 82% in comparison with restraint stiffness of 8.2 kN/mm. From Figure 5.34, it can be observed that, with higher web slenderness ratio (d_w/t_w), the influence of thermal restraint on the reduction of shear capacity ratio (V_{test}/V_{yw}) is more significant.

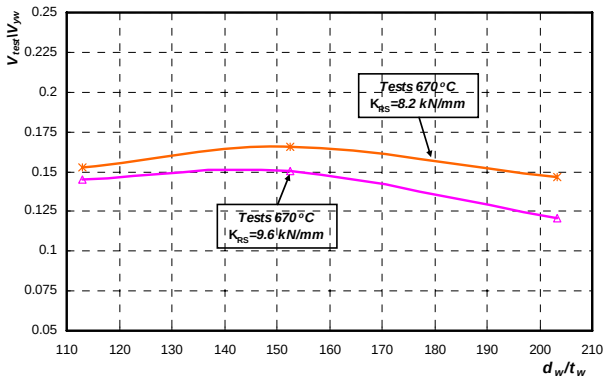

Figure 5.34 Panel Shear Strength Ratios for axial restraint 8.2 kN/mm and 9.6 kN/mm at 670 ^{o}C

5.6 Deflection Characteristics and Analytical Predictions

As described in Section 4.2, a simplified mechanical model has been introduced to predict the shear buckling and ultimate strength of web plates at elevated temperatures based on plate girder theory. In this model, a uniform shear force is applied to the web. This stress state will continue to increase until the applied shear stress reaches the critical shear stress of web panel plate. Once the critical shear stress is reached, the web out-of-plane deflection starts to increase. Additional shear force is resisted by the mobilization of tensile membrane stress in the diagonal band of the web. Failure of plate girder occurs when plastic hinges are formed in the top and bottom flanges bounding the buckled web panel. These hinges together with the diagonal yield zone form a plastic mechanism. In addition, to obtain a mechanical description of beam web panel behaviour under shear, analytical equations have

been developed for modelling out-of-plane and in-plane deflections of web panel as described in Section 4.3 and 4.4 of Chapter 4. Combining these two analytical approaches, relationships between shear force and panel centre out-of-plane, panel in-plane deflections can be predicted analytically. As typical examples, experimental out-of-plane measurements versus analytical predictions are presented in Figure 5.35 for TG3-3, TG4-4, RTG3-2 and RTG4-4, respectively. It can be noticed that the second-order linear elastic theory slightly underestimate actual out-of-plane deflections, since the mechanical model neglects influences from top and bottom flanges. However, this model still gives acceptable agreement with test measurements.

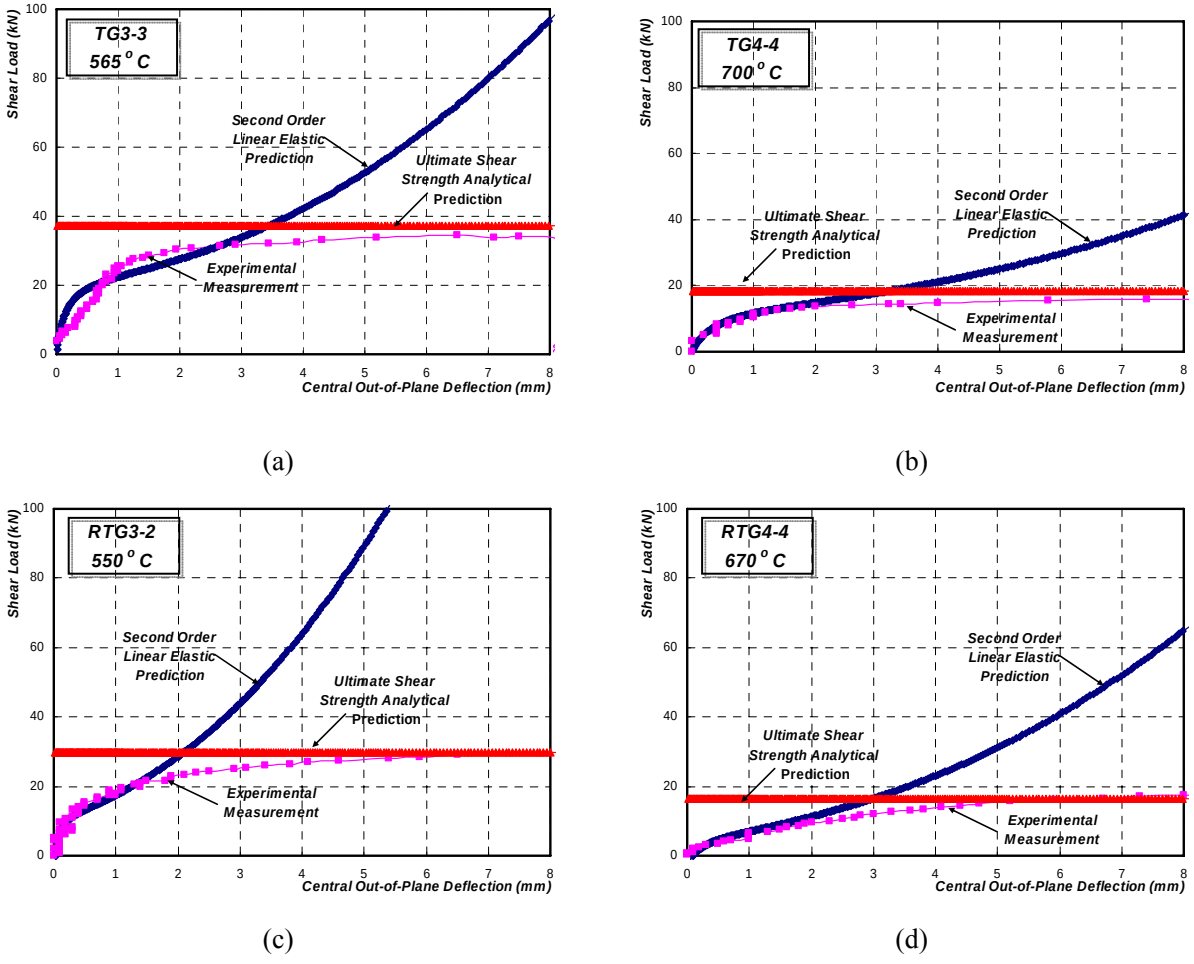

Figure 5.35 Out-of-Plane Deflection Characteristics Comparisons between Experimental and Analytical Predictions

Examples of experimental in-plane deflection measurements, or vertical deflections, will also been compared with analytical predictions and numerical simulations. The comparisons will be presented in Section 6.3. To avoid the effects of non-uniform temperature distribution, numerical simulations are performed on unrestrained plate girders at ambient temperature, viz. specimens TG3-1, TG4-1 and TG5-1. Comparisons among analytical approach, numerical simulations and test measurements are shown in Figure 5.36(a), (b) and (c).

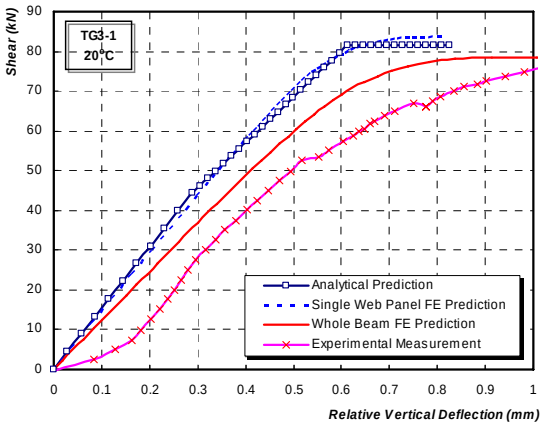

(a)

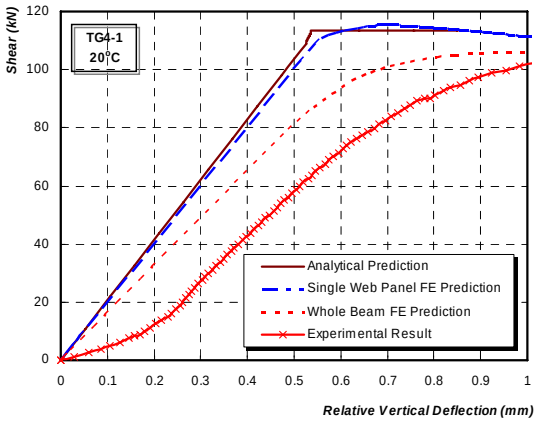

(b)

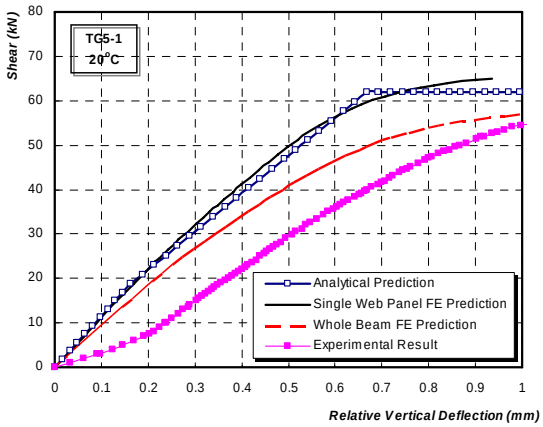

(c)

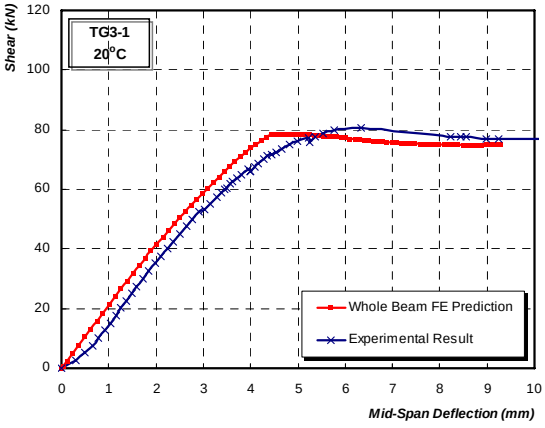

(d)

Figure 5.36 In-Plane Deflection Characteristics Comparisons among Analytical Prediction, Experimental Measurements and Numerical Predictions

Numerical simulations in these comparisons consisted of two parts, as single web panel and whole beam simulations. For single web panel models, only buckled web panels (viz. Panel 1 or 4 for TG3 and TG4 series) have been simulated. Finite element simulations of entire plate girders are described in Section 6.2.2. From comparisons, it is shown that analytical load-deflection predictions are in good agreement with single web panel FE predictions. However, there are clearly discrepancies with experimental measurements and whole beam FE predictions. As discussed in Section 4.4, this analytical approach only considers the web plate subjected to shear or combined shear and compression forces. Web panels of test specimens and FE simulations were subjected to not only dominant shear force but also bending moment effects. Therefore, these analytical predictions somewhat underestimate experimental in-plane deflections. However, as shown in Figure 5.36(d), typical comparison for TG3-1 mid-span vertical deflection between FE predictions and experimental measurements, shows that the whole beam FE simulation shows acceptable capability to predict test specimen deflections. These comparisons will be discussed in Section 6.3. It is also noticed that there is minor difference between the analytical predictions of beam web stiffnesses during pre- and post-buckling stages for such slender beam sections, which is also in accord with numerical predictions.

5.7 Conclusion

In order to verify the proposed analytical models, an experimental program has been carried out on universal column sections and plate girder to investigate the shear behaviour with different web slenderness ratios (d/t) at four isothermal conditions. It is concluded from this experimental investigation that the pure web panel shear yielding can be observed from universal column sections with a much smaller web slenderness ratio at both ambient and elevated temperatures. For slender beam sections, web tension field action (TFA) can be observed under a

relatively smaller shear force. The shear strength of plate girder section reduces significantly with increasing temperature. At certain temperature, the more stocky sections have a higher shear capacity. Moreover, for specimens tested at higher isothermal condition, the shear buckling failure behaviour becomes less apparent due to highly nonlinear mechanical properties of steel material at high temperatures. In addition to unrestrained tests, another series of experimental study has been carried out on plate girders subjected to predominant shear loading at elevated temperatures with thermal axial restraints. From experimental observations, it can be concluded that thermal restraints weaken the ultimate shear capacity of web panels. This influence is more significant at higher thermal restraint, and for web plates with higher slenderness(d_w / t_w). The detailed experimental results for unrestrained and restrained beams will be further compared with analytical and finite element predictions in Chapter 6.

CHAPTER 6

FINITE ELEMENT ANALYSIS OF SHEAR ZONE WITHIN STEEL BEAM-TO-COLUMN JOINT

6.1 Introduction

Mechanical behaviour of steel joint presents complex characteristics even at ambient temperature. At elevated temperatures, this behaviour is much more complicated, with degradation of steel material properties, thermal restraint force, and interaction among different components of steel joint. To obtain an insight of this problem, finite element analysis (FEA) have been used to model various components within steel joint and overall joint behaviour by many researchers as described in Section 2.3. Finite element analysis (FEA), if applied properly, can lead to accurate results, with considerations of complex interactions among various joint components, bolt action, boundary and contact conditions. Therefore, joint modelling by finite element method can save cost and time against actual tests especially for different types of joints. However, finite element model should be validated by test results so that limitations of using FEA can be well addressed, before they can be used for different types of joints.

This chapter presents a FEA for studying behaviour of shear component of a steel joint under elevated temperatures. The FEA was performed by considering the steel joint shear component as an isolated plate girder web panel, in short, web panel. In addition, an entire finite element (FE) model of the plate girder was also developed to simulate the overall behaviour of the beam and to compare it with experimental

results. For the isolated web panel model, the analysis consists of different types of boundary conditions, i.e., thermally unrestrained and restrained conditions. The objectives of this chapter are:

- To construct a simplified FE model for steel joint shear component using a commercial FEA software MSC.Marc Mentat (MSC, 2001);
- To investigate the behaviour of shear component at ambient and elevated temperatures with unrestrained boundary conditions;
- To incorporate thermally restrained boundary condition into the FE model, and subsequently, to investigate the behaviour of shear component under thermal restraint condition;
- To construct a whole beam model and to compare overall behaviour with experimental observations.

In Section 6.2, a brief review on the FE modelling of web panel is given. The model developed to study the behavior of web panel at ambient and elevated temperatures will be presented. An entire FE simulation to study the behaviour of test girders will be described in Section 6.3. The results of FEA will be presented and compared with experimental results and analytical predictions in Section 6.4. Finally, the conclusions will be made in Section 6.5.

6.2 Finite Element Analysis Models

In this study, FEA was performed using a commercial FE software MSC.Marc Mentat (MSC, 2001) to study the behaviour of shear component in the steel beam-to-column joint at both ambient and elevated temperatures. The simplified model is shown in Figure 6.1, which consists of one web panel, top and bottom flanges.

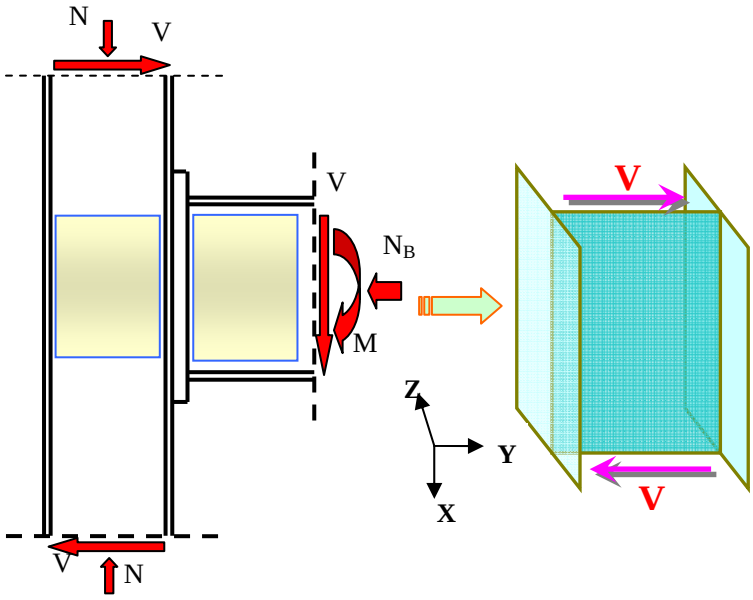

Figure 6.1Simplified FE model of Shear Components of Steel Joint

A quadratic thick shell element (element type 22 in MSC.Marc Mentat Element Library) was used for both web and flanges of shear component. This selected element is an eight-node quadrilateral thick shell element with global displacements and rotations in X, Y and Z directions as degrees of freedom. In current FE, the second-order interpolation is used for coordinates, displacements and rotations. The membrane strains are obtained from strain field and curvatures from rotation field.

In the first part of FE investigation, the FE analysis consisted of two batches, namely, G series and TG series, in which, G series (G1, G2, G3, G4 and G5 series) consisted of G1, G4 and G5 series which had been tested by Rockey *et al.* (1972), Sakai *et al.* (1966) at ambient temperature, and G2 and G3 series which had been tested at both ambient and elevated temperatures by Vimonsatit *et al.* (2005). On the other hand, TG series (TG1, TG2, TG3, TG4 and TG5 series) consisted of test girders, as described in Section 5.2. For each series, ambient (20 ^{o}C) and elevated temperature tests (400, 550 and 700 ^{o}C) were conducted. For example, TG1-1, TG1-2, TG1-3 and TG1-4 represent specimens tested at ambient temperature, 400,

550 and 700 ^{o}C, respectively. Both G and TG series of specimens have been simulated with isolated web panel model and whole beam model. The FE predictions will be compared with experimental results and analytical predictions in Section 6.4. In the second part of FE simulations, the FE analysis consisted of three series, namely, RTG3, RTG4 and RTG5 series. Each series consisted of three specimens (i.e. RTG3-1, RTG3-2, RTG3-3 etc.) tested at three respective furnace temperatures, viz. 400, 550 and 670 ^{o}C, with axial restraint stiffness as 9.6 kN/mm. It should be noted that in the specimen nomenclature, the number after the hyphen indicates constant temperature, viz. "1" is for 400 ^{o}C, "2" for 550 ^{o}C and "3" for 670 ^{o}C, respectively. In addition, each series consisted of one additional specimen marked as "4" tested at 670 ^{o}C but with axial restraint stiffness as 8.2 kN/mm. These three series have been simulated with whole beam model with axial restraint forces. The geometric and material properties of isolated web panel models are listed in Table 6. 1.

Due to complex behaviour of steel at ambient and elevated temperatures, the present study dealt with steel material and geometric nonlinearity problems. Material nonlinearity occurs because this study takes into account plasticity problem. The stress-strain curves for steel material properties at ambient temperature were determined from the experimental data. It can be simplified for the purpose of numerical modelling. At elevated temperature, steel stress-strain characteristics become highly nonlinear compared with that at ambient temperature. Therefore, trilinear-elliptic stress-strain model for steel at elevated temperatures as specified in EC3: Part 1.2 (ENV 1993-1-2) has been utilized in current numerical simulations. Also current finite element programme is capable of simulating real steel mechanical behaviour according to stress-strain characteristics of steel, rather than simplified bi-linear steel stress-strain relationship as used in current analytical predictions as described in Section 5.3.4.

Table 6. 1 Geometric and Material Properties of Isolated Web Panel Models

Model	Geometric Properties						Material Properties (N/mm^2)		References
	t (mm)	b (mm)	d (mm)	B (mm)	T (mm)	A (mm^2)	σ_{yw}	σ_{yf}	
G1	0.965	304.8	304.8	76.2	5	1056	224	289	Rockey *et al.* (1972)
G2	2	305	305	80	6	1570	248	275	Vimonsatit *et al.* (2005)
G3	1.22	305	305	80	6	1332	248	275	Vimonsatit *et al.* (2005)
G4	8	687	560	250	30	19480	432	412	Sakai *et al.* (1966)
G5	8	2000	720	250	30	20760	432	412	Sakai *et al.* (1966)
TG1	6.1	139	139	152.4	6.8	2921	342	359	Chapter 5 of this Thesis
TG2	8	181	181	203.9	12.5	6546	332	325	Chapter 5 of this Thesis
TG3	2	305	305	80	6	1570	288	275	Chapter 5 of this Thesis
TG4	2.7	305	305	80	6	1784	233	277	Chapter 5 of this Thesis
TG5	1.5	305	305	80	6	1418	332	277	Chapter 5 of this Thesis
RTG3	2	305	305	80	6	1570	264	305	Chapter 5 of this Thesis
RTG4	2.7	305	305	80	6	1784	255	368	Chapter 5 of this Thesis
RTG5	1.5	305	305	80	6	1418	332	277	Chapter 5 of this Thesis

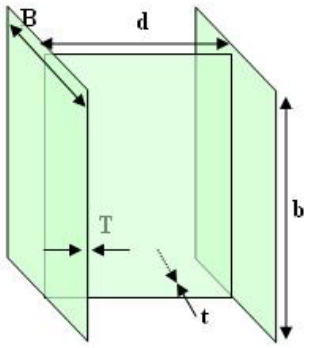

d = Clear depth of web plate between flanges;

b = Clear width of the web plate ;

t = Thickness of the web;

T = Thickness of the flange;

B = Flange width.

Geometric nonlinearity considerations are neither large displacement, small strain, nor large displacement, large strain problem. MSC.Marc Mentat provides procedures for a geometric nonlinearity analysis (MSC, 2001), viz. Lagrangian

Formulation, Eulerian Formulation, and Arbitrary Eulerian-Lagrangian (AEL) Formulation. The analysis procedure incorporated small strain, large displacement and updated Lagrange approach. The large displacement and small strain option allows the programme to take into account the effect of geometric nonlinearity. The updated Lagrange approach was chosen instead of total Lagrange formulation because the former is more economical for the plasticity problem. The solution procedure selected for the present study is a full Newton-Raphson method. This method provides good convergence for most non-linear problems.

6.2.1 Unrestrained Plate Girder Single Web Panel Model

In the present study, shear component of steel joint has been analyzed with FE method at ambient temperature (20 ^{o}C) and elevated temperatures (400, 550 and 700 ^{o}C). The FE model used in this section is one web panel between two adjacent flanges. The detailed FE model and associated boundary conditions are shown in Figure 6.2 and Table 6.2. Current study focused on the steady-state temperature test, the reason being that the electrical heating furnace was not suitable of providing rapid heating rate that is representative in standard fire test. The analysis was carried out in two stages. The first was heating stage, followed by loading stage. Different boundary conditions were used in these two stages. In the heating stage, the edges of right-hand side web panel, top and bottom flanges were free to expand in the horizontal direction (as shown in Figure 6.2). Moreover, degrees of freedom in the Y-direction were allowed for left and the right edges of top flange and web panel to simulate 3D thermal expansion. Nodal temperatures were applied to all nodes of model and increased gradually from 20°C to the desired temperature.

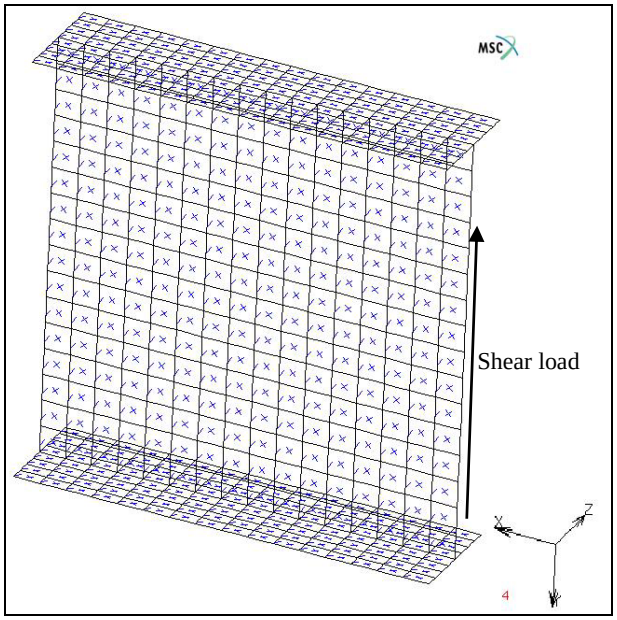

Figure 6.2 FE Model for Unrestrained Shear Component

The second stage simulated the loading process. Shear loading was applied as uniform load along the right edge of web panel (Figure 6.2). Nodal temperatures were maintained at the final temperature specified in the heating stage. During the loading stage, the left edges of web panel (LW), and top (LTF) and bottom (LBF) flanges were assumed to be rigid, allowing only the out-of-plane rotation to facilitate web panel buckling. The right edges of web panel (RW), top (RTF) and bottom (RBF) flanges were fixed in the X and Z-directions, but free to move in the Y-direction to simulate roller-support conditions. The analyses were carried out at three different temperatures, viz. 400, 550, and 700°C, respectively. The corresponding ambient temperature FEA was conducted with same models in which nodal temperatures of FE models were set as constant as 20°C through heating stage. The detailed boundary conditions are listed in Table 6.2. To account for material degradation of steel at elevated temperatures, steel stress-strain-temperature characteristics as specified in EC3 part 1.2 (ENV 1993-1-2) has been adopted in current numerical simulations. The coefficient of thermal expansion (α_T) of steel

was assumed to be independent of temperature and set as 1.4×10^{-5} according to EC3 part 1.2 (ENV 1993-1-2).

Table 6.2 shows boundary conditions applied to all edges of the web panel. In this Table, 1 and 0 represent fixed and free conditions. The left edges of top (LTF) and bottom (LBF) flanges were arranged to remain straight during loading. However, the right edges of the top (RTF) and bottom flanges (RBF) were free along the shear-loading direction (or Y-direction). The left (LW) and right (RW) edges of web panel were allowed to have out-of-plane rotation (θ_y) to facilitate out-of-plane buckling in the web, while the edges of top and bottom flanges were restricted from any rotations as top and bottom flange edges were assumed to be rigid. Shear load was applied as a uniform distributed load along the right web edge in the Y-direction. During loading, the load would be increased gradually from zero to the estimated failure load with constant increment.

Table 6.2 Boundary Conditions for Unrestrained Plate Girder Model

Phase	Edges	x	y	z	θ_x	θ_y	θ_z
Heating Stage	Left Top Flange (LTF)	1	0	1	1	1	1
	Left Bottom Flange (LBF)	1	1	1	1	1	1
	Left Web (LW)	1	0	1	1	1	1
	Right Top Flange (LTF)	0	0	1	1	1	1
	Right Bottom Flange (LBF)	0	1	1	1	1	1
	Right Web (LW)	0	0	1	1	1	1
Loading Stage	Left Top Flange (LTF)	1	1	1	1	1	1
	Left Bottom Flange (LBF)	1	1	1	1	1	1
	Left Web (LW)	1	1	1	1	0	1
	Right Top Flange (LTF)	1	0	1	1	1	1
	Right Bottom Flange (LBF)	1	0	1	1	1	1
	Right Web (LW)	1	0	1	1	0	1

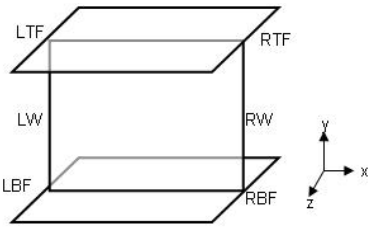

Note: x, y and z are translations; θ_x, θ_y and θ_z are rotations in the x, y and z directions, respectively. 0 denotes free and 1 denotes restraint DOF.

Since the out-of-plane buckling deformation will not occur in perfectly flat plates under the in-plane loading condition of web, a small initial out-of-plane deformation of D/3000 was introduced, where D is the full depth of the web panel. This value is much smaller than the permitted initial out-of-flatness of D/120 in the ANSI/AASHTO/AWS D1.5-96 Bridge Welding Code (AASHTO, 1996). The shapes of initial deformations were based on predicted buckling shapes. In order to study effects of different initial imperfections on the shear capacity of web panel, three different initial imperfections as D/1000, D/1500 and D/3000 were considered on TG4-1 specimen at ambient temperature (20 ^{o}C). The out-of-plane deflection

developments at centre point of TG4-1 web panel for three different imperfections are plotted in Figure 6.3 against shear load. It can be observed that these three initial out-of-plane deformations had insignificant effect on ultimate shear strength. Since investigated web panel is assumed to be perfectly flat in the mechanical modelling, the initial out-of-plane deformation of *D*/3000 was adopted in this FE analysis for both G series and TG series.

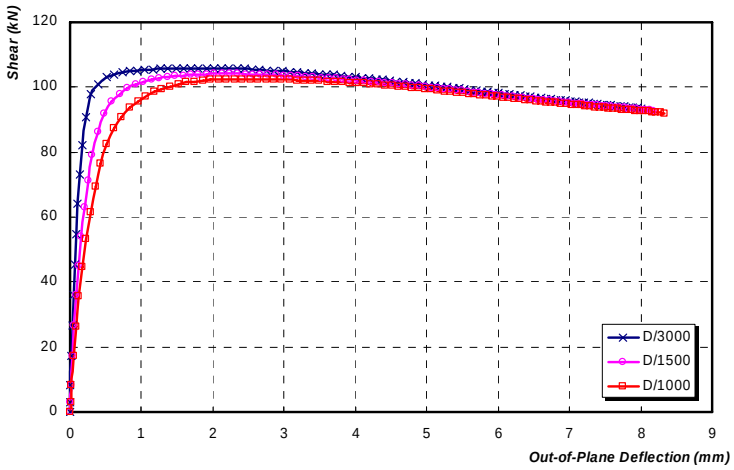

Figure 6.3 TG4-1 Load versus Out-of-Plane Deflection with Different initial Out-of-Plane Deflection

Preliminary finite element analyses on single web panels have been conducted to investigate FE mesh sensitivity. This finite element model consists of one web panel and adjoining flanges. The quadratic thick shell element (element type 22 in MSC.Marc Mentat Element Library) was used for both the web and the flanges, with different mesh sizes for discretization of web panel (6x6, 8x8, 10x10, 12x12, 16x16, 20x20 elements for the entire web panel area). Comparisons among different mesh sizes are shown in Figure 6. 4. This finite element model represents a plate girder subjected to predominant shear (without thermal restraints) at normal temperature, with the same material and geometrical characteristics as RTG3 series, as described in Section 5.4.2.

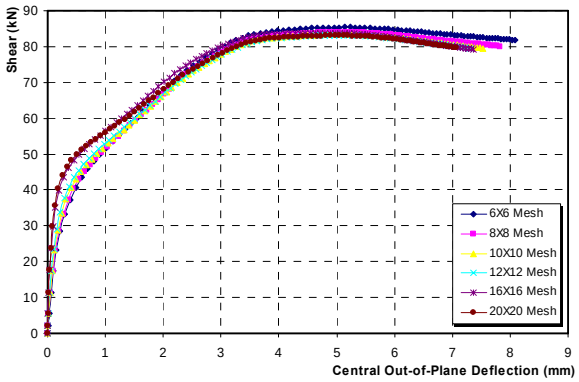

Figure 6. 4 Load vs. Central Out-of-Plane Deflection for Different Meshes

As shown in Figure 6. 4, it is obvious that the ultimate shear capacity predictions are not so sensitive to the selected mesh sizes. In addition, failure modes from each finite element model showed the same buckling behaviour. Initially, it was decided to utilized 16x16 mesh size to represent the web plate of a single web panel. However, to save computational time, a 6x6 mesh size has been adopted for the web plate.

6.2.2 Unrestrained and Restrained Whole Beam FE Model

In this research, shear component of steel beam-to-column joint was simplified into an equivalent girder web panel subjected to shear stress as shown in Figure 6.1. Five series of specimens (TG1, TG2, TG3, TG4 and TG5) have been tested at different temperatures as described in Section 5.2 without thermal restraint effects. In addition, three more series of specimens (RTG3, RTG4 and RTG5) were tested at three temperature levels with thermal restraint effects. The vertical and out-of-plane deflections of specimens were measured by LVDTs during the heating and loading stages. Therefore, it is necessary to construct whole beam model to simulate mechanical behaviour of test specimens at elevated temperatures. Similar to single web panel model, QUAD8 3D thick shell elements (element 22) were used for web, flanges, and stiffeners. Initial out-of-plane deformation of D/3000 was

applied to each of the web panels. Nodal temperatures of 20°C were applied as initial condition. The geometrical properties are shown in Section 5.2.

In accord with FE modelling for single web panel described in Section 6.2.1, the whole beam simulations were also carried in two stages. The first stage represented the heating stage. Temperatures of different parts of beams were increased linearly to recorded measurements by thermocouples during tests. The longitudinal temperature distribution along the beam model was simply set according to thermocouple measurements. Since temperatures at different sections were set to thermocouple measurements approximately, temperature distributions of FE models bear slight differences compared with actual temperature distributions. However, for ambient temperature simulation, the nodal temperature of specimen was maintained at 20°C. For thermally restrained whole beam models, restraint axial forces were increased linearly up till the measured maximum axial force. The second stage represented the loading stage. The load was incrementally applied at mid-span until failure occurred. The boundary conditions for these two load cases are listed in Table 6.3.During the heating stage, the edge of left bottom flange (LBF) was assumed fixed. However, the edge of right bottom flange (RBF) was set to free and thermal elongation was allowed along the X-direction. The edges of left (LW) and right (RW) end web panels were fixed in the Z-direction displacement to avoid the out-of-plane deflection occurring during heating. Temperature increment was applied to all the nodes of web panel, top and bottom flanges. It was increased from ambient (20 ^{o}C) to a specified elevated temperature.

Table 6.3 Boundary Conditions for Whole Beam FE model

Phase	Edges	x	y	z	θ_x	θ_y	θ_z
Heating	LBF	1	1	1	0	0	0
	LW	0	0	1	0	0	0
	RBF	0	1	1	0	0	0
	RW	0	0	1	0	0	0
Loading	LBF	1	1	1	0	0	0
	LW	0	0	1	0	0	0
	RBF	0	1	1	0	0	0
	RW	0	0	1	0	0	0

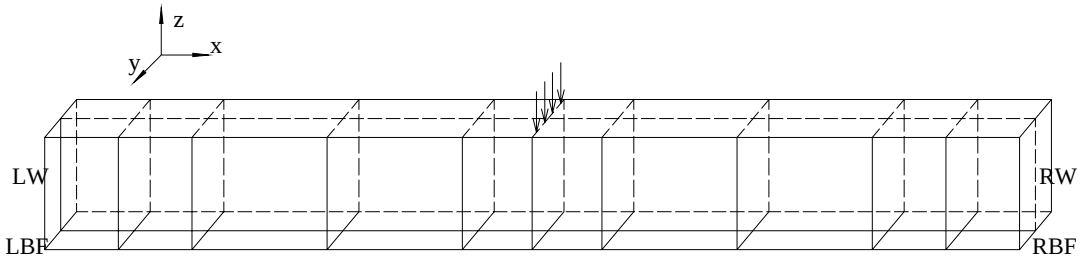

Note: x, y and z are translations; θ_x, θ_y and θ_z are rotations in the x, y and z directions, respectively. 0 denotes free and 1 denotes restraint DOF.

6.3 Finite Element Analysis Results

In general, FEA results of thermally unrestrained case showed that web panel behaviour at elevated temperatures was similar with that at ambient temperature. However, for thermally restrained boundary case, there was non-uniform stress distribution in the web panel at the end of heating. This caused the panel to buckle at a lower load level than that of unrestrained case. More discussions of the FE comparisons with: *I*. unrestrained; *II*. Restrained shear component model; *III*. Whole beam behaviour will be presented in Section 6.4.

6.3.1 FE Predictions of Unrestrained Shear Component at Ambient Temperature

FE predictions showed that the stress distribution was uniform in the web panel at the beginning of loading. With increasing shear, higher stresses were mobilized along the diagonal band of web panel until stresses reached the yield strength of web (σ_{yw}). The equivalent von Mises stress distribution of TG5-1 specimen prior to panel failure is shown in Figure 6.5. After the diagonal web elements reached yield strength, plastic hinges were formed at top and bottom flanges. Finally, with a further increase in shear, web panels developed out-of-plane buckling and failed. The loads versus out-of-plane deflections at the centre of web panels for TG3-1, TG4-1 and TG5-1 (Figure 6.6) show that out-of-plane displacements were very small at the initial loading. After applied shear stress had reached a certain value, out-of-plane displacement started to increase, meaning that the applied stress attained web panel critical shear stresses. With increasing shear, the out-of-plane deflection further increased until it expanded greatly with a little increase of shear stress. This indicated that the diagonal web element stress had reached the material yield strength.

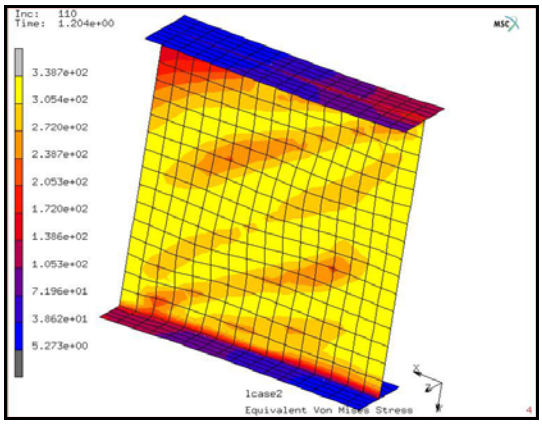

Figure 6.5 von Mises Stress Distribution of TG5-1 Prior to Collapse

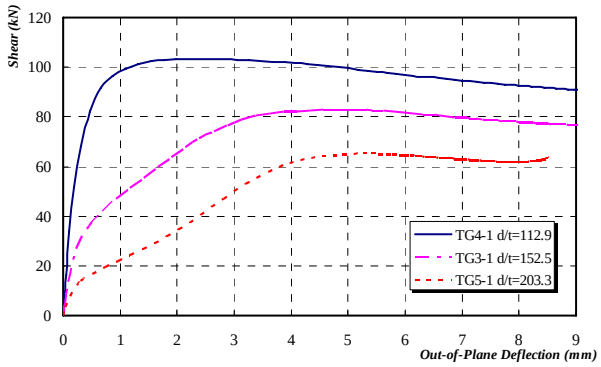

Figure 6.6 Shear Stress versus Out-of-Plane Deflection (TG3-1 TG4-1 TG5-1)

6.3.2 FE Predictions of Unrestrained Shear Component at Elevated Temperatures

As described in Section 6.2.1, the FE model for specimen at elevated temperature undergoes two stages. From FE results, as expected, it was observed that there was no additional stress at the end of heating stage. After the heating stage, at earlier increments of shear stress, the equivalent von Mises stress distribution of web panels was uniform throughout the web panel. With a further increase in shear, the stress of the elements inside the diagonal band of the web panel was greater than the other parts of the panel as shown in Figure 6.7. The stress within the band kept increasing until it reached the yield strength. The whole panel eventually failed, when the plastic hinges developed in the flanges. The detailed failure loads of G1-G5 and TG1-TG5 series at different temperatures will be discussed in Section 6.4.

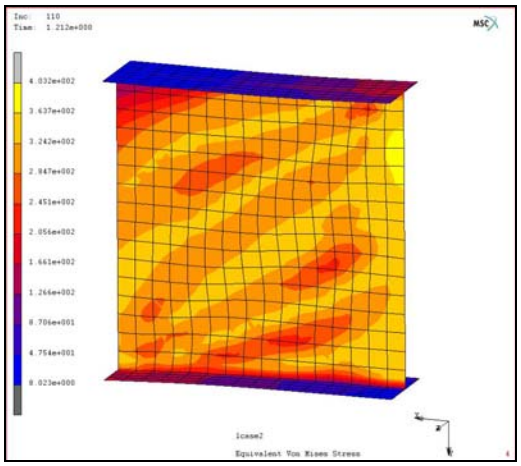

Figure 6.7 von Mises Stress Distribution of TG5-2 Prior to Collapse

6.3.3 FE Results of Whole Beam Simulation for Unrestrained and Restrained Tests

In current study, six series of unrestrained and restrained beam tests (TG3, TG4, TG5, RTG3, RTG4 and RTG5) were also simulated using whole beam models. The material properties of FE models were consistent with material coupon test results as described in Section 5.2 and 5.4. The whole beam model is shown in Figure 6.8. In total, there were around five thousand shell elements in the whole beam model. This, in practice, is not economical to analyze a beam. This FE model is considered here for research purpose, in order to verify test results using actual configuration. Figure 6.9 shows the equivalent von Mises stress distribution for web panel 2 and 3 in TG5 series (400 ^{o}C) at failure. It can be observed that out-of-plane deflection occurred at inner web panels. Due to experimental set-up, the temperature of inner web panels (Panel 2 and Panel 3) was approximately 20 ^{o}C higher than outer panels (Panel 1 and Panel 4). Therefore, material degradation at elevated temperature has slightly greater effect on mechanical behaviour of inner web panels. Besides the temperature effects, bending moment effects of inner web panels were greater than outer web panels. Both of these effects caused inner web panels to fail earlier than outer web panels. For the whole beam model, actual temperature distribution was applied across a section to allow simulation of thermal gradient in the longitudinal

direction, according to thermocouple measurement locations as shown in Figure 5.6. During plate girder tests as described in Section 5.2.6, temperatures at the top and bottom flanges have been monitored by a series of thermocouples attached to the respective surfaces of flanges. Thus, these temperature measurements have been incorporated into whole beam FE model for a more realistic temperature representation for flanges. As shown in Figure 5.6, in addition to two thermocouple measurement points at adjoining flange plates, for web panels there, was one more temperature measurement point at the centre of the section. However, as shown in Figure 5.18, cross-sectional temperature measurements show a rather uniform distribution. Therefore, for simplicity of FE modelling, a uniform cross-sectional temperature distribution has been adopted in the whole beam FE model, but with variation of temperature in the longitudinal directions, as described in Section 5.3.3. The vertical-deflection versus loading curves for TG5-1 (ambient temperature) are shown in Figure 6.10. L1, L2, L3, L4 and L9 indicate the vertical deflections at the LVDT locations (LVDT 1 to 4 and LVDT 9) along the beam measurement points which are shown together with the plotted results. The comparison between FE predictions and experimental results will be presented in Section 6.6.4.

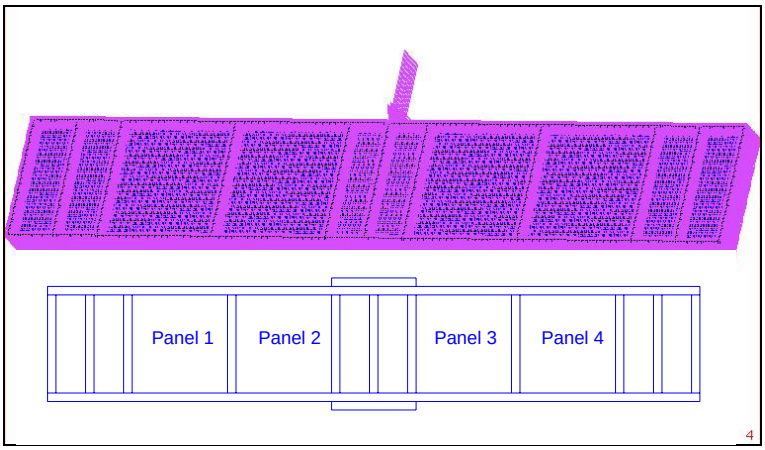

Figure 6.8 Test Beam FE Model (TG5 series)

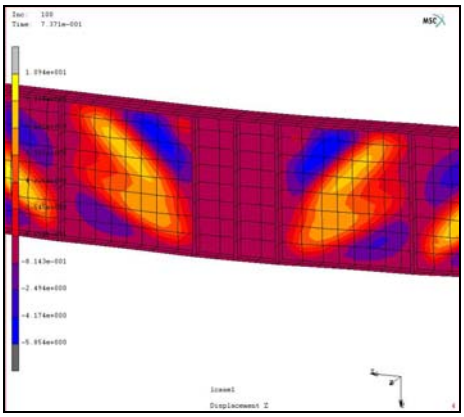

Figure 6.9 von Mises Stress Distribution of TG5-2 Prior to Buckling

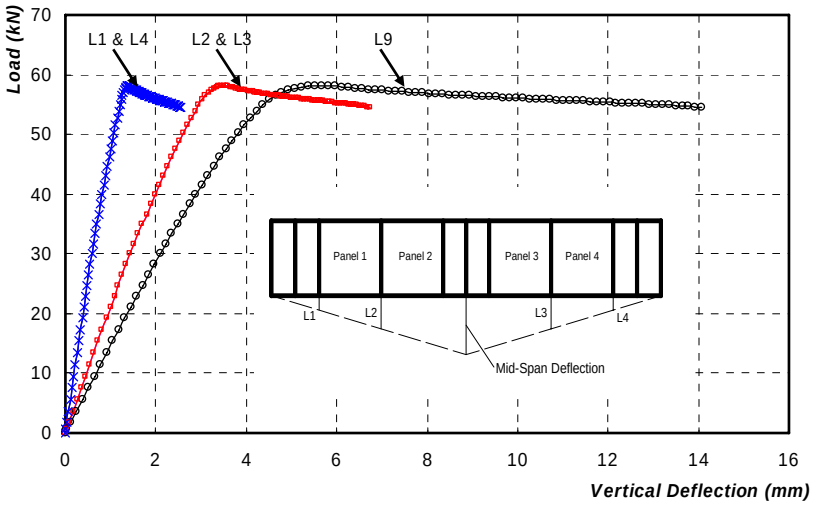

Figure 6.10 Vertical Deflection versus Load for TG5-1 Specimen

6.4 Comparisons of FE Predictions with Test and Analytical Results

In current FE analyses, ten series of specimens (G1 to G5 and TG1 to TG5 series) were studied at ambient temperature, and at elevated temperatures with both restrained and unrestrained boundary conditions. Detailed geometrical and material properties are listed in Table 6. 1. The FE predictions were compared with both test data and analytical predictions.

6.4.1 FE Predictions of Ambient Temperature Tests

In this study, three specimens (TG3-1, TG4-1 and TG5-1) were tested at ambient temperature as described in Section 5.2. The ultimate shear strengths from the

analytical (V_{analy}), FE (V_{FEM}) and test results (V_{test}) of all TG series are listed in Table 6.4 for comparisons. The FE model used was that of single web panel with appropriate boundary conditions described in Section 6.2.1. This case study is particularly important as it is used to verify the accuracy of FE model with test results at ambient temperature.

Table 6.4 Comparisons among FE, Analytical Predictions and Test Results of TG1 to TG5 series at Ambient Temperature

Test Girder	Temp °C	Analytical Predictions		FE Predictions		Test Results		$\frac{V_{test}}{V_{analy}}$	$\frac{V_{analy}}{V_{FEM}}$	$\frac{V_{test}}{V_{FEM}}$
		V_{cr} (kN)	V_{analy} (kN)	$V_{cr,FEM}$ (kN)	V_{FEM} (kN)	$V_{cr,test}$ (kN)	V_{test} (kN)			
TG1-1	20	173.99	192.19	170	190	172.2	193.45	1.01	1.01	1.02
TG2-1	20	288.44	345.65	280	322	270.3	343.8	0.99	1.07	1.07
TG3-1	20	44.36	85.7	45	88	53.35	79.85	0.93	0.97	0.91
TG4-1	20	113.64	113.64	102	112	101.4	111.8	0.98	1.01	0.99
TG5-1	20	18.7	61.92	19	59	21.05	59.6	0.96	1.05	1.01
—	—	—	—	—	—	—	—	0.97[a]	1.02[a]	1.00[a]
—	—	—	—	—	—	—	—	0.03[b]	0.04[b]	0.06[b]

[a] Mean Value [b] Standard Deviation

Comparing FE, test results and analytical predictions, it is evident that the web panel model for shear component predicts mechanical behaviour very accurately. It is particularly encouraging that the standard deviation for V_{test}/V_{FEM} is only 0.06, indicating very consistent comparison between FE and analytical models. Due to careful design and detailing, actual test panels experienced little bending effect. This effect would cause the ultimate shear strength of test girder to be lower than analytical and FE predictions. From the comparison between the FE and experimental results (TG3-1, TG4-1 and TG5-1), it can be observed that ultimate shear strengths of web panel model is higher than experimental results. This FEA behaviour is also expected since the material model adopted is

elastic-perfectly-plastic at normal temperature as shown in Figure 3.4. This model disregards the nonlinearity in the stress-strain model and therefore leads to over-stiff behaviour. This material model, instead of the more realistic experimental stress-strain curve, is used in FE models to compare with analytical model which can only incorporate the material properties shown in Figure 3.4. As described in Section 5.3, strains at the centre of the web panels of TG3, TG4 and TG5 specimens tested at ambient temperature were measured by rosette strain gauges. In addition to results of critical and ultimate shear strength, FE simulations of principal and maximum shear strains were also compared with experimental results in Figure 6.11 (a), (b) and (c) for TG3-1, TG4-1 and TG5-1, respectively.

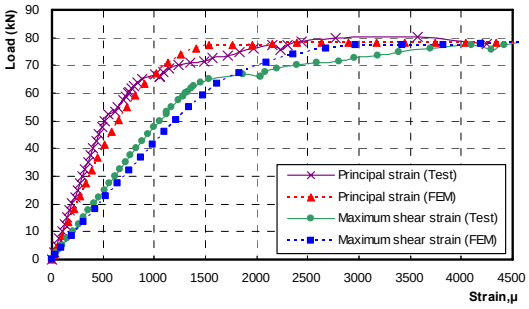

(a) TG3-1 web panel 1

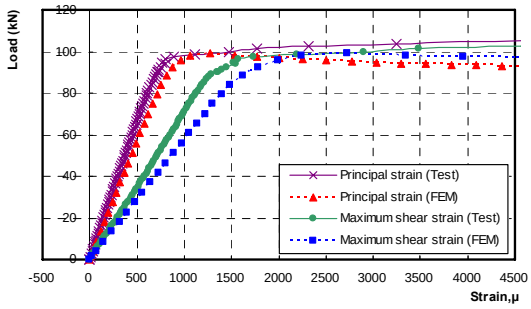

(b) TG4-1 web panel 1

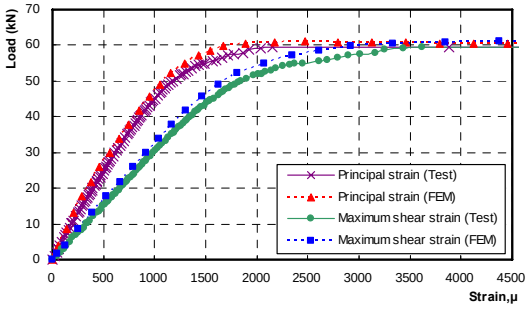

(c) TG5-1 web panel 3

Figure 6.11 Shear Stress versus Principal and Maximum Shear Strain

As shown in Figure 6.11 , it can be observed that there was a little discrepancy between the test results and FE predictions. During instrumentation, rosette strain gauges might not be affixed exactly at the centre of web panels. The

elastic-perfectly-plastic material model also indicated a higher stiffness. All these explain why FE predictions were always on the high side.

For the analysis of G series under ambient temperature, the detailed FE, analytical predictions and test results are listed in Table 6.5. From the comparison between FE predictions and experimental results, it can be concluded that the FE model can simulate the behaviour of web panel under shear force at ambient temperature.

Table 6.5 Comparisons among FE, Analytical Predictions and Test Results of G1 to G5 Series at Ambient Temperature

Girder Model	Temp ^{o}C	Analytical Predictions, V_{analy} (kN)	FE Predictions V_{FEM} (kN)	Test results V_{test} (kN)	$\frac{V_{test}}{V_{analy}}$	$\frac{V_{analy}}{V_{FEM}}$	$\frac{V_{test}}{V_{FEM}}$
G1-1	20	28.77	27	29.35 (Rockey *et al.* 1972)	1.02	1.06	1.09
G2-1	20	77.52	75.4	79.85 (Vimonsatit *et al.* 2005)	1.02	1.03	1.06
G3-1	20	42.83	40.6	43.05 (Vimonsatit *et al.* 2005)	1.01	1.05	1.06
G4-1	20	1160	1185	1195 (Sakai *et al.* 1966)	1.03	0.98	1.01
G5-1	20	1159	1200	1176 (Sakai *et al.* 1966)	0.98	0.99	0.98
—	—	—	—	—	1.02[a]	1.02 [a]	1.04 [a]
—	—	—	—	—	0.02[b]	0.04 [b]	0.05 [b]

[a] Mean Value [b] Standard Deviation

6.4.2 FE Predictions of Thermally Unrestrained Tests at Elevated Temperatures

Ten series of specimens (G1-G5, TG1-TG5) were analyzed at elevated temperatures (400, 550 and 700 ^{o}C) without considerations of thermal restraint force. Part of analytical predictions (TG3, TG4 and TG5 series) has been compared with test results conducted in this study. FE predictions for TG 2 series (400, 550 and 700 ^{o}C) were compared with test results conducted by Vimonsatit *et al.* (2005). FE

simulations were also compared with analytical predictions. The detailed results for TG3, TG4 and TG5 series are given in Table 6.6. The detailed FE and analytical predictions for G1-G5 series are given in Table 6.7.

Table 6.6 Comparisons among FE, Analytical Predictions and Test Results of Unrestrained TG2-TG5 series at Elevated Temperatures

Test Girder	Temp °C	Analytical Predictions		FE Predictions		Test Results		$\frac{V_{test}}{V_{analy}}$	$\frac{V_{analy}}{V_{FEM}}$	$\frac{V_{test}}{V_{FEM}}$
		V_{cr} (kN)	V_{analy} (kN)	$V_{cr,FEM}$ (kN)	V_{FEMt} (kN)	$V_{cr,test}$ (kN)	V_{test} (kN)			
TG2-2	400	288.44	345.65	280	314	260	324.3	0.94	1.10	1.03
TG2-3	550	178.83	214.3	180	198	183.6	234.6	1.09	1.08	1.18
TG2-4	700	66.34	79.5	62	72.6	62.4	74.2	0.93	1.10	1.02
TG3-2	400	31.05	65.2	30	68.9	30.08	67.63	1.04	0.95	0.98
TG3-3	565	18.23	37.13	19.2	35.8	19.87	34.34	0.92	1.04	0.96
TG3-4	690	5.77	15.7	6.4	15.2	7.05	17.15	1.09	1.03	1.13
TG4-2	400	76.34	85.89	67.26	78.8	58.9	77.1	0.90	1.09	0.98
TG4-4	700	14.53	18.19	15	18	10.59	15.94	0.88	1.01	0.89
TG5-2	400	13.43	53.17	18	50.1	17.63	46.4	0.87	1.06	0.93
TG5-3	550	11.51	32.39	10	31.47	13	28.6	0.88	1.03	0.91
TG5-4	700	2.49	11.48	3	10.5	4.5	10.16	0.89	1.09	0.97
—	—	—	—	—	—	—	—	0.95[a]	1.05[a]	1.00[a]
—	—	—	—	—	—	—	—	0.09[b]	0.05[b]	0.09[b]

[a] Mean Value [b] Standard Deviation

From Table 6.6 and Table 6.7, it can be observed that the web panel model at elevated temperatures without thermal restraints can predict shear strength accurately. However, there are slight differences between the analytical and the FE predictions. In the web panel model, the assumed boundary conditions allowed thermal expansion in all three directions during heating. However, the analytical method only allowed 1-D thermal expansion in horizontal direction. Consequently,

geometric changes due to elevated temperature between the web panel model and analytical method are slightly different. The shear strength results of TG3-TG5 series and G1-G5 series from FEA, analytical approach and test results are also plotted in Figure 6.12 (a), (b), (c), (d), (e) and (f) respectively.

Table 6.7 Comparisons among FE and Analytical Predictions of Unrestrained G1 to G5 series at Elevated Temperatures

Girder Model	Temp ^{o}C	Analytical Predictions V_{analy} (kN)	FE Predictions V_{FEMt} (kN)	$\frac{V_{analy}}{V_{FEM}}$
G1-2	400	22.05	23.4	0.94
G1-3	550	13.45	13.8	0.97
G1-4	700	4.74	4.8	0.99
G2-2	400	58.35	58.2	1.00
G2-3	550	35.75	36.9	0.97
G2-4	700	12.36	12.96	0.95
G3-2	400	32.88	31.6	1.04
G3-3	550	20.05	21.85	0.92
G3-4	700	7.07	7.1	1.00
G4-2	400	859.67	871	0.99
G4-3	550	523.06	571	0.92
G4-4	700	186.45	191	0.98
G5-2	400	852.52	951	0.90
G5-3	550	526.82	578	0.91
G5-4	700	174.88	180	0.97
—	—	—	—	0.96[a]
—	—	—	—	0.04[b]

[a] Mean Value [b] Standard Deviation

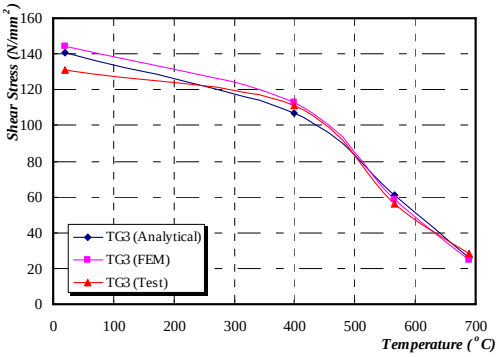

(a) TG3 Series

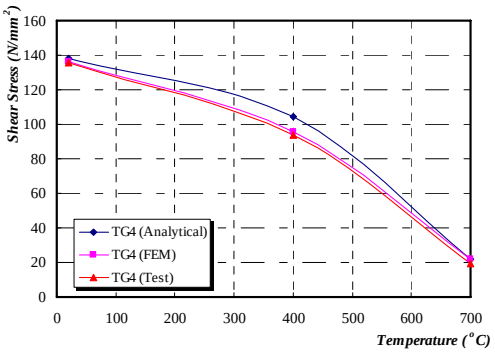

(b) TG4 Series

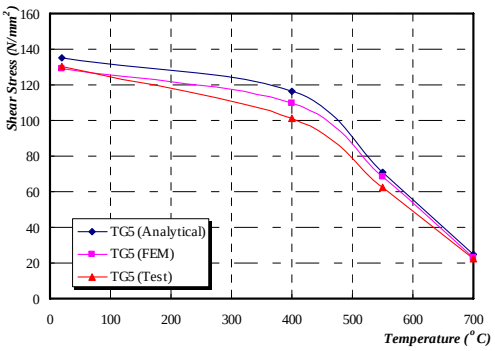

(c) TG5 Series

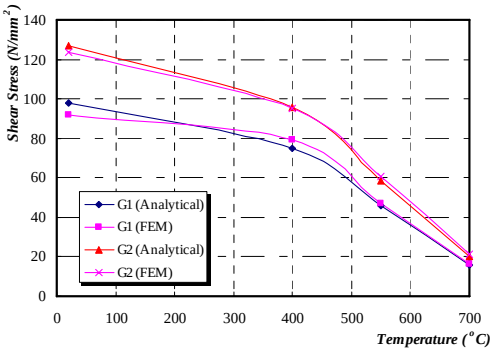

(d) G1 and G2 Series

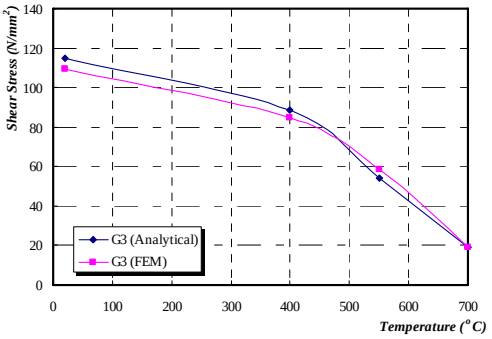

(e) G3 Series

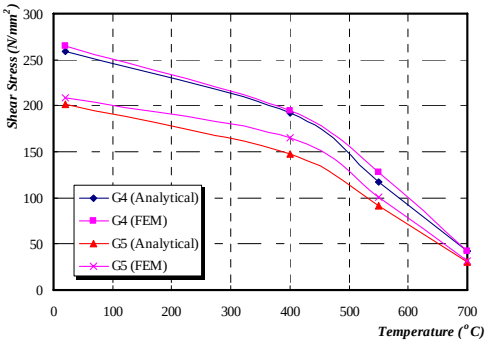

(f) G4 and G5 Series

Figure 6.12 Ultimate Shear Stress vs. Temperature for G1-G5 and TG1-TG3 Series

As described in Section 4.2, the ultimate shear capacity of web panel largely depends on material properties and web slenderness ratio (d/t). TG3, TG4 and TG5 series were designed to study the effects of different web slenderness ratios d/t

on ultimate shear strength of specimens. A comparison between the ultimate shear strength V_{FEM} and the maximum shear strength at ambient temperature is studied, where $V_{yw(20℃)} = \tau_{yw(20℃)} dt$. Figure 6.13 shows variations of ultimate shear stress ratio $V_{FEM} / V_{yw,20}$ with temperature.

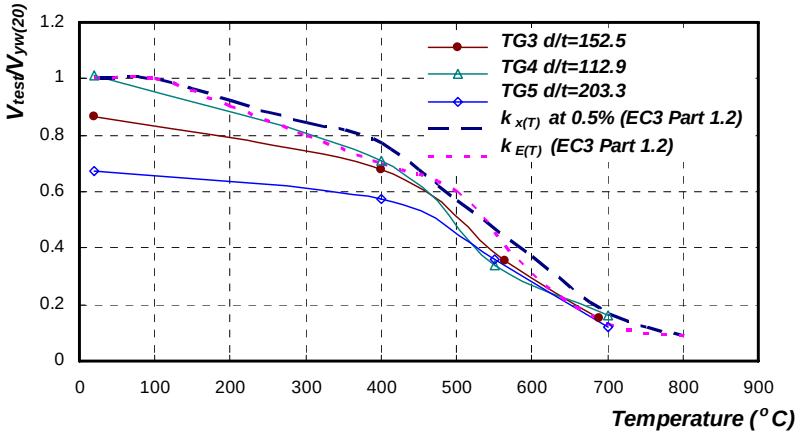

Figure 6.13 Shear Stress Capacity Ratio versus Temperature for TG3, TG4 and TG5

In Figure 6.13, reduction factors of steel yield strength $\left(k_{x(T)}\right)$ and elastic modulus $\left(k_{E(T)}\right)$ at elevated temperatures according to EC 3 Part1.2 (EN 1993-1-2) are plotted with FE predictions for different $\left(d / t\right)$ ratios. It can be noticed that with increasing temperature, the ultimate shear strength of web panel reduces following the trend of material degradation of steel. In addition, it can be observed that web panel with lower web slenderness demonstrates greater shear strength resilience compared with higher slenderness ratio. These FE predictions are consistent with analytical predictions. From Figure 6.13, it can also be observed that the ultimate shear strength of TG4-1 tested at ambient temperature slightly exceeds maximum shear strength of web panel. In the analytical method, the shear stress was assumed to be sustained wholly by the web panel. However, in FEA, it was noticed that the top

and bottom flanges of the FE model also contributed to the ultimate shear strength of web panel. This was particularly significant for lower (d/t) ratio.

6.4.3 FE Predictions of Whole Beam Unrestrained Simulations

Vertical deflections of the whole beam model were compared with experimental results. The deflection points for FE model correspond to LVDTs locations (LVDT1 to LVDT4, and LVDT9) along the specimen. The FE simulations of TG5 series at ambient temperature are compared with experimental results (Figure 6.14).

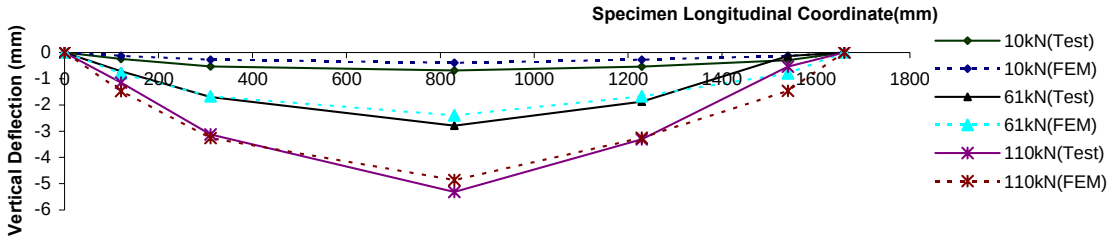

Figure 6.14 Whole Beam Vertical Deflection Comparison of TG5-1 at Ambient Temperature between FE Predictions and Test Results

In Figure 6.14, three load levels (at 10, 61 and 110 kN) are selected as comparison points. As in whole beam model, two beam ends were not allowed to have any vertical deflections to simulate the simply-supported condition. Therefore, the experimental vertical deflections measured by LVDTs in Figure 6.14 had to take account of differential support settlement at the two ends. From comparison, it can be observed that whole beam model is reliable. However, there are some discrepancies between the FE and experimental results as the material model in the FEA is elastic-perfectly-plastic. Material nonlinearity indicating strain-hardening is not considered and will soften the FE curves. In addition to ambient temperature tests, the FE model at elevated temperatures was also included in the present work.

The comparison between FE and experimental results of TG4-4 tested at 700℃ is shown in Figure 6.15.

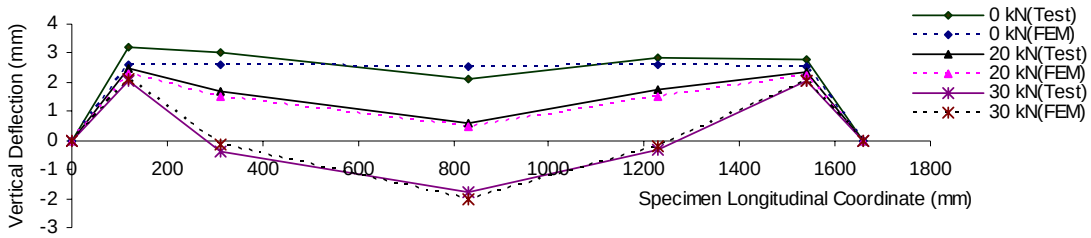

Figure 6.15 Whole Beam Vertical Deflection Comparisons of TG4-4 at Elevated Temperature between FE Predictions and Test Results

From Figure 6.15, it can be observed that the beam expanded upwards during heating. After load was applied at mid-span, the beam started to sag downwards until it failed. In the test set-up, the temperatures inside the web panels were not uniform. Therefore, in the whole beam model for elevated temperature tests, the longitudinal temperature distribution was simply set according to the thermocouple measurements as described in Section 6.3.4. In Figure 6.15, comparisons between FE and experimental results are conducted at three different load levels (at 0, 20 and 30 kN). The FE predictions compare well with experimental results. However, there are some discrepancies between experimental and FE predictions, particularly at 30 kN. Similar to FE model at ambient test, the material model in FE analysis is elastic-perfectly-plastic. Besides, the cross-sectional temperature distribution inside the FE model was assumed to be constant, unlike actual test panel.

6.4.4 FE Predictions of Thermally Restrained Tests

In current research, the effects of thermal restraint force on the behaviour of shear component of steel joint were simulated using a simplified whole beam model, as described in Section 6.2.2. The detailed finite element predictions and experimental results for RTG3 to RTG5 series are listed in Table 6.8. In general, the experimental

V_{test} and FE predicted V_{FEM} agree very well, as shown in Column (9) of Table 6.8, with the mean and standard deviation as 1.004, and 0.059, respectively. Almost all the test results agree well with FE predictions, with the exceptions of RTG4-2 and RTG3-4. It should be noted that in the FE predictions, steel material characteristics has been simulated by the stress-strain-temperature curve as shown in Figure 3.4 (ENV 1993-1-2). Moreover, the shear strength ratio results of RTG3, RTG4 and RTG5 series from FEA and test are also plotted in Figure 6.16 (a), (b), and (c) respectively, with the reduction factors of steel yield strength (k_y) and elastic modulus (k_E) at elevated temperatures according to EC 3 Part1.2 (ENV 1993-1-2).

Table 6.8 Comparisons of Experimental Results with FE Predictions for RTG3, RTG4 and RTG5 Series

Test Series	Test Girder	Test Temperature (^oC)	Restraint Ratios β	Axial Force (kN)	V_{test} (kN)	V_{test}/V_{yw}	V_{FEM} (kN)	V_{test}/V_{FEM}
(1)	(2)	(3)	(4)	(5)	(6)	(7)	(8)	(9)
RTG3	RTG3-1	400	3.8%	43.41	51.7	0.56	54.2	0.95
	RTG3-2	550	3.8%	48.27	26.6	0.29	27.7	0.96
	RTG3-3	670	3.8%	61.02	14	0.15	14.71	0.95
	RTG3-4	670	3.3%	53.92	15.4	0.17	15	1.03
RTG4	RTG4-1	400	3.5%	43.81	69.55	0.57	71.66	0.97
	RTG4-2	550	3.5%	51.32	28.95	0.24	29.36	0.99
	RTG4-3	670	3.5%	62.02	17.55	0.14	18.2	0.96
	RTG4-4	670	3.0%	57.78	18.5	0.15	19.9	0.93
RTG5	RTG5-1	400	5.0%	39.31	42.55	0.49	43.5	0.98
	RTG5-2	550	5.0%	45.59	17.8	0.20	20.85	0.85
	RTG5-3	670	5.0%	51.12	10.6	0.12	11.05	0.96
	RTG5-4	670	4.3%	49.69	12.85	0.15	13.04	0.99
—	—	—	—	—	—	—	—	0.96 [a]
—	—	—	—	—	—	—	—	0.04 [b]

[a] Mean Value [b] Standard Deviation

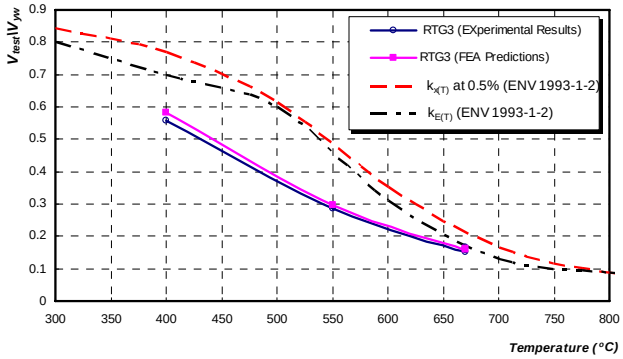

(a) RTG3 Series

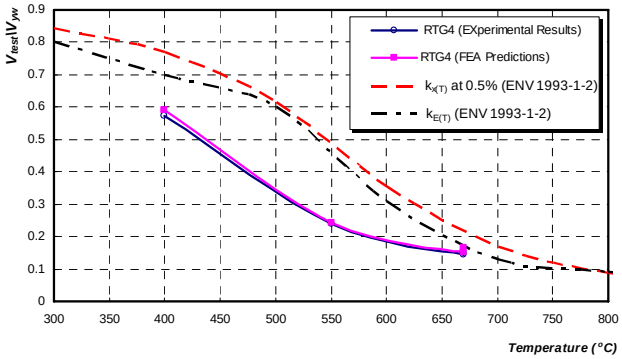

(b) RTG4 Series

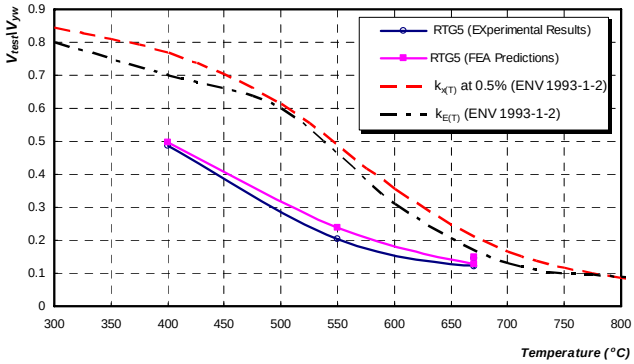

(c) RTG5 Series

Figure 6.16 Shear Strength Ratio Comparisons between FE Predictions and Experimental Results

As a typical example, shear failure can be observed from a sudden increase in out-of-plane deflection as shown in Figure 6.17 (a) for RTG4-4 and Figure 6.17 (b) for RTG5-4 both tested at 670 ^{o}C. The out-of-plane deflection increases up to approximately 85% of ultimate failure load and then the web panel shows a large out-of-plane deflection increase with a minor increase in load above this point. The predicted FE curve is in good agreement with experimental curve with a sudden increase in deflection towards the end. It can also be observed that the FE simulations give slightly conservative strength predictions. However, the difference in ultimate shear strength prediction is small, indicating a good fit to test results.

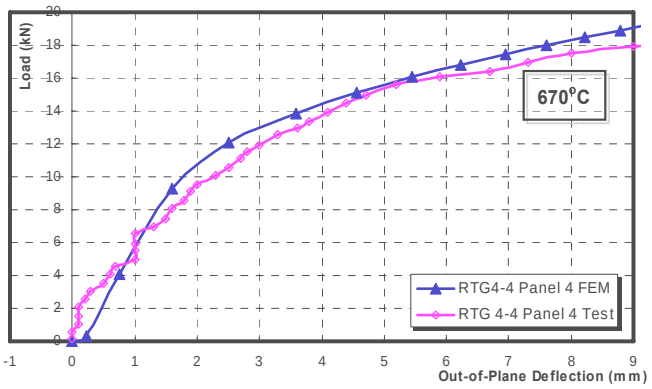

(a) RTG4-4 Panel 4 at 670 °C

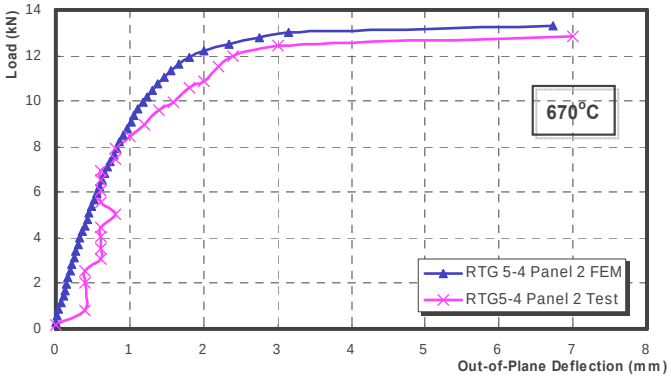

(b) RTG5-4 Panel 2 at 670 °C

Figure 6.17 Comparisons of Shear Load versus Out-of-Plane Deflection between Experimental Results and FE Predictions

Figure 6.18 (a) and (b) show the tensile membrane failure mode of web panels for RTG4 series. It can be seen that plastic hinges are formed in the corners of web panels and in the flanges due to mobilization of tensile field action. The deformed shape and the von Mises stress distribution from FE analysis are also included. Clearly, the deformation is similar to the observed buckled shape.

(a) Deformed shape for RTG4-1 tested at 400 °C

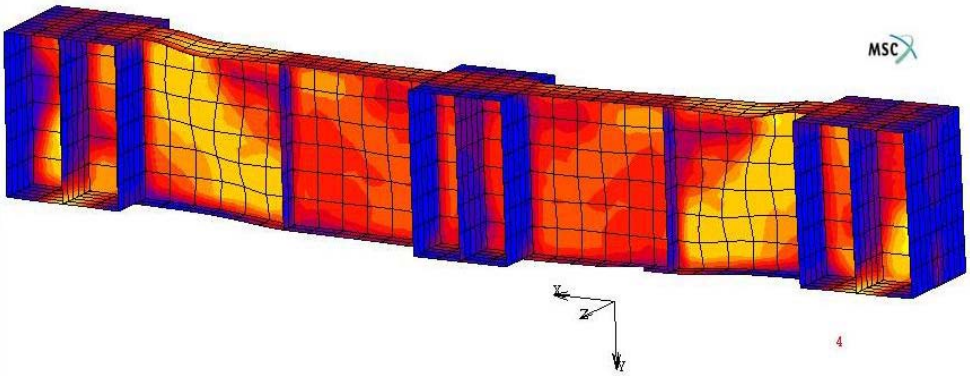

(b) FE Predictions of RTG4-1 tested at 400 °C

Figure 6.18 FE and Experimental Deformed Shape for RTG4-1 Tested at 400 °C

6.5 Conclusion

Comparing FE, analytical predictions and experimental results, it is obvious that proposed FE models are able to predict shear behaviour of test plate girders very accurately, at both ambient and elevated temperatures. Based on FE predictions, it can be concluded that shear behaviour of web panel at elevated temperature is similar to that at ambient temperature. However, due to degradation of steel material properties at elevated temperatures, the shear strength capacity also decreases accordingly. Under restrained boundary conditions, FE models showed similar behaviour with analytical predictions. The thermal restraints of web panel induced additional compressive stresses to web panel. These additional stresses caused the web panel to buckle at a lower shear load compared to the unrestrained case.

CHAPTER 7
EXPERIMENTAL INVESTIGATION OF STEEL BEAM-TO-COLUMN JOINT

7.1 Introduction

During the past decades, a great number of experimental investigations have been carried out to establish moment-rotation relationships for bare steel and composite beam-to-column joints over a wide range of temperature. Investigations described herein focus on extended end-plate beam-to-column joint at elevated temperatures, with consideration of axial restraint force from surrounding unheated structure. A mechanical approach is developed to define the rotational characteristics of steel joints at both ambient and elevated temperatures. The idea is to implement joints as semi-rigid springs in the analyses of steel framed structures in fire in future work.

7.2 Steel Beam-to-Column Joint Experimental Set-up

In total, there were six extended end-plate beam-to-column joints tested as "cruciform" assemblies in two groups. In the first group, three cruciform specimens (CR1, CR2 and CR3) were tested at 700 ^{o}C with axial compressive force at 0, 2.5 and 4% of plastic squashing capacity of the beam section at ambient temperature. Based on reduction factors for yield strength in Eurocode 3 part 1.2 (EN 1993-1-2), the axial load ratios were 0, 10.2 and 16.3% at 700 ^{o}C. The objective of test of this group is to investigate the effect of axial restraint on steel joint behaviour at 700 ^{o}C. This temperature was chosen as it represents the high end of elevated temperature test. In the second group, three more cruciforms (CR4, CR5 and CR6) were tested at 400, 550 and 700 ^{o}C, respectively, under unrestrained boundary conditions.

These tests were conducted to obtain the moment-rotation-temperature characteristics at three isothermal conditions. These two groups of assemblies consisted of identical beam and column sections for comparison purpose. The first three specimens had 20 mm thick end-plates. In the failure modes, one or two bolts appeared to undergo large extension due to significant tensile force. Thus in the second group of specimens, to obtain a clear picture of beam web shear component, thicker end-plates of 40 mm were used.

7.2.1 Development of Cruciform Test Programme

The cruciform testing system (Figure 7.1) consisted of a boxed-up electrical heating furnace (⑥), a transverse hydraulic jack (⑤) and an axial restraint system (①,⑦,⑩). The transverse hydraulic jack (⑤) was utilized as a loading device attached to an external portal frame system (④). A horizontal mounted hydraulic jack (①) provided axial force onto the beam sections of cruciform specimen. In addition, there were two fork support systems (⑧) seated onto supports (⑨) which prevented rotations of beam ends.

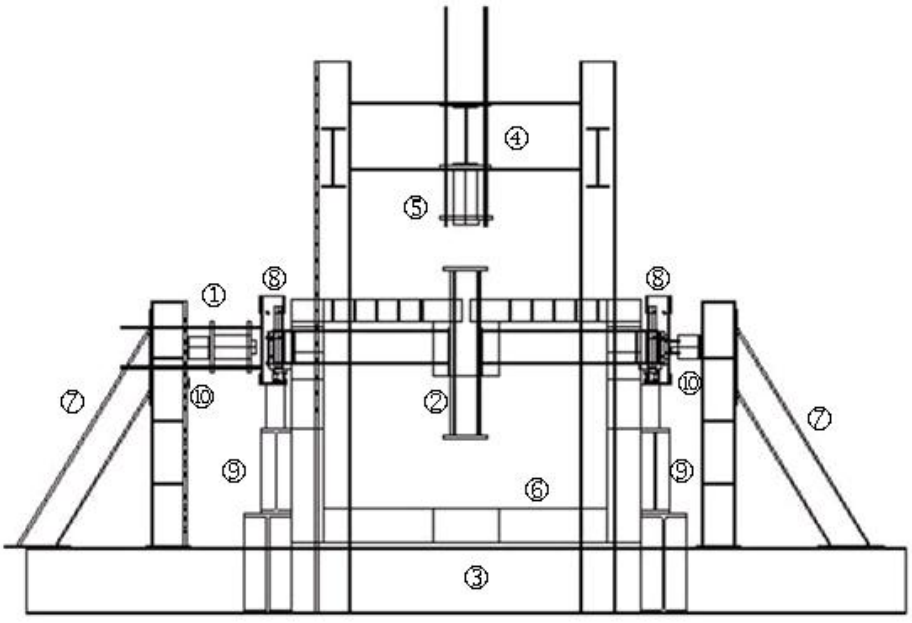

① Axial Hydraulic Jack
② Cruciform Specimen
③ Support Beam
④ Loading Portal Frame
⑤ Transverse Hydraulic Jack
⑥ Heating Furnace
⑦ Reaction Frame
⑧ Fork Support System
⑨ Support
⑩ Restraint Beam

Figure 7.1 Elevation View of Cruciform Test Set-Up

7.2.2 Cruciform Specimen Specifications

A typical cruciform specimen consisting of two 1.6m UB 305x102x25kg/m beams symmetrically framing into the flanges of a 1.5m high UC 254x254x107kg/m section is shown in Figure 7.2. Steel of all sections are of Grade 43. An extended end-plate joint was chosen for investigation, since it is one of conventional steel joints in construction practice. Besides, the work focuses on the shear component of beam-to-column joint, instead of joint performance. Thus, it is prudent to select a rigid joint instead of a weak joint. For the first group of specimens (CR1, CR2 and CR3), 20 mm thick end-plates were chosen with four M20 Grade 8.8 bolts and four M27 Grade 10.9 bolts, which provide sufficient tensile strength in the tension region of joints. The second group of specimens (CR4, CR5 and CR6) had similar assemblies with the first group. They consisted of two UB 305x102x25kg/m Grade 43 beams, 1.652m long, symmetrically framing into the flanges of an upright UC 254x254x107kg/m column, as shown in Figure 7.3. In order to prevent the end plates from bending which would cause bolt failure, a thicker end-plate of 40 mm and eight M27 Grade 10.9 bolts were used instead. Besides, to prevent beam flange from buckling, additional cover plates of 16 mm were welded onto the top (in compression) and bottom flanges (in tension) of beam sections as shown in Figure 7.2 and Figure 7.3.

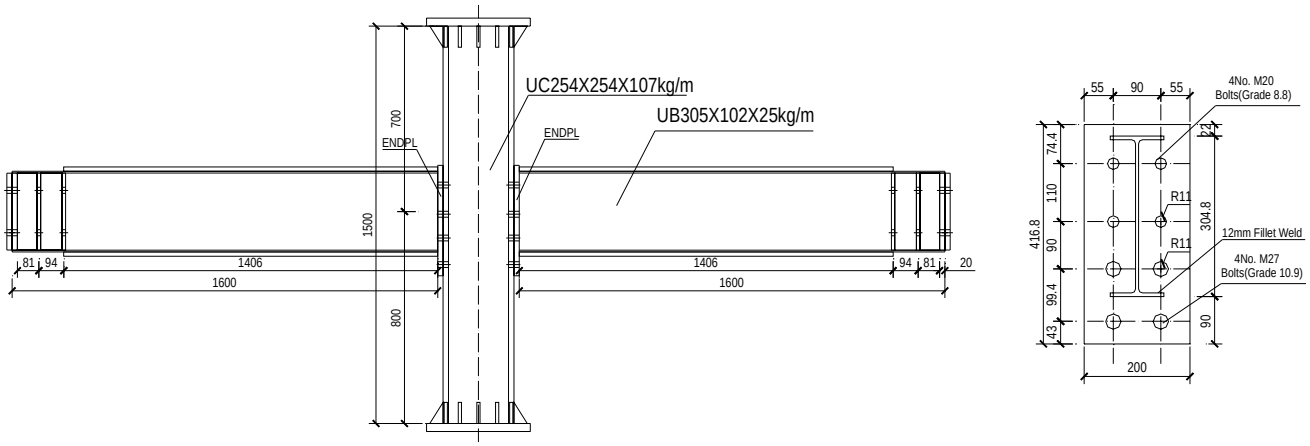

Figure 7.2 Bare Steel Extended End-Plate Joint Detail (CR1, CR2 and CR3)

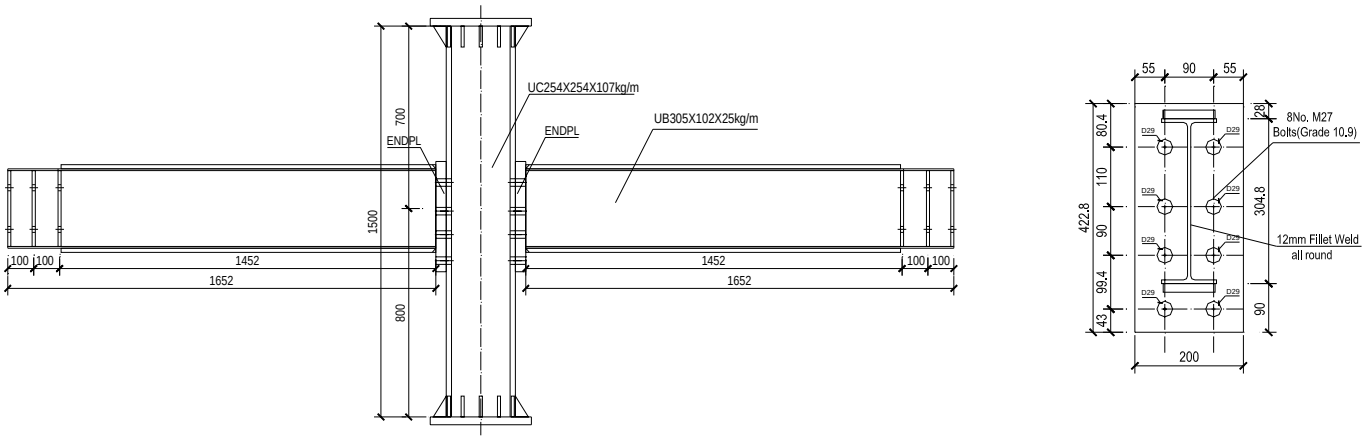

Figure 7.3 Bare Steel Extended End-Plate Joint Detail (CR4, CR5 and CR6)

Prior to testing, material tests at ambient temperature and geometrical properties were measured and presented in Table 7.1. Material properties at elevated temperatures were obtained from steel material strength and stiffness reduction factors as specified in Eurocode 3 part 1.2 (EN 1993-1-2).

Table 7.1 Material and Geometrical Property of Cruciform Specimen

Specimen	Section	Coupon Location	Thickness (mm)	Young's Modulus E (MPa)	Yield Stress, f_y (MPa)	Ultimate Stress, f_u (MPa)
CR1	Column	Flange	20.5	208328	293	465
		Web	13	213975	333	480
CR2	Beam	Flange	6.8	209000	337	482
CR3		Web	5.8	213000	333	475
	End-plate		20	218372	340	469
CR4	Column	Flange	20.5	208328	293	465
		Web	13	213975	333	480
CR5	Beam	Flange	6.8	205000	438	530
CR6		Web	5.8	218000	322	455
	End-plate		40	213630	376	557

7.2.3 Heating Facility

To obtain a relatively large uniform heating volume for the cruciform specimens, an electrical heating furnace was designed and fabricated, consisting of four individual heating panels with a maximum operating temperature of 900 ^{o}C as shown in Figure 7.4. Overall dimension of the assembled furnace is 3.1m long, 1.7m wide and 2.2m high. Each electrical heating panel is composed of several heating modules with metallic spiral heating elements embedded in foamed ceramic fibre insulation. The exposed surfaces of each heating module were coated with one layer of hardener to prevent spalling. Each heating module was firmly secured onto a stainless steel frame. There was 75 mm ceramic fibre board insulation to minimize heat loss. In addition, stainless steel frames were chosen to construct the heating panel framework with stainless steel sheets as outer casing. A few trial tests have been conducted to determine a realistic heating rate and to extract the moisture content inside the heating panels. From these tests, it was decided to adopt a heating rate of 7^{o}C per minute. This rate is within the practical heating range for steel sections by BS5950 Part 8 (BS5950-8), which stipulates a value from 5 ^{o}C/minute (for well insulated sections) to 20 ^{o}C/minute (for poorly insulated sections).

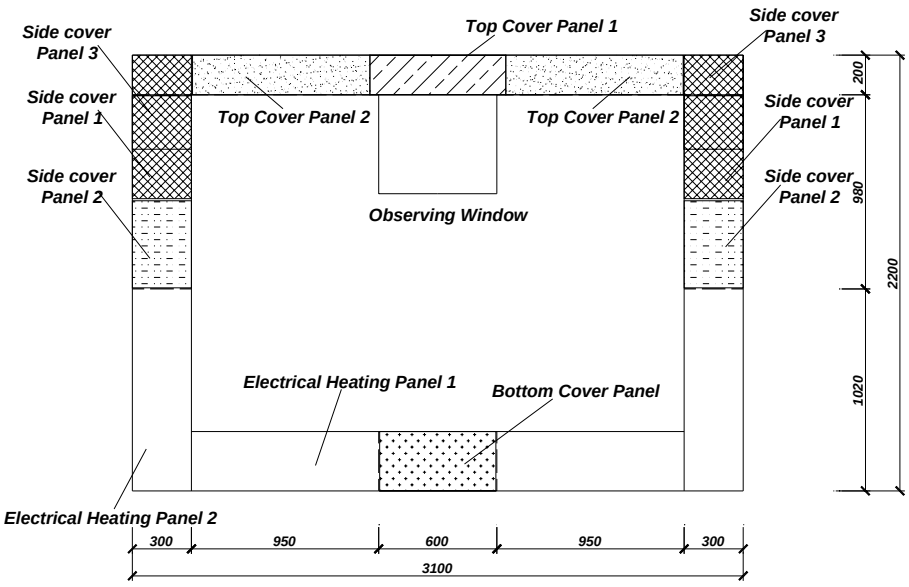

Figure 7.4 Elevation View of Electrical Heating Furnace

7.2.4 Loading Facility and Restraint Systems

The whole loading facility system of one ENERPAC hydraulic jack to provide vertical load at the top of a cruciform specimen and a two-portal-frame reaction system is shown in Figure 7.1. Vertical loads were measured by an annular compression load cell with 500 kN capacity, which was placed in between the hydraulic jack and the column head. A rocker bearing was also inserted between the load cell and column top to ensure verticality of applied force. The jack was manually driven with the load cell connected to a portable data logger control system. Based on the test set-up for restrained plate girder in Section 5.4, the ***axial restraint system*** was adjusted to provide certain axial restraint force onto the beam sections of cruciform specimens. This axial restraint system configuration is illustrated in Figure 7.1. The restraint system consists of one restraint beam (⑩) (UC203x203x46kg/m) together with two reaction A-frames (⑦) as shown in Figure 7.7. One hydraulic jack (①) was installed on the mid-span of the left restraint beam to provide axial force onto the beam sections of cruciform specimens. On the right hand side, a specially designed flexible roller joint was connected between the restraint beam (⑩) and cruciform specimen. The axial restraint force was monitored by two compression load cells with 300 kN capacity each, placed between the cruciforms and the restraint beams at each end as shown in Figure 7.7. As shown in Figure 7.5 and Figure 7.6, for the second group of tests (CR4, CR5 and CR6), to prevent lateral torsional buckling and out-of-plane global buckling of beam sections, an additional ***lateral restraint system*** has been fabricated and attached to external portal frame (⑧) as shown in Figure 7.6. The lateral restraint system consists of three restraint support plate systems (④) to provide lateral restraints to the upright column and two attached beam sections. In addition, roller plate system (⑤) allowed the cruciform specimen to deflect vertically. The restraint support plates (④) were welded to lateral restraint beams (③), supported by cantilever transfer beam (②) and connected to reaction beams (①) as shown in Figure 7.6.

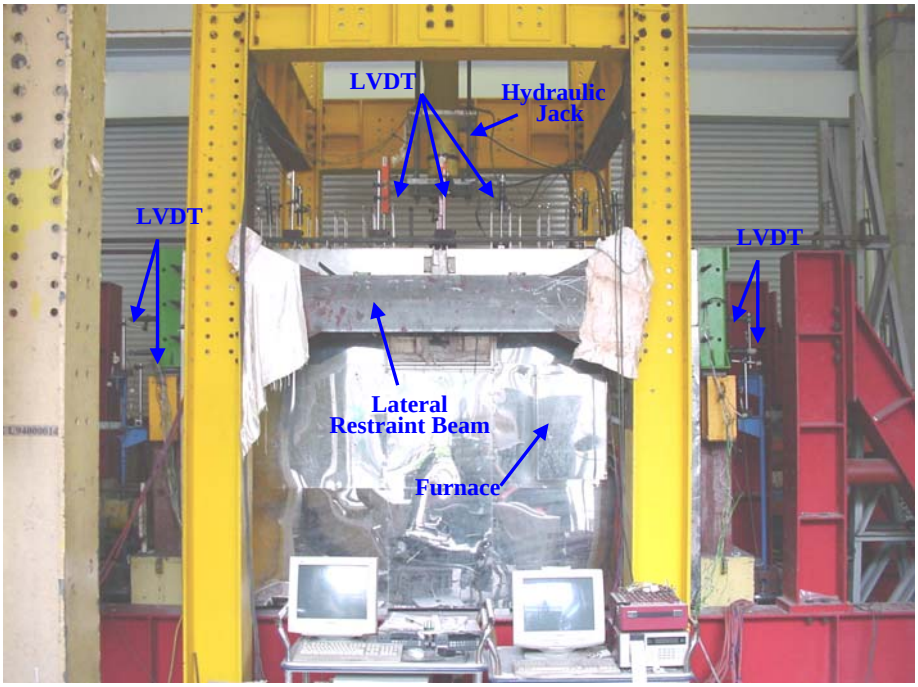

Figure 7.5 Unrestrained Cruciform Test Set-up

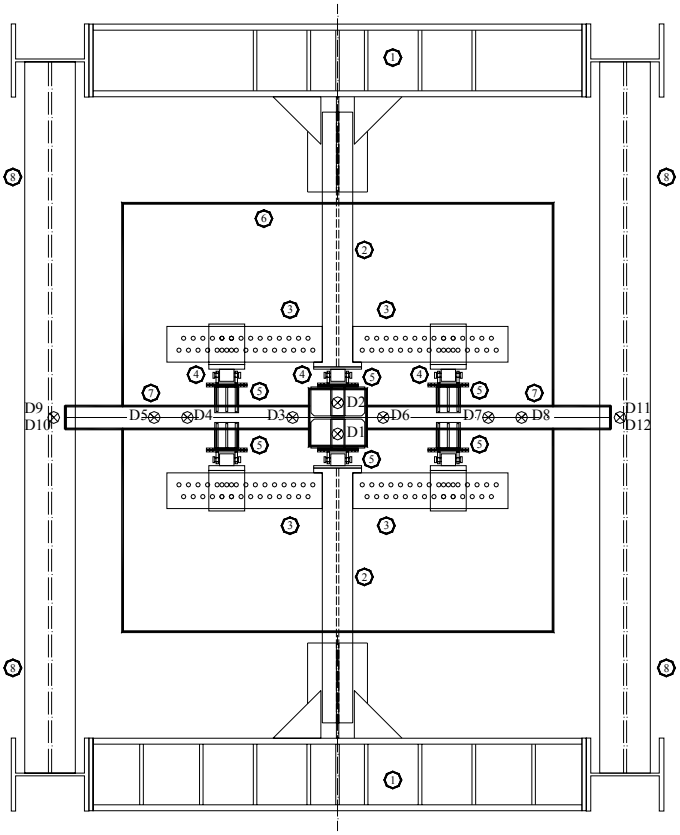

① Reaction Beam
② Cantilever Transfer Beam
③ Lateral Restraint Beam
④ Restraint Support Plate
⑤ Roller Plate
⑥ Heating Furnace
⑦ Cruciform Specimen
⑧ Portal Frame System
⊗ LVDTs

Figure 7.6 Plan View of Lateral Restraint System for CR4, CR5 and CR6

7.2.5 Deflection Acquisition System (LVDTs)

To obtain a good description of the development of in-plane deflections, ten sets of linear variable differential transducers (LVDTs) were utilized to monitor the beam vertical deflections for CR1, CR2 and CR3, which consisted of L2 to L11 as illustrated in Figure 7.7. These LVDTs were situated at five locations along the centre line of the top flange of each beam, at distances of 270, 470, 670, 870 and 1070 mm from the face of upright column flange. There was one additional LVDT (L1) at the top of column to measure the vertical displacement during test.

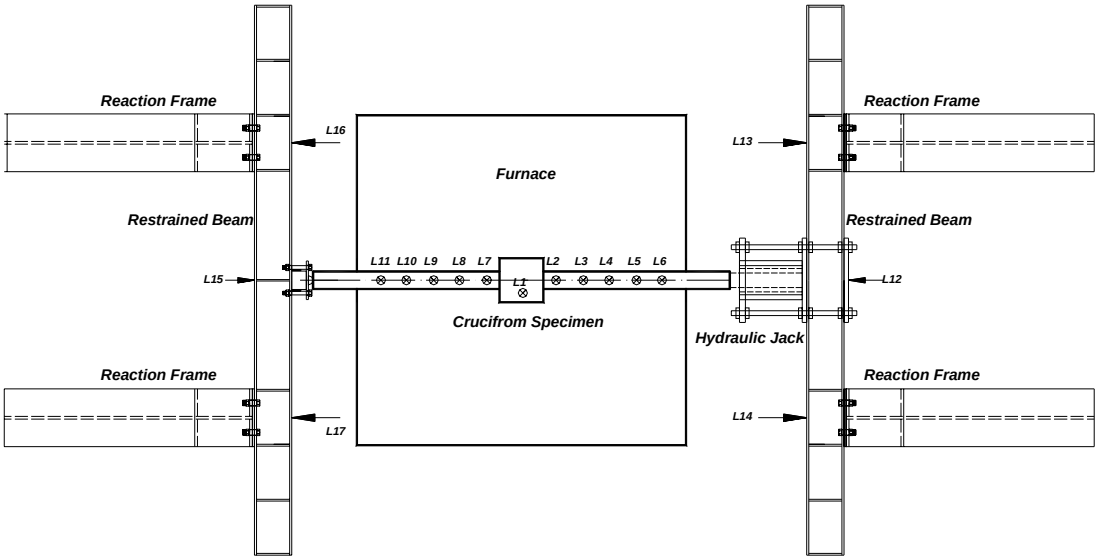

Figure 7.7 Plan View of Deflection Transducers Locations (CR1, CR2 and CR3)

Due to the presence of elevated temperature inside the furnace, ceramic rods were used to transfer vertical deflections of test specimens to LVDTs outside of furnace (L1 to L11 as shown in Figure 7.7). Three LVDTs (L12, L13 and L14) were used to measure the mid-span deformation and two supports settlements of right restraint beam. Similarly, three LVDTs (L15, L16, and L17) were used to monitor the horizontal mid-span deformation and settlements of left restraint beam. For unrestrained cruciform tests (CR4, CR5 and CR6), in order to obtain explicit

rotation measurements of beam sections, two sets of LVDTs (D9, D10 and D11, D12) were placed at each end of beam section outside the furnace at ± 120 mm distance from horizontal central axis, as shown in Figure 7.6. Based on experience from the first group of specimens, column deflections were monitored by two LVDTs (D1 and D2) with a measurement capacity of 300 mm at each side of column top stiffener. Another three LVDTs were installed onto each beam section to record beam vertical deflections as (D3, D4, D5 and D6, D7, D8).

7.2.6 Temperature Distribution Acquisitions

During the elevated temperature tests, temperature distributions within cruciform specimens were measured by thermocouples at locations shown in Figure 7.8 until the steel joint reached the desired uniform temperature.

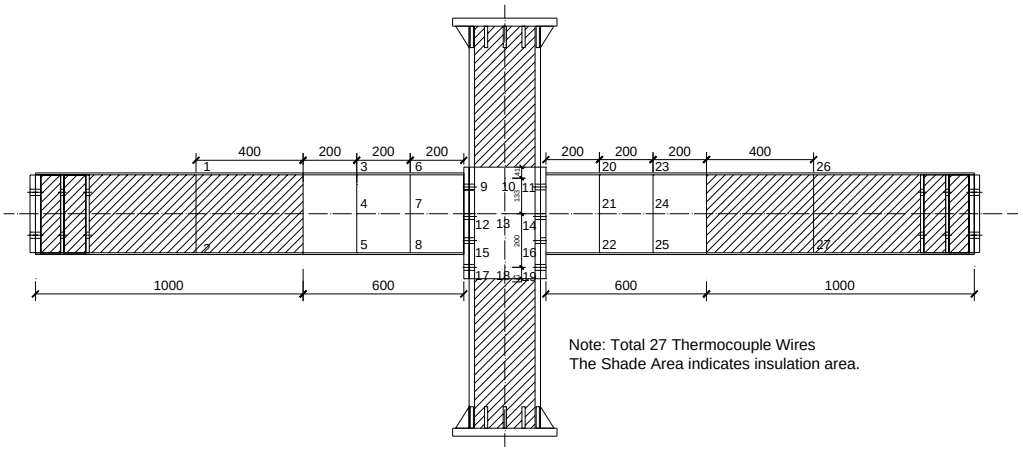

Figure 7.8 Thermocouple Wire Locations

As shown in Figure 7.8, to obtain a clear picture of temperature distribution within the left and right beam sections, eight K-type thermocouple wires with 1.6 mm sheath were attached onto surfaces of web plate, top and bottom flanges. There were eight additional thermocouple wires to monitor the temperatures of high strength bolts as shown in Figure 7.8. In addition, temperature of column web panel have also been recorded at three elevations along the column axis. Besides the

specimen temperature distributions, furnace temperature was monitored by two thermocouple wires attached to the side heating panels. All thermocouple wires were connected to Fluke HYDRA temperature acquisition system and recorded at time interval of fifteen seconds. For the first group of specimens, remote parts of beam and column sections from the joint zone were thermally protected using ceramic fibre wools to reduce the possibility of failure and to reduce heat transport to external air and axial hydraulic jack. Top flange and web of the beam sections within about 600 mm from either face of the joint, and the column section within steel joint were exposed to radiation of heating furnace as shown in Figure 7.8. In contrast, for the second group of specimens (CR4, CR5 and CR6), remote parts of beam sections were not thermally insulated since there was no axial jack attached onto beam sections. Therefore, only remote parts of column sections were insulated using ceramic fibre wools.

7.3 Cruciform Test Procedure

Steady-state heating has been used in current experimental programme. This was because the main objective was to obtain moment-rotation-temperature characteristics of bare steel end-plate joints at isothermal condition. Therefore, a uniform temperature distribution within the joint specimen was desirable, with minimal temperature differences. During the heating stage, the furnace and the specimen temperatures were monitored by K-type thermocouple wires and recorded at fifteen seconds interval. To minimize the heat loss, the openings at both sides and at the top for the protruded beams and column were heavily insulated by wool and insulation cloth. As described in Section 7.2.3, there were three cruciform specimens tested at 700 ^{o}C (CR1, CR2 and CR3) with three different restraint force levels. The experimental procedure consisted of three steps: *1.* Load the beam axially to desired level; *2.* Heat the cruciform specimen to desired temperature distribution and manually maintain the horizontal applied load; *3.* Apply vertical

load at the column top until the joint fails. For the second group of tests, there were three cruciform specimens (CR4, CR5 and CR6) tested under unrestrained boundary conditions. The experimental procedure consisted of two steps: *1.* Heat the cruciform specimen to desired temperature distribution; *2.* Apply vertical load at the column top until the joint fails.

7.4 Cruciform Experimental Results and Discussions

This programme is to obtain moment-rotation characteristics of a steel joint at different temperature levels and with various axial restraint force ratios in beams. This part of experimental work consisted of three cruciform specimens tested at 700 ^{o}C with axial restraint force ratio at 0, 2.5 and 4% of plastic squashing capacity of beam sections at ambient temperature. Another three cruciform specimens were tested at 400, 550 and 700 ^{o}C without axial restraint force. These three temperatures were selected due to that they represent significant degradations of steel material properties as shown in Figure 3.5 and Figure 3.6.

7.4.1 Restrained Cruciform Test Temperature Measurement

Temperature distributions of restrained cruciform specimens have been recorded by twenty-seven thermocouples as shown in Figure 7.8. Figure 7.9 shows typical temperature developments for CR1 specimen.

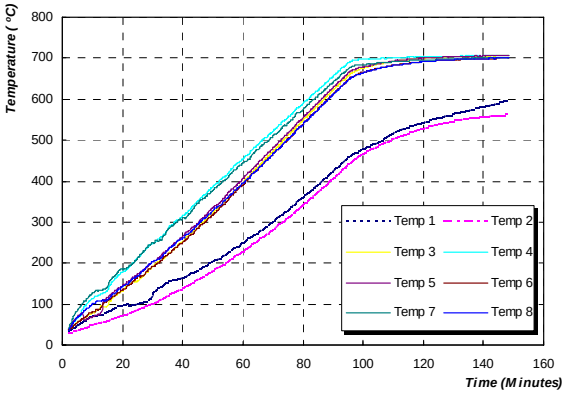

(a) Left Beam Temperature Distribution

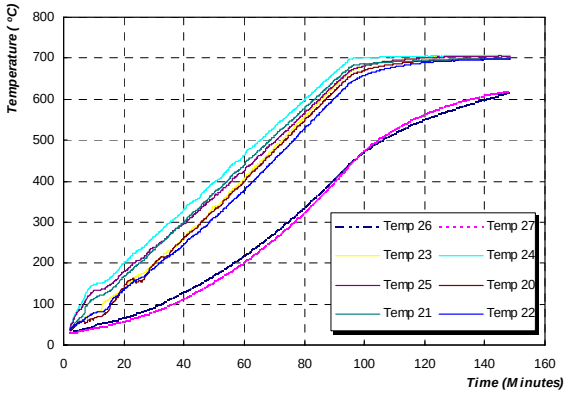

(b) Right Beam Temperature Distribution

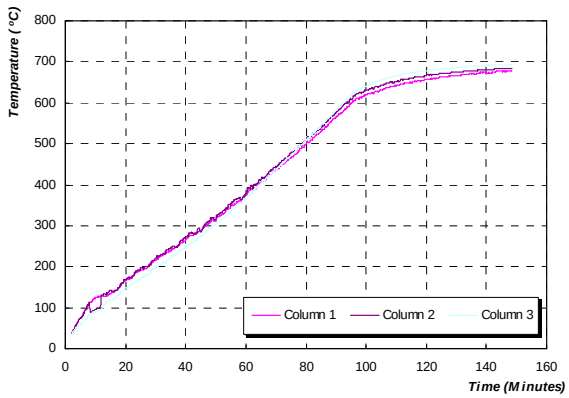

(c) Column Web Panel Temperature Distribution

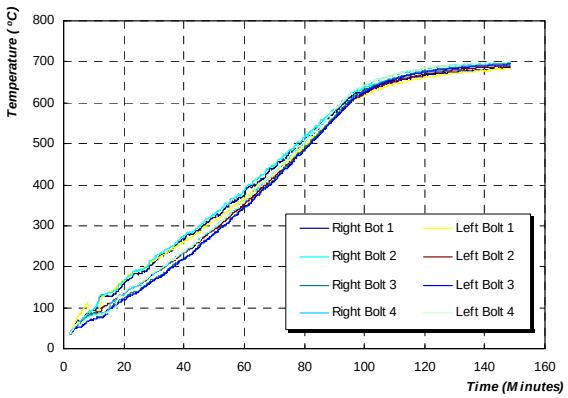

(d) Connecting Bolts Temperature Distribution

Figure 7.9 Typical Temperature Distribution of CR1

Figure 7.9(a) and (b) represent temperature distributions for left and right beams. Due to thermal insulation, bottom flange temperatures (Temp 5 and 8 for left beam, Temp 22 and 25 for right beam) increase slowly as compared to beam web panels and top flange. Temperature difference among bottom flange, web panel and top flange of the beam section increases to about 30 ^{o}C after 100 minutes of heating when joint area of specimen reaches the target temperature (700 ^{o}C). Due to heavy thermal insulation, temperature distributions within the insulated areas of left and right beams (Temp 1 and 2 for left beam, Temp 26 and 27 for right beam) rise much more slowly than the exposed area. Temperature difference between the insulated area and the exposed area approaches to approximately 120 ^{o}C after CR1 specimen reaches desired temperature at 700 ^{o}C as shown in Figure 7.9(a). Due to heat loss through radiation from the observing window of furnace (as shown in Figure 7.4), there is a clear temperature difference of 30 ^{o}C between the column web panel and the beam sections as shown in Figure 7.9(a), (b) and (c). Similarly, due to insulation and heat loss through radiation, it can be observed that temperature of the bottom row of bolts (right bolt 4 and left bolt 4 as shown in Figure 7.9(d)) increase slightly more slowly than the upper row of bolts. However, temperature difference between the bottom row of bolts and other rows decreases to as small as 10 ^{o}C as shown in Figure 7.9(d).

Since CR1, CR2 and CR3 were tested at a rather high temperature of 700 ^{o}C, average relative temperature distributions of test cruciform assemblies are summarized in Table 7.2. Temperature measurements across the beam sections were determined based on average thermocouple readings of the same locations at left and right beams. The same approach was adopted for temperature measurement of bolt rows. For ease of reference, relative temperature measurements in Table 7.2 are presented in a non-dimensional form, obtained by dividing average thermocouple measurements by the reference temperature at beam top flange.

In Table 7.2, there is negligible temperature variation in the beam area adjacent to steel joint, viz. beam top flange and web. Therefore, the joint area temperature can be represented by the average value of these two measurements. However, beam bottom flanges have been thermally insulated with a maximum difference of 0.9% for CR3 specimen. Due to heavy insulation at remote parts of beam from the joint area, relative temperature measurements show a maximum difference of approximately 13% compared to beam top flange temperatures. Due to heat loss by radiation and column thermal insulations, bolts and column web temperatures at the top of joint area is approximately 2% lower than the beam top flange temperature. However, this difference decreases significantly for bolts and column webs in the centre and bottom area of joint. It can be seen that the average furnace atmosphere temperature is approximately 2% higher than the beam top flange temperature. Table 7.2 also shows cross-sectional average temperature measurements for beam sections, bolts and column web as S1 to S5 for CR1, CR2 and CR3 as shown in Table 7.2. Clearly, it can be seen that there is a temperature gradient along the beam length. Due to heat loss from observing windows, the average section temperatures for S2, S4 and S5 are slightly lower than the reference section S1. In addition, because of thermal insulation at section S3, average temperature at this part shows a significant decrease.

Table 7.2 Relative Temperature Measurements for CR1, CR2 and CR3

Location	CR1	CR2	CR3	Average	Location	CR1	CR2	CR3	Average
T1	1.000	1.000	1.000	1.000	T10	0.961	0.969	0.985	0.972
T2	1.000	0.992	1.006	0.999	T11	0.969	0.977	0.993	0.980
T3	1.000	0.999	0.997	0.999	T12	0.983	0.991	1.004	0.992
T4*	0.842	0.826	0.925	0.864	S1	1.000	0.997	1.001	0.999
T5*	0.794	0.838	0.965	0.866	S2	0.992	0.991	0.993	0.992
T6	0.973	0.977	0.978	0.976	S3*	0.818	0.832	0.945	0.865
T7	0.979	0.983	0.985	0.982	S4	0.982	0.986	0.990	0.986
T8	0.986	0.989	0.998	0.991	S5	0.971	0.979	0.994	0.981
T9	0.990	0.994	0.999	0.994	Furnace	1.002	1.001	1.016	1.006

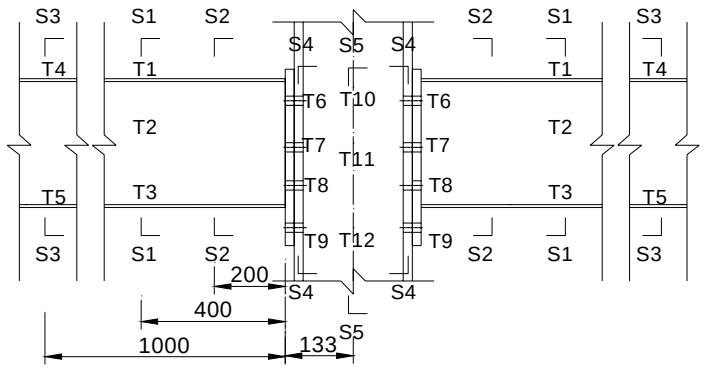

* Thermal Insulation Area

7.4.2 Restrained Cruciform Test Deflection Characteristics

No axial compressive force was applied to the first cruciform specimen (CR1) tested when joint average temperature reached 700 ^{o}C. Detailed experimental results are shown in Figure 7.10. As presented in Section 7.2.5, there were ten LVDTs measuring vertical deflections along both left and right beam top flanges (Figure 7.7). Corresponding beam deflection measurements of CR1 are shown in Figure 7.10(a) and (b). From the load-deflection curves, it can be seen that vertical deflection measurements increase linearly up to certain load (approximately 36 kN). Then run-away deflection occurs with further load increment until the failure load approaches 60 kN. In addition, it can be noticed that small negative deflection

occurs before vertical load is applied. This is because temperature of beam top flange and web panel increased faster than that of bottom flange as shown in Figure 7.9. Besides, it is shown that vertical deflections of both left and right beams are in reasonably good agreement. This validates the set-up of thermal insulation and cruciform specimens. Similarly, measured vertical deflection at the column top is shown in Figure 7.10 (c). It can be seen that thermal expansion at the column top was approximately 2 mm before vertical load was applied. This is close to theoretical prediction of thermal expansion of column which is 2.5 mm. After vertical load approached failure load (approximately 60 kN), vertical deflection increased rapidly to 50 mm, and eventually grew to around 80 mm due to spread of plasticity in the steel specimen. At failure, the column vertical deflection increased significantly, and it was difficult to continue applying the vertical load due to rapid deflection. After the test, it was observed that failure of specimen was mainly due to yielding of the end-plate adjacent to the beam bottom flange as shown in Figure 8.7, and out-of-plane deflection in the beam web panel as described in Section 7.4.3. Average rotations obtained from beam displacements for left and right joints are compared in Figure 7.10(d). It can be seen that rotations for both joints are in good agreement. However, initial negative rotation of the left joint is slightly less than that of the right joint. This difference becomes negligible after applied moment exceeds 20 kNm. It can also be seen that the left and the right joints are capable of resisting moment up to around 30 kNm without experiencing any significant rotations. When moment approaches 50 kNm, joint rotation increase significantly, resulting in a plateau of moment-rotation curves followed by joint failure.

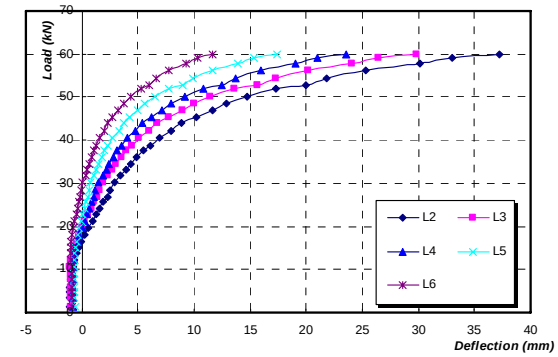

(a) Left Beam

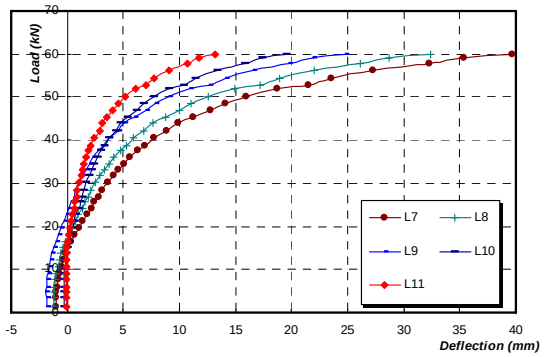

(b) Right Beam

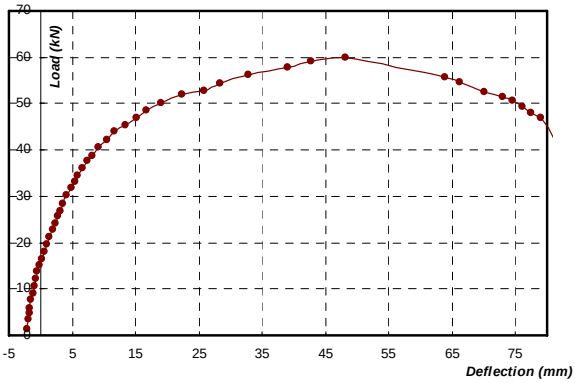

(c) Column Top

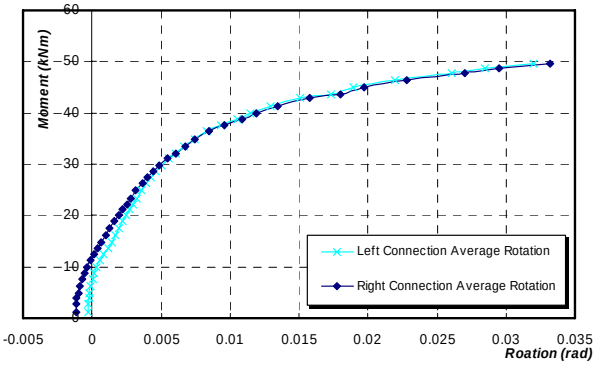

(d) Beam Rotations

Figure 7.10 Deflection and Rotation Measurements of CR1

For CR2 test, 45 kN axial force was applied to beam sections before vertical load was applied, which was 2.5% of compressive capacity of beam section at ambient temperature. Recorded deflections and rotations are given in Figure 7.11. From vertical beam deflection measurements in Figure 7.11(a) and (b), it can be seen that negative deflection measurements for both left and right beams are greater than CR1 test, due to axial compressive force and thermal bowing of beams at elevated temperature. Also, it can be found that compared with CR1, both the left and the right beams show stiffer load-deflection characteristics before load reaches 30 kN. This is because of larger negative beam deflections after heating stage. When external load reaches 40 kN, the beams start to sag downwards. Applied axial restraint force can induce significant increase of beam deflections and speed up the run-away deflection, due to P-δ effect.

Load-versus-column top deflection relationship of CR2 is shown in Figure 7.11(c). It can be seen that relative thermal expansion measurement at column top was around 3 mm before loading was applied. Vertical deflection of column top increased linearly up to 15 mm. Then the load-deflection curve followed a nonlinear shape and a plateau indicating joint failure. Figure 7.11 (d) shows joint rotations versus applied moment. It can be seen that there is a good agreement between the left and the right joints. Both joints can sustain up to 30 kNm of moment without any significant rotations. After which, joint rotations started to increase progressively due to spread of plasticity in the joints, mainly due to a combination of yielding of end-plate and out-of-plane deflections at beam web panels. The bending moment sustained by the joints was slightly reduced in comparison with CR1 due to axial compression.

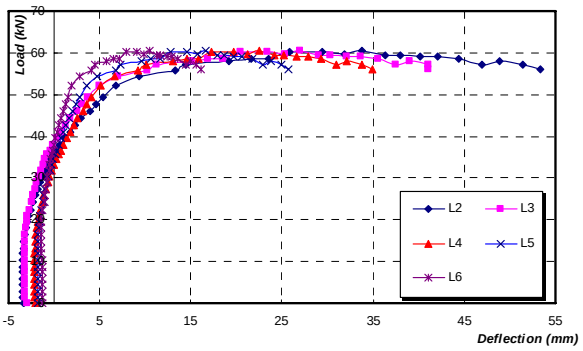

(a) Left Beam

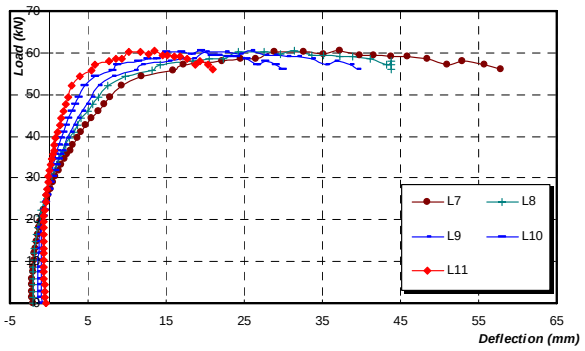

(b) Right Beam

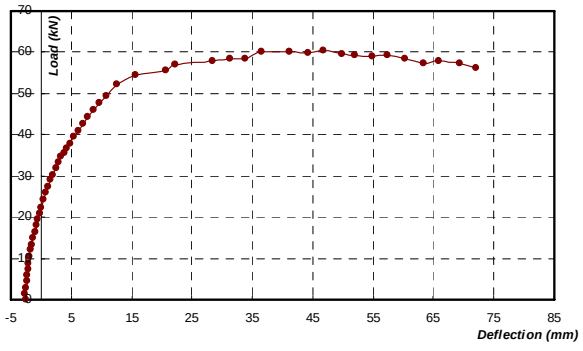

(c) Column Top

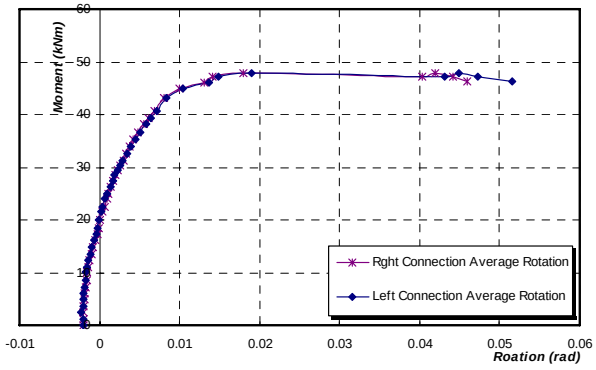

(d) Beam Rotations

Figure 7.11 Deflection and Rotation Measurements of CR2

CR3 was tested at 700 ^{o}C with 72 kN axial compressive force, which was 4% of compression capacity of beam section at ambient temperature. Beam vertical deflection measurements are shown in Figure 7.12 (a) and (b), except for LVDT5 and 11 due to malfunctions. It can be seen that negative deflection measurements for two beams are smaller than the previous two tests (CR1 and CR2), due to higher temperature of beam web panels compared to top and bottom flanges as shown in Table 7.2. In the presence of high axial compression, vertical deflections increased linearly up to 25 kN. With increasing load, the beams started to deflect rapidly until the joint failed at 50 kN, which was mostly due to a combination of yielding of end-plate and out-of-plane deflections at beam web panels.

Vertical deflection at column top versus load is shown in Figure 7.12(c). It can be seen that there is similar load-deflection characteristics between column top and the beams. Vertical deflection of column top increases up to around 65 mm when load reaches failure value. The beam rotations for left and right joints are shown in Figure 7.12(d). It can be seen that there are minor variations between the rotations measured for these two joints. Due to higher axial compressive force, ultimate bending moment of joints is reduced to 45 kNm in comparison to that of CR1 and CR2 specimens.

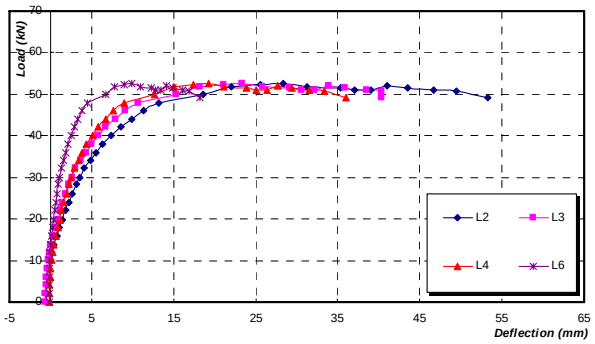

(a) Left Beam

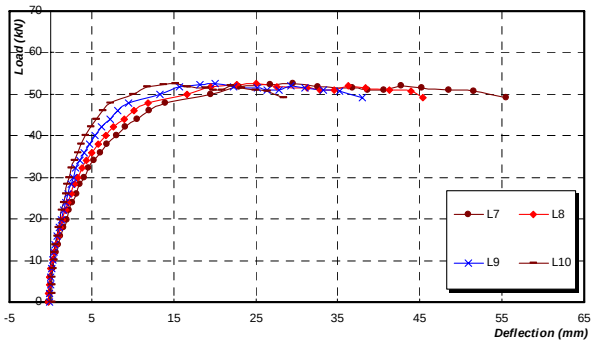

(b) Right Beam

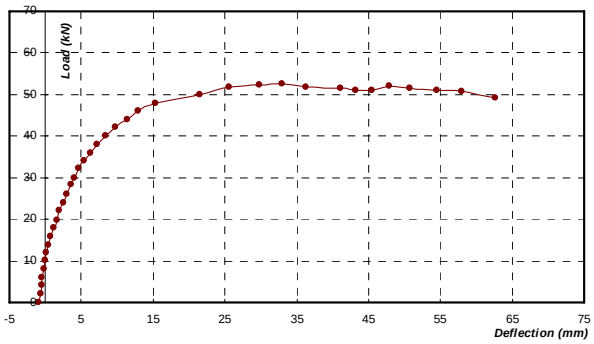

(c) Column Top

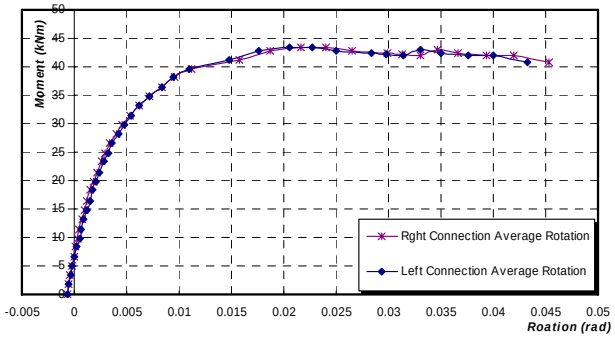

(d) Beam Rotations

Figure 7.12 Deflection and Rotation Measurements of CR3

Detailed deflection and rotation characteristics for the first group of cruciform tests are illustrated in Figure 7.10 to 7.12. From these measurements, it can be seen that there is good agreement between the rotations of the left and the right joints for each test indicating the loading arrangement was rather symmetrical. Load-deflection characteristics from CR2 test was slightly stiffer than CR1 due to larger negative beam deflections in CR2 after the heating stage just before loading was applied. In the presence of axial restraint which induced P-δ effect and additional compressive stress in the critical compression zone, a reduction in the joint moment capacity can be observed for CR2 and CR3 compared with CR1 tested without thermal restraint. Tested cruciforms showed clearly out-of-plane deflection in the beam web panels, as described in Section 7.4.3. In addition, for CR1, CR2 and CR3, significant bending deformations were observed at the end-plate adjacent to the beam bottom flange due to significant tensile stress from bending moment action. This was confirmed with numerical simulations in Section 8.3.3. Generally, in these three restrained specimens, CR1 shows the greatest end-plate bending deflection due to a greater tensile force transferred from the beam bottom flange, followed by CR2, and then CR3. It should be noted that, for CR2 and CR3, bending deformations in end plates are not as significant compared to CR1 due to axial compressive forces.

7.4.3 Beam Web Measurements of Restrained Cruciform Tests

For the first group of steel joint tests, all three specimens (CR1, CR2 and CR3) show that certain out-of-plane deflections can be found for beam web panels adjacent to the steel joints. Thus, for purpose of obtaining accurate deflection behaviour, cruciform specimens have been dismantled, with the beam sections measured by a special scanning system. These three specimens were measured after tests to ascertain if shear web buckling has occurred in the web. In this section, this scanning system and measurements will be introduced and discussed.

This scanning system (Figure 7.13) consists of one measuring frame, an adjustable sitting table, a vertical line transducer, a transverse deflection transducer and one automatic hoisting system. In this system, the out-of-plane deflections were measured by the transverse deflection transducer along each reference line. The transducer was raised by the hoisting system. To obtain an accurate profile measurement, seven longitudinal reference lines were first drawn onto the beam sections (Figure 7.14). The measurements started from the vertical reference line 50 mm apart from the beam left vertical stiffener as shown in Figure 7.14. The measuring procedure consisted of three stages: *I.* Erect the beam section onto the sitting table, with welded end-plate on top; *II.* Calibrate initial positions of line and transverse transducers; and *III.* Measure out-of-plane deflections along each reference line.

Typical out-of-plane deflection measurements from beam web panels of CR2 are shown in Figure 7.15. For left beam measurements, right end of beam web represents area adjacent to steel joint. The converse is true for the right beam measurement. From Figure 7.15, it can be seen that both the left and the right beam webs show out-of-plane buckling near steel joint. The maximum out-of-plane deflections are 6 mm and 8 mm, respectively. Though these out-of-plane deflections

are insignificant in comparison with vertical deflections of test cruciforms, it is clear that, for this group of specimens, shear buckling has occurred in the beam web near to joint.

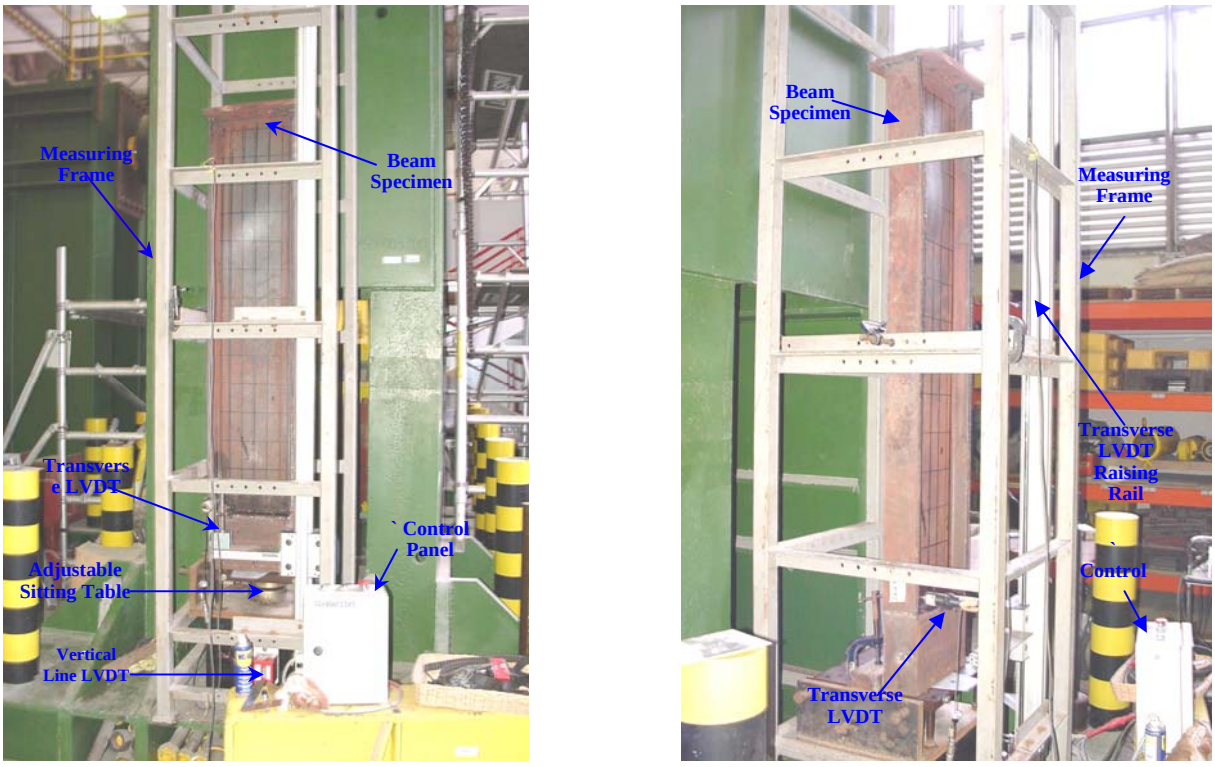

Figure 7.13 Measurement Scanning System Details

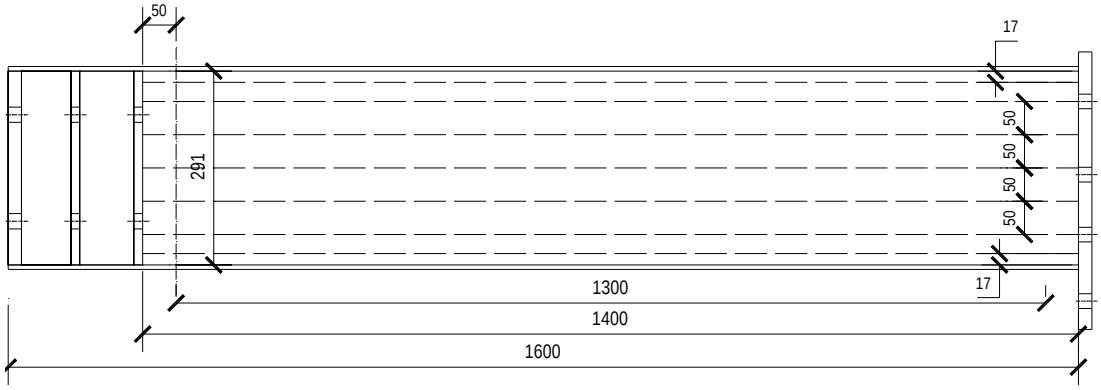

Figure 7.14 Measurement Reference Lines for Left Beam Section of Cruciform

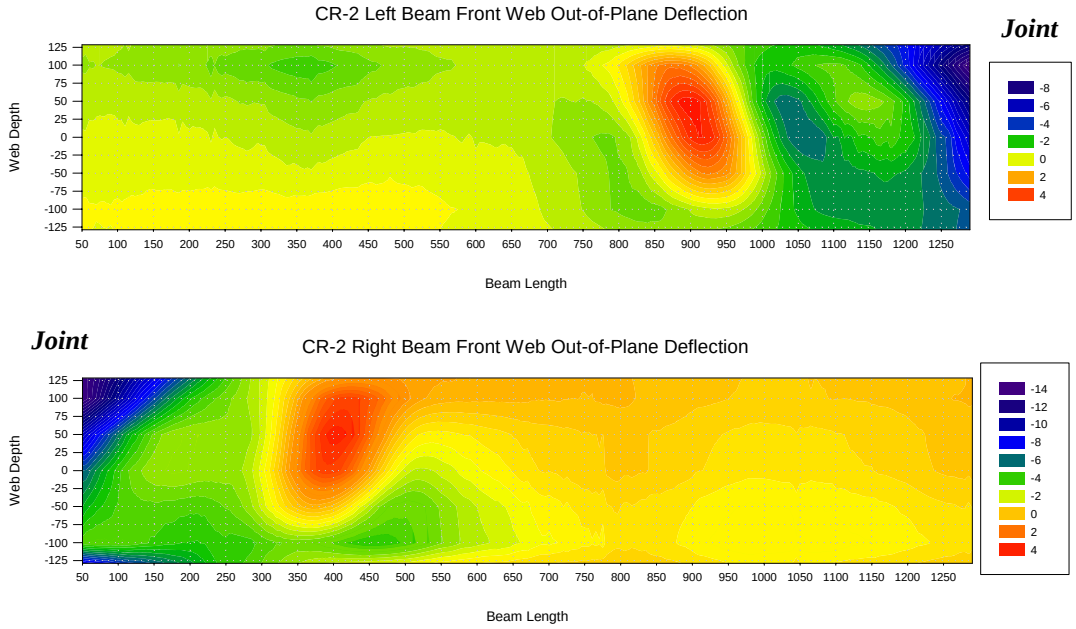

Figure 7.15 Test Web Panel Out-of-Plane Deflection Measurement of CR2

7.4.4 Initial Imperfection Measurement of Unrestrained Tests

From testing of the first group of specimens, it was realized that initial out-of-plane imperfection has considerable influences on beam web shear behaviour, as described in Section 6.2. Thus, for the second group of specimens (CR4, CR5 and CR6), prior to assembly with column sections, initial imperfections of beam web panels have been measured by the scanning system as shown in Figure 7.13. However, only three longitudinal reference lines were drawn onto the beam webs, that is, the web midline and other two reference lines at 70 mm distance from the midline, as shown in Figure 7.16. Different from the first group of measurements, scanning was started from the vertical reference line at 50 mm distance from the end-plate.

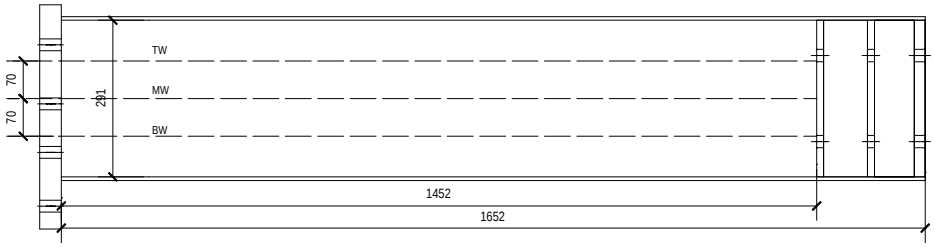

Figure 7.16 Measurement Reference Lines for Unrestrained Cruciform Tests

Initial out-of-plane imperfection measurements were conducted on six beam sections. Typical measurements of left beam web of CR4 are shown in Figure 7.17.

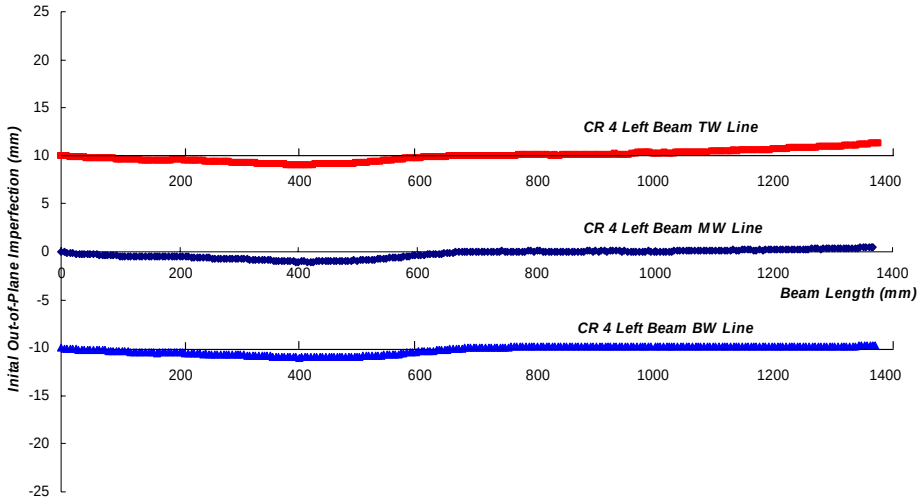

Figure 7.17 Initial Out-of-Plane Deflection Measurements for CR4 Left Beam Web

It can be seen that the initial imperfections along three reference lines (BW, MW and TW) indicate similar deflected trends along beam length. The maximum relative initial imperfections are located near to the beam end stiffeners. In comparison, there is less imperfection in the web panel near to the welded end-plate. The detailed maximum initial out-of-plane imperfections of CR4, CR5 and CR6 are shown in Table 7.3. The measured initial imperfections will be introduced into the numerical simulations as described in Section 8.3 for CR4, CR5 and CR6. However, due to time constraint, initial beam web out-of-plane imperfections of the first group of specimen (CR1, CR2 and CR3) were assumed as half-wave sinusoidal curve along the beam length in finite element simulations, with maximum magnitude of imperfection as D/3000. This is in accord to the assumption used in plate girder numerical analyses presented in Section 6.2. In addition, due to significant beam out-of-plane deflections occurred after the second group of tests, deflected shapes for this group of specimens showed no need to be scanned, which will be presented in Section 8.3, with comparisons to finite element simulations.

Table 7.3 Maximum Initial Out-of-Plane Measurements for Unrestrained Cruciform Beam Sections

Cruciform Specimen	Left Beam	Maximum Imperfection (mm)	Right Beam	Maximum Imperfection (mm)
CR4	TW	1.3107	TW	2.0124
	MW	1.0523	MW	1.8281
	BW	1.0025	BW	0.7133
CR5	TW	2.2413	TW	2.5910
	MW	1.4105	MW	1.1126
	BW	0.6271	BW	0.8095
CR6	TW	0.9676	TW	2.7484
	MW	0.8430	MW	2.1259
	BW	0.4500	BW	0.7861

7.4.5 Unrestrained Cruciform Test Temperature Measurements

For the second group of cruciform tests, three specimens (CR4, CR5 and CR6) were tested at 400, 550 and 700 ^{o}C. Temperature distributions have been recorded by attached thermocouple wires as shown in Figure 7.8. Typical temperature developments for CR4 test are shown in Figure 7.18.

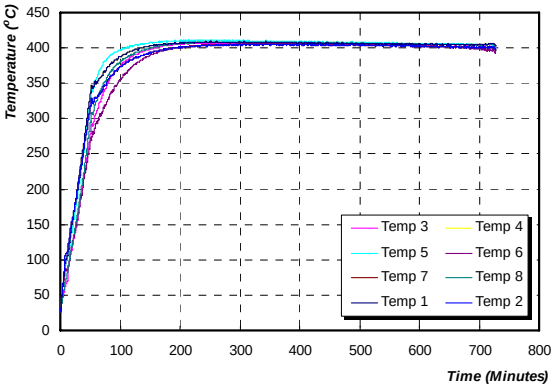

(a) Left Beam Temperature Distribution

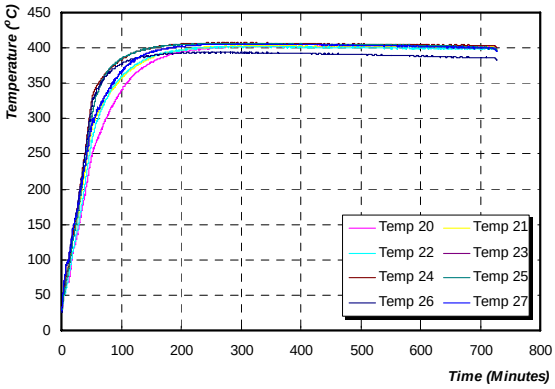

(b) Right Beam Temperature Distribution

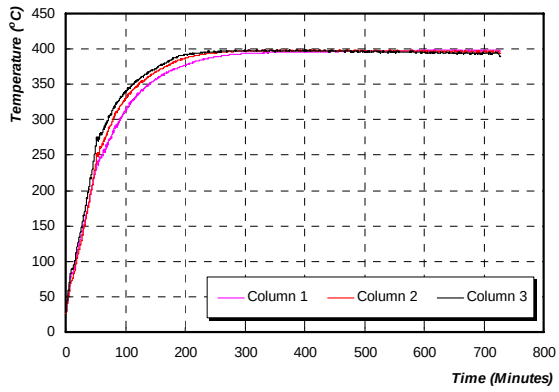

(c) Column Web Panel Temperature Distribution

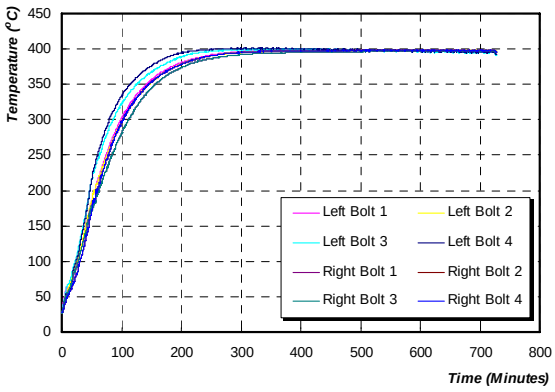

(d) Connecting Bolts Temperature Distribution

Figure 7.18 Typical Temperature Distribution of CR4

Figure 7.18(a) and (b) present temperature distributions for the left and the right beams of CR4. Different from the first group of tests, beam sections were not insulated at the remote parts, since there was no axial load applied at the beam ends. From temperature developments as shown in Figure 7.18(a) and (b), it can be seen that, disregarding presence of small discrepancy, beam sections eventually reach approximately uniform temperature distributions. This is because furnace was normally kept heating for extra 200 minutes after furnace control temperature reached target level. For this group of test, observing windows of furnace were blocked by lateral restraint beams as shown in Figure 7.6. This reduced heat radiation loss. Thus, it can be seen that a more uniform temperature distribution was achieved for both column web and bolts as shown in Figure 7.18(c) and (d).

Similar to the first group of tests, the average relative temperature distributions of the second group of tests are summarized in Table 7.4. Due to geometric symmetry of specimens, the average temperatures of both beams and bolts are determined from the records of thermocouple readings at the same locations on either side of the joints. All the relative temperature measurements in Table 7.4 are obtained through dividing the average thermocouple readings by the reference temperature at the beam top flange. For CR4, CR5 and CR6, these reference temperatures are

402.6, 547.3 and 699.4°C, respectively. From Table 7.4, it can be seen that the temperature of beam top flange in remote area is approximately 2% lower than that of beam top flange adjacent to steel joint, due to thermal insulation from cover panels of furnace. However, temperature differences among other parts of specimens are relatively insignificant compared to the first group, indicating uniform temperature distribution across the sections in these three specimens. Besides, the average furnace atmosphere temperature was about 1.5% higher than the beam top flange temperature. In addition, from sectional average temperatures (S1 to S5), there is negligible temperature gradient along the beam length.

Table 7.4 Relative Temperature Measurements for CR4, CR5 and CR6

Location	CR1	CR2	CR3	Average	Location	CR1	CR2	CR3	Average
T1	1.000	1.000	1.000	1.000	T10	0.978	0.995	0.990	0.988
T2	1.003	1.000	1.000	1.001	T11	0.984	0.989	0.986	0.986
T3	1.002	1.000	1.000	1.001	T12	0.983	1.000	0.991	0.991
T4*	0.968	0.976	0.977	0.974	S1	1.002	1.000	1.000	1.001
T5*	1.002	0.999	1.003	1.001	S2	0.993	0.999	0.999	0.997
T6	0.983	0.997	1.001	0.994	S3	0.985	0.987	0.990	0.987
T7	0.981	1.000	0.986	0.989	S4	0.985	1.001	0.993	0.993
T8	0.988	1.004	0.993	0.995	S5	0.981	0.995	0.989	0.989
T9	0.990	1.004	0.994	0.996	Furnace	1.006	1.022	1.002	1.010

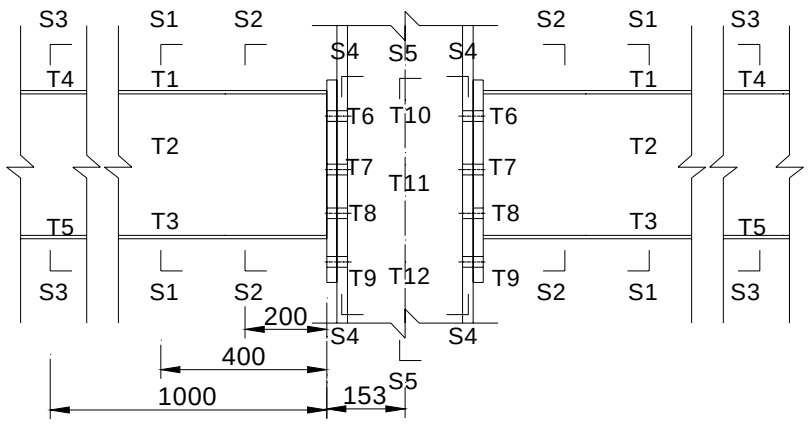

* Beam Remote Area from Steel Joint

7.4.6 Unrestrained Cruciform Test Deflection Characteristics

For the second group of tests, vertical deflections of left and right beams were monitored by three LVDTs (D3 to D5 and D6 to D8 as shown in Figure 7.6), at distance of 270, 870 and 1070 mm from column flange. Vertical deflections at column top were recorded by two deflection transducers (D1 and D2) with 300 mm stroke. Moreover, another two sets of LVDTs (D9, D10 and D11, D12) were installed at each end of beam sections, to obtain explicit beam rotations.

CR4 was tested at 400 ^{o}C without axial compressive force. Vertical deflections of left and right beams are shown in Figure 7.19(a) and (b), respectively. It can be seen that both left and right beams are capable of resisting vertical load up to approximately 250 kN. After this value, the load-deflection curve becomes nonlinear up to around 350 kN, indicating yielding of beam web shear component inside the steel joints. With further load increment there is progressive run-away of deflection until failure is reached at about 380 kN. Although left beam deflects at a slightly faster rate than right beam, it can be noticed that vertical deflections of both left and right beams are in reasonable agreement. It is also noticed that vertical deflection at D6 stops at around 95 mm, due to measurement stroke of 100 mm.

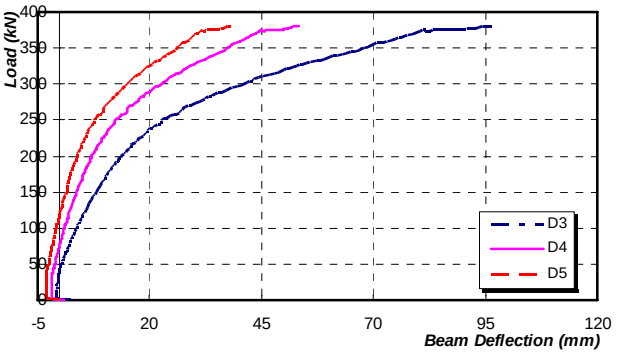

(a) Left Beam

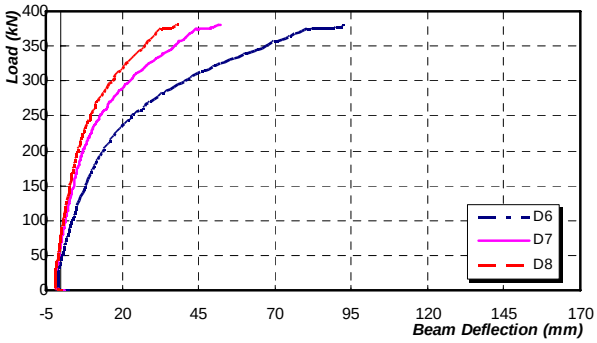

(b) Right Beam

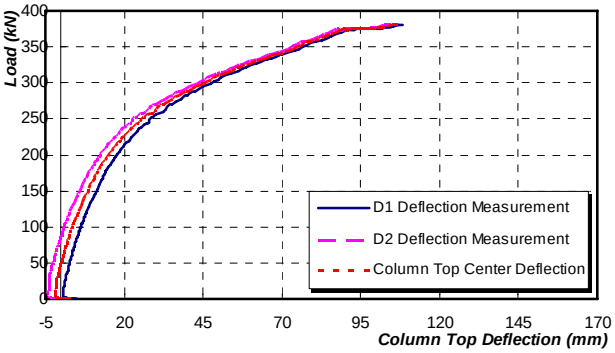

(c) Column Top

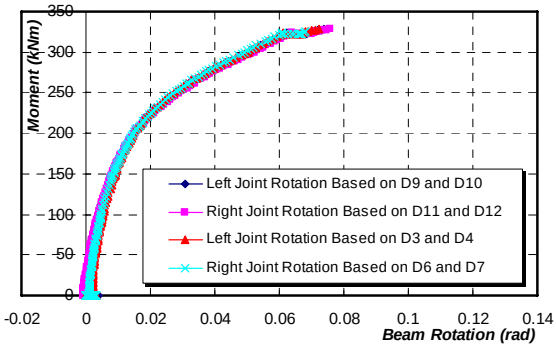

(d) Beam Rotations

Figure 7.19 Deflection and Rotation Measurements of CR4

Column vertical deflections obtained from average measurements of D1 and D2 of CR4 are shown in Figure 7.19 (c). CR4 was tested at 400°C with no external restraint. It can be seen that initial thermal expansion was not exactly equal from D1 and D2 measurements, possibly due to frictions between roller plates (⑤) and restraint support plate systems (④) as shown in Figure 7.6. However, this difference became negligible when applied load exceeded 300 kN. There was an approximately linear increase in deflection up to around 250 kN. Beyond this limit, vertical deflection increased significantly up to around 70 mm, and finally reaching 110 mm at joint failure. This was due to formation of tensile field action in the beam web panels, similar to shear failure mode in plate girders, as shown in Figure 8.8 (a). Rotations obtained from beam end deflections (D9, D10 and D10, D11) for both left and right beams are compared in Figure 7.19(d). In addition, rotations derived from beam vertical deflections are also incorporated as supplementary verifications. It can be seen that rotations for left and right joints are in good agreement. Rotations of joints linearly increase up to 0.02 radians, with bending moment reaching approximately 220 kNm. Beyond this limit, rotation starts to increase rapidly indicating yielding of steel joints. Rotations reach a plateau after exceeding 0.07 radians, representing joint failure. Figure 7.19(d) also compares rotations derived from beam end and vertical deflection measurements. They are in good agreement.

Second Specimen CR 5 was loaded till failure at 550°C. Beam vertical deflections recorded by transducers are shown in Figure 7.20 (a) and (b), respectively. It can be seen that initial negative deflections for both left and right beams were greater than those of CR4 test due to higher test temperature. Similar to CR4, beams showed smooth deflection response until vertical load reached 150 kN. Above this limit, vertical deflections of specimen increased rapidly with slight loading increment. And finally, at around 150 kN, it was difficult to further increase applied loads, indicating joint failure due to significant beam out-of-plane deflections.

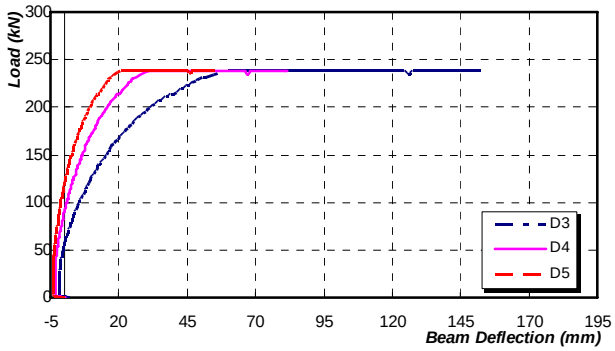

(a) Left Beam

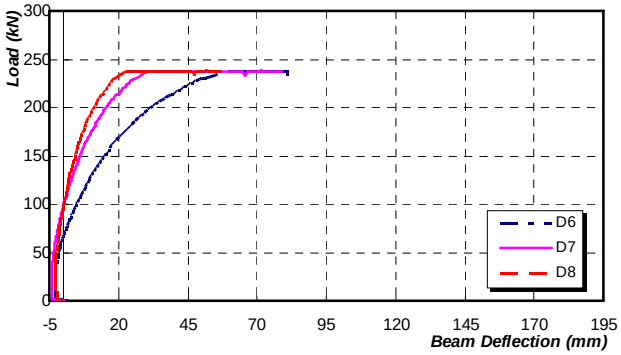

(b) Right Beam

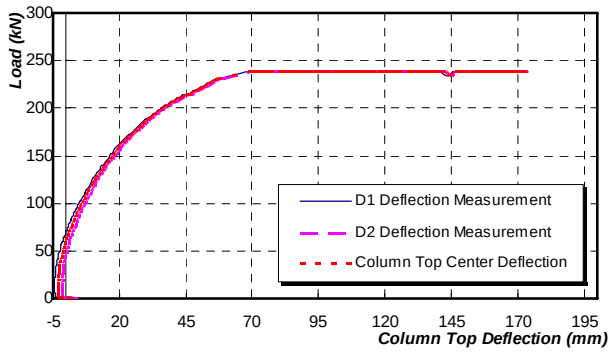

(c) Column Top

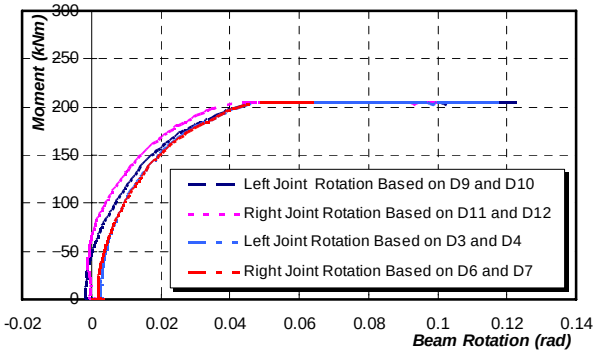

(d) Beam Rotations

Figure 7.20 Deflection and Rotation Measurements of CR5

Average vertical deflection of column top is shown in Figure 7.20(c) compared with deflection measurements by D1 and D2. Due to elimination of frictions induced by lateral restraint system, it can be seen that measurements by two deflection transducers are in good agreement. Vertical deflection of column top increases linearly to 70 mm and finally reaches 172 mm. Beam rotations obtained from vertical and horizontal end displacement measurements are compared in Figure

7.20(d). It can be seen that rotations derived from vertical deflections show a slightly more flexible behaviour. However, the agreement is generally acceptable.

As the third specimen of this group, CR6 was loaded under a uniform temperature of 700 ^{o}C. Vertical deflection measurements of beams are shown in Figure 7.21 (a) and (b), respectively. It can be seen that negative deflection measurements for two beams were greater than previous two tests (CR4 and CR5), due to even higher isothermal temperature. From load-deflection relationships, vertical deflections increased linearly up to approximately 70 kN with a rapid growth until failure load (approximately 87 kN), which was mainly due to a combination of slipping of bottom rows of bolts in tension and out-of-plane deformations in beam web as described in Section 8.3.3.

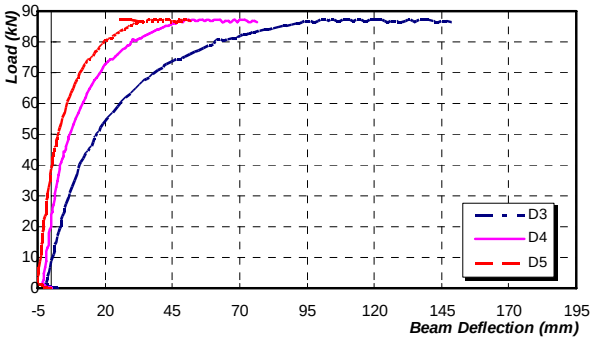

(a) Left Beam

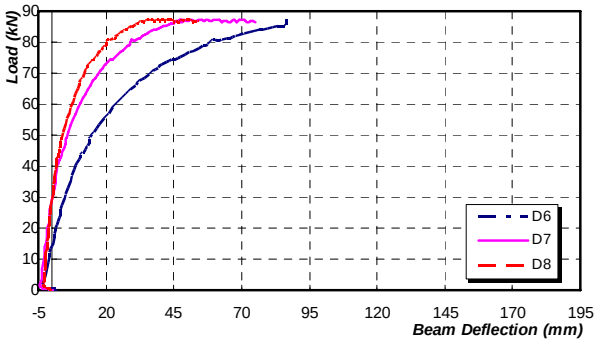

(b) Right Beam

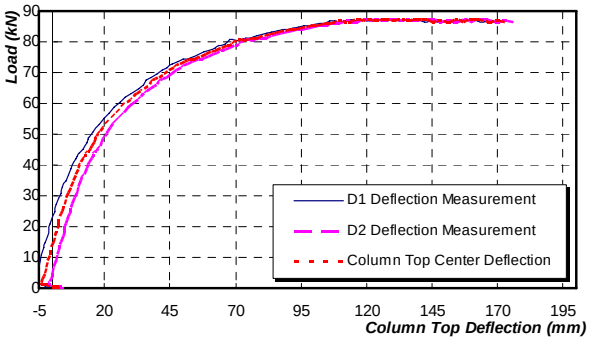

(c) Column Top

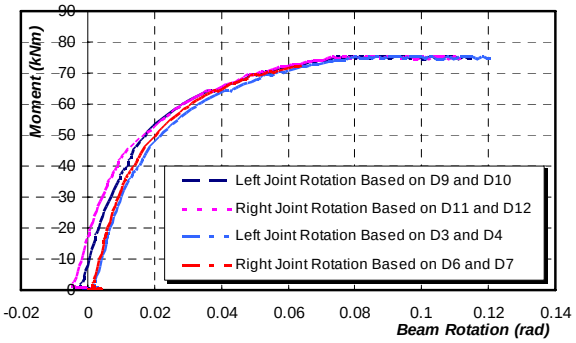

(d) Beam Rotations

Figure 7.21 Deflection and Rotation Measurements of CR6

Average vertical deflection of column top obtained from transducers D1 and D2 are presented in Figure 7.21(c). Column top deflection increases significantly when

load reaches approximately 87 kN. However, it can be noticed that CR6 shows a significant increase in ultimate strength, in comparison with CR1 tested at 700 ^{o}C without axial compressive force. This is due to modifications of cruciform specification as described in Section 7.2.2, with thicker end-plate and larger diameter bolts. Rotations obtained from both vertical and horizontal end deflections are compared in Figure 7.21(d). It can be seen that there is a close correlation between the left and the right joints.

Detailed joint responses for the second group of unrestrained cruciform tests (CR4 to CR6) are presented in Figure 7.19 to 7.21. For these three specimens tested at three different isothermal temperatures, rotational characteristics obtained from the beam end deflections and vertical deflections show a similar trend. Based on deflection measurements, it may be seen that there is a progressive degradation in the bearing capacity and stiffness of joints with increasing temperature. Due to the presence of flange cover plates, CR4 specimen shows significant out-of-plane deflections in the web panel region adjacent to the steel joint. Test results will be compared with numerical simulations in Section 8.3.3. However, at a higher temperature of 700^{o}C, CR6 specimen exhibits less significant out-of-plane deformation for web plate, because that the steel material stress-strain curve does not have a distinct demarcation point between the elastic and the plastic stages. At this temperature, it is analogous to a rubbery material with continuous non-linearity. Thus, at much higher isothermal temperature such as 700 ^{o}C, under increasing load the web plate simply softens.

7.5 Conclusion

The “Component-Based” method was utilized to explore the mechanical behaviour of typical steel beam-to-column end-plate joint at elevated temperatures. Therefore, it is crucial to investigate the behaviour of overall joint experimentally with

considerations of thermal restraint effects. In this research, six steel joint specimens (cruciform assemblies) have been tested at elevated temperatures with and without thermal restraint effects. Moment-rotation characteristics of both restrained and unrestrained cruciform specimens are obtained. These results will be compared with analytical and finite element analyses in Section 8.3.

CHAPTER 8

STEEL BEAM-TO-COLUMN JOINT NUMERICAL AND MECHANICAL MODELLING

8.1 Introduction

In conventional studies about mechanical behaviour of steel framed structure, steel beam-to-column joints are normally idealized as either perfectly rigid or perfectly pinned. Nevertheless, actual behaviour of steel joint, namely, semi-rigid joint, can not be incorporated into steel framed structural analyses, unless accurate mechanical modelling technique can be established at both ambient and elevated temperatures.

As described in Chapter 2, during past few decades, there have been a number of analytical methods to represent steel joint rotational characteristics over a wide range of joint types and assemblages. In this study, a "Component-based" method has been adopted to describe extended end-plate joint behaviour at both ambient and elevated temperatures. Particular emphasis is on shear component of beam web panel. In addition, as a powerful and alternative technique, finite element (FE) model has also been developed to simulate rotational behaviour of such joint. Finite element analysis (FEA) can provide accurate predictions incorporating complicated interactions among various joint components. Therefore, joint modelling by finite element method can save experimental cost and time. But the FE models have to be validated by test results in the first place.

This chapter presents a FE simulation of rotational characteristics of steel joint at elevated temperatures, with both unrestrained and restrained boundary conditions. A suitable FE model has been constructed to simulate rotational behaviour of steel beam-to-column joint in a cruciform assembly form. The objectives of this part of numerical simulations are:

- To construct a suitable FE model for steel beam-to-column joint using commercial FEA software MSC.Marc Mentat (MSC, 2001);
- To investigate mechanical behaviour of steel beam-to-column joint at elevated temperatures with unrestrained boundary conditions;
- To investigate mechanical behaviour of steel beam-to-column joint incorporating thermal restraint effects at elevated temperatures;

8.2 Steel Beam-to-Column Joint Numerical Modelling

Finite element analyses have been conducted using a commercial FEA software package MSC. Marc Mentat (MSC, 2001) at higher temperatures. The simplified FE model of cruciform specimen is illustrated in Figure 8.1.

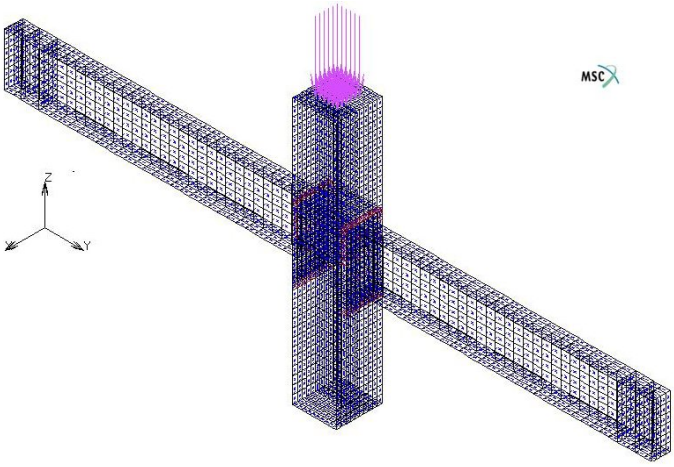

Figure 8.1 Steel Beam-to-Column Joint Finite Element Model

Beam, column and end-plates are modelled by a quadratic thick shell element (element type 22 in MSC.Marc Mentat Element Library). This selected element is

an eight-node quadrilateral thick shell element, with global displacements and rotations in X, Y and Z directions as degrees of freedom. In current finite element analyses, second-order interpolation technique is used for coordinates, displacements and rotations. The membrane strains are obtained from strain field, and curvatures from rotation field.

In addition to eight-node shell element, connecting bolts (as shown in Figure 7.2 and Figure 7.3) are simulated by three sets of springs, representing both axial tension stiffness and another two dimensional shear stiffnesses. These are specified in Eurocode 3 Part 1.8 (EN 1993-1-8) incorporating strength reduction factors for bolts at fire limit state in Eurocode 3 Part 1.2 (EN 1993-1-2). Another type of spring with special characteristic was used to simulate contact links between the edge of end-plate and adjacent column flange surface. Steel material properties obtained from material coupon tests performed at ambient temperature have been used in this analysis.

Unlike bilinear stress-strain model adopted in previous plate girder finite element analyses (Section 6.2), a trilinear-elliptic stress-strain model is adopted in this part of finite element simulation, which incorporated strain-hardening as specified in Eurocode 3 Part 1.2 (EN 1993-1-2) at elevated temperatures. In this chapter, both restrained and unrestrained steel beam-to-column joints will be investigated using the proposed FE model. Geometrical and material properties of restrained cruciform specimens (CR1, CR2 and CR3) and unrestrained cruciform specimens (CR4, CR5 and CR6) are in accord with experimental measurements as described in Section 7.2. The detailed FE results will be compared with experimental and analytical predictions in the following sections.

8.2.1 FE Model of Restrained Steel Beam-to-Column Joint

In the first part of cruciform simulations, restrained boundary conditions are modelled to compare with CR1, CR2 and CR3 tests. The cruciform tests were conducted under steady-state heating (as described in Section 7.2). Numerical analysis was carried out in three stages, viz. *1.* Axial loading stage; *2.* Heating Stage; *3.* Vertical loading stage. Different boundary conditions were used in these three stages (as shown in Table 8.1).

Table 8.1 shows the boundary conditions for cruciform FE model edges. In this table, "●" represents fixed condition and "○" represents free condition. In the axial loading and heating stages, the bottom flanges of left and right beam ends (LST and RST) were free to expand in the horizontal direction (Y-direction). Moreover, left and right ends of beam (LB and RB) were allowed to move in Z-direction to simulate beam thermal expansion. However, beam rotations refer to Z-direction were restricted in LB and RB, to simulate the beam end rotational restraints (⑧) as shown in Figure 7.1. Before heating stage, axial load was applied normal to the beam end surface and was kept constant through heating and vertical loading stages. In the heating stage, nodal temperature increments were set for different heating area of FE models and increased gradually from 20°C to measured temperatures.

In the vertical loading stage, vertical load was applied as a uniform distributed face load onto the centre area of column top. At this stage, edges of both the left and right beams (LST and RST) were set free in the horizontal direction (Y-direction) to simulate roller supports at each end of cruciform specimens. Moreover, vertical edges of the left and right beam stiffeners (LB and RB) were fixed for X-direction movement and Z-direction rotation to simulate rotational restraint effects as described in Section 7.2.

Table 8.1 Boundary Conditions for Restrained Cruciform FE Model

Stage	Edges	x	y	z	θ_x	θ_y	θ_z
Axial Loading	LST	●	○	●	○	●	○
	LB	●	○	○	○	○	●
	RST	●	○	●	○	●	○
	RB	●	○	○	○	○	●
Heating	LST	●	○	●	○	●	○
	LB	●	○	○	○	○	●
	RST	●	○	●	○	●	○
	RB	●	○	○	○	○	●
Vertical Loading	LST	●	○	●	○	●	○
	LB	●	○	○	○	○	●
	RST	●	○	●	○	●	○
	RB	●	○	○	○	○	●

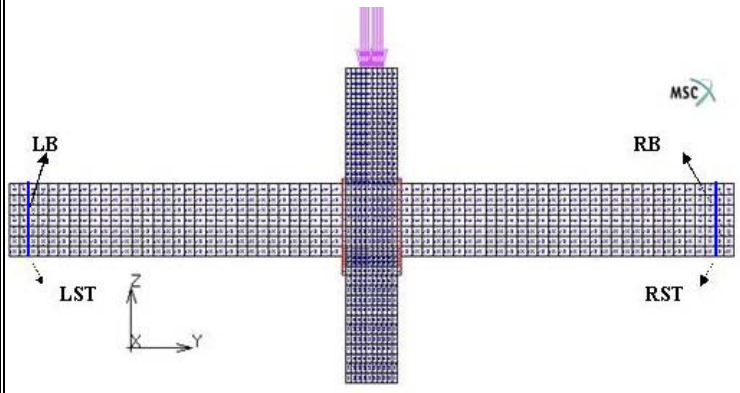

Note: x, y and z are translations;
θ_x, θ_y and θ_z are rotations in x, y and z directions, respectively;

○ denotes free
● denotes restraint DOF.

8.2.2 FE Model of Unrestrained Steel Beam-to-Column Joint

To obtain a good understanding of steel beam-to-column joint at different elevated temperature levels, numerical simulations were conducted to compare with experimental observations from CR4, CR5 and CR6 tests. Similarly, this part of numerical analysis was carried out in two stages, such as, *1*. Heating Stage; *2*.

Vertical loading stage. Separate boundary conditions were used in these two stages (as shown in Table 8.2).

Table 8.2 Boundary Conditions for Unrestrained Cruciform FE Model

Stage	Edges	x	y	z	θ_x	θ_y	θ_z
Heating	LST	●	○	●	○	●	○
	LB	●	○	○	○	○	●
	RST	●	○	●	○	●	○
	RB	●	○	○	○	○	●
	LR	●	○	○	○	○	●
Vertical Loading	LST	●	○	●	○	●	○
	LB	●	○	○	○	○	●
	RST	●	○	●	○	●	○
	RB	●	○	○	○	○	●
	LR	●	○	○	○	○	●

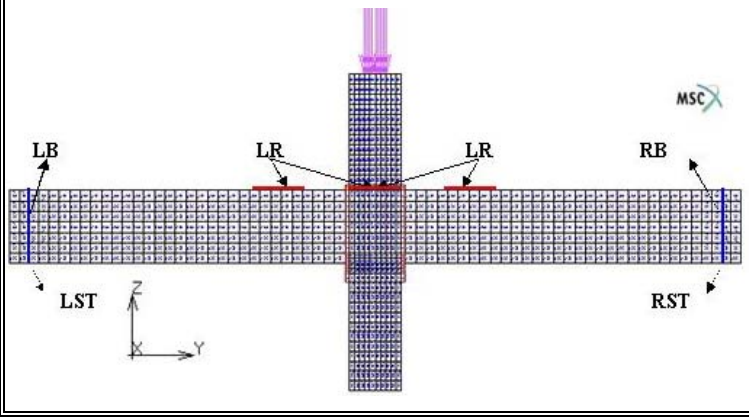

Note: x, y and z are translations;
θ_x, θ_y and θ_z are rotations in x, y and z directions, respectively;

○ denotes free and
● denotes restraint DOF.

In the heating stage, the bottom flanges of left and right end of beam (LST and RST) was set free to expand in horizontal (Y-direction) to simulate beam thermal expansion. Nodal temperatures were applied to all nodes of FE model and increased gradually from 20°C to desired final temperatures. In the vertical loading stage, edges of both left and right beam (LST and RST) were fixed in X- and Z-direction simulating roller supports at each end of specimen. Similar to restrained cruciform FE model, rotational restraint system effects were simulated by fixing vertical edges

of both left and right beam stiffeners (LB and RB) in the X-direction movement and Z-direction rotation. In addition, lateral restraint system effects were simulated by fixing movements in X-direction for lateral restrained area (LR) as shown in Figure 7.6. To obtain a clear beam web panel buckling behaviour, measured initial out-of-plane imperfections (as described in Section 7.4) were introduced into FE model. The beam web nodal imperfections were applied onto FE mesh nodes as approximate curves along the beam length.

8.2.3 Verifications of FE Steel Beam-to-Column Joint Model

To verify the FE models, FE simulations were first conducted for tests performed by Bailey (1999) at ambient temperature. In his experimental investigations, different column failure modes have been studied with cruciform assemblies. Column web panel shear test (Test 9) was compared with numerical predictions from the FE model. Details of cruciform specimen are given as follows.

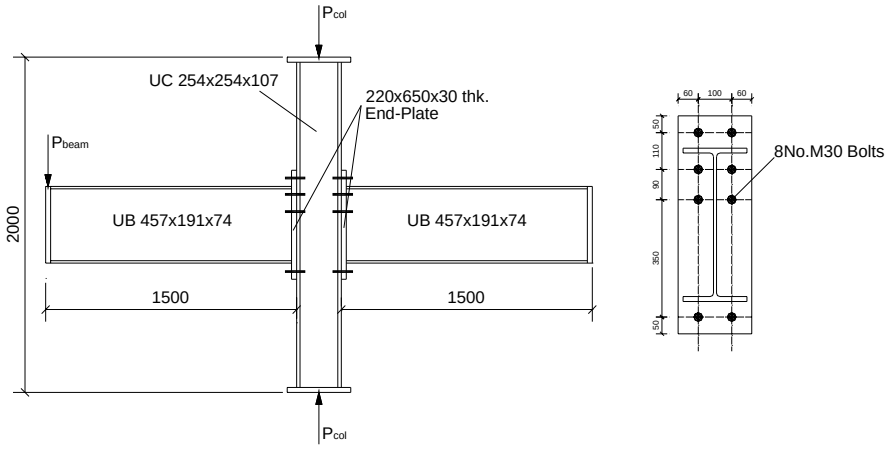

Figure 8.2 Web Buckling Test Cruciform Specifications (Bailey, 1999)

Vertical load P_{col} was first applied onto column up to a desired value. Then another vertical load P_{beam} was applied incrementally at the beam end, as shown in Figure 8.2. With increasing P_{beam}, column load P_{col} started to decrease at the same rate to

maintain a constant load level in lower-part of column. From the numerical analysis, it can be observed that proposed FE model could simulate rotational behaviour of specimens at ambient temperature. The von Mises stress distribution of column web buckling is shown in Figure 8.3. Moment-rotation relationship obtained from experimental and FE investigation is shown in Figure 8.4.

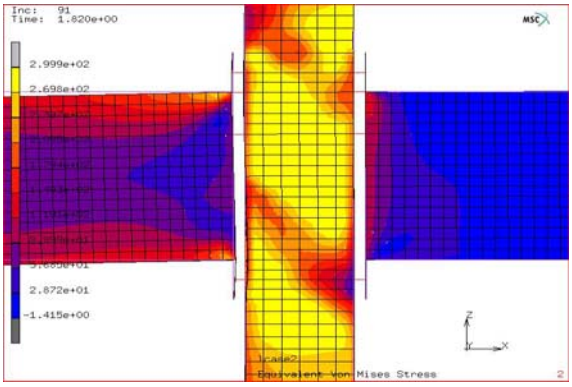

Figure 8.3 Failure Mode for Ambient Temperature Cruciform Test

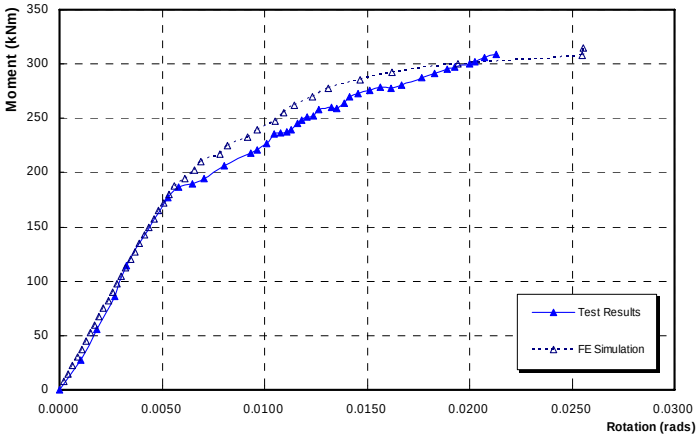

Figure 8.4 FE and Test Results for Ambient Temperature Cruciform Test

Although column web out-of-plane deformation is restrained, to some extent, by column flanges, such restraint will be reduced by axial load applied onto column section. Thus, from Figure 8.3, an inclined yield stress distribution can be seen in the column web panel zone, indicating column web shear buckling due to single-sided bending for test specimen. From comparisons as shown in Figure 8.4, proposed FE model is capable of predicting initial rotational stiffness and bending moment capacity of joint accurately.

8.3 FE Predictions of Steel Beam-to-Column Joint

Generally, FE results for thermally restrained tests, viz. CR1, CR2 and CR3, showed that beam web panels exhibited small out-of-plane deformation, in addition to bending of end-plate near the tension flange (bottom flange) of beams. Nevertheless, for thermally unrestrained specimens (CR4, CR5 and CR6), FE predictions showed that beam web panel near steel joint could develop significant out-of-plane deformations, similar to tensile field action in plate girder under shear. Detailed discussions about FE predictions of both thermally restrained and unrestrained cruciform tests will be presented in Section 8.3.1 and 8.3.2.

8.3.1 FE Predictions of Thermally Restrained Steel Joint

FE predictions showed that equivalent von Mises stress distribution was quite uniform within the steel joint at the end of heating stage. With increasing column load, higher stresses were formed in beam web panels and end-plates. Finally, end-plates developed significant bending deflections near beam bottom flanges.

Typical FE predictions for CR2 tests are shown in Figure 8.5. From load-versus-deflection of column top, predicted deflection compares closely with test results. Although with higher restraint force level (2.5%), FE predictions show less stiff behaviour, since compressive restraint force was manually kept constant from deviations during tests. However, this compressive force has been kept constant during heating and vertical loading stages in finite element simulations. In addition, minor difference in temperature distributions between FE models and test specimens also contribute to the discrepancies between FE predictions and experimental results. In addition, vertical deflections of beams at L2, L3, L9 and L10 (Figure 7.7) are also compared with FE predictions, as shown in Figure 8.5(b), (c). Similarly, FE predictions show less stiff behaviour. Despite these discrepancies, FE simulations are reasonably close to test results. As described in Section 7.4,

rotational characteristics of joints were obtained from beam vertical deflection measurements. Thus, corresponding FE perditions are compared with experimental results as shown in Figure 8.5(d). From both comparisons, it can be seen that FE predictions are in close agreement with experimental measurements. However, slight discrepancies may be attributed by differences in the temperature field and to a small extent on associated material properties.

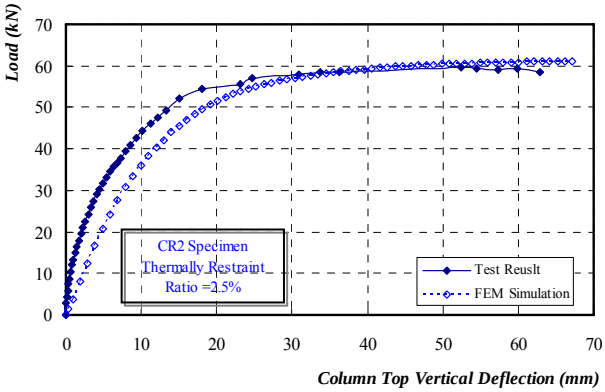

(a)

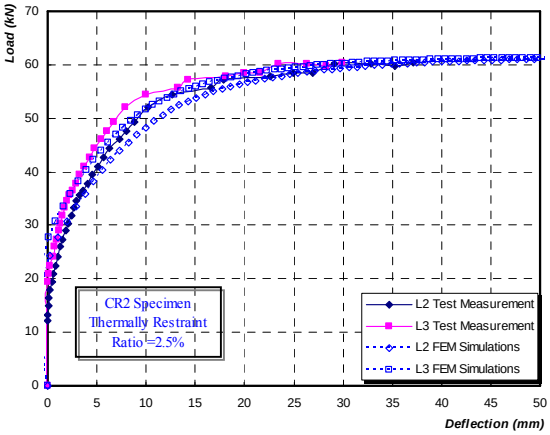

(b)

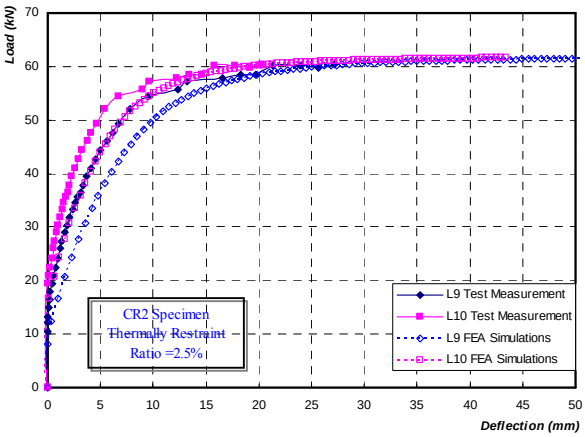

(c)

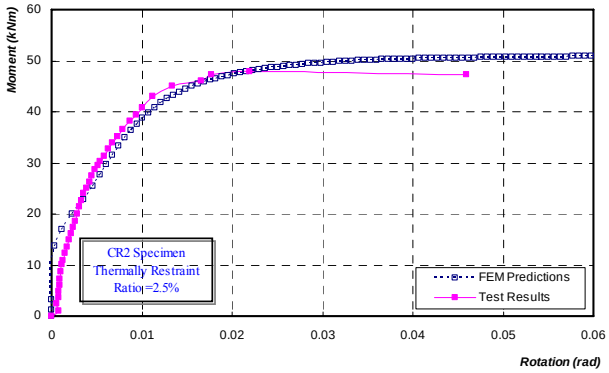

(d)

Figure 8.5 Comparison between FE Predictions and Experimental Results for CR2

8.3.2 FE Predictions of Thermally Unrestrained Steel Joint

As described in Section 7.4, in the second group of tests, three cruciform specimens were tested at 400, 550 and 700 ^{o}C without any thermal restraint. Figure 8.6(a) presents comparisons between FE predictions and experimental measurements of column top deflection. It can be seen that FE model gives good agreement with actual joint behaviour at elevated temperatures. Due to a more uniform temperature distribution across the cruciform specimen and absence of axial compressive force, FE predictions for this group of tests (CR4, CR5 and CR6) show a better correlation compared with the first group of tests.

In addition, vertical deflection measurements of connected beam sections are compared with FE results as shown in Figure 8.6(b) and (c). It can be seen that proposed FE model shows good agreement with test results. However, there are slight discrepancies between FE predictions and experimental measurements, possibly due to friction between roller plates and restraint support plates, which in certain extent hinder the beam sections from deflecting freely. As described in Section 7.4, the rotational characteristics were derived based on beam end deflections, which are compared with FE predictions in Figure 8.6(d). The FE predictions present an acceptable agreement with experimental response. However, discrepancies between test results and FE predictions are primarily due to the unpredictable frictions during tests.

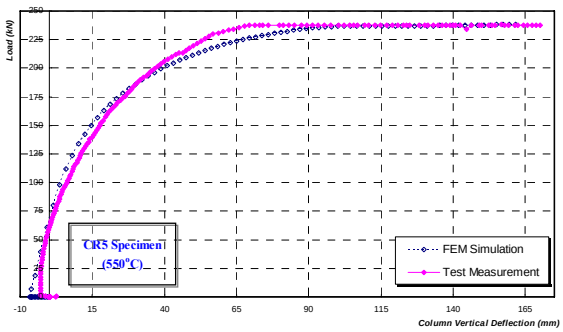

(a)

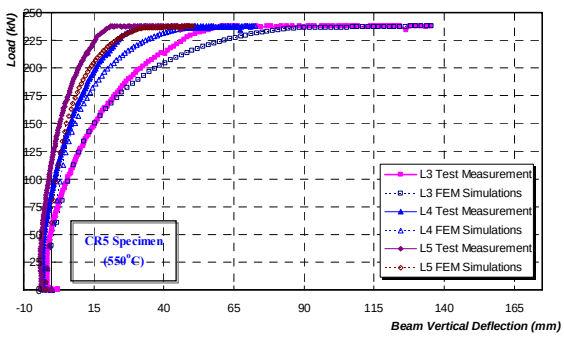

(b)

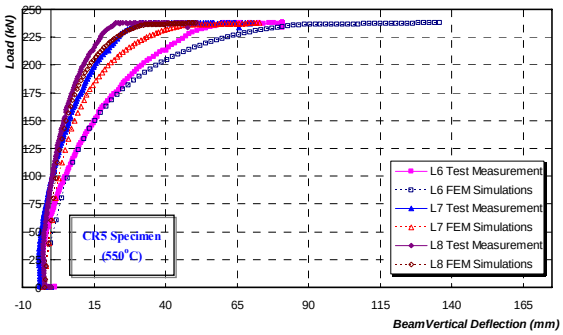

(c)

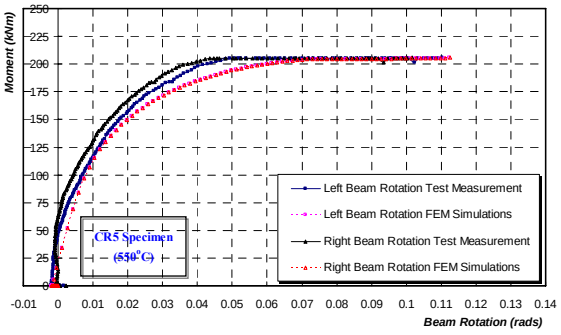

(d)

Figure 8.6 Comparison between FE Predictions and Experimental Results for CR5

8.3.3 Failure Modes and Comparisons of Cruciform Tests

The first group of specimens (CR1, CR2 and CR3) were tested at 700 ^{o}C, with axial load ratios as 0, 2.5 and 4% of beam plastic squashing capacity. In addition to out-of-plane deflection in the beam web panels, as described in Section 7.4, significant bending deformations can be observed at the end-plate adjacent to the beam bottom flanges (in tension) as shown in Figure 8.7. The behaviour is similar to FE predictions. Clearly, CR1 shows the greatest end-plate bending deflection due to tensile force transferred from the beam bottom flanges. The beam sections were subjected to axial compressive forces for CR2 and CR3, that is, the gap between the end-plate and column flanges decreases with increasing axial restraint, as shown in Figure 8.7(b) and (c). However, these applied axial forces induce significant increase of beam deflections due to P-δ effect. In addition, Figure 8.7(a) shows bending of bottom rows for bolts CR1, due to end-plate bending and reducing bolt resistance at high temperature. However, CR2 and CR3 show less bolt slip in Figure 8.7(b) and (c) due to applied axial compressive force onto the beam sections. This failure mode is reasonable since the thickness of end-plate was only 20mm and cover plate thickness on beam flange was 16mm. Therefore, in order to obtain a clear picture of beam web shear component, thicker end-plate (40mm) was used for the second group of cruciform specimens.

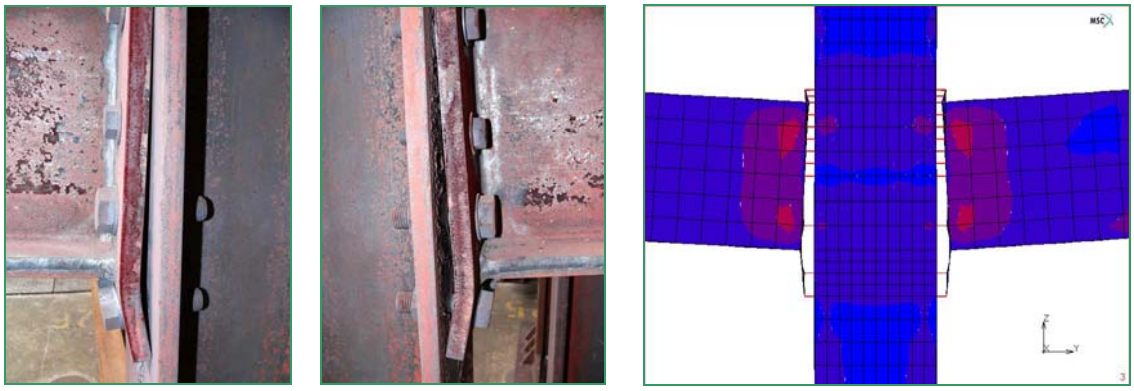

(a) CR1 Cruciform tested at 700 ^{o}C with 0% axial load

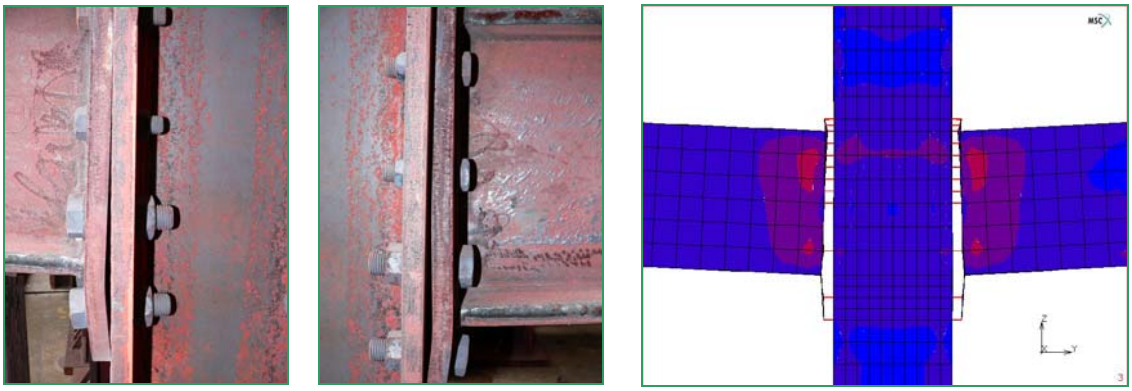

(b) CR2 Cruciform tested at 700 ^{o}C with 2.5% axial load

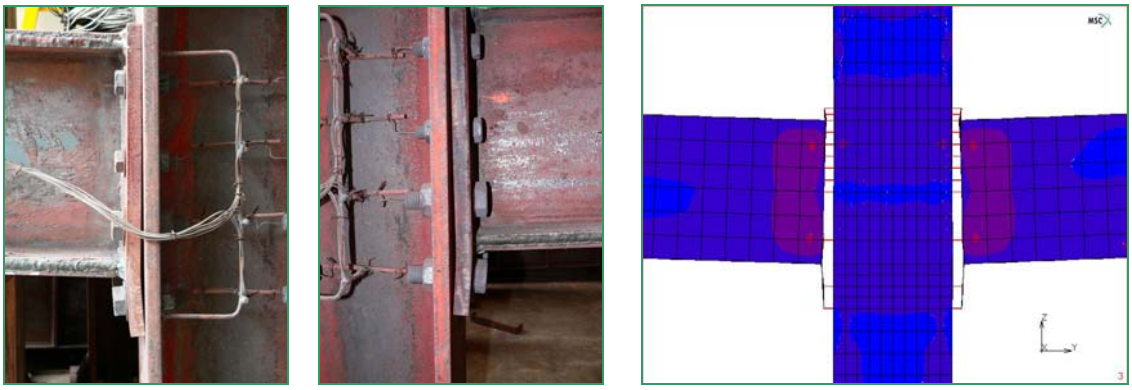

(c) CR3 Cruciform tested at 700 ^{o}C with 4% axial load

Figure 8.7 Comparisons of Failure Modes for Restrained Cruciform Test

For the second group of cruciform specimens, FE predictions show that both left and right beam web panels developed out-of-plane deflections (X-direction) adjacent to the end-plates. Figure 8.8(a) presents FE simulations and experimental

failure modes for CR4 specimen tested at 400 ^{o}C. From comparison, it can be seen that beam web panels formed tensile field action similar to shear failure mode in plate girder web panel, as described in Section 4.2. The joint tests have to be stopped when column deflection approached 190 mm to avoid damaging the furnace. However, numerical simulations could continue, showing significant out-of-plane deflections due to spread of plasticity in beam web panel. Similar web out-of-plane deformation behaviour can be observed from FE predictions and experimental photos for CR5 as shown in Figure 8.8(b). However, at higher temperature (700 ^{o}C), steel material stress-strain relationship becomes highly nonlinear and the distinction between elastic and plastic stage becomes blurred (Figure 3.6). Thus, both FE prediction and experimental results for CR6 exhibited less apparent out-of-plane deformations as shown in Figure 8.8(c). In addition, due to degradation of bolts at higher temperature, the failure mode for CR6 is a combination of slipping of bottom rows of bolts in tension and out-of-plane deformations in beam web.

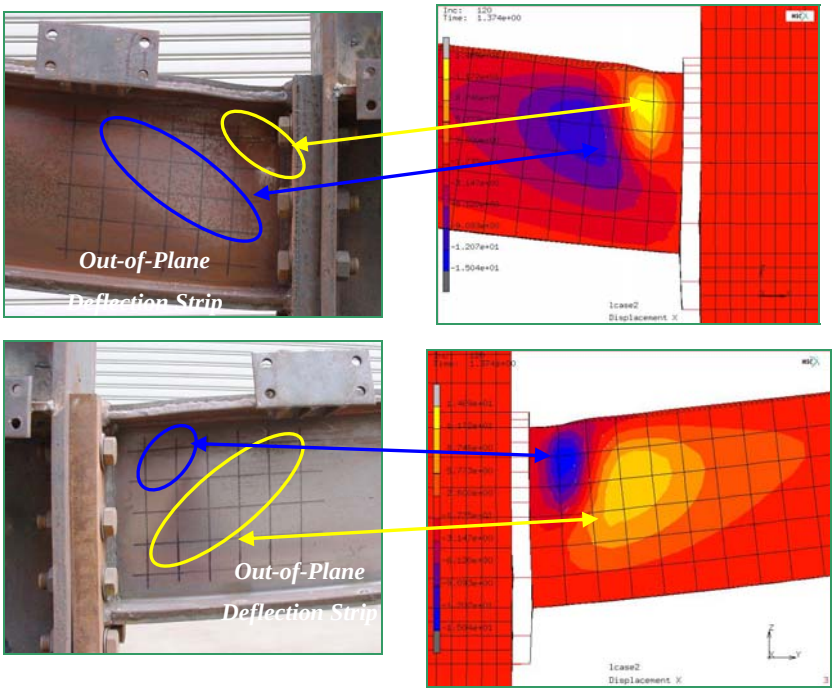

(a) CR4 Cruciform tested at 400 ^{o}C

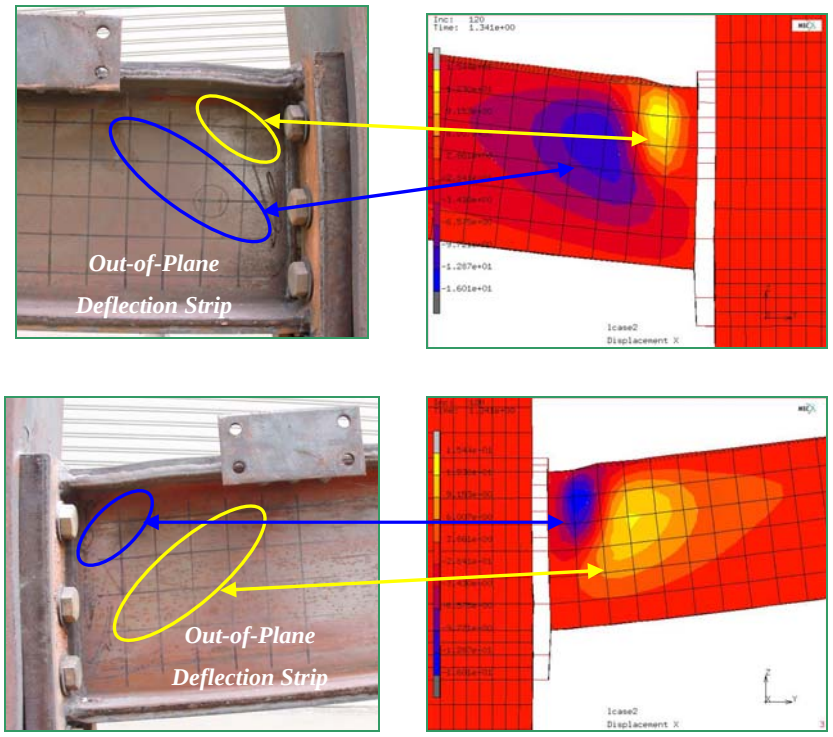

(b) CR5 Cruciform tested at 550 °C

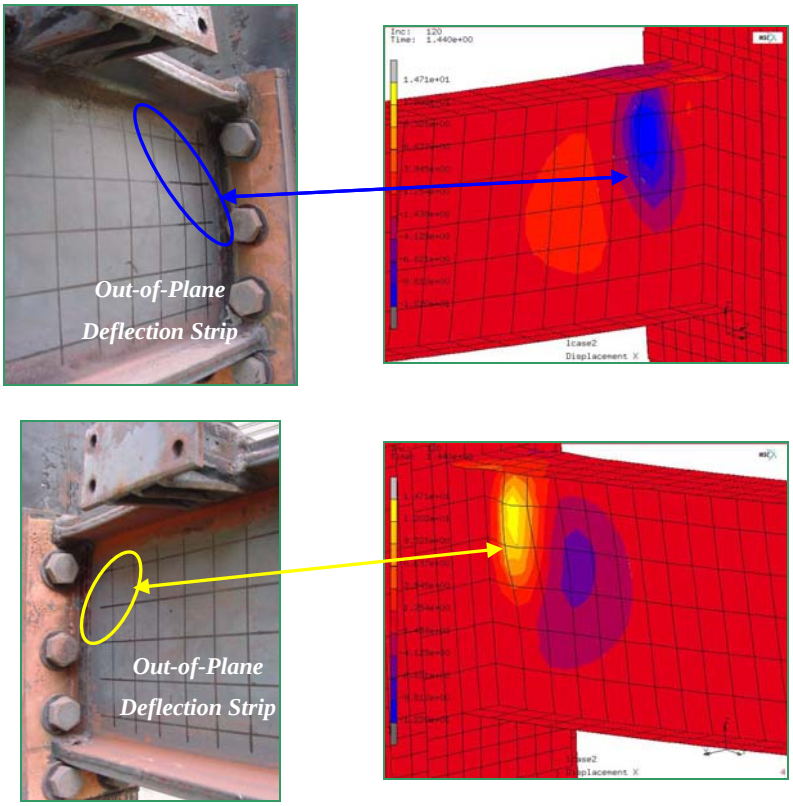

(c) CR6 Cruciform tested at 700 °C

Figure 8.8 Comparisons of Failure Modes for Unrestrained Cruciform Test

Typical overall failure mode for CR4 is shown in Figure 8.9(a) and (b), with a comparison between FE and actual failure mode. This specimen is selected for the following discussion on stress and strain analysis, as it represents typical behaviour of cruciform specimen under fire conditions. It has a more uniform temperature field compared to the first three specimens, and its behaviour is quite similar to that of CR5 and CR6. The contours in the FE model show out-of-plane deformations at failure. It can be seen that tensile yielding zones are formed in the beam web panels adjacent to column flanges. As shown in Figure 8.9(a), there is positive out-of-plane deflection formed in the left beam web of cruciform. However, negative out-of-plane deflection can be found on the left beam, almost in an anti-symmetric mode to the first. It is in accord with observed failure mode as shown in Figure 8.9 (b). From the two failure modes shown in Figure 8.9(a) and (b), clearly, shear deformation is significant and should be taken into account in the joint modelling when using "Component-based" method (see Section 8.4).

From Figure 8.9(a) and (b), proposed FE model could predict the overall deformation of cruciform specimen accurately. Due to high cost associated with strain gauges, it is impractical to install a great number of strain measurements for elevated temperature tests. Besides, it is difficult to obtain stress distribution across the section based on a few strain gauges. Thus, FE model is used to provide valuable information about the stress development within the test specimen during the loading stage. Figure 8.10 shows maximum out-of-plane deflection versus bending moment for the right beam of CR4, as shown in Figure 8.9. From Figure 8.10, there are pre- and post-buckling stages for beam web panel. Four different points have been selected to describe the stress development in the beam web based on equivalent von Mises and principal stresses, as shown in Figure 8.11.

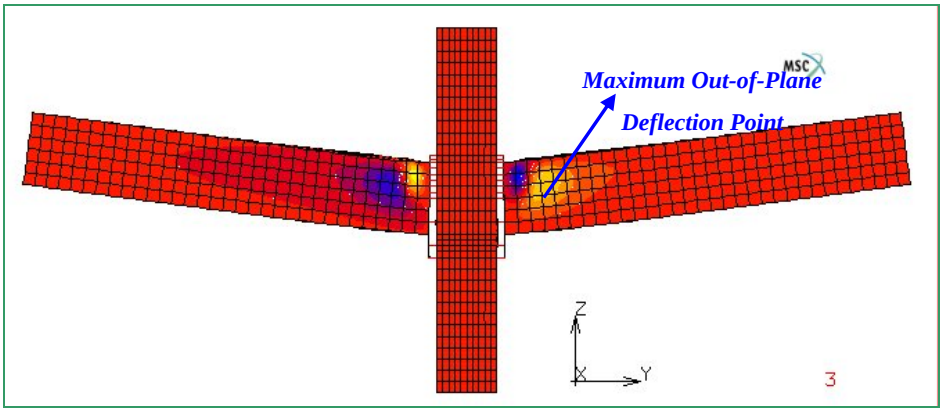

(a)

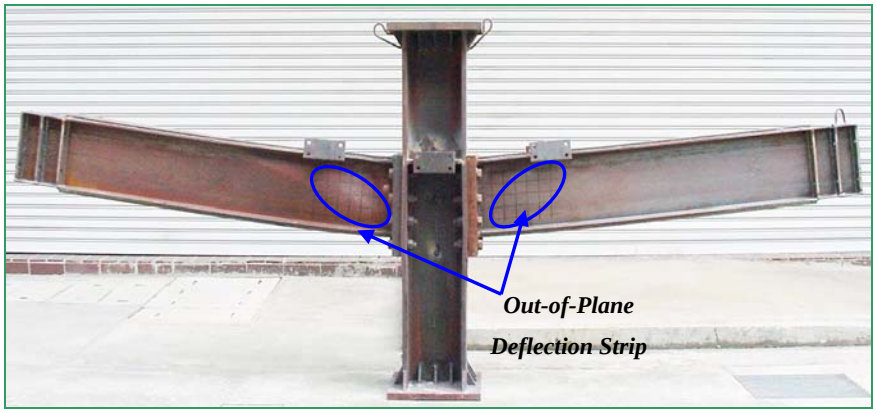

(b)

Figure 8.9 Typical Failure Mode Comparison between FE Prediction and CR4 Test

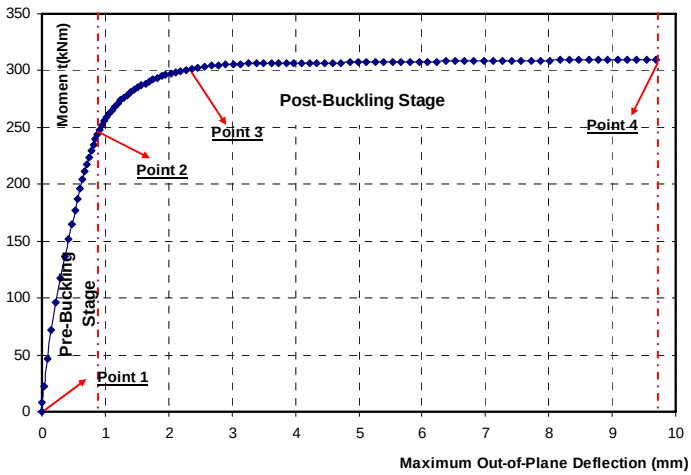

Figure 8.10 Moment versus Maximum Out-of-Plane Deflection for CR4

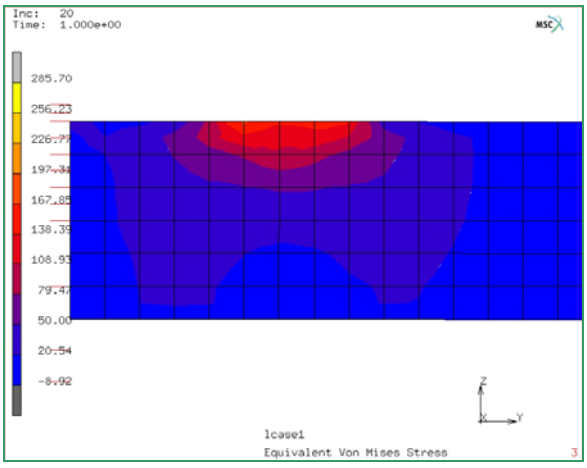

(a) Point 1 Equivalent von Mises Stress Distribution

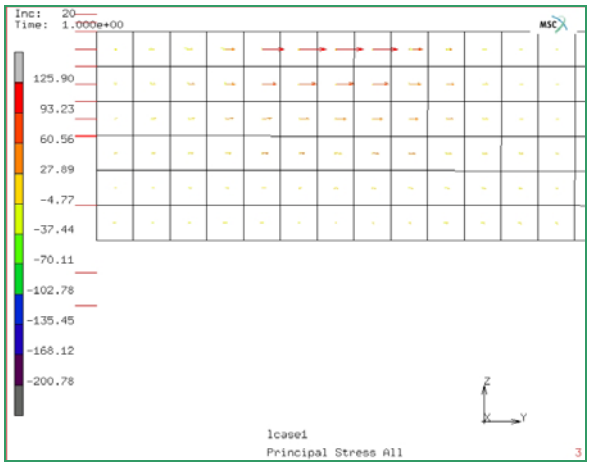

(b) Point 1 Principal Stress Distribution

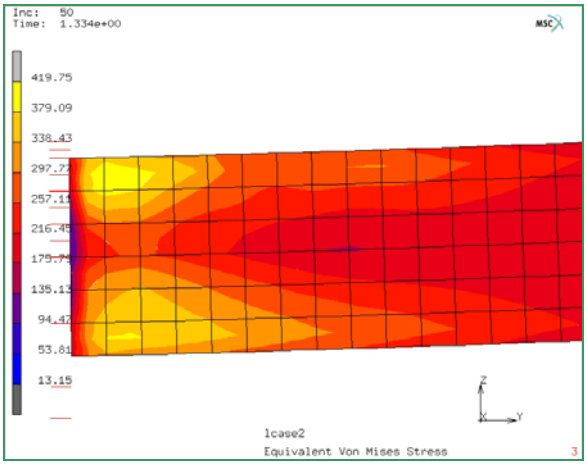

(c) Point 2 Equivalent von Mises Stress Distribution

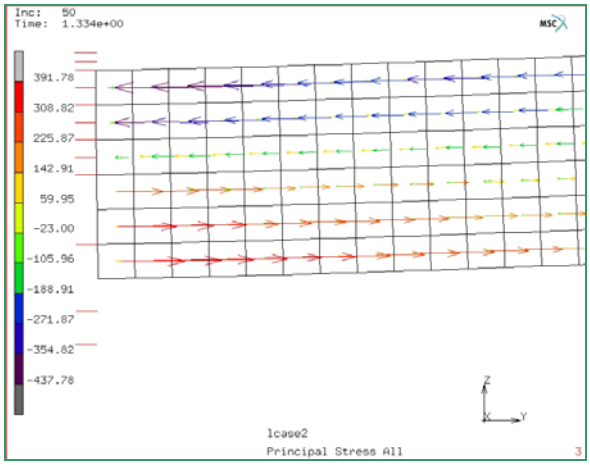

(d) Point 2 Principal Stress Distribution

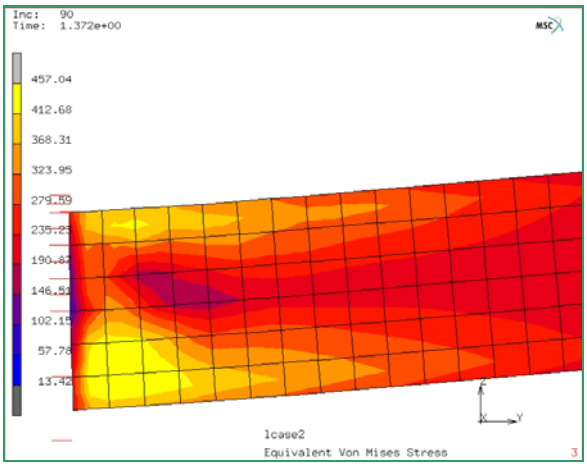

(e) Point 3 Equivalent von Mises Stress Distribution

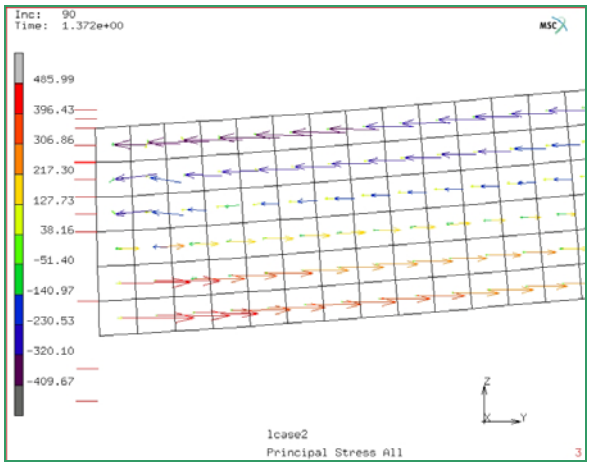

(f) Point 3 Principal Stress Distribution

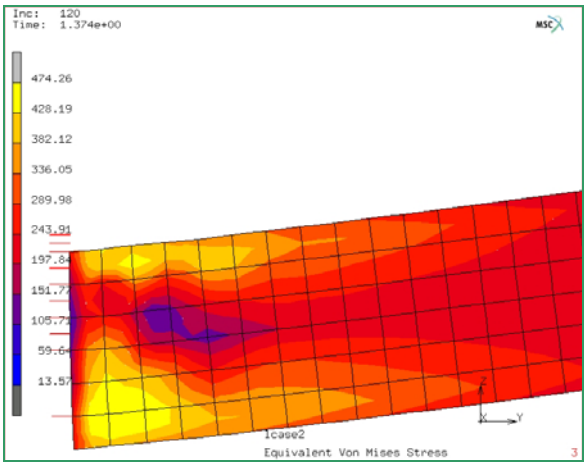

(g) Point 4 Equivalent von Mises Stress Distribution

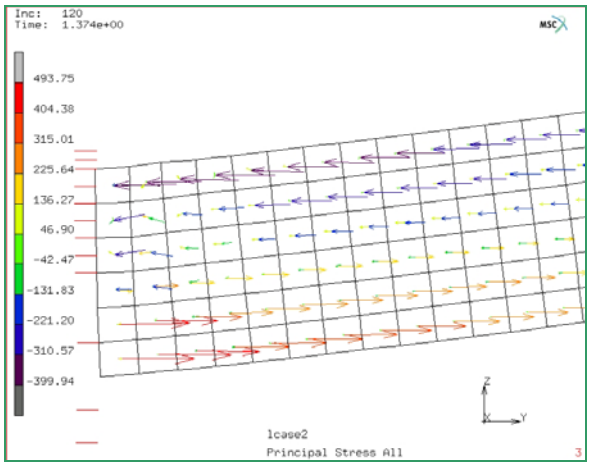

(h) Point 4 Principal Stress Distribution

Figure 8.11 Equivalent von Mises Stress and Principal Stress Distribution for Beam Web of CR4 at Separate Stages

By examining the equivalent von Mises stress scalar and principal stress distribution as shown in Figure 8.11, stress concentration can be observed from Figure 8.11(a) and (b) at the top flange of beam, within the lateral restrained area at the beginning of vertical loading stage. This is due to lateral restraint system as described in Section 7.2, which exerts some influences on the beam out-of-plane deflection. However, the local stress concentration diminishes after vertical load is applied. At the end of pre-buckling stage (Point 2 as shown in Figure 8.10), there is uniform distribution of equivalent von Mises stress at the top and bottom parts of beam web in Figure 8.11 (c), which are under compression and tension, respectively. It is in accord with beam bending behaviour, and agrees well with principal stress distribution in Figure 8.11 (d). After the beam web starts to develop out-of-plane deflection (Point 3 as shown in Figure 8.10), plasticity spreads within the bottom part of beam web, which is under tension as shown in Figure 8.11 (e). In addition, a small area of beam top flange starts to yield due to compression. However, as shown in Figure 8.11 (e) and (g), there is some *stress release* in the buckled area of beam web. This region is in accord with the *buckled shape* of CR4 specimen as illustrated in Figure 8.12(a) and (b). After yielding has occurred at the top part of beam web adjacent to the end-plates, the local region also buckles due to significant

compression from bending moment. However, it can also be noticed that the final buckling shape of beam web panel is similar with the tensile field action (TFA) failure mode of beams in the Cardington fire tests, which is analogous to the shear failure of plate girders at elevated temperatures. Therefore, the development of out-of-plane beam web deflection is due to a combined action from bending moment and shear force. It should be noted that these two actions have been separately considered in the "Component-based" mechanical modelling.

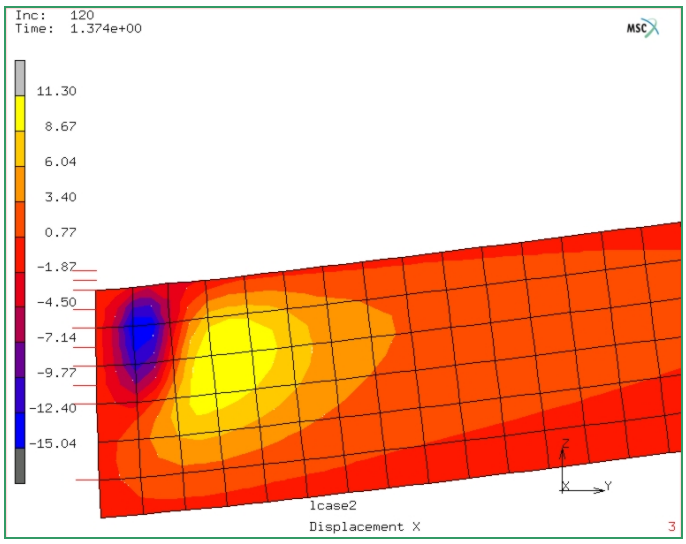

Figure 8.12 Beam Out-of-Plane Deflection Distribution at Failure Stage of CR4

Bending moment capacities for restrained and unrestrained joint tests are compared with FE and analytical predictions. The detailed comparisons are given in Table 8.3. In general, the experimental M_{test} and FE predicted M_{FEM} compare well, as shown in Column (8) of Table 8.3, with the mean value and standard deviation as 1.005, and 0.035, respectively. The discrepancy between FE prediction and test result for CR4 is primarily due to friction of lateral restraint system during the test. In addition, FE analyses slightly over predict moment capacities for CR1 and CR2. This is mainly attributed to differences in the temperature field. However, this discrepancy becomes negligible for CR5 and CR6 since there is a more uniform temperature distribution across the specimens. Detailed descriptions of analytical procedure will be presented in Section 8.4.

Table 8.3 Comparisons of Experimental Results with FE and Analytical Predictions

Test Cruciform	Temperature (^oC)	Axial Force Ratio	M_{test} (kNm)	M_{analy} (kNm)	M_{FEM} (kNm)	$\frac{M_{analy}}{M_{test}}$	$\frac{M_{FEM}}{M_{test}}$	$\frac{M_{FEM}}{M_{analy}}$
(1)	(2)	(3)	(4)	(5)	(6)	(7)	(8)	(9)
CR1	700	0%	49.89	51.82	51.99	1.04	1.04	1.00
CR2	700	2.5%	47.85	46.61	49.67	0.97	1.04	1.07
CR3	700	4%	43.06	42.48	42.48	0.99	0.99	1.00
CR4	400	0%	328.33	311.77	310.74	0.95	0.95	1.00
CR5	550	0%	205.06	199.11	206.09	0.97	1.01	1.04
CR6	700	0%	75.40	71.95	76.26	0.95	1.01	1.06
—	—	—	—	—	—	0.979[a]	1.005[a]	1.027[a]
—	—	—	—	—	—	0.032[b]	0.035[b]	0.031[b]

[a] Mean Value [b] Standard Deviation

8.4 Steel Beam-to-Column Joint Spring Stiffness Model at Elevated Temperatures

During current experimental investigations, moment-rotation characteristics for typical extended end-plate steel joint have been recorded for three elevated temperatures and three axial thermal restraints. However, it is costly and impractical to conduct numerous tests to obtain a wide range of steel joint behaviour at different elevated temperatures. Thus, there are a number of techniques for modelling steel joints at ambient temperature. However, to date, there are a very limited number of studies on steel joint behaviour at elevated temperatures. Therefore, it is necessary to provide an accurate prediction technique of steel joint rotational characteristics at both ambient and elevated temperatures. This can then be implemented in structural analysis for ambient and elevated temperatures. As descried in Section 2.6, "Component-Based" method is able to bridge the gap between tests and complex FE models. Consequently, this method was selected as the basis to model the rotational characteristics of extended end-plate steel beam-to-column joint in current investigations.

8.4.1 "Component-Based" Mechanical Model for Extended End-plate Steel Joint

"Component-Based" method is a mechanical modelling technique. The novelty is that it can predict steel joint behaviour throughout moment-rotation relationship at elevated temperatures by assembling contributions from individual mechanical components within steel joints. In this context, a steel joint is assumed to be a set of rigid and deformable elements. Thus, assuming negligible interactions among different components, overall rotational behaviour of steel joint can be obtained by superimposing stiffnesses of individual components in compression, tension and shear zones. The shear component in beam web within steel joint is analogous to a typical plate girder web panel loaded under shear in Section 4.1. Thus, it is possible to predict different joint failure modes due to deformational behaviour of shear component. In addition, influences of thermal restraint at elevated temperatures were also incorporated into overall steel joint mechanical model. As described in Section 2.6, with "Component-Based" method, a steel joint could be modelled into a two-dimensional mechanical spring model. The overall steel joint rotation is assumed to develop about the centre line of beam compression flange. The stiffnesses of individual component are simulated by different springs as shown in Figure 8.13. The overall spring model consists of the following components:

- Column Web in Shear (cws)
- Column Web in Compression (cwc)
- Beam flange in Compression (bfc)
- Column Web in Tension(cwt)
- Column Flange in Tension(cft)
- End-plate in Tension(ept)
- Bolts in Tension(bt)
- Beam Web in Shear(bws)

This mechanical model was extended from the work by Faella *et al.* (2000). In their model, N_b and N_c represent axial thermal restraint forces induced by surrounding unheated sub-structures at fire conditions, M represents bending moment of steel beam-to-column joint and V represents shear force. Components influencing both rotational stiffness and capacity are represented by elastic-perfectly-plastic spring

elements. Notably, the beam flange in compression, which provides a limit of rotational resistance, is represented by a rigid-plastic spring element. Moreover, beam web in shear is simplified into a rotational spring element by the author, with elastic-perfectly-plastic response.

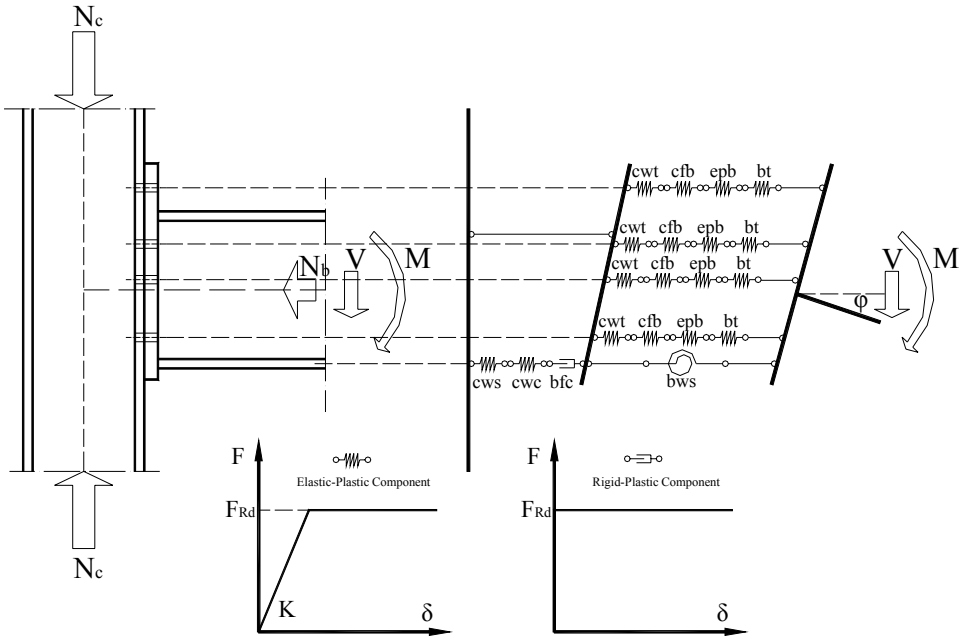

Figure 8.13 Steel Beam-to-Column End-plate Joint Spring Model

According to Eurocode 3: Part 1.8 (EN 1993-1-8), flexural resistance $M_{j,Rd}$ of steel beam-to-column end-plate joint is defined by the following relationship:

$$M_{j,Rd} = \sum_{i=1}^{n} h_i F_{i,Rd} \tag{8.1}$$

where: $F_{i,Rd}$ is resistance of $i-th$ bolt row; h_i is distance of $i-th$ bolt row from the centre of compression. In addition, resistance of each bolt group cannot exceed the one of the components independent of bolt rows (column web in compression and shear, beam flange in compression and beam web in shear).

Rotational stiffness of steel joint subjected to only bending moment M can be obtained by the following form, with incorporation of rotational stiffness K_{bws} of beam web shear component suggested by the author.

$$K_\varphi = \frac{h_t^{\,2}}{\dfrac{1}{K_{cws}} + \dfrac{1}{K_{cwc}} + \dfrac{1}{K_t} + \dfrac{h_t^{\,2}}{K_{bws}}} \quad \text{in which,} \quad K_t = \frac{\sum_{i=1}^{n} K_{ti} h_i}{h_t} \quad \text{and} \quad h_t = \frac{\sum_{i=1}^{n} K_{ti} h_i^{\,2}}{\sum_{i=1}^{n} k_{ti} h_i} \tag{8.2}$$

where: K_{ti} is equivalent stiffness of $i-th$ bolt row; h_t is lever arm length; K_{cwc} is compressive stiffness of column web; K_{cws} is equivalent shear stiffness of column web; K_{bws} is equivalent rotational shear stiffness of beam web panel.

In addition, Sokol *et al.* (2002) proposed the rotational stiffness joint depends on the bending moment M is influenced by normal axial compressive force N applied onto beam sections. Thus, the rotational stiffness of joint under combination of bending moment and axial compressive force in this study can be obtained as:

$$K_\varphi' = \frac{M_{ult}}{M_{ult} - Ne_0} K_\varphi \quad \text{in which,} \quad e_0 = \frac{z_c K_{cwc} - z_t K_t}{K_t + K_{cwc}} \tag{8.3}$$

in which: M_{ult} is pure bending moment capacity of joint; z_c and z_t are distance from beam section centre to compression and tension zones.

The following assumptions are adopted in current mechanical model:

- Material properties for beams, column and end-plates are based on those obtained from material tests, as described in Section 7.2. Nominal values are adopted for bolts.
- Degradation of mechanical properties of steel at elevated temperature is based on Eurocode 3: Part 1.2 (EN 1993-1-2), with a strain level of 2% for strength. The degradations of bolts stiffness and strength are based on Eurocode 3: part 1.2 (EN 1993-1-2), as described in Section 3.4.
- Both geometrical imperfections of beam sections and temperature distributions across sections are based on actual test results.

In the following sections, descriptions of various components within compression and tension zones will be presented and discussed briefly.

8.4.2 Simplified Mechanical Predictions for Tension Zone

In steel beam-to-column end-plate joints, major components within the tension zone compose of column flange, column web panel, beam flange, end-plate and rows of bolts. All these components can be simplified into an equivalent T-stub as shown in Figure 8.14.

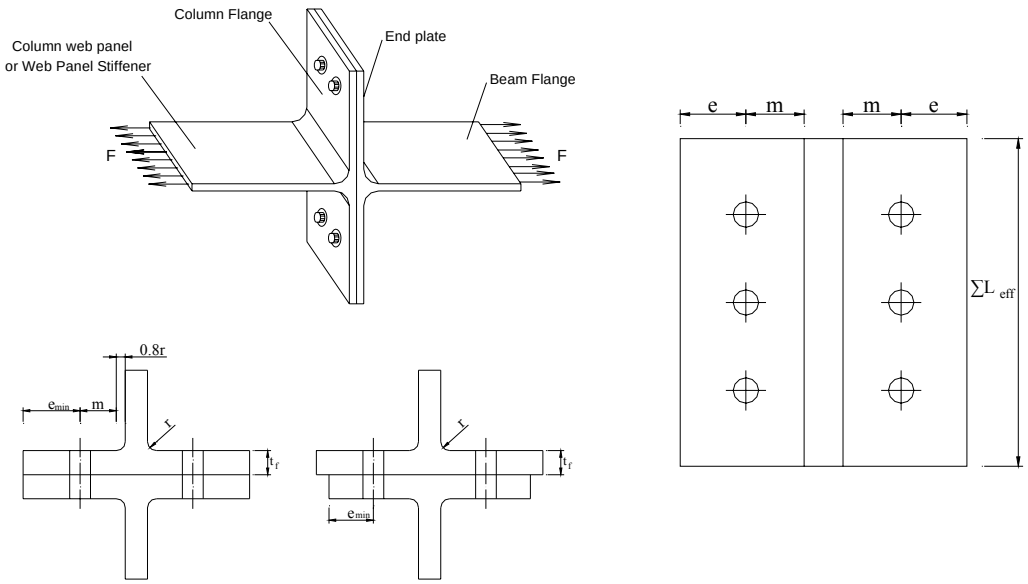

Figure 8.14 Simplified T-stub Model and Dimensions (EN 1993-1-8)

In Eurocode 3: Part 1.8 (EN 1993-1-8), three different failure modes are specified with corresponding simplified formulae to calculate the strength and stiffness of T-stub. The three failure modes are shown in Figure 8.15.

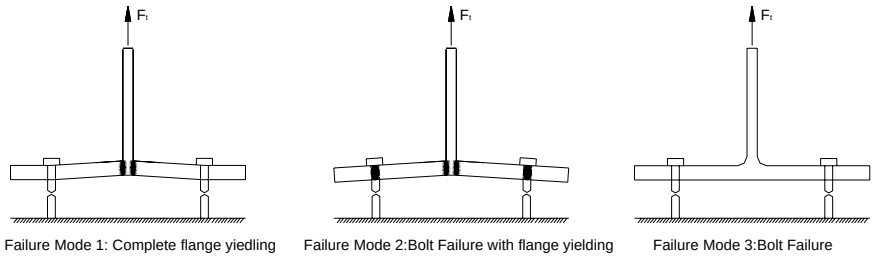

Figure 8.15 Failure Modes for T-stub Assembly

Tensile resistance of T-stub according to respective failure mode is specified as follows:

Failure Mode 1: $F_1 = \dfrac{4M_{cf,Rd}}{m}$ (8.4)

Failure Mode 2: $F_2 = \dfrac{2M_{cf,Rd} + n\sum B_{Rd}}{m+n}$ (8.5)

Failure Mode 3: $F_3 = \sum B_{Rd}$ (8.6)

in which: F_i is resistance of T-stub at failure mode i; $M_{cf,Rd}$ is flexural strength of T-stub flange, equal to $0.25\sum l_{eff} t_{cf}^{\ 2} \sigma_{cfy}$; B_{Rd} is design tension strength of single bolt; $n = e_{\min}$ but $n \le 1.25m$. Detailed $e_{\min}$ and m are shown in Figure 8.14. Thus, the resistance of each bolt-row can be obtained by the minimum value according to different failure modes.

In addition to T-stub tensile resistance, stiffnesses of various mechanical components within T-stub are given as follows, which are summarized by Faella *et al.* (2000):

➢ *Column Flange and End-plate in Bending*

Effective widths of column flange and end-plate in bending are based on a 45° spread from bolt head. Thus, the respective stiffness of column flange and end-plate are described as the following forms:

$$K_{cft} = E_{cf,T} \frac{0.5b'_{eff,cf}\, t_{cf}^{\ 3}}{m_{cf}^{\ 3}} \quad (8.7)$$

$$K_{ept} = E_{ep,T} \frac{0.5b'_{eff,ep}\, t_{ep}^{\ 3}}{m_{ep}^{\ 3}} \quad (8.8)$$

where: $b'_{eff,cf}$ and $b'_{eff,ep}$ are effective width for column flange and end-plate, respectively; t_{cf} is column flange thickness; t_{ep} is end-plate thickness; m_{cf} is distance between bolt shank centre and column flange root fillet; m_{ep} is distance between bolt shank centre and weld between beam and end-plate.

➢ *Column Web in Tension*

Stiffness of spring element respecting column web in tension is expressed as:

$$K_{cwt} = E_{cw,T} \frac{b'_{eff,cwt}\, t_{cw}}{d_{cw}} \tag{8.9}$$

where: $b'_{ef,cwt}$ is effective width of column web in tension, equal to $b'_{eff,cf}$; t_{cw} is column web thickness; d_{cw} is column depth between root fillets; t_{bf} is beam flange thickness; a_p is throat thickness of weld.

➢ *Bolt in Tension*

As specified in Eurocode 3: Part 1.8 (EN 1993-1-8), stiffness of a bolt in tension can be expressed as:

$$K_{bt} = E_{b,T} \frac{1.6 A_s}{L_b} \tag{8.10}$$

where: A_s is bolt shaft area; L_b is bolt elongation length as sum of connected plates, thickness of washers and half of nut and bolt head.

With descriptions of stiffness of each component in tension zone, the overall tension stiffness of $i-th$ bolt row can be derived as:

$$\frac{1}{K_{t,i}} = \frac{1}{K_{cwt,i}} + \frac{1}{K_{cft,i}} + \frac{1}{K_{ept,i}} + \frac{1}{K_{bt,i}} \tag{8.11}$$

Where: $K_{t,i}$ is equivalent stiffness of $i-th$ bolt row; $K_{cwt,i}$, $K_{cft,i}$, $K_{ept,i}$ and $K_{bt,i}$ are equivalent tensile stiffness of column web, column flange, end-plate and bolts of $i-th$ bolt row.

8.4.3 Simplified Mechanical Predictions for Compression Zone

The key components within compression zone consist of column web, column flange, and beam bottom flange. Corresponding failure modes in this zone mainly

consist of local buckling and crushing of column web. Faella *et al.* (2000) specified the effective width of column web in compression as:

$$b'_{eff,cwc} = t_{bf} + 2\sqrt{2}a_p + 2t_{ep} + 2\left(t_{cf} + r_c\right) \tag{8.12}$$

This effective width is based on compressive force transmitted from beam flange with a $2.5:1$ gradient through column flange and column web-to-flange area.

Initial stiffness of column web in compression is specified in a similar form to column web in tension, as follows:

$$K_{cwc,T} = E_{cw,T}\frac{b'_{eff,cwc}\,t_{cw}}{d_{cw}} \tag{8.13}$$

The crushing resistance of column web in compression is given by:

$$F_{cwc,Rd} = \rho\sigma_{cwy,T}t_{cw}b'_{eff,cwc}/\gamma_{M0} \tag{8.14}$$

where: $\sigma_{cwy,T}$ is yield strength of column web at elevated temperature T; t_{cw} is column web thickness; ρ is correction coefficient considering effects from column web compressive stress due to axial load and bending.

Column web in compression also can also fail in buckling. A number of researchers have conducted investigations of stability of column web in compression (Aribert *et al.* 1990, Faella *et al.* 1995., etc.) The buckling resistance of column web in compression is given by:

$$F'_{cwc,Rd} = F_{cwc,Rd}\left[\frac{1}{\lambda}\left(1-\frac{0.22}{\lambda}\right)\right] \quad \text{for} \quad \lambda = \left(\frac{b'_{eff,cwc}\,t_{cw}\sigma_{cwy,T}}{F_{cr}}\right)^{1/2} > 0.67 \tag{8.15}$$

in which, $F_{cr} = \dfrac{\pi E_{cw,T}t_{cw}^{\,3}}{3\left(1-\nu^2\right)d_{cw}}$; for $\lambda \le 0.67$, $F'_{cwc,Rd} = F_{cwc,Rd}$.

Evaluations of rotational resistance and initial rotational stiffness of joints, according to mechanical descriptions of tension and compression zones suggested by Faella *et al.* (2000), give close agreements with experimental results conducted by a number of researchers. Faella's proposed analytical method gives a significant improvement over Eurocode 3: Part 8 (EN 1993-1-8). Thus, these mechanical descriptions are incorporated into overall steel joint model in current study. The author's contribution lies in the incorporation of beam shear component, which will be introduced in Section 8.4.4.

8.4.4 Simplified Mechanical Predictions for Shear Zone

For single-sided beam-to-column joints or double-sided joints but subjected to unsymmetrical bending moments, unstiffened column web panel will withstand shear action. Eurocode 3, Part 1.8 (EN 1993-1-8) specifies shear resistance of unstiffened column web panels is given by:

$$V_{cws,Rd} = \frac{0.9\sigma_{cwy,T} A_{vc}}{\sqrt{3}\gamma_{M0}} \tag{8.16}$$

in which, A_{vc} is shear area of column web panel, and is equal to $A_{vc} - 2b_{cf}t_{cf} + (t_{cw} + 2r_c)t_{cf}$; $\sigma_{cwy,T}$ is yield strength of column web T.

The rotational stiffness of a column web panel under shear force is specified by Eurocode 3: Part 1.8. (EN 1993-1-8) as follows.

$$K_{cws} = \frac{G_{cw} A_{vc}}{\beta h_t} = \frac{0.38 E_{cw} A_{vc}}{\beta h_t} \tag{8.17}$$

where: h_t is column lever arm length; β is transformation parameter from internal actions applied onto steel joint, which is equal to 0 in case of internal joint with symmetrical end moments.

For bare steel beam-to-column joints and composite joints, beam web panel may show yielding or buckling behaviour due to shear and compressive force (Li *et al.* 1996[a], 1996[b]). Therefore, rotation of beam web panel due to shear and corresponding bending moment should be considered when calculating the steel joint rotational stiffness and capacity. For rectangular simply supported plates, Chapman and Davidson (1987) found that, for web aspect ratio (b_w / d_w) larger than 1, both critical shear stress and tension field resistance diminish with increasing b_w / d_w. However, this decreasing trend approaches a constant beyond the limit of $b_w / d_w = 3$, for separate plates with three slenderness ratios (80, 120 and 180). Therefore, for current investigation, the buckling length of beam (b_w) is assumed as $3d_w$ (d_w is depth of beam web). As described in Section 4.2 and 4.3, shear capacity of beam web panel and load versus panel deflection at elevated temperatures have been derived based on classical plate girder shear theory and stability theory with consideration of thermal restraint effect. Nevertheless, "Component-Based" analysis of steel joint requires consideration incorporations of relationship between shear force and web in-plane deflection (vertical deflection). As described in Section 4.4, the respective rotational stiffness of shear component in the beam web panel for pre- and post-buckling stage is expressed as:

$$k_{\Phi,cr} = GdtL_B = \frac{EdtL_B}{2(1+\nu)} \qquad k_{\Phi,u}' = \frac{EV_{ult}^m L_B \left(V_{ult}^m c - 4M_{pfr}\right)}{\left(\sigma_t^y\right)^2 cdt} \tag{8.18}$$

in which: L_B is beam length. Corresponding shear capacity can be obtained from the analytical method as presented in Section 4.2. However, as described in Section 5.6, there is minor difference between the analytical predictions of beam web stiffnesses during pre- and post-buckling stages for such slender beam sections in shear. Thus, simplified rotational stiffness of beam web shear component at pre-buckling stage

will be incorporated into the "Componet-based" model for both pre- and post-buckling stages, as discussed in Section 8.4.5.

8.4.5 Moment-Rotation Relationship of Steel Joints

Based on the derivations of rotational stiffness and capacity for respective components, initial overall rotational stiffness of the steel joint can be obtained from Equation 8.2. In this section, the author proposes a trilinear mathematical representation to simulate the overall steel joint response as specified in Eurocode 3 (EN 1993-1-8) and shown in Figure 8.16.

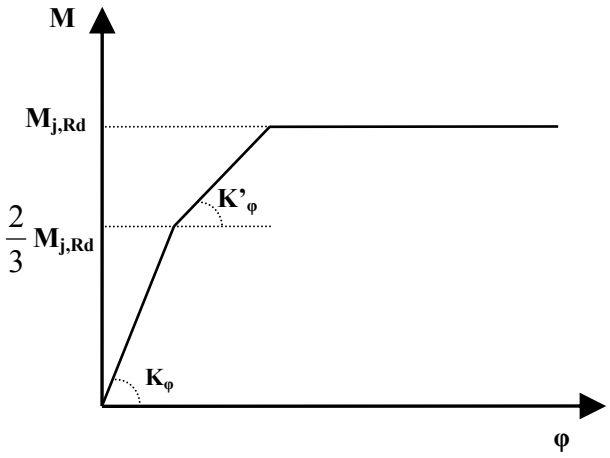

Figure 8.16 Trilinear Approximation of Steel Joint Moment-Rotation Relationship (EN 1993-1-8)

For the first branch of moment-rotation curve, initial elastic linear behaviour of steel joint is defined as:

$$M = K_{\varphi}\varphi \quad \text{for} \quad M \le 2M_{j,Rd}/3 \tag{8.19}$$

The second branch represents the nonlinear rotational characteristics of steel joint, obtained from the following expression.

$$M = \frac{K_{\varphi}}{\left(1.5\frac{M}{M_{j,Rd}}\right)^{\xi}}\varphi \quad \text{for} \quad 2M_{j,Rd}/3 < M \le M_{j,Rd} \tag{8.20}$$

in which, coefficient ξ depends on joint types, which is equal to 2.7 for welded and end-plate joints and 3.1 for seat angle joints as specified in Eurocode 3 (EN 1993-1-8). Thus, for current study, the post-yielding rotational stiffness is simplified as $K'_{\varphi} \approx K_{\varphi} / 7$.

Although Eurocode 3 (EN 1993-1-8) neglects strain-hardening effect of steel, this beneficial characteristic can be incorporated into moment-rotation relationship by introducing of rotational stiffness at strain-hardening stage as $K_{\varphi} /(E / E_h)$, where E / E_h is strain hardening ratio of steel material and K_{φ} is initial rotational stiffness of steel joint. Notably, steel material has little strain-hardening behaviour at elevated temperatures (Figure 3.6), thus, this effect is insignificant for steel joints at higher temperatures. The author derives a simplified rotational and capacity model for extended end-plate steel joint, based on different mechanical components including beam web shear component.

The proposed analytical modeling of joint was validated by both restrained and unrestrained cruciform specimens. The assumed temperature distribution and material properties were those obtained experimentally as described in Section 7.4. First, as shown in Figure 8.17, analytical predictions of joint rotational behaviour without incorporation of beam web shear component are compared with test results for six cruciform specimens in current investigation. It is evident that, without consideration of shear component, this analytical model slightly over-estimates the rotational stiffnesses for the first group of restrained joint tests (CR1, CR2 and CR3), as shown in Figure 8.17 (a), (b) and (c). As described in Section 8.3.3, the first group of cruciform specimens shows a combined failure mode of end-plate bending and beam web in shear. This causes some discrepancies in the rotational stiffness between analytical predictions and experimental measurements for this

group of tests. However, for the second group of tests (CR4, CR5 and CR6), analytical predictions without shear component (Figure 8.17 (d)) illustrate much stiffer rotational behaviour when compared with experimental measurements. This is because the beam web shear failure mode dominated the deflection developments for this group of specimens, which consisted of relatively slender beam section but much thicker end-plate compared with CR1, CR2 and CR3, to prevent local bending of end-plate at elevated temperatures. As a contrast, comparisons between analytical predictions incorporating the shear component in beam web and test results (CR1 to CR3, CR4 to CR6) are shown in Figure 8.18 (a), (b), (c) and (d).

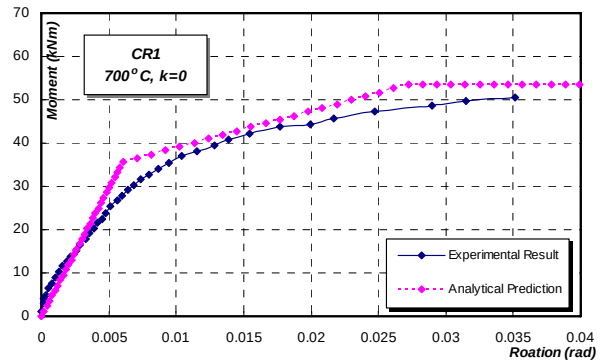

(a)

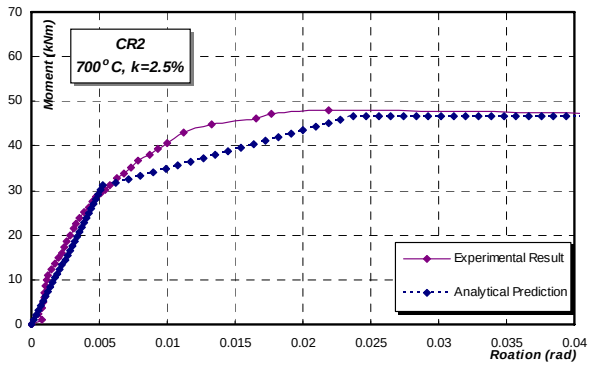

(b)

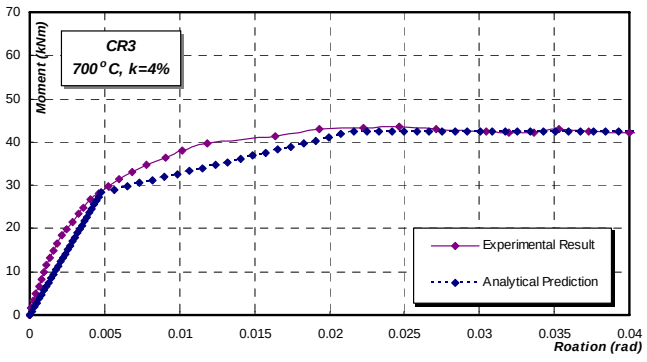

(c)

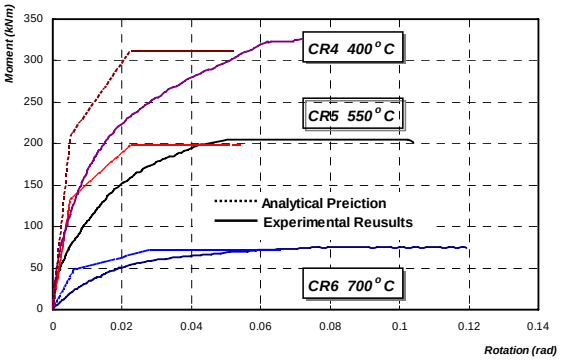

(d)

Figure 8.17Comparison between Analytical Prediction and Test Results without Shear Component in Beam Web

Clearly, as shown in Figure 8.18 (a), (b) and (c), for the first group of tests (CR1, CR2 and CR3), there is a good correlation between these analytical predictions and experimental measurements with shear component introduced, the stiffnesses of

joints are lesser compared to theoretical prediction in Figure 8.17 (a), (b) and (c). For the second group of test (CR4, CR5 and CR6), when comparing between analytical predictions without and with shear component in the beam web panel (Figure 8.17 (d) and Figure 8.18 (d)), it is evident that the proposed analytical model gives much better agreement in terms of rotational stiffness.

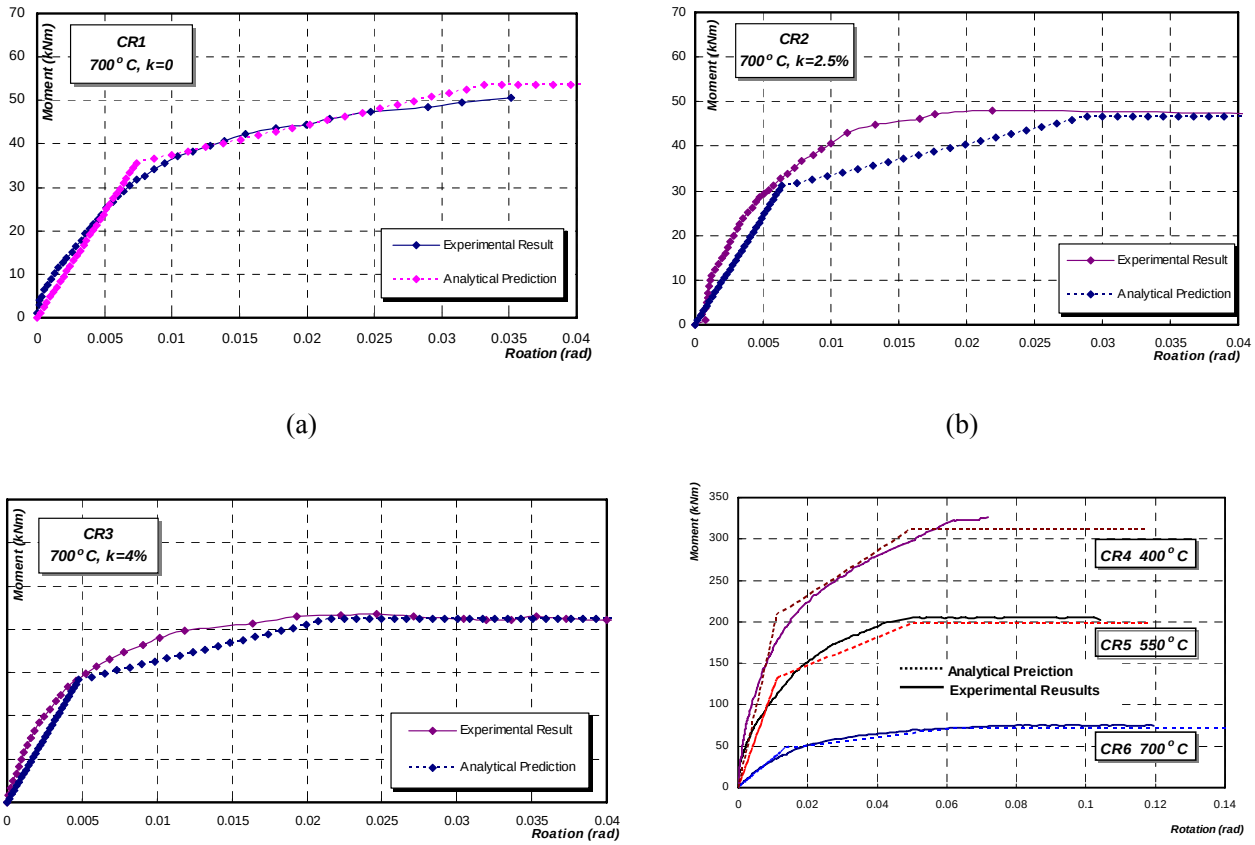

Figure 8.18 Comparison between Analytical Prediction and Test Results with Shear Component in Beam Web

8.5 Conclusion

A series of FE simulations have been conducted for current cruciform tests, with reasonable agreement with test results at elevated temperatures. Thus, it can be concluded the FE models are able to predict the steel joint behaviour accurately. Some discrepancies were due to imprecise temperature distribution and to a small extent, associated material properties. To provide an accurate prediction method for

steel joint rotational characteristics at both ambient and elevated temperatures, an analytical method called "Component-Based" method is extended to include the shear component in beam web. Mechanical descriptions for different components within compression and tension zones are reviewed, with incorporation of analytical equation for shear component in beam web. Moment-rotation results obtained from this analytical model show acceptable agreements compared with test results. Thus, proposed mechanical model is able to predict behaviour for extended end-plate joint. It can also be concluded the "Component-Based" model is accurate and economical compared to the complex FE analysis. It offers practical benefits in predicting failure mechanism and moment-rotation behaviour for such kind of joint. Furthermore, this analytical method allows different temperature distribution for each component of steel joint, to obtain a more realistic prediction of steel joint rotational characteristics under elevated temperatures. Finally, this method can also be extended to composite joints, which is outside the scope of this study.

CHAPTER 9
CONCLUSIONS AND FURTHER RECOMMENDATIONS

9.1 Introduction

Until recently, provisions of adequate fire protections for steel and composite structures are mainly through prescriptive path by applying sufficient fire protection materials for beams and columns. It should be noted that conventional fire protections for structural steel can add up to 30% to the cost of the bare steelwork (Lawson, 2001). This represents a significant addition to the construction cost, and places steel structures at a disadvantage compared with concrete structures. Therefore, to minimize fire protection costs provides a strong impetus to research work on fire effects on steel structures. Based on these research programmes, a "Performance-Based" design approach has evolved and adopted by the European building authorities. This design approach is now considered as a part of "Fire Safety Engineering", which is a holistic approach, integrating a wide range of activities such as structural engineering, building services, mechanical engineering, etc.

Until recently, some research studies have been conducted to investigate the influence of temperature on steel structures and isolated members (Cooke *et al.* 1987, Faris *et al.* 1998, Tang *et al.* 2001, Liu *et al.* 2002, Huang *et al.* 2004, 2006, Tan *et al.* 2006, etc.). Because steel members are assembled together through joints, there is a pressing need to better understand the joint behaviour and its effect on

overall behaviour of steel framed structures under fire conditions. However, to date, there has only been a limited number of experimental investigations conducted with relatively few types of joints at elevated temperatures. In addition, due to complexity and diversity of steel joints, it is more convenient to consider a joint as an assembly of various mechanical components, basically, as tension, compression and shear zones, viz. “Component-Based” method.

Current research focuses on experimental, numerical and analytical investigations of beam web component within the shear zone, at both ambient and elevated temperatures. With incorporation of other components from compression and tension zones, a “Component-Based” model was constructed to represent rotational characteristics of typical extended end-plate joints at ambient and elevated temperatures. This model has been verified by experimental results and finite element analyses in Section 8.4.

9.2 Mechanical Investigations of Beam Web Shear Component

In typical steel beam-to-column extended end-plate joints, mechanical components within the shear zone consist of column web and beam web panels subjected to shear force, and under fire conditions, restraint compressive force induced by adjacent cooler structures. In this study, the beam web shear component is further simplified into an equivalent girder web panel subjected to shear force.

9.2.1 Experimental Investigation of Shear Component

In the first part of experimental investigation of beam web shear component, five series of beams (TG1, TG2, TG3, TG4 and TG5) were tested at ambient and elevated temperatures without thermal restraint effects. In addition, three more series of beams (RTG3, RTG4 and RTG5) were tested under thermal restraint at higher temperatures. These series have different web slenderness ratios and material properties. From unrestrained tests, it was observed that shear yielding occurred in

the web of universal column sections (with stocky web slenderness) at both ambient and elevated temperatures. For slender beams, web tension field action (TFA) was observed under a relatively smaller shear force. Ultimate shear strength of plate girder section reduced significantly with increasing temperature. Moreover, at higher temperature, shear buckling failure became less apparent due to significantly nonlinear strain-stress characteristics of steel. For three series of thermal restrained tests on beams with slender webs, web tension field action behaviour was observed. From measurements, it is concluded that the thermal restraints weakened the ultimate shear capacity of plate girder web panel compared with unrestrained plate girders. This influence appeared to be more significant with higher thermal restraints, and with greater web plate slenderness (d_w / t_w).

9.2.2 Mechanical and FEM Investigations of Shear Component

During current analytical investigations, first, an analytical approach to predict plate buckling and ultimate shear strengths at elevated temperature has been improved from classic plate girder theory at normal temperature. This classical theory of plate girders in shear under normal ambient condition has been extended to incorporate temperature-dependent material properties and thermally-induced axial stress in fire conditions. The derived equations form the basis for the analysis of steel plate girders subjected to shear web buckling under fire conditions. The predicted shear strengths from this work compare reasonably well with both experimental results and FE predictions. From current investigations, it is shown that the shear strength of a plate girder web panel reduces corresponding to an increase in temperature, as well as thermal restraint stress.

In addition, to obtain a clear description of beam web panel under shear, mathematical models have been used to study the in-plane and out-of-plane deflections under pure shear and combination of shear and induced compression

under fire conditions. In this research, Galerkin's energy method has been applied to analyze pre- and post-buckling out-of-plane deflection characteristics web plates of plate girders at elevated temperatures. This part of analytical investigation concerns plates with various initial imperfections, plate aspect ratios and compressive stress ratios. Theoretical predictions show that, with the same initial imperfection ratios, rectangular plates present similar load-deflection behaviour. However, shear buckling strength is greatly influenced by plate aspect ratios. With a combination of shear and compressive loads, both square and rectangular plates exhibit similar load-deflection relationships due to lower compressive stress ratios. Besides, a simple analytical approach has also been presented to depict in-plane deflection developments for web plates. Proposed analytical approaches for both out-of-plane and in-plane web plate deflection predictions have been verified by experimental measurements and finite element simulations. These approaches offer a practical and economical way of predicting deflection characteristics for plates, and are relatively convenient to be used in structural practices.

In addition to analytical investigations, a series of finite element analysis (FEA) has also been conducted with MSC.Marc Mentat (MSC, 2001). Both single beam web panel model and whole beam model were studied. From comparison among FEA, analytical and experimental results, it is clear that proposed FE models were able to predict shear behaviour of beam web panel accurately at both ambient and elevated temperatures. Under restrained boundary conditions, FE models gave good agreements with analytical predictions. For beams subjected to thermal restraint, these additional stresses caused the beam web panel to buckle at a lower shear stress compared to unrestrained specimens.

9.3 Experimental Investigations of Steel Beam-to-Column Joint

In this part of experimental investigations, typical bare steel extended end-plate beam-to-column joints have been tested to obtain moment-rotational characteristics

of steel joints. The objective was to provide verifications for the proposed "Component-Based" joint model. Six steel joints were tested as "cruciform" assemblies, which consisted of three cruciform specimens (CR1, CR2 and CR3) tested with thermal restraint forces and another three cruciform specimens (CR4, CR5 and CR6) tested under thermally unrestrained boundary conditions to investigate the shear component in beam web panel.

From the three thermally restrained cruciform tests, it was observed that both left and right connected beams showed almost symmetrical deflection development. From deflection measurements at the beam ends, moment-rotation relationships can be obtained. It was noticed that axial restraint force has significant effect on steel joint moment capacity at higher temperature. Current design standard, Eurocode 3, Part 1.8 (EN1993-1-8) only considers axial force effect when it exceeds 5% of squash load of member cross-section. Therefore, it is suggested that in steel joint modelling at fire conditions, axial thermal restraint forces should be incorporated into the beam and column components. From restrained cruciform tests, in addition to out-of-plane deflection in the beam web panels, significant bending deformations can be observed at the end-plate adjacent to the beam bottom flanges (in tension). CR1 shows the greatest end-plate bending deflection due to tensile force transferred from the beam bottom flanges. The gap between the end-plate and column flanges for CR2 and CR3 specimens decreased with increasing axial restraint. For thermally unrestrained cruciform tests, due to lateral support system, there was clear beam web tension field action near the column for the specimen (CR4) tested at 400 ^{o}C. But such behaviour was not pronounced at 550 ^{o}C and 700 ^{o}C (CR5 and CR6). This was due to already highly nonlinear steel material characteristics at these temperatures. Based on these obtained moment -rotation-temperature characteristics, it is anticipated that these results will be beneficial in validating "Component-Based" modelling for steel joints under fire conditions.

9.4 Numerical and Mechanical Investigations of Steel Joint

As a supplementary verification, FE models were constructed for currently investigated steel beam-to-column joints using MSC.Marc Mentat (MSC, 2001). Quadratic eight-node thick shell element was chosen for discretization of beams, columns and end-plates. In addition, the bolts were simulated with three sets of springs representing axial tension and two-dimensional shear stiffnesses. To represent cruciform specimens more realistically, measured initial beam web out-of-plane imperfections of the beam section were applied onto FE mesh as approximate curves along the beam length, as well as temperature distributions obtained from experimental investigations. From comparison between predictions and test results, the FE models could predict the steel joint behaviour accurately, which consisted moment-rotation characteristics and failure behaviour, etc. Nevertheless, small discrepancies existed and were mainly due to imprecise temperature distribution and to a small extent, associated material properties.

With application of “Component-Based” method, steel joint behaviour can be idealized as a combination of separate mechanical components in designated mechanical area. In current investigation, proposed analytical models of the beam web shear component have been incorporated with other components within compression and tension zones. Simplified joint analytical model was established by superimposing respective stiffness of each component in different zones. The moment-rotation result obtained from this mechanical model gave acceptable agreement with test results, especially suitable for the experimental results from cruciform tests with beam shear failure. Therefore, proposed mechanical model can predict the behaviour of such joint well. Moreover, current “Component-Based” analysis approach allows different temperatures for the components in the joint. This means that the “Component-Based” method can give more realistic simulations of steel joints in fire conditions.

9.5 Recommendations for Future Works

Current research work in NTU represents the first step forward of investigating the applicability of "Component-Based" method to steel joint behaviour under fire conditions. In this research, the shear component in the beam web region has been singled out and studied analytically. Moreover, thermal restraint effect has been addressed. Major components in tension and compression zones, have been studied experimentally and analytically by several researchers (Spyrou 2002, Block 2004[a], etc.). However, there still remain some other components in the steel joint which require detailed experimental and analytical investigations. One such example is the ***beam flange in compression***. In addition to investigations of individual components, ***interactions*** among several components should also be addressed, especially between column web in shear and column flange in tension or compression, or between beam web in shear and flange in compression. Only with these further studies, a holistic understanding of steel joint behaviour is possible in the future, by substituting the joints as semi-rigid springs which represent the respective stiffness and strength of individual components.

Besides, commercial finite element program has yielded reasonably good agreement with test results. However, it still needs further improvement, particularly in the area of ***contact phenomenon*** between the bolts and the connecting elements, representations of material degradation at elevated temperatures, etc. It is evident that that the use of such finite element programs could offer a much cheaper alternative to testing, providing an improved understanding of the joint behaviour through parametric studies. Besides, these FE models can also be used to validate "Component-Based" model. Thus, what remains is the actual implementation of individual components as semi-rigid springs in structural analyses, which is for future research.

REFERENCES

AASHTO (American Association of State Highway and Transportation) (1996) "Official Standard Specification of Highway Bridge", 16th Edition, Washington, D.C.

Aggarwal, A.K. and Coates, R.C., (1986),"Strength Criteria for Bolted Beam-Column Connections", Journal of Constructional Steel Research, Vol.**7**, pp213-227.

Al-Jabri, K. S., Lennon, T., Burgess, I. W. and Plank, R. J. (1998), "Behaviour of Steel and Composite Beam-Column Connections in Fire", Journal of Constructional Steel Research, Vol. **46**(1-3), Paper No. 180.

Al-Jabri, K.S. (1999), "The Behaviour of steel and composite Beam-Column Connections in fire", PhD thesis, Department of Civil and Structural Engineering, University of Sheffield.

Al-Jabri, K.S., Burgess, I.W. and Plank, R.J., (2005), "Moment Rotation Temperature Curves for Semi-Rigid Joints", Journal of Constructional Steel Research, Vol.**61**, pp281-303.

Al-Jabri, K.S., Seibi, A. and Karrech, A., (2006), "Modelling of Unstiffened Flush End-plate Bolted Connections in Fire", Journal of Constructional Steel Research, Vol.**62**, pp151-159.

Altmann, R. Maquoi, R. and Jaspart, J.P., (1991), "Experimental Study of the Non-Linear Behaviour of Beam-to-Column Composite Joints", Journal of Constructional Steel Research, Vol.**18**, pp45-54.

Ang, K.M. and Morris, G.A. (1984),"Analysis of Three-Dimensional Frames with Flexible Beam-Column Connections", Canadian Journal of Civil Engineering, Vol.**11**, pp245-254.

Aribert, J. M., Lachal, A. and Moheissen, M. (1990), "Interaction du Voilement et de la Résistance Plastigue de l'àme d'un Profilé Laminé Soumis à Undoable Compression Locale", Construction Métallique, No.**2**. (as cited by Faella et al, 2000).

ASIC (1963), "Specification for the Design, Fabrication and Erection of Structural Steel for Building", American Institute of Steel Construction, New York, USA.

Bahaari, M.R and Sherbourne, A.N. (1997), "Finite Element Prediction of End Plate Bolted Connection Behaviour. II: Analytical Formulation", Journal of Structural Engineering, ASCE, Vol.**123** (2), pp165-175.

Bailey, C.G. and Newman, G.M. (1998), "The Design of Steel Framed Buildings without Applied Fire Protection", The Structural Engineer, Vol.**76**(5), pp 77-81.

Bailey, C.G. (1999), "The Influence of Local and Global Forces on Column Design", Final Report prepared for Department of the Environment, Transport and the Regions, Building Research Establishment Ltd, UK.

Bailey, J.R. (1970), "Strength and Rigidity of Bolted Beam-to-Column Connections", Conference on Joints in Structures, University of Sheffield, UK.

Baker, J.F. (1934) (as cited by Sherbourne and Bahaari, 1997) "Steel Structures Research Committee, Second Report", Department of Scientific and Industrial Research, London.

Basler, K. (1961[a]), "Strength of Plate Girder in Shear", Journal of Structural Division, ASCE, No.**87**, ST**7**, 151-180.

Basler, K. (1961[b]), "Strength of Plate Girder under combined Bending and Shear", Journal of Structural Division, ASCE, No.**87**, ST**7**, 181-197.

Basler, K. and Thurlimann, B. (1959), "Plate girder research". In proc. AISC National Engineering Conf. New York, USA.

Batho and Rowan (1934), "Steel Structures Research Committee, First Report", Department of Scientific and Industrial Research, HMSO, London.

Bernoulli, J., (1789), "Nova Ata", Vol.**5** (St. Petersburg).

Block, F.M., Burgess, I.W., Davison, J. B. and Plank, R.J., (2004[a]), "A Component Approach to Modelling Steelwork Connections in Fire: Behaviour of column Webs in Compression", Proceedings of the 2004 Structures Congress - Building on the Past: Securing the Future, pp1163-1170, Nashville, USA.

Block, F.M., Burgess, I.W. and Davison, J. B., (2004[b]), "Numerical and Analytical Studies of Joint Component Behaviour in Fire", Proceedings of Third International Workshop-Structure in Fire, pp383-395.

Bose, S.K., McNeice, G.M. and Sherbourne, A.N. (1972), "Column Webs in Steel Beam to Column Connection. Part 1 Formation and Verification", Computers and Structures, Vol.**2**, pp253-279.

BS 3692 (1967), "Metric Precision Hexagon Bolts, Screws and Nuts", British Standards Institution.

BS 4360 (1979), "Specifications for Weldable Structural Steels", British Standards Institution.

BS 476: Part 20 (1987), "Fire Tests on Building Materials and Structures - Part 20: Method for Determination of the Fire Resistance of Elements of Construction", British Standards Institution.

BS 5950: Part 1 (1990), "Structural Use of Steelwork in Building, Code of Practice for Design in Simple and Continuous Construction: hot rolled sections", British Standards Institution.

BS 5950: Part 1 (2000), "Structural Use of Steelwork in Building, Code of Practice for Design-Rolled and Welded Sections", British Standards Institution.

BS 5950: Part 8 (2003), "Structural use of steelwork in building, Code of Practice for Fire Resistance Design", British Standards Institution.

Building Regulations, (1991), "Approved Document B : Fire Safety", Loss Prevention Council.

Bursi, O.S. and Jaspart, J.P. (1997[a]), "Benchmarks for Finite Element Modelling of Bolted Steel Connections", Journal of Constructional Steel Research, Vol.**43**(1-3), pp17-42.

Bursi, O.S. and Jaspart, J.P. (1997[b]), "Calibration of a Finite Element Model for Isolated Bolted End-Plate Steel Connections", Journal of Constructional Steel Research, Vol.**44**(3), pp225-262.

Bursi, O.S. and Jaspart, J.P. (1998), "Basic Issues in the Finite Element Simulation of Extended End Plate Connections", Computers and Structures, Vol.**69**, pp361-382.

Calladine, C. R. (1973), "Plastic theory for collapse of plate girders under combined shearing force and bending moment", The Structural Engineer, Vol.**51** (4), 147-154.

Chapman, J.C. and Davidson, P.C., (1987), "Behaviour and design of full-depth web panels in shear", The Structural Engineer, Vol.**65B**, No.4, pp65-77.

Chen W. F. and Lui, E. M., (1985), "Beam-to-Column moment resisting Connection: Steel framed structures Stability and Strength", Elsevier Applied Science Publishers.

Cheung, Y.K. (1976), "Finite Strip Method in Structural Analysis", Pergamon Press.

Coan, J.M. and Urbaba, I., (1951), "Large-Deflection Theory for Plate With Small Initial curvature Loaded in Edge Compression", Journal of Applied Mechanics, ASME, Vol.**43**, pp143-151.

Colson, A. and Louveau, J.M. (1983), "Connection Incidence on the Inelastic Behaviour of steel Structures", Euromech Colloquium, 174.

Cooke, G.M.E. (1988) "An introduction to the mechanical properties of structural steel at elevated temperatures", Fire Safety Journal, Vol.**13**, No.1, pp 45-54.

Davison, J.B., Kirby, P.A. and Nethercot, D.A., (1987), "Rotational Stiffness Characteristics of Steel Beam-to-Column Connections", Journal of Constructional Steel Research, Vol.**8**, pp17-54.

Dawson, R.G. (1971), (as cited by Murray, 1986) "Local Buckling of Thin-Walled Structural Forms", Ph.D Thesis, University of London.

ECCS (European Convention for Constructional Steelwork) (1983) "European Recommendations for the Fire Safety of Steel Structure", Elsevier, Amsterdam.

El-Rimawi, J.A. (1989) "The Behaviour of Flexural Members under Fire Condition", Ph.D Thesis, University of Sheffield, UK.

El-Rimawi, J.A., Burgess, I.W. and Plank, R.J., (1997), "Influence of connection stiffness on the behaviour of steel beams in fire", Journal of Constructional Steel Research, Vol.**43**, pp1-15.

Euler, L. (1766), "De Motu Vibratorio Tympanorum", Novi Commentari Acac., Petroplot., Vol.**10**, pp243-260.

Eurocode 3, Part 1.1 (1992), "Design of steel structures: Part 1.1 General Rules and rules for buildings", ENV 1993-1-1, Commission of European Communities, Brussels, Belgium.

Eurocode 3, Part 1.1 Annex J (1992), "Design of steel structures: Part 1.1 General Rules and rules for buildings", ENV 1993-1-1, Commission of European Communities, Brussels, Belgium.

Eurocode 3, Part 1.1 (2002), "Design of steel structures: Part 1.1 General Rules and rules for buildings", EN 1993-1-1, Commission of European Communities, Brussels, Belgium.

Eurocode 3, Part 1.2 (1995), "Design of steel structures: Part 1.2 General Rules, Structural Fire Design", ENV 1993-1-2, Commission of European Communities, Brussels, Belgium.

Eurocode 3, Part 1.2 (2002), "Design of steel structures: Part1.2 General Rules, Structural fire design", EN 1993-1-2, Commission of European Communities, Brussels, Belgium.

Eurocode 3, Part 1.8 (2002), "Design of steel structures: Part1.8 Design of Joints", EN 1993-1-8, Commission of European Communities, Brussels, Belgium.

Faella, C., Piluso, V. and Rizzano, V. (1995), "Modelling of the Moment-Rotation Curve of Welded Connections: Proposal to Improve Eurocode 3 Annex J", Italian Conference on Steel Construction, Riva del Garda. (as cited by Faella et al. 2000)

Faella, C., Piluso, V. and Rizzano, V. (2000), "Structural Steel Semirigid Connections: Theory, Design and Software", CRC Press LLC, Florida, US.

Faris, A. Ali, Shepherd, P., Randell, M., Simms, I. W., O'Connor, D. J. and Burgess, I. W., (1998), "Effect of Axial Restraint on the Fire Resistance of Steel Columns", Journal of Constructional Steel Research, Vol.**46**(1-3), pp305-306.

Fok, C.D. (1980), "Effects of Initial Imperfections on the Elastic Post-Buckling Behaviour of Flat Plates", Ph.D. Thesis, Monash University.

Franssen, J.M. (1987) "Etude du Comportement au feu des structures mixtes acier-béton", Ph.D Thesis, Université de Liège.

Frye, M.J. and Morris, G.A. (1975), "Analysis of Flexibly Connected Steel Frames", Canadian Journal of Civil Engineering, Vol.**2**, pp280-291.

Gebbeken, N. and Rothert, H. and Binder, B. (1994), "On the numerical Analysis of Endplate Connection", Journal of Constructional Steel Research, Vol.**30**, pp26-32.

Ghobarah, A., Osman, A. and Korol, R.M., (1990) "Behaviour of Extended End-plate Connections under Cyclic Loading", Engineering Structure, Vol.**12**, pp15-27.

Green, J.R. and Southwell, R.V. (1946), "Relaxation Applied to Engineering Problems VIIIA: Problems Relating to Large Transverse Displacements of Thin Elastic Plates", Phil. Trans., Serial. A. pp59.

Harding, J. E., and Dowling, P. J. (1978), "The Basis of The Proposed New Design Rules for the Strength of Web Plates and Other Panels Subject to Complex Edge Loading", Stability Problems in Engineering Structures and Components, Richards T. H. and Stanley, P., eds., Applied Science Publishers, London, 355-376.

Hendrick, D.M. and Murray, T.M., (1984), "Column Web Compression Strength at End-Plate Connections", Engineering Journal, AISC, Vol.**21**, pp161-169.

Horne, M.R. and Morris, L.J., (1981), "Plastic Design of Low-rise Frames", Granada, Publishing Ltd.

Huang, Z. F. and Tan, K. H. (2004), "Effects of External Bending Moments and Heating Schemes on the Responses of Thermally Restrained Steel Columns", Engineering Structures, Vol.**26**(6), pp769-780.

International Organisation for Standardisation, (1985), "Fire Resistance Test-Elements of Building Construction", ISO834, International Standards Organization.

Janss, J., Jaspart, J.P. and Maquoi, R., (1989), "Experimental Study of the Non-linear Behaviour of Beam-to-Column Bolted Joints", Connections in Steel Structures: Behaviour, Strength and Design, Elsevier Applied Science Publishers, London, pp96-103.

Jaspart, J.P., (2000), "General Report: Session on Connections", Journal of Construction Steel Research, Vol.**55**, pp69-89.

Johnson, L.G., Cannon, J.C. and Spooner, L.A., (1960), "High Tensile Preloaded Bolted Joints", British Welding Journal, Vol.**7**, No.9, pp560-569.

Johnson, R.P. and Law, C.L.C., (1981), "Semi-Rigid Joints for Composite Frames", Joints in Structural Steelwork, The Design and Performance of Semi-Rigid Joints in Steel and Composite Structures and Their Influence on Structural Behaviour, Teesside Polytechnic, Pentech Press, pp3.3-3.19.

Johnston, B.G. and Deits, G.R., (1942), "Tests of Miscellaneous Welded building Connections", Welding Journal, Vol.**21**, pp560-569.

Jones, S.W., Kirby, P.A. and Nethercot, D.A. (1980), "Effects of Semi-Rigid Connections on Steel Column Strength", Journal of Constructional Steel Research, Vol. **1**, pp38-46.

Kato, B., Chen, W.F. and Nakao, M., (1988), "Effects of Joint-panel Shear Deformation on Frames", Journal of Constructional Steel Research, Vol.**10**, pp269-320.

Kirby, B. R. (1995) "The Behaviour of High Strength Grade 8.8 Bolts in Fire", Journal of Constructional Steel Research, Vol.**33**, pp.3-38.

Kirby, B. R. and Preston, R. R. (1988) "High temperature properties of Hot Rolled , Structural Steels for Using in Fire Engineering Design Studies", Fire Safety Journal, Vol.**13**, No.1, pp.27-37.

Kirchhoff (1877), "Mechanik", 2nd Edition, pp.450.

Kishi, N. and Chen, W.F., (1987), "Moment-Rotation Relations of Semirigid Connections with Angles", Journal of Structural Engineering, ASCE, Vol.**116**(7), pp1813-1834.

Kishi, N., Chen, W.F., Matsuoka, K.G. and Nomachi, S.G., (1988[a]), "Moment-Rotation Relation of Top- and Seat- Angle with Double Web –Angle Connections", Connections in Steel Structures: Behaviour, Strength and Design, Elsevier Applied Science Publishers, London, pp121-134.

Kishi, N., Chen, W.F., Matsuoka, K.G. and Nomachi, S.G., (1988[b]), "Moment-Rotation Relation of Single/Double Web-Angle Connections", Connections in Steel Structures: Behaviour, Strength and Design, Elsevier Applied Science Publishers, London, pp135-149.

Kharrazi, M.H., Ventura, C.E. and Prion, H.G.L., (2004), "Bending and Shear Analysis and Design of Ductile Steel Plate Walls", 13th Word Conference on Earthquake Engineering, Vancouver, B.C., Canada.

Krawinker, H., Bertero, V.V. and Popov, E.P., (1975), "Shear Behaviour of Steel Frame Joints", Journal of Structural Engineering, ASCE, Vol.**101**(11), pp 2317-2336.

Krishnamurthy, N. (1980), "Modelling and Prediction of Steel Bolted Connection Behaviour", Computers and Structures, Vol.**11**, pp75-82.

Krishnamurthy, N. and Graddy, D.E. (1976), "Correlation Between 2- and 3-Dimensional Finite Element Analysis of Steel Bolted End-Plate Connections", Computers and Structures, Vol.**6**, pp381-389.

Kukreti, A.R., Murray, T.M. and Abolmaali, A., (1987), "End-Plate Connection Moment-Rotation Relationship", Journal of Constructional Steel Research, Vol.**8**, pp137-157.

Latter, R., (1994), "The European Market for Constructional Steelwork", New Steel Construction, Vol.**2**(5).

Lawson, R. M. (1990), "Behaviour of steel beam-to-column connections in fire", The Structural Engineer, Vol.**68**(14), pp263-271.

Lawson, R. M., (2001), "Fire engineering design of steel and composite buildings", Journal of Constructional Steel Research, Vol.**57**(12), pp1233-1247.

Lee, S. C., and Yoo, C. H. (1998) "Strength of Plate Girder Web Panels under Pure Shear", Journal of Structural Engineering, ASCE, Vol **124**, No.2, pp184-194.

Lee, S. C., Davidson, J. S., and Yoo, C. H. (1996) "Shear Buckling Coefficients of plate girder web panels", Computers and Structures, Vol **59**, No.5, pp789-795.

Lennon, T. and Jones, L.C. (1995), "Elevated temperature composite connection moment-rotation tests", International Rep. Building Research Establishment, Watford, England.

Leston-Jones, L.C. (1997[a]), "The influence of Semi-Rigid Connections on the Performance of Steel Framed Structures in Fire", PhD thesis, Department of Civil and Structural Engineering, University of Sheffield.

Leston-Jones, L.C., Burgess, I.W., Lennon, T. and Plank, R.J. (1997[b]), "Elevated-Temperature Moment-Rotation tests on Steelwork Connections", Proceedings of the Institution of Civil Engineers, Structures and Buildings, Vol.**122** (4), pp410-419.

Levy, S. and Greeman, S. (1942), "Bending with Large Deflection of a Clamped Rectangular Plate with Length Width Ratio of 1.5 under Normal Pressure", NACA, TN No.853.

Lewitt, C.W., Chesson, E. and Munse, W.H., (1969), "Restraint Characteristics of Flexible and Bolted Beam to Column Connections", University of Illinois, Engineering Experiment Station Bulletin No.500.

Li, T.Q., Nethercot, D.A. and Choo, B.S., (1996[a]), "Behaviour of Flush End-plate Composite Connections with Unbalanced Moment and Variable Shear/Moment Ratios- I. Experimental Behaviour", Journal of Constructional Steel Research, Vol.**38**, pp125-164.

Li, T.Q., Nethercot, D.A. and Choo, B.S., (1996[b]), "Behaviour of Flush End-plate Composite Connections with Unbalanced Moment and Variable Shear/Moment Ratios- I. Prediction of Moment Capacity", Journal of Constructional Steel Research, Vol.**38**, pp165-198.

Liew, J.Y.R., White. D.W. and Chen, W.F., (1993[a]), "Limit States Design of Semi-Rigid Frames using Advanced Analysis: Part 1: Connection Modelling and Classification", Journal of Constructional Steel Research, Vol.**26**, pp1-27.

Liew, J.Y.R., White. D.W. and Chen, W.F., (1993[b]), "Limit States Design of Semi-Rigid Frames using Advanced Analysis: Part 2: Analysis and Design", Journal of Constructional Steel Research, Vol.**26**, pp29-57.

Liew, J.Y.R. and Chen, W.F., (1995), "Analysis and Design of Steel Frames Considering Panel Joint Deformations", Journal of Structural Engineering, ASCE, Vol. **121**(10), pp1531-1540.

Liew, J.Y.R., Teo, T.H. and Shanmugam, N.E., (2004[a]), "Composite Joints Subject to Reversal of Loading-Part 1: Experimental Study", Journal of Constructional Steel Research, Vol.**60**, pp221-246.

Liew, J.Y.R., Teo, T.H. and Shanmugam, N.E., (2004[b]), "Composite Joints Subject to Reversal of Loading-Part 2: Analytical Assessments", Journal of Constructional Steel Research, Vol.**60**, pp247-268.

Liew, J.Y.R., Teo, T.H., Shanmugam, N.E. and C.H. Yu, (2000), "Testing of Steel-Concrete Composite Connection and Appraisal of Results", Journal of Constructional Steel Research, Vol.**56**, pp117150.

Lipson, S.L. (1968), "Single Angle and Single Plate Framing Connections", Canadian Structural Engineering Conference, Toronto, pp141-162.

Liu T.C.H. (1996), "Finite Element Modelling of Behaviors of Steel Beams and Connections in Fire", Journal of Constructional Steel Research, Vol. 36(3), pp181-199.

Liu T.C.H. (1999), "Moment Rotation Temperature Characteristics of Steel Composite Connections", Journal of Structural Engineering, ASCE, Vol. **125**(10), pp1188-1197.

Liu, T.C.H., Fahad, M. K. and Davies, J. M., (2002), "Experimental Investigation of Behaviour of Axially Restrained Steel Beams in Fire", Journal of Constructional Steel Research, Vol.**58**, pp1211-1230.

Lui, E.M. and Chen, W.F. (1986), "Analysis and Behaviour of Flexibly-Jointed Frames", Engineering Structures, Vol.**8**(2), pp107-115.

Mandal, P. and Calladine, C.R., (2003), "Lateral-torsional Buckling of Beams and the Southwell Plot", International Journal of Mechanical Sciences, Vol.**44**(12), pp2557-2571.

Marguerre, K. (1938), (as cited by Murray, 1986), "Zur Theorie der Gekrummmter Plate Grosser Formanderug", Proc. Fifth int. Congress appl. Mech. Pp.93.

Moncartz, P.D. and Gerstle, K.H., (1981) "Steel Frames with Non-linear Connections", Journal of Structural Division, ASCE, Vol.**107**(8), pp1427-1441.

MSC. Marc Mentat (2001), "MSC. MARC User Guide Version 2001", MSC Software Corporation, California, USA.

Murray, N. W. (1983), "Ultimate Capacity of Stiffened Plates in Compression", Chapter 5, Plated Structures, Stability and Strength, Narayanam, N.W., ed., Applied Science Publishers, London, 135-163.

Murray, N. W. (1986), "Introduction to the Theory of Thin-Walled Structures", Clarendon Press, 447p. ed., Applied Science Publishers, London and New York, 135-163.

Murray, N.W. and Thieruf, G. (1980), "Tables for the Design and Analysis of Stiffened Steel Plates", Vieweg, Braunschweig.

Narayanan, R. (1983), "Plated Structures, Stability and Strength", Applied Science Publishers, London and New York, 260p.

Narayanan, R. (1992), "Plate girders", Chapter 17, Steel Designers' Manual, The Steel Construction Institute, Owens, G.W. and Knowles, P. R., eds., 5th Edition., Blackwell Scientific Publications.

Navier, L. (1823). "Bill. Soc. Phil. Math.", Paris.

Nethercot, D.A., (1985[a]), "Joint Action and design of steel frames", the Structural Engineer, Vol.64 (12).

Nethercot, D.A., (1985[b]), "Ulitisation of Experimentally Obtained Connection Data in Assessing the Performance of Steel Frames", Connection Flexibility and Steel Frames, American Society of Civil Engineer, USA, pp13-37.

Patel, K.V. and Chen, W.F. (1984), "Nonlinear Analysis of Steel Moment Connections", Journal of Structural Engineering, ASCE, Vol.**110**(8), pp1861-1875.

Porter, D. M., Rockey, K. C., and Evans, H. R. (1975), "The collapse behaviour of plate girders loaded in shear", The Structural Engineer, Vol **53**, No.8, pp313-325.

Ramberg, W. and Osgood, W.R. (1942) "Description of Stress-Strain Curves by Three Parameters", NACA Technical Report, No.902.

Ramberg, W. and Osgood, W.R. (1943) (as cited by Ang and Morris, 1984) "Description of Stress-Strain Curves by Three Parameters," NACA, Technical Note, No. 902.

Rathburn, J.C. (1936) (as cited by Sherbourne and Bahaari, 1997) "Elastic Properties of Riveted Connections", Transactions of the American Society of Civil Engineers, **101**, pp524-563.

Rhodes, J. (2003), "Some Observations on the Post-buckling Behaviour of Thin Plates and Thin-walled Members", Thin-Walled Structures, Vol. **41**, pp207-226.

Rhodes, J. and Harvey, J.M. (1971), "The Local Bucklin and Post Local Buckling Behaviour of Thin-walled Beams", The Aeronautical Quarterly, November.

Richard, R.M. and Abbott, B.J. (1975), "Versatile Elastic-Plastic Stress-Strain Formula", Journal of Engineering Mechanics, ASCE,. Vol.**101** (4), pp511-515.

Rockey, K. C., Evans, H. R., and Porter, D. M., (1978), "A design method for predicting the collapse behaviour of plate girders", Proc. Instn. Civ. Engrs., Part 2, 85-112.

Rocky, K. C. and Skaloud, M. (1972), "The ultimate load behaviour of plate girders loaded in shear", The Structural Engineer, Vol.**50**, No.1, pp29-47.

Romstad, K.M., and Subramanian, C.V., (1970) "Analysis of Frames with Partial Connection Rigidity", Journal of Structural Division, ASCE, Vol.**96**(11), pp2283-2300.

Saint Venant (1883), "Disscussions in Theories de lelsticite des crops solids", pp.704.

Sakai, F., Doi, K., Nishino, F., and Okumwa, T., (1966), "Failure tests of plate girders using large sized models", Structural Engineering Laboratory Report, Department of Civil Engineering, University of Tokyo.

Sakumoto, Y., Keira, K., Furumura, F. and Ave, T. (1993) "Tests of Fire-Resistant Bolts and Joints", Journal of Structural Engineering, ASCE, Vol.**119**(11), pp3131-3150.

Sakumoto, Y., Yamaguchi, T., Ohashi, M., and Saito, H. (1992) "High-Temperature Properties of Fire-Resistant Steel for Buildings", Journal of Structural Engineering, ASCE, Vol.**118**(2), pp392-407.

Sherbourne, A.N. (1961), "Bolted Beam to Column Connections", The Structural Engineer, Vol.**39,** pp203-210.

Sherbourne, A.N. and Bahaari, M.R. (1997), "Finite Element Prediction of End Plate Bolted Connection Behaviour. I: Parametric Study", Journal of Structural Engineering, ASCE, Vol.**123** (2), pp157-164.

Shields, T.J. and Silcock, G.W.H., (1987), "Buildings and Fire", Longman Scientific and Technical.

Sibai, W.A. and Frey, F. (1988), "Numerical Simulation of the Behaviour up to Collapse of Two Welded Unstiffened One-Side Flange Connection", Connections in Steel Structures: Behaviour, Strength and Design, Elsevier Applied Science Publishers, London, pp85-92.

Sokol, Z., Wald, F., Delabre, V., Muzeau, J.P. and Švarc M., (2002), "Design of End Plate Joints Subject to Moment and Normal Force", Eurosteel 2002 Conference, Coimbra.

Spyrou, S. (2002), "Development of a Component-Based Model of steel Beam-to-Column Joint at elevated temperatures", PhD Thesis, Department of Civil and Structural Engineering, University of Sheffield.

Spyrou, S. and Davison, J.B., (2001), "Displacement Measurement in Studies of Steel T-stub Connections", Journal of Constructional Steel Research, Vol.**57**(6), pp647-659.

Spyrou, S., Davison, J. B., Burgess, I. W. and Plank, R.J., (2004[a]), "Experimental and Analytical Investigation of the 'Compression Zone' Component within a Steel Joint at Elevated Temperatures", Journal of Constructional Steel Research, Vol.**60**(6), pp841-865.

Spyrou, S., Davison, J. B., Burgess, I. W. and Plank, R.J., (2004[b]), "Experimental and Analytical Investigation of the 'Tension Zone' Component within a Steel Joint at Elevated Temperatures", Journal of Constructional Steel Research, Vol.**60**(6), pp867-896.

Spyrou, S., Davison, J. B., Burgess, I. W. and Plank, R.J., (2004[c]), "Experimental and Analytical Studies of Steel Joint Component at Elevated Temperatures", Fire and Materials, Vol. **28**(2-4), pp83-94.

Sumner, E.A. and Murray, T.M., (2002),"Behaviour of Extended End-plate Connections Subject to Cyclic Loading", Journal of Structural Engineering, Vol.**128**, pp501-508.

Surtees, J.O. and Mann, A.P., (1970), "End Plate Connections in Plastically Designed Structures", Conference on Joints in Structures, University of Sheffield, UK.

Tan, K. H., and Qian, Z. H. (2006), "Experimental Behaviour of Thermally Restrained Plate Girder Loaded in Shear at Elevated Temperature", Journal of Constructional Steel Research, (under review)

Timoshenko, S.P. and Gere, J.M. (1961), "Theory of Elastic Stability", (Second Edition), McGraw-Hill Book Company, New York.

Tschemernegg, F., (1988[a]), "On the Nonlinear Behaviour of Joints in Steel Frames", Connections in Steel Structures: Behaviour, Strength and Design, Elsevier Applied Science Publishers, London, pp158-165.

Tschemernegg, F. and Humer, C., (1988[b]), "The Design of Structural Steel Frames under Consideration of the Non-linear Behaviour of Joints", Journal of Constructional Steel Research, Vol.**11**, pp73-103.

Vimonsatit, V., Tan, K. H., Ting, S.K. (2005), "Shear Strength of Plate Girder Web Panel at Elevated Temperatures", Journal of Constructional Steel Research, (under review).

Vimonsatit, V., Tan, K. H., and Qian, Z. H.,(2006), "Testing of Plate Girder Web Panel Loaded in Shear at Elevated Temperature", Journal of Structural Engineering, ASCE, (in press).

von Karman (1910), (as cited by Murray, 1986), "Festigkeitsprobleme im Maschinenbau", Encyklopadie der Mathematischen Wissenschaften, Vol. **4**, B.G. Teubner, Leipzig.

Wagner, H. (1931), "Flat sheet metal girder with very thin metal web", National Advisory Committee for Aeronautics (NACA).

Wald, F., da Silva, L. S., Moore, D. and Santiago, A. (2004), "Experimental Behaviour of Steel Joints under Natural Fire", ECCS / AISC Workshop - Connections in Steel Structures V, Amsterdam, The Netherlands.

Wales, M.W. and Rossow, E.C., (1982), "Coupled Moment-Axial Force Behaviour in Bolted Joints", Journal of Structural Engineering, ASCE, Vol.**129**, pp1250-1266.

Walker, A.C., (1969), "The Post-buckling Behaviour of Simply Supported Square Plate", The Aeronautical Quarterly, XX, pp203-222.

Wang, C.T. (1948), "Non-Linear Large Deflection Boundary Value Problems of Rectangular Plates", NACA, TN No.1425.

Williams, D.G. and walker, A.C. (1975), "Explicit Solutions for the design of Initially Deformed Plates Subjected to Compression", Proc. Inst. Civil Engineers, Vol.**59**, pp763-787.

Wilson, W.H. and Moore, H.F., (1917), "Tests to determine the rigidity of Riveted Joints in Steel Structures", University of Illinois, Engineering Experimentation Station, Bulletin No. 104, Urbana, USA.

Witteveen, J., Stark, Jan.W.B., Bijlaard, Frans. S.K. and Zoetemeijer, P., （1982）, "Welded and Bolted Beam-to-Column Connections", Journal of the Structural Division, ASCE, Vol.**108** (2), pp433-455.

Xiao, Y., Choo, B.S. and Nethercot, D.A., (1994), "Composite Connections in Steel and Concrete. I. Experimental Behaviour of Composite Beam-Column Connections", Journal of Constructional Steel Research, Vol.**31**, pp3-30.

Yamaki, N. (1959), "Post-Buckling Behaviour of Rectangular Plates with small Initial Curvature Loaded in Edge Compression", Journal of Applied Mechanics, Vol.**26**.

Yee, Y.L. and Melchers, R.E., (1986), "Moment-Rotation Curves for Bolted Connections", Journal of Structural Engineering, ASCE, Vol.**112(**3), pp615-635.

Zandonini, R. and Zanon, P., (1989), "Experimental Analysis of End Plate Connections", Connections in Steel Structures: Behaviour, Strength and Design, Elsevier Applied Science Publishers, London, pp41-51.

Zaras, J. Rhodes, J. and Krolak, M. (1992), "Buckling and Post-Buckling Behaviour of rectangular Plates under Linearly Varying Compression and Shear: Part 1-Theoretical Analysis", Thin-Walled Structures, Vol. **14**, pp59-87.

Zoetemeijer, P., (1983), "Summary of the Research on Bolted Beam-to-Column Connections", Report No.6-85-M, Steven Laboratory, Delft.